Title
Detection of Hidden Defects in Stiffened and Fiber-Metal Laminate Composite Aircraft and Aerospace Structural Components using Ultrasonic Guided Waves

Author
Tai, Wai Hong Hong

Publication Date
2020

Peer reviewed|Thesis/dissertation

UNIVERSITY OF CALIFORNIA

Los Angeles

Detection of Hidden Defects in Stiffened and Fiber-Metal Laminate Composite Aircraft and Aerospace Structural Components using Ultrasonic Guided Waves

A dissertation submitted in partial satisfaction of the

requirements for the degree of Doctor of Philosophy

in Mechanical Engineering

by

Wai Hong Tai

2020

ABSTRACT OF THE DISSERTATION

Detection of Hidden Defects in Stiffened and Fiber-Metal Laminate Composite Aircraft and Aerospace Structural Components using Ultrasonic Guided Waves

by

Wai Hong Tai

Doctor of Philosophy in Mechanical Engineering

University of California, Los Angeles, 2020

Professor Ajit K. Mal, Chair

The objective of this research is to develop an improved nondestructive evaluation (NDE) technique to inspect composite aircraft and aerospace structures. This work presents an efficient and versatile numerical modeling tool to aid in the design of cost-effective non-destructive evaluation technologies. The global-local method, which combines finite element discretization and Lamb wave modal expansion is used. An extension to the traditional global local method is made to couple the source problem with the scattering problems to deal with a surface source generating Lamb waves that interact with defects in multilayered structures. The modeling tool is first validated against analytical solution and the finite element method. Since the relationship between ultrasonic signal change and the nature of defects is complex, the efficient modeling tool is used to create a library of many damage inspection scenarios for FML and stiffened composites. The waveforms associated to the different damage cases are then used to establish a set of damage indices for damage characterization.

The dissertation of Wai Hong Tai is approved.

Nsar Ghoniem

Lihua Jin

Jenn-Ming Yang

Ajit Mal, Committee Chair

University of California, Los Angeles

2020

TABLE OF CONTENTS

LIST OF FIGURES

LIST OF TABELS

ACKNOWLEDGEMENTS

I would like to express my deepest gratitude to professor Ajit Mal for his guidance and support for the entirety of my graduate studies. Every single aspect of this work is shaped by his tireless teaching and mentoring throughout the many insightful discussions and careful explanations. I would also like to thank professor Ghoniem, professor Jin, professor Yang, professor Schaal, and professor Goyal to be my committee members and give me important feedback during prospectus and their review for the final defense. In particular, I would like to thank professor Schaal for his immensely valuable inputs and contributions to this work. I would also like to give my thanks to professor Goyal, Dr. Jacob Rome and the Aerospace Corporation for their continues support for this research and bring industry applications into this work. I would like to give my heartfelt appreciation to my lab members Leonardo Araque and Lifu Wang for their long time support, input and contributions to this work.

VITA

2011-2014	B.S. Mechanical Engineering, Cum Laude, University of California at Los Angeles
2014-2015	M.S. Mechanical Engineering, University of California at Los Angeles
2018	Ph.D. Advanced to Candidacy

PUBLICATIONS

1. Tai, S., Kotobuki, F., Wang, L., and Mal, A. (May 11, 2020). "Modeling Ultrasonic Elastic Waves in Fiber-Metal Laminate Structures in Presence of Sources and Defects." ASME. ASME J Nondestructive Evaluation. November 2020; 3(4): 041102.

2. S. Tai, L. Wang, L. Araque, A. Mal and C. Schaal, "Effects of Homogenization and Quasi-Isotropy Assumptions on Guided Wave-Based Nondestructive Testing Methods," in *International Workshop on Structural Health Monitoring 2019*, Stanford , 2019

3. C. Schaal, S. Tai and A. Mal, "On the Assumption of Transverse Isotropy of a Honeycomb Sandwich Panel for NDT Applications," in *Health Monitoring of Structural and Biological Systems 2017*, Protland, 2017.

4. Steffen Tai, Fumika Kotobuki, Ajit Mal, Christoph Schaal, "Numerical and experimental investigation of damage detection in stiffened composite panels using guided ultrasonic waves," Proc. SPIE 11381, Health Monitoring of Structural and Biological Systems XIV, 1138102 (6 May 2020);

Chapter 1 Introduction

1.1 Background and Motivation

1.1.1 A Brief Introduction to Non-Destructive Evaluation of Aerospace Structures

This research is motivated by the need to develop efficient and cost-effective non-destructive evaluation (NDE) for aerospace structures. Unlike civil, automotive or naval structures, aerospace structures are subjected to more demanding weight restrictions. Designed for a reasonable service life, the flight structures are often being operated close to their design limits to make their applications economically viable. Therefore, it has been a well-accepted philosophy to include periodic inspections into their manufacturing process and service life to minimize the risk of their structural failure. The goal of inspection is to detect and to determine the criticality of defects that may occur during manufacturing or in service. A decision can then be made to determine whether or what corrective actions are needed. Such is the principle of non-destructive evaluation (NDE). The safety and the life cycle cost of defect-critical structures are closely related to the quality of the NDE that are subjected to during their operation. The NDE technique should have a high probability of detection, is low cost, reliable, efficient, and simple to use. Another challenge that has become more pronounced is the data size collected from an inspection. Advanced NDE methods (e.g. CT scan) have detailed sensing and are generating an increasingly large amount of data [1]. The data processing, storage, interrogation, and analytics become inefficient when all the raw sensing data is stored for the entire service life of the structure. Thus, an effective NDE should be able to inspect a large structure with less data requirements.

Different Types of NDE Techniques

A variety of NDE techniques are used in industry including visual inspection, ultrasonic testing, thermography, liquid penetrant testing, high energy radiography, computer-tomography (CT), and Eddy current based methods. The details of the methods can be found in a variety of sources available in the open literature, e.g., [2].

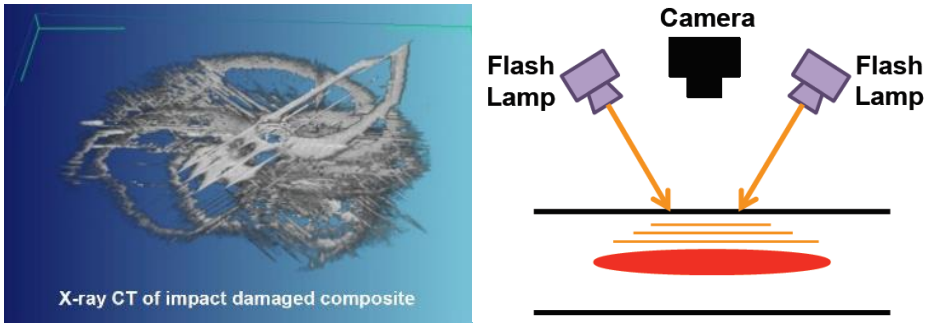

Figure 1-1 CT reconstruct X-ray scan result into detailed 3D image of damage, and thermography schematic (Image: [3])

While each technique is effective in detecting certain types of defect in some structures, most of them lack the speed and accuracy to inspect large structures with a high degree of confidence. As an example, radiographical and CT techniques have a very high fidelity (less than 0.5mm resolution) and can yield detailed information on small defects. However, the size of the inspection area must be very small because of the small area coverage of the equipment. Moreover, the associated equipment is expensive thus restricting the commercial applicability of the method to large structures. Liquid penetrant testing and thermography can inspect a larger area and can reveal small defect with good details. However, neither method can detect and characterize deep subsurface defects. In addition, thermal source and liquid dye might not be adaptable to some inspection conditions. Eddy current based method is applicable only to conductive materials. In contrast, ultrasound-based tests have a much wider range of applicability and the necessary hardware to provide the most flexible inspection scheme. The

detectable size and types of defects are also abundant. The area of inspection can also be quite large in many cases but may require significant time and effort to cover. The cost and availability of ultrasound testing (UT) is reasonable, and thus most Aerospace structures are inspected by ultrasound based NDE methods. However, the reliability of UT varies across inspection scenarios, and requires adequate training of skilled technicians as in other NDE techniques. Because of the flexibility of UT, it is usually the most preferable method for general inspection. However, the UT inspection of a larger areas is inefficient with conventional through-thickness inspection, and access to surfaces above or below the damage is not always possible. Alternatively, NDE using guided ultrasonic waves, as illustrated in Figure 1-2 has the potential to localize damage in a large area with a relatively small number of surface mounted transducers. Due to their long propagation distance, guided waves can be excited from a source transducer mounted at one end of a structure and receiving transducers can be mounted on the other end to detect damage in the area in between. [4] [5] [6]. If a detailed characterization of the defects is needed, it can be supplemented by other higher resolution NDE techniques to fully characterize the damage. UT could be combined with other methods for detailed local inspection to form a comprehensive evaluation. Since ultrasound-based methods are widely used, advancements in this approach can be highly beneficial in a wide range of applications.

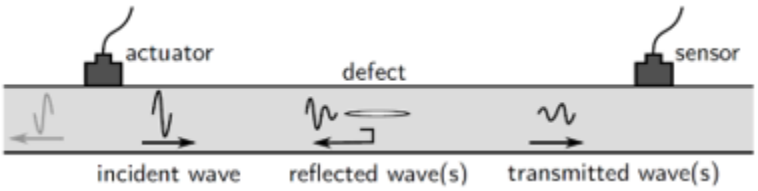

Figure 1-2 Guided waves in plate can be used to detect damage with a small number of surface mounted transducers by examining the changes in the transmitted or reflected waves

1.1.2 Some NDE Requirements for Launch Vehicle Structures

Launch vehicle (LV) are important to ensure the reliable and on-time delivery of often very expensive, and time sensitive payloads into orbit. These payloads are essential to communications, navigation, and space exploration. As the demands for lowering cost, faster production, and heavier launch requirements are increased, the LV structural designs become increasingly complex and present significant challenge to their NDE requirements. In this section, some important structural considerations of launch vehicles and their NDE needs are discussed.

Structural Components of a Launch Vehicle (LV)

The primary structures include main propellant tanks, inter-stages, inter-tanks, fairings, engine thrust structures, and payload fittings/adapters. The first four are large shell structures subjected high pressure, and aerodynamic loads. Figure 1-3 shows how these shell structures are situated in a schematic of a prototypical launch vehicle. The figure shows the solid rocket motors (red arrows), the core shells structures which could be propellent tank structure or composite segments (purple arrows) which are large pressurized shells and payload fairings (green arrows). These components could be connected by bolted joint indicated by the blue arrows.

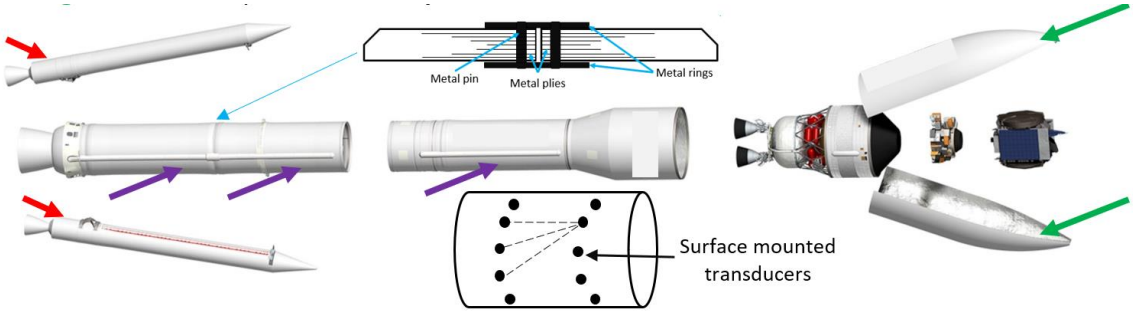

Figure 1-3 An illustration of typical LV components made up with large cylindrical shell structures that could be inspected by guided wave based NDE with surface mounted transducers.

The extreme demand in structural performance in LV prompts the use of composites, and advanced composite structures (such as Fiber Metal Laminates or FML and sandwich structures). The usage of composites in LV is usually in large sizes and with critical functionalities. In the upcoming generation of vehicles, composite based components such as composite overwrap pressure vessels (COPV), graphite epoxy solid rocket motors (GEM) and filament wound composite pressure vessels (Figure 1-4), are now being designed and manufactured in ever larger sizes than were used in previous generations. The increase in size presents new challenges for inspection.

Figure 1-4 (L) Composite overwrap pressure vessel (Image: structures.aero). (R) Graphite epoxy motor (Image: spaceflight101), (B) Filament wound composite pressure vessel (Image: AIAA.org)

The payload and the launch vehicle are extremely costly and any failure during launch can have highly detrimental consequences. As an example, the SpaceX launch pad static fire failure on Sep 1, 2016, was related to a void in the liner of a composite overwrapped pressure vessel carrying liquid oxygen. The oxygen was trapped in the liner void and ignited due to friction

ignition from composite fiber breakage [7]. This failure resulted in the complete loss of the satellite payload (valued at approximately $200 million), the vehicle, and significant damage to the launch pad (Figure 1-5). It also resulted in halting launch operations for over four months.

Figure 1-5 COPV failure caused the loss of payload, vehicle and damage to the launch facility during SpaceX Sep 1 2016 pre-launch (Image: US Launch Report).

Launch Vehicle NDE Considerations

The way a launch vehicle incorporates NDE to ensure successful operation is quite different from what is done in the aeronautical industry. Traditionally, aircrafts are inspected in regular intervals over their service life. Thus, the needs for aircraft industry are to have a more efficient method to reduce the out-of-service inspection time, and to increase the inspection sensitivity in order to reduce the time between inspections. Then of course, the idea of structural health monitoring (SHM) became the future goal for the industry, where through continuous monitoring, any defects that occur during service would be reported to the operator with enough information to determine its criticality. A decision could then be made on whether to return to ground or if the plane could continue servicing. This concept of SHM can eliminate the need for regular inspection and allows the aircraft to be in service continuously [8]. Launch vehicles, however, could not apply this philosophy because it is impractical to reverse a launch in mid-air. Even with the emerging reusable launch vehicle, SHM is still not practical because of the weight

restriction and the extremely low tolerance of failure (partly due to the even lower damage tolerance in design for weight savings). For launch vehicles, the philosophy is 100% mission assurance through an incremental build process, with validation and verification testing that are "test-like-you-fly [3]." That is, throughout the build process, there are a series of qualification and acceptance tests, and NDE is integrated into these steps. Thus, the launch vehicle industry is facing two fundamental NDE challenges, 1) the time cost of installing and removing the NDE instrumentation, making inspection in every test prohibitive, 2) as the vehicles are made larger, and with complex composite structures makes inspection difficult and less reliable. Consider the example of the progression of a solid rocket motor shown in Figure 1-6.

Figure 1-6 (L) Empty composite segment case (Image: Airforce-technology.com), (ML) prepare for hydro-pressurize test (Image: Spaceflight Insider) (MR) Segment after solid fuel casting (Image: nasaspaceflight.com), (R) Static fire test (Image: Northrop Grumman Newsroom).

The composite segment case is wound, the segment-end joining rings are installed, and are subjected to NDE. Then the insulation lining is installed and is hydro-pressurized-proof tested. Subsequently the solid fuel is cast, and the critically important NDE is done to ensure that there is no gap between the fuel, the lining, and the case. Multiple segments are then joined together for use. NDE is done to inspect the joint quality. The interweaving between testing and inspection could be greatly speeded up if the NDE procedure can be easily integrated with testing. Lamb wave based NDE is one of the most potent solutions for this since it can inspect a large area of a shell structure with minimal field deployable sensor instrumentation. Thus, it

opens up the possibility to conduct evaluation during the many qualification and acceptant tests and offers more information than the existing practice of using local acoustic methods that are primarily based on acoustic emission.

1.1.3 Fiber Metal Laminate Composite Structures in Aerospace Applications

Fiber Metal Laminates (FML) can be described as laminated materials consisting of thin layers of metal sheets and fiber layers embedded in an adhesive system [9]. The breath of FML research is immense because of the relevance of decades of metallic and polymer matrix composites (PMC) development. Therefore, in this section only a brief description of the application history, general discussion of some of the key considerations of using FML, and a key application in launch vehicle is given here.

FML Applications in Aircrafts

Among the very first FML concept appears in the 1970s with the use of Aramid Reinforced Aluminum Laminate (ARALL) lead by Schliekelmann at Fokker Aircraft, Vogelesang and Schijve at Delf University [10]. Some of the practical reasons for using FML include, the high cost, and technical difficulties to produce large scale composites. To reduce the risk of using full size composites, bonding metal sheets with PMC is a reasonable engineering decision [10]. Early research combining the effort of Fokker, Delf and the Dutch National Laboratory (NLR) produced an F-27 wing panel demo article [10]. It was found that the fatigue performance of FML parts is far superior to that of their metal and PMC counterparts because of the fiber-bridging effect. The stiff aramid fibers adjacent to the metal layer keep the crack in the metal layer from opening. Throughout the 1980s, ARALL saw applications into various aircraft secondary structures such as cargo doors, and panels. Standardization of ARALL grades motivated by the industry made designing aircrafts with the ARALL material system possible

[10]. In the late 1980s and in the 1990s, an updated FML design with glass fibers reinforced aluminum (GLARE) emerged to improve the weak fiber capability in ARALL. GLARE shows excellent impact resistant, chemical resistance and burn-through properties [11]. When GLARE can be joined by splicing techniques, it has seen wider range of applications in airbus (A380, A340, A320) in the form of fuselage sections, stiffener, floor panel, etc. as well as in structural repair and other functions. In 2000s, other variants with carbon fiber-based PMC, and other metal constituents (such as titanium) appeared for enhanced performance. This new class of FML boost a higher temperature capability which is suitable for more space applications.

The quality of FML structures is highly dependent on the adhesive bonding between the metal layers and the PMCs. Different bonding (surface) treatments (e.g. mechanical, chemical, electrochemical, etc.) have been studied for better bonding. The other important effects would be the layup design. The number of plies, orientation and layup placement can be tailored for specific load applications. A more detailed summary of FML designs can be found in [12].

Potential FML Applications in Space Industry

The newer class of carbon-fiber epoxy/titanium based FML has strong potential to be applied to launch vehicles because of their mechanical performance and the familiarity of using composites in the space industry. Yet, the application of Carbon-Reinforced/Ti based FML is very limited. A key study of a spacecraft payload adaptor done by Fink et. al. [13] shows a comprehensive set of results to demonstrate the performance increase with the use of FML. In that study, a series of coupon testing is done with different Ti content to evaluate bearing strength showing that their bearing capability outperformed the composite counterparts. This study also includes larger component testing to evaluate the bolted joint performance near a region of multiple rows of bolt holes. This study provides important insights on how CFRP/Ti

FML can improve joint design. Current composite joint design requires thickness increase near the joint section. The asymmetric thickness increases usually induce some bending load. In addition, multiple rows of pins are needed to distribute the bearing load to a wider section of composite. With the use of the hybrid FML near the joint region (as shown in Figure 1-7), the bearing capacity would increase, and less row of pins would be needed. Then, the composite section would no longer require a thickness increase. As a result, the launch vehicle weight is reduced resulting in a larger payload capacity with a shorter assembling time.

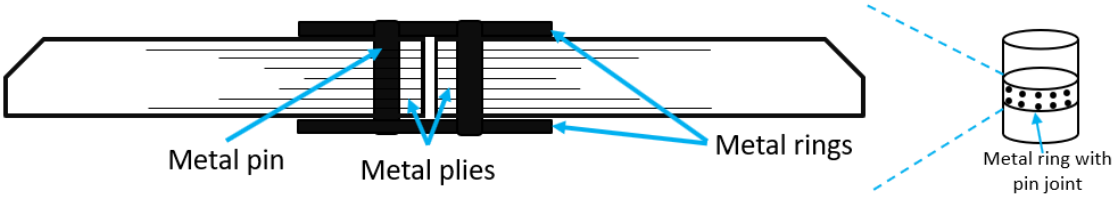

Figure 1-7 Using hybrid FML near joint can increase bearing performance for joining composite segments

However, no FML is used in current launch vehicle because of the lack of adequate knowledge in their design. Furthermore, for such design to be used in an active vehicle, a reliable NDE technique must be in place. Thus, the fundamental research of the NDE aspect of FML structures would greatly benefit future launch vehicle designs.

1.2 Scope of Research

The relatively uniform cylindrical structure in LV is ideal for using Lamb waves to detect damage in large areas by mounting ultrasonic transducers near the end of each segments. This work aims to address the fundamental research needs in implementing ultrasonic sensor network on composite LV segments. In order to develop the signal processing techniques for accurate damage characterization, the nature of the Lamb wave interaction with defects must be well understood. The objective of this study is 1) develop a general and numerically efficient modeling tool that is capable of representing the diverse range of ultrasonic inspection scenarios.

2) this tool can then be used to create a library of ultrasonic signals for different types of possible defects and finally, 3) to demonstrate a framework that uses this signal library to characterize the defects. Figure 1-8 summarizes the major components of this dissertation.

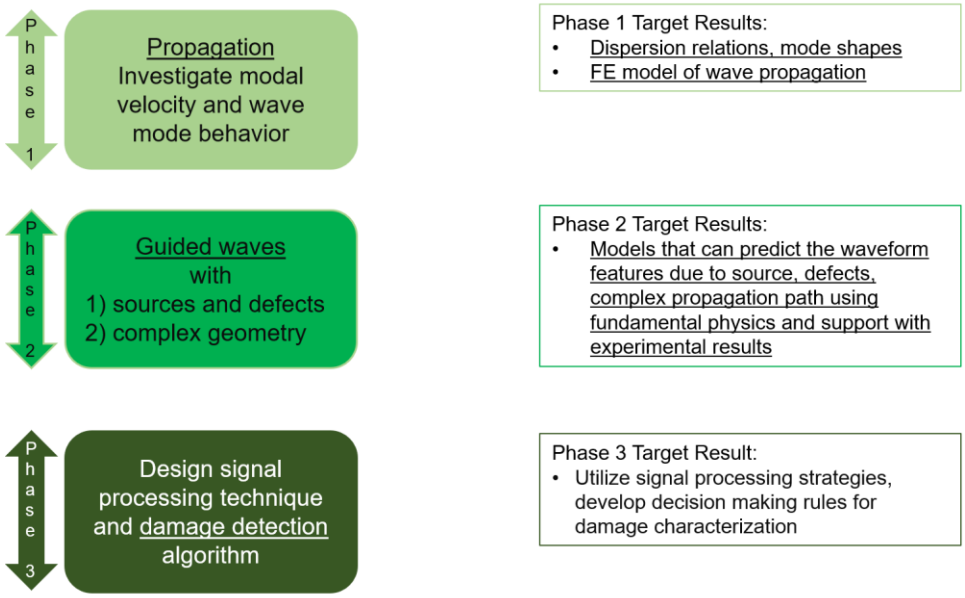

Figure 1-8 Breakdown of scope of research

The first phase is to study the wave propagation in multilayer medium without defects. **Chapter 2** presents the wave propagation theory for computing the dispersion curves and the modal functions, which describe the free wave propagation characteristics in composite structures. This is achieved by using the global matrix (chapter 2.1) and the waveguide finite element method (chapter 2.2). These results are validated by the available theoretical solutions and experimental measurements. **Chapter 3** presents the global local method (GLM), a semi-analytical method to model the Lamb wave response to sources and defects. The dispersion curves and the modal functions from phase 1 are the input for the global local method in phase 2. Furthermore, the numerical and modelling considerations for using the GLM are discussed in detail to insure a robust implementation. Continuing with phase 2, **Chapter 4** presents a detailed study of the interaction of selected defects with Lamb waves in FML to determine their

waveform characteristics. By building many GL models, structural configurations, defect types and sizes are modeled to create a waveform library. Then, the library is used in phase 3 to select the sensitive scattering characteristics to develop characterization strategies with a number of damage indices. Finally, numerical test cases with unknown damage types are applied to the proposed strategy to simulate an inspection. The robustness of the damage indices and the method of their characterization are discussed. **Chapter 5** presents the waveform library for stiffened composite structures. The various GL models are used to determine the feasibility of using Lamb waves to characterize hidden damages in a multi-stiffener configuration.

Chapter 2 Lamb Wave Propagation in Multilayered Plates

Propagating waves that guide energy along the plate are generally referred to as Lamb waves. The propagation of harmonic waves in isotropic plates and their applications to NDE have been studied extensively. Readers are referred to the following standard literatures for a detailed discussion [14] [15] [16] [17]. In this chapter, a brief description is given for the Lamb wave propagation in a laminated plate structure that is free of defects. An analytical method, the global matrix method (GMM), and a semi-analytical method, the waveguide finite element (WFE) method, are used to calculate the dispersion curve and modal functions that are used in the global-local method in Chapter 3.

2.1 The Global Matrix Method

The Lamb wave solution of the elastic wave propagation in a multilayered medium can be formulated from the solution of a single layer and then consider their interactions between layers. A matrix formulation can account for all the different layers systematically and then the system of matrix equations can be solved numerically.

2.1.1 A Review of the Global Matrix Method

The early use of matrix procedure to device solution for elastic wave in plate problem are done by Thomson [18] and Haskell [19]. Thomson introduces the transfer matrix to correlate the displacement, and stresses between two layers. Then, the solution for the multilayered system can then be found as a product of the transfer matrices to relate each layer to the top layer. Although the matrix size is relatively small, and thus have a smaller computational storage requirement, the method is not numerically stable if the frequency-thickness product is large. This is because the formulation involves a matrix inversion of an exponential term with

frequency and thickness in the exponent that can become large. The matrix method introduced by Knopoff [20], considers the SH wave propagation in multilayered medium, assembles the matrices of displacement/stress continuity for all layers all at once. Although the matrix storage requirement is larger, the numerically instability problem in transfer matrix method can be completely avoided by the global matrix method. The computational storage nowadays is ample for most personal computers, and the robustness of the global matrix method is desirable. Mal introduced the global matrix method for guided waves in general multilayer isotropic and composite laminates, and special half space problems [21]. The composite laminate problem is also formulated using the global matrix [22]. The global matrix method is effective in modelling the contributions for each layer of a composite plate. The dispersion curves are validated with leaky Lamb wave experiment [23]. The global matrix equations are in general complex valued and are very difficult to interpret and solve. The global matrix method can also be modified to include interface slip in the form of displacement jumps, and to solve for the force response when the multilayered system is subjected to surface loads [22].

2.1.2 Global Matrix Method for a Transversely Isotropic Material

A review of the formulation for the modal solution of wave propagation in a multilayer system in which the individual layers are transversely isotropic with their symmetry axes are normal to their layers is given in this section.

Formulating the Layer Matrix Equations

Consider one layer in the multilayered system shown Figure 2-1, in which the material is assumed to be isotropic in x_1-x_2 plane and is symmetric about the x_3 axis.

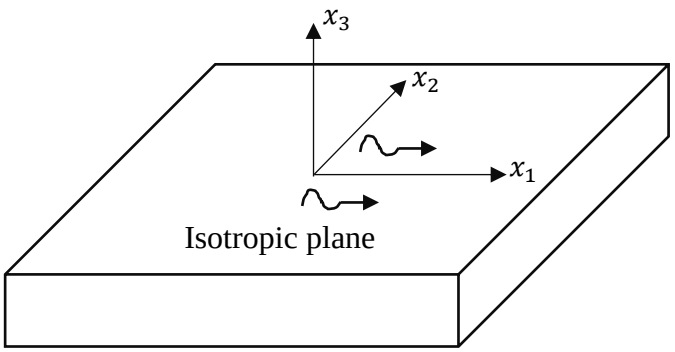

Figure 2-1 A layer, described by a transversely isotropic medium with symmetry about the x_3 axis. The Lamb waves are assumed to propagate in the x_1 direction

Assuming a plane-strain model on x_1-x_3 plane, the displacements associated with time harmonic Lamb waves propagating along the x_1 direction, have the form

$$u_j = A_j e^{i(kx_1 - \omega t) - \eta x_3} \tag{2-1}$$

where A_j is the frequency dependent amplitude, k is the wavenumber, ω is the angular frequency, and η is a function to be determined by satisfying the equation of motion, strain-displacement relations and material law. The equation of motion in absence of body force is given by

$$\frac{\partial \sigma_{11}}{\partial x_1} + \frac{\partial \sigma_{13}}{\partial x_3} - \rho \frac{\partial^2 u_1}{\partial t^2} = 0$$

$$\frac{\partial \sigma_{13}}{\partial x_1} + \frac{\partial \sigma_{33}}{\partial x_3} - \rho \frac{\partial^2 u_3}{\partial t^2} = 0 \tag{2-2}$$

The linear transversely isotropic stress-strain relation under the plane strain conditions is

$$\begin{Bmatrix} \sigma_{11} \\ \sigma_{33} \\ \sigma_{13} \end{Bmatrix} = \begin{bmatrix} C_{11} & C_{13} & 0 \\ C_{13} & C_{33} & 0 \\ 0 & 0 & (C_{11} - C_{13}) \end{bmatrix} \begin{Bmatrix} u_{1,1} \\ u_{3,3} \\ \frac{1}{2}(u_{1,3} + u_{3,1}) \end{Bmatrix} \tag{2-3}$$

The constants (C_s) are defined in terms of the more commonly used elastic constants in the appendix section 2.3.

Substituting the expression for the displacements given in (2-1) into the constitutive relations in (2-3), the stresses can be obtained as

$$\sigma_{11} = C_{11}(iku_1) + C_{13}(-\eta u_3) \qquad \sigma_{33} = C_{13}iku_1 + C_{33}(-\eta u_3)$$

$$\sigma_{13} = (C_{11} - C_{13})[-\eta u_1 + iku_3]$$

(2-4)

Defining $C_{44} = C_{11} - C_{13}$, and substituting the stresses from (2-4) into the equation of motion (2-2) results in the following system of homogeneous equations for the unknown constants A_1 and A_3

$$\begin{bmatrix} \eta^2 C_{44} + \rho\omega^2 - k^2 C_{11} & -ik\eta(C_{13} + C_{44}) \\ -ik\eta(C_{13} + C_{44}) & \eta^2 C_{33} + \rho\omega^2 - k^2 C_{44} \end{bmatrix} \begin{Bmatrix} A_1 \\ A_3 \end{Bmatrix} = \begin{Bmatrix} 0 \\ 0 \end{Bmatrix}$$

(2-5)

For a non-trivial solution for A_1 and A_3, η is determined from the root of the following quartic equation

$$\eta^4 + \eta^2 k^2 \left[\frac{\rho c^2}{C_{33}} + \frac{\rho c^2}{C_{44}} - \frac{C_{11}C_{33} - C_{13}^2 - 2C_{13}C_{44}}{C_{33}C_{44}}\right] + k^4 \left(\frac{\rho c^2}{C_{44}} - 1\right)\left(\frac{\rho c^2}{C_{33}} - \frac{C_{11}}{C_{33}}\right) = 0$$

(2-6)

where $k = \frac{\omega}{c}$ and c is the phase velocity.

With the definitions of the bulk wave velocities,

$$c_{1L} = \sqrt{\frac{C_{11}}{\rho}} \qquad c_{3L} = \sqrt{\frac{C_{33}}{\rho}} \qquad c_{3T} = \sqrt{\frac{C_{44}}{\rho}}$$

(2-7)

The constant η can be obtained as

$\pm\eta_{1,2} = k\sqrt{\frac{-A \pm \sqrt{A^2 - 4B}}{2}}$ where $Im(\eta_j) < 0$ for decaying wave in the thickness direction

(2-8)

and, $A = \frac{c^2}{C_{3L}^2} + \frac{c^2}{C_{3T}^2} - \frac{C_{11}C_{33} - C_{13}^2 - 2C_{13}C_{44}}{C_{33}C_{44}}$ and $B = \left(\frac{c^2}{C_{3T}^2} - 1\right)\left(\frac{c^2}{C_{3L}^2} - \frac{C_{11}}{C_{33}}\right)$. The $\pm$ sign indicate the upward and downward propagating bulk waves as illustrated in Figure 2-2.

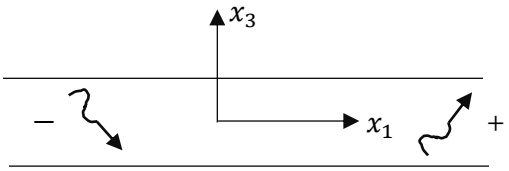

Figure 2-2 The upward and downward propagating wave in the η definition

The relationship between the horizontal and vertical displacement components, must satisfy the system of equations (2-5) and yield the ratio of amplitudes

$$\frac{A_3}{A_1} = \frac{k^2 C_{11} - \rho\omega^2 - \eta_j^2 C_{44}}{-ik\eta_j(C_{13} + C_{44})} \equiv \beta_j$$

(2-9)

From the original assumed form of displacement in (2-1), η is related to the wavenumber component in the thickness direction that corresponds to the bulk waves that propagate upward or downward. Since the ratio defined as β_j would have upward (+) and downward (-) propagating directionality (Figure 2-2) it is written as $\beta_j^{\pm}$ respectively. The next step is to write the displacements and stresses for a single layer and apply the appropriate boundary conditions.

Displacements and stresses in the mth layer

Consider the m^{th} layer occupying the region $z_{m-1} < z < z_m$, as shown in Figure 2-3.

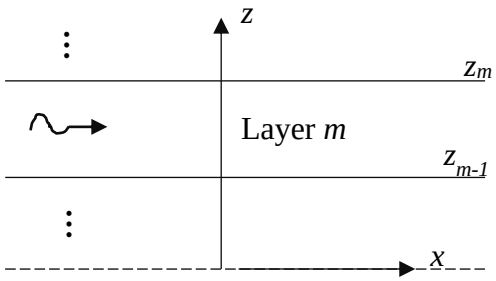

Figure 2-3 A layer (layer *m*), described by the coordinate system (*x*, *z*)

For this generic layer, the displacements are written as

$$u(x,z,\omega,k) = U(z,\omega,k)\, e^{i(kx-\omega t)} \tag{2-10}$$

For simplicity, the term $e^{i(kx-\omega t)}$ is omitted in the following derivations, so that the displacement components are given as

$$U_x(z,\omega,k) = \left[C_1 e^{-\eta_1(z-z_{m-1})} + C_2 e^{-\eta_2(z-z_{m-1})} + C_3 e^{-\eta_1(z_m-z)} + C_4 e^{-\eta_2(z_m-z)}\right] \tag{2-11}$$

$$U_z(z,\omega,k) = \left[\beta_1 C_1 e^{-\eta_1(z-z_{m-1})} + \beta_2 e^{-\eta_2(z-z_{m-1})} - \beta_1 C_3 e^{-\eta_1(z_m-z)} - \beta_2 C_4 e^{-\eta_2(z_m-z)}\right] \tag{2-12}$$

Substituting these expressions in equation (2-4), the stresses become

$$\begin{aligned} S_{xx}(z,\omega,k) = {} & C_1[ikC_{11} - C_{13}\beta_1\eta_1]e^{-\eta_1(z-z_{m-1})} + C_2[ikC_{11} - C_{13}\beta_2\eta_2]e^{-\eta_2(z-z_{m-1})} \\ & + C_3[ikC_{11} - C_{13}\beta_1\eta_1]e^{-\eta_1(z_m-z)} + C_4[ikC_{11} - C_{13}\beta_2\eta_2]e^{-\eta_2(z_m-z)} \end{aligned} \tag{2-13}$$

$$\begin{aligned} S_{xz}(z,\omega,k) = {} & C_1C_{44}[-\eta_1 + ik\beta_1]e^{-\eta_1(z-z_{m-1})} + C_2C_{44}[-\eta_2 + ik\beta_2]e^{-\eta_2(z-z_{m-1})} \\ & + C_3C_{44}[\eta_1 - ik\beta_1]e^{-\eta_1(z_m-z)} + C_4C_{44}[\eta_2 + ik\beta_2]e^{-\eta_2(z_m-z)} \end{aligned} \tag{2-14}$$

$$\begin{aligned} S_{zz}(z,\omega,k) = {} & C_1[ikC_{13} - C_{33}\beta_1\eta_1]e^{-\eta_1(z-z_{m-1})} + C_2[ikC_{13} - C_{33}\beta_2\eta_2]e^{-\eta_2(z-z_{m-1})} \\ & + C_3[ikC_{13} - C_{33}\beta_1\eta_1]e^{-\eta_1(z_m-z)} + C_4[ikC_{13} - C_{33}\beta_2\eta_2]e^{-\eta_2(z_m-z)} \end{aligned}$$

(2-15)

The displacements and traction components at the interfaces between layers *m*-1 and *m*, given in equations (2-11),(2-12),(2-14) and (2-15) are written in matrix form as

$$\begin{Bmatrix} U_x \\ U_z \\ S_{xz} \\ S_{zz} \end{Bmatrix} = \begin{bmatrix} q_{11} & q_{12} & q_{11} & q_{12} \\ q_{21} & q_{22} & -q_{21} & -q_{22} \\ q_{31} & q_{32} & -q_{31} & -q_{32} \\ q_{41} & q_{42} & q_{41} & q_{42} \end{bmatrix} \begin{bmatrix} e^{-\eta_1(z-z_{m-1})} & 0 & 0 & 0 \\ 0 & e^{-\eta_2(z-z_{m-1})} & 0 & 0 \\ 0 & 0 & e^{-\eta_1(z_m-z)} & 0 \\ 0 & 0 & 0 & e^{-\eta_2(z_m-z)} \end{bmatrix} \begin{Bmatrix} C_1 \\ C_2 \\ C_3 \\ C_4 \end{Bmatrix}$$

(2-16)

with the following substitutions

$$q_{11} = 1 \qquad q_{12} = 1$$

$$q_{21} = \beta_1 \qquad q_{22} = \beta_2$$

$$q_{31} = C_{44}[-\eta_1 + ik\beta_1] \qquad q_{32} = C_{44}[-\eta_2 + ik\beta_2]$$

$$q_{41} = [ikC_{13} - C_{33}\beta_1\eta_1] \qquad q_{42} = [ikC_{13} - C_{33}\beta_2\eta_2]$$

(2-17)

To further simplify the description of (2-16), define the following block matrices

$$[Q(m)] = \begin{bmatrix} Q_{11}^m & Q_{12}^m \\ Q_{21}^m & Q_{22}^m \end{bmatrix}$$

(2-18)

$$[E(z,m)] = Diag[e_1(z-z_{m-1})\ e_2(z-z_{m-1})\ \ e_1(z_m-z)\ e_2(z_m-z)] = \begin{bmatrix} E_1 & \mathbf{0} \\ \mathbf{0} & E_2 \end{bmatrix}$$

(2-19)

where $e_j = e^{-\eta_j}$. Note that E_1, and E_2 correspond to upward and downward propagating waves, respectively.

$$\{C(m)\} = \begin{Bmatrix} C_m^- \\ C_m^+ \end{Bmatrix}$$

(2-20)

Therefore, C_m^- and $C_m^+$are the amplitude coefficients for the downward and upward propagating waves, respectively.

Equation (2-16) can now be written in a more compact form as

$$\begin{Bmatrix} U_x^m \\ U_z^m \\ S_{xz}^m \\ S_{zz}^m \end{Bmatrix} = [Q(m)][\mathrm{E}(z,m)]\{C_m\} \tag{2-21}$$

Interface Conditions and Boundary Conditions

The notations shown in Figure 2-4 are used to define the layered structure. For a stack of *N* layers, the first layer, of thickness h_1 has bottom surface at $z = 0$. The top surface of layer 1 is interfaced with layer 2 at $z = h_1$.

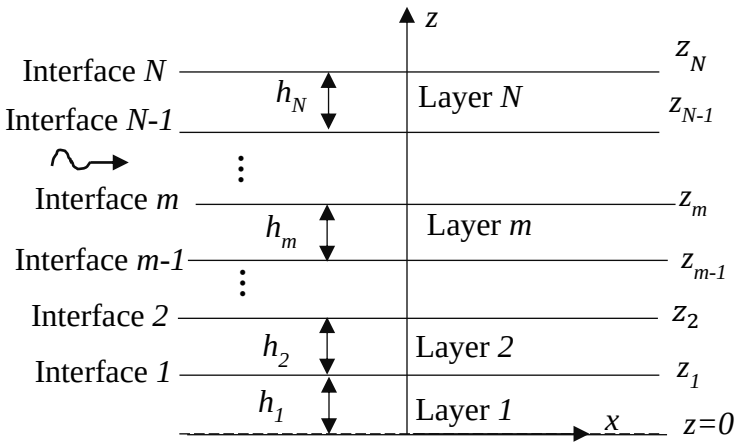

Figure 2-4 The coordinate system for assembling the global matrix equations for a multilayered system

For a general layer *m*, between interface layer *m-1* and *m*, the lower surface is at $z = z_{m-1}$ and the upper surface is at $z = z_m$. We can then describe the continuity conditions for the traction and displacement components at the interfaces as shown in Figure 2-4. Noting that the traction components at the bottom face of layer *m* is

$$S^{layer\ m}(z_{m-1}) = [Q(m)E(z_{m-1})]\{C(m)\} \tag{2-22}$$

shall be equal to the traction components at the top surface of layer *m-1*, which are

$$S^{layer\ m-1}(z_m) = [Q(m-1)E(z_m)]\{C(m-1)\}$$

(2-23)

The continuity of displacements and traction at the interface I_{m-1} yields

$$\begin{bmatrix} Q_{11}^m & Q_{12}^m \\ Q_{21}^m & Q_{22}^m \end{bmatrix} \begin{bmatrix} 1 & 0 & 0 & 0 \\ 0 & 1 & 0 & 0 \\ 0 & 0 & e^{-\eta_1 h_m} & 0 \\ 0 & 0 & 0 & e^{-\eta_2 h_m} \end{bmatrix} \begin{Bmatrix} C_m^- \\ C_m^+ \end{Bmatrix} = \begin{bmatrix} Q_{11}^{m-1} & Q_{12}^{m-1} \\ Q_{21}^{m-1} & Q_{22}^{m-1} \end{bmatrix} \begin{bmatrix} e^{-\eta_1 h_{m-1}} & 0 & 0 & 0 \\ 0 & e^{-\eta_2 h_{m-1}} & 0 & 0 \\ 0 & 0 & 1 & 0 \\ 0 & 0 & 0 & 1 \end{bmatrix} \begin{Bmatrix} C_{m-1}^- \\ C_{m-1}^+ \end{Bmatrix}$$

(2-24)

For the top layer *N*, the traction free boundary condition at the at the top surface $z = z_N$ is

$$\begin{Bmatrix} S_{xz} \\ S_{zz} \end{Bmatrix} = [Q_{21}^N][E_1^N(z_N)]\{C_N^-\} + [Q_{22}^N]\{C_N^+\} = \{\mathbf{0}\}$$

(2-25)

For the bottom layer, the traction free boundary condition at the at the bottom surface gives

$$\begin{Bmatrix} S_{xz} \\ S_{zz} \end{Bmatrix} = [Q_{21}^1]\{C_1^-\} + [Q_{22}^1][E_2^1(0)]\{C_1^+\} = \{\mathbf{0}\}$$

(2-26)

The Dispersion Equations for a Layered Medium in Global Matrix Form

Using the traction free boundary conditions (2-25), (2-26) at the top and bottom surfaces of the plate, and then use the continuity conditions (2-24) across all the interfaces, the global matrix system written in equation (2-27) below represents the equation for free wave propagation in the multilayered medium.

$$
\begin{Bmatrix}
S_{xz}^{Bottom} \\ S_{zz}^{Bottom} \\ \hline
U_x^{I_1} \\ U_z^{I_1} \\ S_{xz}^{I_1} \\ S_{zz}^{I_1} \\ \hline
U_x^{I_2} \\ U_z^{I_2} \\ S_{xz}^{I_2} \\ S_{zz}^{I_2} \\ \hline
\vdots \\ \hline
U_x^{I_i} \\ U_z^{I_i} \\ S_{xz}^{I_i} \\ S_{zz}^{I_i} \\ \hline
\vdots \\ \hline
U_x^{I_{N-1}} \\ U_z^{I_{N-1}} \\ S_{xz}^{I_{N-1}} \\ S_{zz}^{I_{N-1}} \\ \hline
S_{xz}^{Top} \\ S_{zz}^{Top}
\end{Bmatrix}
=
\underbrace{\left[\begin{array}{cc|cc|cc|cc}
Q_{21}^1 & Q_{22}^1E_1^1 & \mathbf{0} & \mathbf{0} & \mathbf{0} & \mathbf{0} & \cdots & \mathbf{0} \\
-Q_{11}^1E_1^1 & -Q_{21}^1 & Q_{11}^2 & Q_{12}^2E_2^2 & \mathbf{0} & \mathbf{0} & \cdots & \mathbf{0} \\
-Q_{21}^1E_1^1 & -Q_{22}^1 & Q_{21}^2 & Q_{12}^2E_2^2 & \ddots & \ddots & \ddots & \mathbf{0} \\ \hline
\mathbf{0} & \mathbf{0} & -Q_{11}^2E_1^2 & -Q_{21}^2 & Q_{11}^3 & Q_{12}^3E_2^3 & \cdots & \mathbf{0} \\
\vdots & \vdots & -Q_{21}^2E_1^2 & -Q_{22}^2 & Q_{21}^3 & Q_{22}^3E_2^3 & \cdots & \mathbf{0} \\ \hline
\vdots & \vdots & \ddots & \ddots & \ddots & \ddots & \vdots & \mathbf{0} \\ \hline
\mathbf{0} & \cdots & -Q_{11}^iE_1^i & -Q_{21}^i & Q_{11}^{i+1} & Q_{12}^{i+1}E_2^{i+1} & \cdots & \mathbf{0} \\
\mathbf{0} & \cdots & -Q_{21}^iE_1^i & -Q_{22}^i & Q_{21}^{i+1} & Q_{22}^{i+1}E_2^{i+1} & \cdots & \mathbf{0} \\ \hline
\vdots & \ddots & \ddots & \ddots & \ddots & \ddots & \ddots & \vdots \\ \hline
\vdots & \ddots & \ddots & \ddots & -Q_{11}^{N-1}E_1^{N-1} & -Q_{21}^{N-1} & Q_{11}^N & Q_{12}^NE_2^N \\
\vdots & \ddots & \ddots & \ddots & -Q_{21}^{N-1}E_1^{N-1} & -Q_{22}^{N-1} & Q_{11}^N & Q_{22}^NE_2^N \\ \hline
\mathbf{0} & \cdots & \cdots & \cdots & \cdots & \mathbf{0} & Q_{21}^NE_1^N & Q_{22}^N
\end{array}\right]}_{\widehat{\boldsymbol{G}}}
\begin{Bmatrix}
C_1^- \\ C_1^+ \\ C_2^- \\ C_2^+ \\ C_3^- \\ C_3^+ \\ \vdots \\ C_m^- \\ C_m^+ \\ \vdots \\ C_{N-1}^- \\ C_{N-1}^+ \\ C_N^- \\ C_N^+
\end{Bmatrix}
= \mathbf{0}
$$

(2-27)

For a non-trivial solution, the determinant of the matrix $\widehat{\boldsymbol{G}} = 0$, represents the dispersion equation for the multilayered system. Solving for the root *k* from this equation is not trivial. An efficient root identification and root tracing (finding) scheme is presented in [27], and [28].

2.1.3 The Dispersion Equation for a Single Layer using the Global Matrix Method

For a multilayered medium, the behavior of the dispersion curves is extremely complex, due to the highly coupled nature of the system of transcendental system of equations (2-27). Furthermore, the computational effort of calculating the determinant can be very high for a system with many layers. This is especially true since the dispersion relation needs to be computed many times over a wide range of frequencies in order to generate reliable solutions in the time domain, and for root searching. In practice, many composite structures have a symmetric and balanced layup, where there are same number of plies above and below the mid-

plane. In such cases, the size of the matrix can be reduced by only considering half of the layers. Furthermore, it is often time of interest to separate the contributions of the symmetric and anti-symmetric modes. The dispersion curves obtained from the solution of equation (2-27) contain both the symmetric and antisymmetric modes. In this section, the reduction of the dispersion equation obtained from the global matrix for a single layer case is presented to demonstrate how to separate the two modes.

Reduction of the Global Matrix for a Transversely Isotropic Plate

Consider the following definition of a layer of thickness $h = 2H$ as shown in Figure 2-5, and apply the traction free boundary conditions in the standard global matrix procedure.

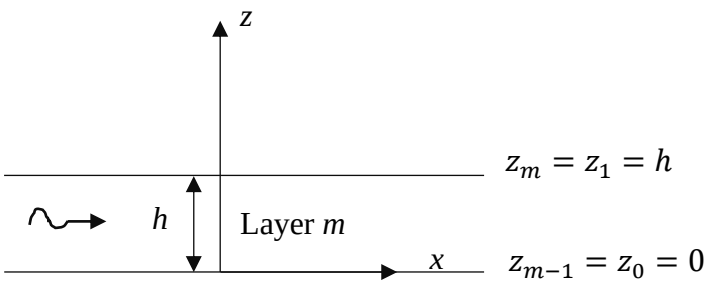

Figure 2-5 Coordinate system for global matrix formulation for one layer

The stresses in equation (2-16) are evaluated at the top surface with $z_m = h$ and $z_{m-1} = 0$ using the block matrix defined in (2-17) and (2-18) to give

$$\begin{Bmatrix} S_{xz}(h) \\ S_{zz}(h) \end{Bmatrix} = \begin{bmatrix} Q_{21}^1 & Q_{22}^1 \end{bmatrix} \begin{bmatrix} e^{-\eta_1(h-0)} & 0 & 0 & 0 \\ 0 & e^{-\eta_2(h-0)} & 0 & 0 \\ 0 & 0 & e^{-\eta_1(h-h)} & 0 \\ 0 & 0 & 0 & e^{-\eta_2(h-h)} \end{bmatrix} \begin{Bmatrix} C_1 \\ C_2 \\ C_3 \\ C_4 \end{Bmatrix} = \begin{Bmatrix} 0 \\ 0 \end{Bmatrix}$$

$$\begin{Bmatrix} S_{xz}(0) \\ S_{zz}(0) \end{Bmatrix} = \begin{bmatrix} Q_{21}^1 & Q_{22}^1 \end{bmatrix} \begin{bmatrix} e^{-\eta_1(0-0)} & 0 & 0 & 0 \\ 0 & e^{-\eta_2(0-0)} & 0 & 0 \\ 0 & 0 & e^{-\eta_1(h-0)} & 0 \\ 0 & 0 & 0 & e^{-\eta_2(h-0)} \end{bmatrix} \begin{Bmatrix} C_1 \\ C_2 \\ C_3 \\ C_4 \end{Bmatrix} = \begin{Bmatrix} 0 \\ 0 \end{Bmatrix} \quad (2\text{-}28)$$

For compactness in writing the matrix determinant, define

$$e_1 = e^{-\eta_1 h} \qquad\qquad e_2 = e^{-\eta_2 h}$$

(2-29)

The dispersion equation written in global matrix form is then

$$\begin{Bmatrix} S_{xz}(0) \\ S_{zz}(0) \\ S_{xz}(h) \\ S_{zz}(h) \end{Bmatrix} = \begin{bmatrix} q_{31} & q_{32} & -q_{31}e_1 & -q_{32}e_2 \\ q_{41} & q_{42} & q_{41}e_1 & q_{42}e_2 \\ q_{31}e_1 & q_{32}e_2 & -q_{31} & -q_{32} \\ q_{41}e_1 & q_{42}e_2 & q_{41} & q_{42} \end{bmatrix} \begin{Bmatrix} C_1 \\ C_2 \\ C_3 \\ C_4 \end{Bmatrix} = \{\mathbf{0}\}$$

(2-30)

To calculate the determinant, it is important to group the terms $[q_{31}q_{42} - q_{32}q_{41}]$, $[q_{31}q_{42} + q_{32}q_{41}]$ $[q_{31}q_{42}q_{32}q_{41}]$, and factor out e_1^2, e_2^2 and $e_1^2 e_2^2$. For instance, the first term in the determinant is written as,

$$q_{31}\begin{vmatrix} q_{42} & q_{41}e_1 & q_{42}e_2 \\ q_{32}e_2 & -q_{31} & -q_{32} \\ q_{42}e_2 & q_{41} & q_{42} \end{vmatrix}$$

$$= q_{31}\{q_{42}[-q_{31}q_{42} + q_{32}q_{41}] - q_{41}e_1[q_{32}q_{42}e_2 + q_{32}q_{42}e_2] + q_{42}e_2[q_{32}q_{41}e_2 + q_{31}q_{42}e_2]\}$$

$$= -q_{31}q_{42}[q_{31}q_{42} - q_{32}q_{41}] - 2q_{31}q_{42}q_{32}q_{41}e_1e_2 + q_{31}q_{42}e_2^2[q_{31}q_{42} + q_{32}q_{41}]$$

Calculating the rest of the terms gives the dispersion equation

$$[q_{31}q_{42} - q_{32}q_{41}]^2\{1 + e_1^2e_2^2\} - [q_{31}q_{42} + q_{32}q_{41}]^2\{e_1^2 + e_2^2\} + 8q_{31}q_{42}q_{32}q_{41}e_1e_2 = 0$$

(2-31)

To better compare with the well-known dispersion equation as shown in Appendix 2.2, the term $[q_{31}q_{42} - q_{32}q_{41}]$ is rewritten using the definitions listed in (2-17) as

$$[q_{31}q_{42} - q_{32}q_{41}] = C_{44}[-\eta_1 + ik\beta_1][ikC_{13} - C_{33}\beta_2\eta_2] - C_{44}[-\eta_2 + ik\beta_2][ikC_{13} - C_{33}\beta_1\eta_1]$$

(2-32)

Since the right-hand side of the standard form of the dispersion equation does not have the wavenumber, it is factored out from η_j such that $\eta_j = k\bar{\eta}_j$ and $\beta_j = -\frac{C_{11} - \rho c^2 - \bar{\eta}_j C_{44}}{i\bar{\eta}_j(C_{13} + C_{44})} =$

$\frac{i[C_{11} - \rho c^2 - \bar{\eta}_j C_{44}]}{\bar{\eta}_j(C_{13} + C_{44})} = i\bar{\beta}_j$

$$[q_{31}q_{42} - q_{32}q_{41}] = k^4 C_{33}C_{44}\left\{\left[-\bar{\eta}_1 - \bar{\beta}_1\right]\left[\frac{C_{13}}{C_{33}} - \bar{\eta}_2\bar{\beta}_2\right] + \left[\bar{\eta}_2 - \bar{\beta}_2\right]\left[\frac{C_{13}}{C_{33}} - \bar{\eta}_1\bar{\beta}_1\right]\right\}$$

(2-33)

Similarly, the other term is

$$[q_{31}q_{42} + q_{32}q_{41}] = k^4 C_{33}C_{44}\left\{-\left[\bar{\eta}_1 + \bar{\beta}_1\right]\left[\frac{C_{13}}{C_{33}} - \bar{\eta}_2\bar{\beta}_2\right] - \left[\bar{\eta}_2 - \bar{\beta}_2\right]\left[\frac{C_{13}}{C_{33}} - \bar{\eta}_1\bar{\beta}_1\right]\right\}$$

(2-34)

To better compare this with the standard dispersion equation, the following terms are defined

$$Æ = \left[\bar{\eta}_1 + \bar{\beta}_1\right]\left[\frac{C_{13}}{C_{33}} - \bar{\eta}_2\bar{\beta}_2\right] \qquad Å = \left[\bar{\eta}_2 - \bar{\beta}_2\right]\left[\frac{C_{13}}{C_{33}} - \bar{\eta}_1\bar{\beta}_1\right]$$

(2-35)

Recalling the right-hand side of the dispersion equation is

$$\frac{A_1\left[A_2^2 - \frac{C_{11}}{C_{13}}\left(\frac{c^2}{C_{1L}^2} - 1\right)\right]\left[\frac{C_{13}}{C_{33}}\left(\frac{C_{13}}{C_{44}} + 1\right) + A_1^2 + \frac{C_{11}}{C_{44}}\left(\frac{c^2}{C_{1L}^2} - 1\right)\right]}{A_2\left[A_1^2 - \frac{C_{11}}{C_{13}}\left(\frac{c^2}{C_{1L}^2} - 1\right)\right]\left[\frac{C_{13}}{C_{33}}\left(\frac{C_{13}}{C_{44}} + 1\right) + A_2^2 + \frac{C_{11}}{C_{44}}\left(\frac{c^2}{C_{1L}^2} - 1\right)\right]}$$

(2-36)

Using $C_{11} = \rho C_{1L}^2$ and $C_{44} = \rho C_{3T}^2$, $\bar{\beta}_j$ and $\bar{\eta}_j$ can be expressed in the forms,

$$\bar{\beta}_j = \frac{1 - \frac{\rho c^2}{C_{11}} - \frac{\bar{\eta}_j^2 C_{44}}{C_{11}}}{\frac{\bar{\eta}_j(C_{13} + C_{44})}{C_{11}}} \qquad \bar{\eta}_j = \sqrt{\frac{-A \pm \sqrt{A^2 - 4B}}{2}} = A_{1,2}$$

(2-37)

From equation (2-35), and (2-37), the terms obtained from the global matrix equation can be rewritten as

$$Æ = \left[A_1 + C_{11}\left[\frac{1 - \frac{c^2}{C_{1L}^2} - A_1^2\left(\frac{C_{44}}{C_{11}}\right)}{A_1(C_{13} + C_{44})}\right]\right]\left[\frac{C_{13}}{C_{33}} - \frac{C_{11}\left(1 - \frac{c^2}{C_{1L}^2} - A_2^2\left(\frac{C_{44}}{C_{11}}\right)\right)}{C_{13} + C_{44}}\right]$$

(2-38)

Factoring out $\left(\frac{C_{13}}{C_{13}+C_{44}}\right)\left(\frac{C_{44}}{C_{13}+C_{44}}\right)$ from (2-38) to obtain,

$$Æ = \left(\frac{C_{13}}{C_{13}+C_{44}}\right)\left(\frac{C_{44}}{C_{13}+C_{44}}\right)\frac{1}{A_1}\left[A_1^2 - \frac{C_{11}}{C_{33}}\left(\frac{c^2}{C_{1L}^2}-1\right)\right]\left[\frac{C_{13}}{C_{33}}\left(\frac{C_{13}}{C_{44}}-1\right) + A_2^2 + \frac{C_{11}}{C_{44}}\left(\frac{c^2}{C_{1L}^2}-1\right)\right]$$

(2-39)

Whereas for Å, by using equation (2-37) Å can be expressed in terms of bulk wave velocities and elastic properties in the following form

$$Å = \left[A_2 + C_{11}\left[\frac{1-\frac{c^2}{C_{1L}^2} - A_2^2\left(\frac{C_{44}}{C_{11}}\right)}{A_2(C_{13}+C_{44})}\right]\right]\left[\frac{C_{13}}{C_{33}} - \frac{C_{11}\left(1-\frac{c^2}{C_{1L}^2} - A_1^2\left(\frac{C_{44}}{C_{11}}\right)\right)}{C_{13}+C_{44}}\right]$$

$$Å = \left(\frac{C_{13}}{C_{13}+C_{44}}\right)\left(\frac{C_{44}}{C_{13}+C_{44}}\right)\frac{1}{A_2}\left[A_2^2 - \frac{C_{11}}{C_{33}}\left(\frac{c^2}{C_{1L}^2}-1\right)\right]\left[\frac{C_{13}}{C_{33}}\left(\frac{C_{13}}{C_{44}}-1\right) + A_1^2 + \frac{C_{11}}{C_{44}}\left(\frac{c^2}{C_{1L}^2}-1\right)\right]$$

(2-40)

Denote the right-hand side of the dispersion equation by,

$$RHSB = \left[A_1^2 - \frac{C_{11}}{C_{13}}\left(\frac{c^2}{C_{1L}^2}-1\right)\right]\left[\frac{C_{13}}{C_{33}}\left(\frac{C_{13}}{C_{44}}-1\right) + A_2^2 + \frac{C_{11}}{C_{44}}\left(\frac{c^2}{C_{1L}^2}-1\right)\right]$$

$$RHST = \left[A_2^2 - \frac{C_{11}}{C_{13}}\left(\frac{c^2}{C_{1L}^2}-1\right)\right]\left[\frac{C_{13}}{C_{33}}\left(\frac{C_{13}}{C_{44}}-1\right) + A_1^2 + \frac{C_{11}}{C_{44}}\left(\frac{c^2}{C_{1L}^2}-1\right)\right]$$

The terms $q_{31}q_{42}$ is related to the numerator of the right-hand side in the standard form of the dispersion equation and, the term $q_{32}q_{41}$is related to the denominator of the right-hand side.

Let $\bar{A} = \frac{A_1}{RHSB}$ and $\bar{B} = \frac{RHST}{A_2}$, the dispersion equation obtained from the global matrix approach in (2-31) can be written in the form to better compare with the standard form

$$[\bar{A}-\bar{B}]^2\{1+e_1^2e_2^2\} - [\bar{A}+\bar{B}]^2\{e_1^2+e_2^2\} + 8\bar{A}\bar{B}e_1e_2 = 0$$

(2-41)

Expanding the product $[\bar{A} \pm \bar{B}]^2$ in (2-41), and collecting $\bar{A}$ and $\bar{B}$ terms give the dispersion equation

$$\bar{A}^2[1 + e_1^2e_2^2 - e_1^2 - e_2^2] - 2\bar{A}\bar{B}[1 + e_1^2e_2^2 + e_1^2 + e_2^2 - 4e_1e_2] + \bar{B}^2[1 + e_1^2e_2^2 - e_1^2 - e_2^2] = 0 \tag{2-42}$$

Divide equation (2-42) by $\bar{A}^2$ to obtain

$$1 - \left(\frac{2\bar{B}}{\bar{A}}\right)\frac{[1 + e_1^2 + e_2^2 + e_1^2e_2^2 - 4e_1e_2]}{[1 - e_1^2 - e_2^2 + e_1^2e_2^2]} + \left(\frac{\bar{B}}{\bar{A}}\right)^2 = 0 \tag{2-43}$$

Recalling that the dispersion equations for the symmetric, and anti-symmetric cases,

$$\frac{\tanh(\eta_1 H)}{\tanh(\eta_2 H)} = \frac{\bar{B}}{\bar{A}} \qquad \frac{\tanh(\eta_2 H)}{\tanh(\eta_1 H)} = \frac{\bar{B}}{\bar{A}} \tag{2-44}$$

where *H* is the half plate thickness so that *h=2H*. Using the identity $\tanh(x) = \frac{1-e^{-2x}}{1+e^{-2x}}$

The product of the two dispersion equations is

$$\left[\frac{(1 - e_1)(1 + e_2)}{(1 + e_1)(1 - e_2)} - \frac{\bar{B}}{\bar{A}}\right]\left[\frac{(1 - e_2)(1 + e_1)}{(1 + e_2)(1 - e_1)} - \frac{\bar{B}}{\bar{A}}\right] = 0 \tag{2-45}$$

Finally, by expanding equation (2-45), equation (2-43) is found to be identical to equation (2-45). The implication of this exercise is that, the dispersion equation obtained from the global matrix approach is a product of the symmetric and anti-symmetric equations, and the term $[q_{31}q_{42}\ q_{32}q_{41}]$ is the numerator and the denominator of the frequency independent right-hand side of the standard dispersion equation as shown in (2-44) and (2-36).

2.1.4 Separation of Symmetric and Anti-Symmetric Dispersion Equations in the Global Matrix Method

By applying the appropriate boundary conditions at the mid-plane, the dispersion equations for a balanced and symmetric layup can be separated into the two families reducing the matrix size by half. A formal proof for a single layer is presented here for symmetric and anti-symmetric cases.

Symmetric Case

Consider the upper-half of an original plate with thickness 2H with the origin at mid-plane as shown in Figure 2-6.

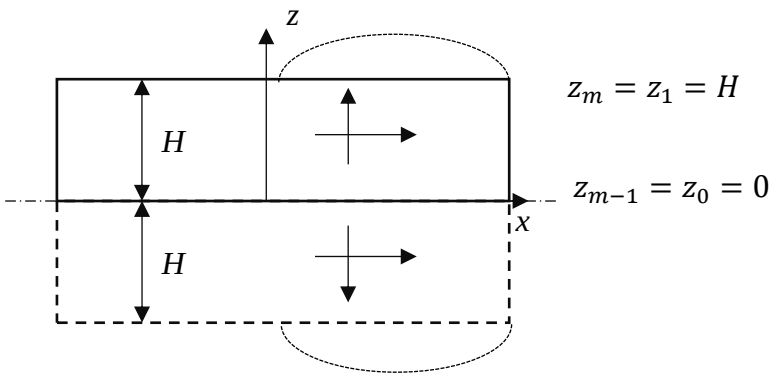

Figure 2-6 For symmetric case, write the dispersion equation of the upper-half using global matrix

For the symmetric problem, the displacements shown by the arrows would have the same sign for the horizontal components and have opposite sign for the vertical components above and below the mid-plane of the plate. This implies that for the half-plate, the conditions at the mid-plane can be replaced by new boundary conditions

$$u_z = 0 \qquad \sigma_{xz} = 0 \tag{2-46}$$

The top surface of the half plate is traction free (2-46). Thus, using the layer matrix equation (2-16), the definitions of q in equation (2-17), and the definitions of the e_s in equation (2-19), and (2-29), the global matrix equation for the new problem can be written as

$$\begin{Bmatrix} U_z(0) \\ S_{xz}(0) \\ S_{xz}(H) \\ S_{zz}(H) \end{Bmatrix} = \begin{bmatrix} q_{21} & q_{22} & -q_{21}e_1 & -q_{22}e_2 \\ q_{31} & q_{32} & -q_{31}e_1 & q_{32}e_2 \\ q_{31}e_1 & q_{32}e_2 & -q_{31} & q_{32} \\ q_{41}e_1 & q_{42}e_2 & q_{41} & -q_{42} \end{bmatrix} \begin{Bmatrix} C_1 \\ C_2 \\ C_3 \\ C_4 \end{Bmatrix} = \{\mathbf{0}\} \tag{2-47}$$

For non-trivial solution of (2-47), the determinant of the matrix gives the symmetric dispersion equation. As suggested in section 2.1.3, the term $q_{31}q_{42}\ q_{32}q_{41}$represents the right-hand side of the standard form of the dispersion equation. The first determinant term is shown here as an illustration.

$$q_{21}\begin{vmatrix} q_{31} & -q_{31}e_1 & q_{32}e_2 \\ q_{32}e_2 & -q_{31} & q_{32} \\ q_{42}e_2 & q_{41} & -q_{42} \end{vmatrix}$$

$$= q_{21}\{q_{32}[q_{31}q_{42} - q_{32}q_{41}] - q_{31}e_1[2q_{32}q_{42}e_2] + q_{32}e_2[q_{32}q_{41}e_2 + q_{31}q_{42}e_2]\}$$

$$= q_{21}q_{32}[q_{31}q_{42} - q_{32}q_{41}] - 2q_{21}q_{31}q_{32}q_{42}e_1e_2 + q_{21}q_{32}e_2^2[q_{31}q_{42} + q_{32}q_{41}]$$

After calculating the remaining three terms of determinant, the dispersion equation is

$$[q_{21}q_{32} - q_{22}q_{31}][q_{31}q_{42} - q_{32}q_{41}](1 - e_1^2e_2^2) - [q_{21}q_{32} - q_{22}q_{31}][q_{31}q_{42} + q_{32}q_{41}](e_1^2 - e_2^2) = 0 \tag{2-48}$$

Since the term $[q_{21}q_{32} - q_{22}q_{31}] = \beta_1 C_{44}[-\eta_2 + ik\beta_2] - \beta_2 C_{44}[-\eta_1 + ik\beta_1]$ can be factored out and is not equal to 0, the term $[q_{31}q_{42} - q_{32}q_{41}](1 - e_1^2e_2^2) - [q_{21}q_{32} - q_{22}q_{31}][q_{31}q_{42} + q_{32}q_{41}](e_1^2 - e_2^2) = 0$ is the dispersion equation. Using the substitution of $[q_{31}q_{42} \pm q_{32}q_{41}]$ with the material properties, velocities as in (2-33),(2-34) and the development through (2-41), it is concluded that $[q_{31}q_{42} \pm q_{32}q_{41}] = [\bar{A} \pm \bar{B}]$ (Recall $\bar{A}$ and $\bar{B}$ are the denominator and the

numerator of the dispersion equation in equation (2-44)). Then the dispersion equation from equation (2-48) becomes

$$\left[\bar{A} - B\right](1 - e_1^2 e_2^2) - \left[\bar{A} + B\right](e_1^2 - e_2^2) = 0$$

(2-49)

Collect the $\bar{A}$ and $\bar{B}$ terms gives,

$$\bar{A}(1 - e_1^2 e_2^2 - e_1^2 + e_2^2) - \bar{B}(1 - e_1^2 e_2^2 + e_1^2 - e_2^2) = 0$$

$$\frac{(1 - e_1^2 e_2^2 - e_1^2 + e_2^2)}{(1 - e_1^2 e_2^2 + e_1^2 - e_2^2)} = \frac{\bar{B}}{\bar{A}}$$

(2-50)

Using the hyperbolic tangent functions in the form of $1 \pm e_j^2$ to factor the left-hand side,

$$\frac{(1 - e_1^2)(1 + e_2^2)}{(1 + e_1^2)(1 - e_2^2)} = \frac{\bar{B}}{\bar{A}}$$

(2-51)

And using the definitions $e_1 = e^{-\eta_1 H}$ and $e_2 = e^{-\eta_2 H}$, equation (2-51) becomes

$$\frac{(1 - e^{-\eta_1 2H})(1 + e^{-\eta_2 2H})}{(1 + e^{-\eta_{12} H})(1 - e^{-\eta_2 2H})} = \frac{\bar{B}}{\bar{A}}$$

(2-52)

Apply the trigonometric identity $\tanh(x) = \frac{1-e^{-2x}}{1+e^{-2x}}$ gives the standard form of the symmetric dispersion equation,

$$\frac{\tanh(\eta_1 H)}{\tanh(\eta_2 H)} = \frac{\bar{B}}{\bar{A}} = \frac{A_1\left[A_2^2 - \frac{C_{11}}{C_{13}}\left(\frac{c^2}{C_{1L}^2} - 1\right)\right]\left[\frac{C_{13}}{C_{33}}\left(\frac{C_{13}}{C_{44}} + 1\right) + A_1^2 + \frac{C_{11}}{C_{44}}\left(\frac{c^2}{C_{1L}^2} - 1\right)\right]}{A_2\left[A_1^2 - \frac{C_{11}}{C_{13}}\left(\frac{c^2}{C_{1L}^2} - 1\right)\right]\left[\frac{C_{13}}{C_{33}}\left(\frac{C_{13}}{C_{44}} + 1\right) + A_2^2 + \frac{C_{11}}{C_{44}}\left(\frac{c^2}{C_{1L}^2} - 1\right)\right]}$$

(2-53)

Equation (2-53) is identical to the transversely isotropic dispersion equation derived in [29], which is also given in the appendix section 2.2.

Anti-Symmetric Dispersion Equation from Global Matrix Method

For anti-symmetric case, the updated representative boundary conditions at the mid-plane can be inferred form Figure 2-7 to be

$$u_x = 0 \qquad \sigma_{zz} = 0 \tag{2-54}$$

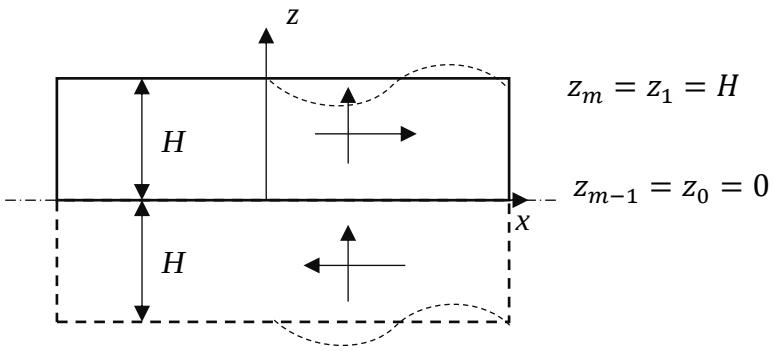

Figure 2-7 For anti-symmetric case, write the dispersion equation of the upper-half using global matrix

Using the layer matrix equations (2-16) to write the boundary conditions, the only difference between the anti-symmetric and symmetric case is in the first two rows of the matrix equation

$$\begin{Bmatrix} U_x(0) \\ S_{zz}(0) \\ S_{xz}(H) \\ S_{zz}(H) \end{Bmatrix} = \begin{bmatrix} q_{11} & q_{12} & q_{11}e_1 & -q_{12}e_2 \\ q_{41} & q_{42} & q_{41}e_1 & -q_{42}e_2 \\ q_{31}e_1 & q_{32}e_2 & -q_{31} & q_{32} \\ q_{41}e_1 & q_{42}e_2 & q_{41} & -q_{42} \end{bmatrix} \begin{Bmatrix} C_1 \\ C_2 \\ C_3 \\ C_4 \end{Bmatrix} = \{\mathbf{0}\} \tag{2-55}$$

The first term of the determinant is,

$$q_{11} \begin{vmatrix} q_{42} & q_{41}e_1 & -q_{42}e_2 \\ q_{32}e_2 & -q_{31} & q_{32} \\ q_{42}e_2 & q_{41} & -q_{42} \end{vmatrix}$$

$$= q_{11}\{q_{42}[q_{31}q_{42} - q_{32}q_{41}] - q_{41}e_1[-2q_{32}q_{42}e_2] - q_{42}e_2[q_{32}q_{41}e_2 + q_{31}q_{42}e_2]\}$$

$$= q_{11}q_{42}[q_{31}q_{42} - q_{32}q_{41}] + 2q_{11}q_{41}q_{32}q_{42}e_1e_2 - q_{11}q_{42}e_2^2[q_{31}q_{42} + q_{32}q_{41}]$$

After collecting terms form all the minor determinants. The dispersion equation is then

$$[q_{11}q_{42} - q_{12}q_{41}][q_{31}q_{42} - q_{32}q_{41}](1 - e_1^2e_2^2) - [q_{11}q_{42} - q_{12}q_{41}][q_{31}q_{42} + q_{32}q_{41}](e_1^2 - e_2^2) = 0$$

(2-56)

Equation (2-56) has the same form as the symmetric case (2-48) with the only difference of having $[q_{11}q_{42} - q_{12}q_{41}]$ instead of $[q_{21}q_{32} - q_{22}q_{31}]$. Thus equation (2-56) is written as

$$\left[\bar{A} - B\right](1 - e_1^2 e_2^2) + \left[\bar{A} + B\right](e_1^2 - e_2^2) = 0$$

(2-57)

And to be factored as

$$\frac{(1 - e_1^2 e_2^2 + e_1^2 - e_2^2)}{(1 - e_1^2 e_2^2 - e_1^2 + e_2^2)} = \frac{\bar{B}}{\bar{A}} = \frac{(1 + e_1^2)(1 - e_2^2)}{(1 - e_1^2)(1 + e_2^2)}$$

(2-58)

For completeness, using the definitions of $e_1 = e^{-\eta_1 H}$ and $e_2 = e^{-\eta_2 H}$to obtain the standard form

$$\frac{(1 + e^{-\eta_1 2H})(1 - e^{-\eta_2 2H})}{(1 - e^{-\eta_{12} H})(1 + e^{-\eta_2 2H})} = \frac{\tanh(\eta_2 H)}{\tanh(\eta_1 H)} = \frac{\bar{B}}{\bar{A}}$$

(2-59)

Thus, we have concluded that the symmetric and anti-symmetric dispersion equations can be obtained by using only the upper half of a homogeneous plate.

2.2 The Waveguide Finite Element Method

2.2.1 A Review of the Wave Guide Finite Element Method

The Wave Guide finite element (WFE) method is semi-analytical procedure to model elastic wave propagation in frequency domain. Mace et. al. developed the method to model wave motions in different structural waveguides such as plates and channels [30]. Duhamel et. al. applied the method to analyze the wave modes in simple frames and beam structures [31]. The WFE method has been applied to study wave motion in complex waveguides with difficult-to-find analytical solutions such as fluid-filled corrugated pipes [32], multi-wire cable systems [33], and honeycomb core sandwich structures [34] [35]. Renno et. al. modified the WFE method to find the forced response of a structure [36].

2.2.2 Formulation of the WFE Method

Consider an infinite plate with thickness *2H*, with the waveguide segment of length Δh that is repeated in the *z*-direction, as shown in Figure 2-8.

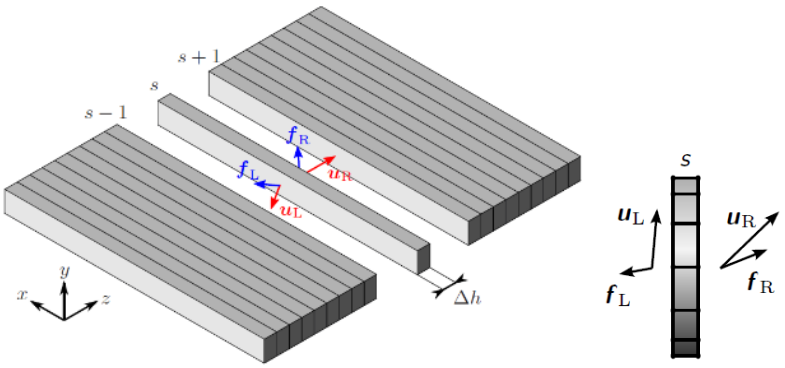

Figure 2-8 A section of plate is the waveguide, *s*

The segment *s* is described by the FE equation of motion given below with the mass and stiffness matrices denoted by $\boldsymbol{M}$, and $\boldsymbol{K}$, respectively.

$$\boldsymbol{M\ddot{u} + Ku = f}$$

(2-60)

The vectors $\boldsymbol{u}$ and $\boldsymbol{f}$ are the nodal displacements and forces of the waveguide segment.

Assuming harmonic motion in the form $e^{-i\omega t}$, the equation of motion (2-60) becomes

$$\begin{bmatrix} \bar{\boldsymbol{D}}_{\boldsymbol{LL}} & \bar{\boldsymbol{D}}_{\boldsymbol{LI}} & \bar{\boldsymbol{D}}_{\boldsymbol{LR}} \\ \bar{\boldsymbol{D}}_{\boldsymbol{IL}} & \bar{\boldsymbol{D}}_{\boldsymbol{II}} & \bar{\boldsymbol{D}}_{\boldsymbol{IR}} \\ \bar{\boldsymbol{D}}_{\boldsymbol{RL}} & \bar{\boldsymbol{D}}_{\boldsymbol{RI}} & \bar{\boldsymbol{D}}_{\boldsymbol{RR}} \end{bmatrix} \begin{Bmatrix} \boldsymbol{u}_{\boldsymbol{L}} \\ \boldsymbol{u}_{\boldsymbol{I}} \\ \boldsymbol{u}_{\boldsymbol{R}} \end{Bmatrix} = \begin{Bmatrix} \boldsymbol{f}_{\boldsymbol{L}} \\ \boldsymbol{0} \\ \boldsymbol{f}_{\boldsymbol{R}} \end{Bmatrix}$$

(2-61)

where $\bar{\boldsymbol{D}} = -\boldsymbol{\omega}^{\boldsymbol{2}}\boldsymbol{M} + \boldsymbol{K}$ is the dynamic stiffness matrix, and the subscripts in (2-62) denote the partition of the degrees of freedom (DOF) associated with the left side, the interior and the right side of the segment. In order to apply the segment continuity condition, the interior DOFs are expressed in terms of the left and right DOFs as

$$\begin{aligned} \boldsymbol{D}_{\boldsymbol{LL}} &= \bar{\boldsymbol{D}}_{\boldsymbol{LL}} - \bar{\boldsymbol{D}}_{\boldsymbol{LI}}\bar{\boldsymbol{D}}_{\boldsymbol{II}}^{-\boldsymbol{1}}\bar{\boldsymbol{D}}_{\boldsymbol{IL}} \qquad \boldsymbol{D}_{\boldsymbol{LR}} = \bar{\boldsymbol{D}}_{\boldsymbol{LR}} - \bar{\boldsymbol{D}}_{\boldsymbol{LI}}\bar{\boldsymbol{D}}_{\boldsymbol{II}}^{-\boldsymbol{1}}\bar{\boldsymbol{D}}_{\boldsymbol{IR}} \\ \boldsymbol{D}_{\boldsymbol{RL}} &= \bar{\boldsymbol{D}}_{\boldsymbol{RL}} - \bar{\boldsymbol{D}}_{\boldsymbol{RI}}\bar{\boldsymbol{D}}_{\boldsymbol{II}}^{-\boldsymbol{1}}\bar{\boldsymbol{D}}_{\boldsymbol{IL}} \qquad \boldsymbol{D}_{\boldsymbol{RR}} = \bar{\boldsymbol{D}}_{\boldsymbol{RR}} - \bar{\boldsymbol{D}}_{\boldsymbol{RI}}\bar{\boldsymbol{D}}_{\boldsymbol{II}}^{-\boldsymbol{1}}\bar{\boldsymbol{D}}_{\boldsymbol{IR}} \end{aligned}$$

(2-62)

Equation (2-61) can then be condensed into the form

$$\begin{bmatrix} \boldsymbol{D}_{\boldsymbol{LL}} & \boldsymbol{D}_{\boldsymbol{LR}} \\ \boldsymbol{D}_{\boldsymbol{RL}} & \boldsymbol{D}_{\boldsymbol{RR}} \end{bmatrix} \begin{bmatrix} \boldsymbol{u}_{\boldsymbol{L}} \\ \boldsymbol{u}_{\boldsymbol{R}} \end{bmatrix} = \begin{bmatrix} \boldsymbol{f}_{\boldsymbol{L}} \\ \boldsymbol{f}_{\boldsymbol{R}} \end{bmatrix}$$

(2-63)

Since the right face of waveguide segment *s* should have field continuity with the left face of segment *s+1*,

$$\boldsymbol{u}_{\boldsymbol{R}}^{\boldsymbol{S}} = \boldsymbol{u}_{\boldsymbol{L}}^{\boldsymbol{s+1}} \text{ and } \boldsymbol{f}_{\boldsymbol{R}}^{\boldsymbol{s}} = \boldsymbol{f}_{\boldsymbol{L}}^{\boldsymbol{s+1}}$$

(2-64)

Inserting the continuity conditions (2-64) into the equilibrium equation (2-63), a system of matrix equations is obtained in which the downstream displacement and force components are expressed explicitly in terms of the upstream displacement and force components in the form

$$\begin{bmatrix} \boldsymbol{u}_{\boldsymbol{L}^{s+1}} \\ \boldsymbol{f}_{\boldsymbol{L}}^{\boldsymbol{s+1}} \end{bmatrix} = \begin{bmatrix} -\boldsymbol{D}_{\boldsymbol{LR}}^{-\boldsymbol{1}}\boldsymbol{D}_{\boldsymbol{LL}} & \boldsymbol{D}_{\boldsymbol{LR}}^{-\boldsymbol{1}} \\ -\boldsymbol{D}_{\boldsymbol{RL}} + \boldsymbol{D}_{\boldsymbol{RR}}\boldsymbol{D}_{\boldsymbol{LR}}^{-\boldsymbol{1}}\boldsymbol{D}_{\boldsymbol{LL}} & -\boldsymbol{D}_{\boldsymbol{RR}}\boldsymbol{D}_{\boldsymbol{LR}}^{-\boldsymbol{1}} \end{bmatrix} \begin{bmatrix} \boldsymbol{u}_{\boldsymbol{L}}^{\boldsymbol{s}} \\ \boldsymbol{f}_{\boldsymbol{L}}^{\boldsymbol{s}} \end{bmatrix} = \boldsymbol{T} \begin{bmatrix} \boldsymbol{u}_{\boldsymbol{L}}^{\boldsymbol{s}} \\ \boldsymbol{f}_{\boldsymbol{L}}^{\boldsymbol{s}} \end{bmatrix}$$

(2-65)

Using the substitution $\lambda = e^{ik\Delta h}$ to represent the phase shift of the wave that travels through the waveguide segment with length Δh, the downstream displacements and forces can be expressed as $\boldsymbol{u_L^{s+1}} = \boldsymbol{\lambda u_L^s}$ *and* $\boldsymbol{f_L^{s+1}} = \boldsymbol{\lambda f_L^s}$ where *k* is the angular wavenumber. The following eigenvalue equation represents the free wave propagation in the plate

$$\boldsymbol{T}\begin{bmatrix}\boldsymbol{u_L^s}\\ \boldsymbol{f_L^s}\end{bmatrix} = \boldsymbol{\lambda}\begin{bmatrix}\boldsymbol{u_L^s}\\ \boldsymbol{f_L^s}\end{bmatrix}$$

(2-66)

Solving the equation gives the values of λ the wavenumber can be obtained as,

$$k = -\frac{i}{\Delta h} Ln\,(\lambda)$$

(2-67)

The phase velocity c_p and the group velocity c_g can be calculated from the well-known relations

$$c_p = \frac{\omega}{k} \qquad c_g = \frac{\partial \omega}{\partial k}$$

(2-68)

Alternatively, using energy transport velocity formula given in [37], the inaccuracies associated with numerical differentiation in calculating the group velocity can be avoided

$$c_g = \frac{< P >}{< H >}$$

(2-69)

where $< P >$ is the time-averaged power flow over the cross-section of the waveguide, and $< H >$ is the time-averaged sum of the potential and kinetic energy densities in the waveguide.

$$< P > = \frac{1}{2}\omega Im\{\boldsymbol{f_L^H u_L}\}$$

(2-70)

$$< H >= \frac{1}{4\Delta H}\omega^2 Re\{\boldsymbol{u^H M u}\} + \frac{1}{4\Delta H} Re\{\boldsymbol{u^H K u}\}$$

(2-71)

where $\mathbf{u}^H$ denotes the complex conjugate transpose of the vector **u**.

Lamb Wave Mode Identification Based on Wavenumbers

The wavenumbers calculated from the equation (2-67) is in general complex with the number of eigenvalues equal to the number of degrees of freedom in the FE discretization. Since these wavenumbers are the roots of the dispersion equation, it is useful to classify them base on the physical characteristics of the Lamb waves. In the subsequent discussions, it is assumed that the waveguide in consideration is a plate that is balanced and symmetric about its mid-plane. Figure 2-9 shows the typical root distribution on the complex *k*-plane for an aluminum plate.

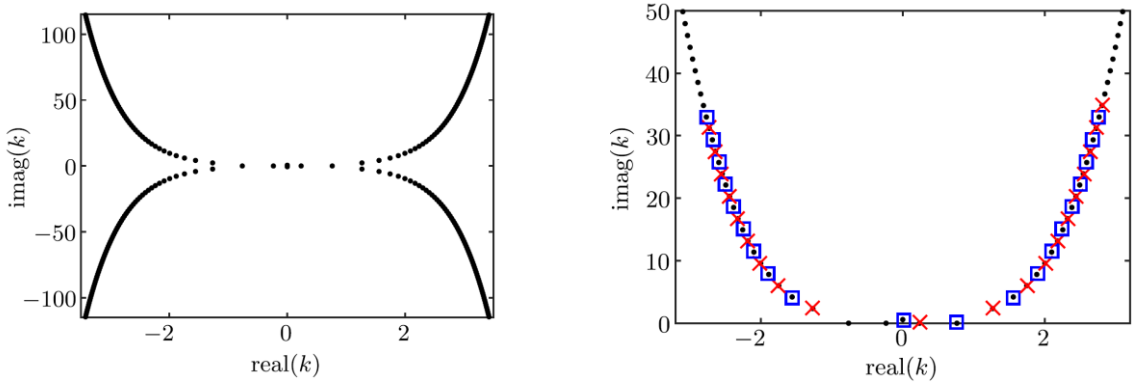

(a) All complex roots found by WFE

(b) Roots associated with right propagating waves for symmetric (x) and anti-symmetric modes (▫)

Figure 2-9 The complex wavenumbers for a 1.78mm thick aluminum plate

The wavenumber *k* appears in all four quadrants and they are not independent. For each *k*, there are other roots $-k, k^*$ and $-k^*$. Furthermore, *k* can be real, pure imaginary or complex. Recall from equation (2-1) that the displacement has the form e^{ikx_1} , the real value of *k* corresponds to the propagating waves with no decay in two-dimensional problems. The complex roots correspond to evanescent waves that decay exponentially x_1, with the rate of decay depending on the imaginary part of the wavenumber. The purely imaginary roots are associated with waves that decay exponentially but do not propagate. It should be noted that the sign of the real part *k*

indicates the direction of propagation. For $x_1 \geq 0$, the right propagating waves would have a positive real part, and a positive imaginary part such that the wave amplitude decreases with increasing propagation distance. There is, however, some exceptions to these rules when a positive real wavenumber is associated to a negative group velocity. For some materials, such as aluminum near the cut-off frequency of the S_2 mode, the derivative $\frac{\partial \omega}{\partial k}$ is negative, resulting in the well-known behavior of "backward power flow" as pointed out in [38]. In such case, to select the right propagating non-decaying wave, the positive group velocity is used as the determining condition along with a negligible imaginary part. After the wavenumbers are classified into real, imaginary, and complex, the real roots are then sorted in descending magnitude of the real part because the higher modes would be more likely to have a higher phase velocity. The imaginary and the complex roots are sorted with increasing magnitude of the imaginary part which have a slower rate of decay and therefore are more dominant. Although an infinite number of complex roots can satisfy the Lamb wave dispersion equation and WFE can only calculate as many of those roots as there are the degrees of freedom, typically a subset of those roots is sufficient to obtain an accurate solution when using Lamb mode expansion. For the remaining analysis, 40 complex roots in the first quadrant are kept. Finally, when the waveguide is balanced and symmetric such that the Lamb modes can be separated into symmetric and anti-symmetric modes, the wavenumbers are further separated into the two families. To do so, the eigenvectors for each wavenumber obtained from equation (2-66) are used to evaluate the displacement components at the top and bottom nodes to satisfy the symmetry and anti-symmetry as shown in Figure 2-6 and Figure 2-7.

3D Waveguide Segment Periodic Boundary Conditions

For this research, the primary focus is the elastic wave propagation in plates with infinite in-plane dimensions, and the periodic boundary condition is used to restrict the eigenvalue problem to only model Lamb waves. Consider the waveguide section sketched in Figure 2-10, which represents a small section of the plate segment s in Figure 2-8 with guided waves propagating in the z direction.

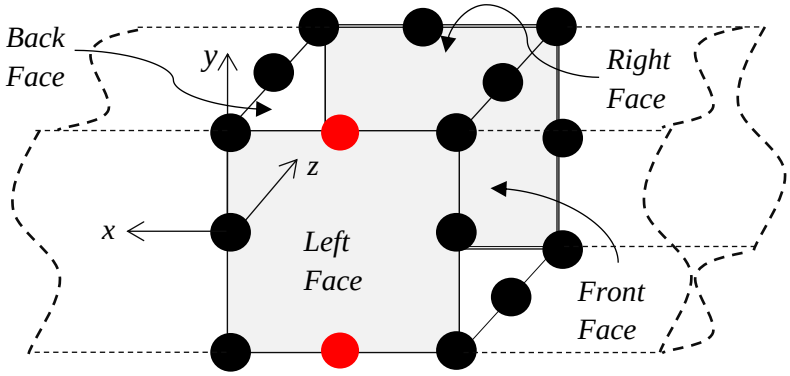

Figure 2-10 Nodes in the FE waveguide segment are subjected to periodic boundary conditions, and the red dots are the nodes which the displacement components are used to determine whether a mode is symmetric or anti-symmetric

Since the plate is long in the x direction, the waveguide section will be periodic, and the associated periodic boundary condition is $u_x = 0$ for all nodes on the front and back faces of the waveguide (parallel to y-z plane). This is a more restrictive condition than the plane-strain condition in which $\frac{\partial u_x}{\partial x} = 0$ gives $u_x^{front} = u_x^{back}$. It is worth mentioning that the degrees of freedom in equation (2-61) are active (i.e., with the fixed DOFs removed).

Numerical Considerations

The standard form of the eigenvalue problem in (2-66) can be ill-conditioned at higher frequencies and may result in missing roots or in mode shapes that could not be classified into symmetric/antisymmetric modes properly. The first numerical issue is that the upper half and the

lower half of the displacement-nodal force vector $\begin{bmatrix} \boldsymbol{u_L^s} \\ \boldsymbol{f_L^s} \end{bmatrix}$ is of significantly different order in magnitude. By introducing an α factor with the norm of the submatrices

$$\alpha = \frac{\left\| \boldsymbol{D_{LR}^{-1}} \right\|}{\left\| -\boldsymbol{D_{LR}^{-1}} \boldsymbol{D_{LL}} \right\|} \tag{2-72}$$

the new eigenvalue problem is written in terms of the normalized vector $\begin{bmatrix} \boldsymbol{u_L^s} \\ \alpha \boldsymbol{f_L^s} \end{bmatrix}$. Inspecting equation (2-65), $-\boldsymbol{D_{LR}^{-1}} \boldsymbol{D_{LL}}$ is multiplying the displacement vector whereas $-\boldsymbol{D_{LR}^{-1}} \boldsymbol{D_{LL}}$is multiplying the nodal force vector. The α factor can then be used to rescale the eigenvalue problem to become

$$\begin{bmatrix} -\boldsymbol{D_{LR}^{-1}} \boldsymbol{D_{LL}} & \boldsymbol{D_{LR}^{-1}}/\alpha \\ (-\boldsymbol{D_{RL}} + \boldsymbol{D_{RR}} \boldsymbol{D_{LR}^{-1}} \boldsymbol{D_{LL}})\alpha & -\boldsymbol{D_{RR}} \boldsymbol{D_{LR}^{-1}} \end{bmatrix} \begin{bmatrix} \boldsymbol{u_L^s} \\ \boldsymbol{f_L^s} \end{bmatrix} = \boldsymbol{\lambda} \begin{bmatrix} \boldsymbol{u_L^s} \\ \alpha \boldsymbol{f_L^s} \end{bmatrix} \tag{2-73}$$

Furthermore, when the number of interior DOFs increases relative to the number of boundary DOFs, the numerical error in the matrix inverse calculation of $\boldsymbol{D_{LR}}$ is prominent. Maess et. al. proposed [32] to reformulate the eigenvalue problem to use the general form of the eigenvalue problem as in (2-74) to avoid using the inverse matrices as in equation (2-73).

$$\begin{bmatrix} \boldsymbol{D_{LL}} & -\boldsymbol{I} \\ \boldsymbol{D_{RL}} & \boldsymbol{0} \end{bmatrix} \begin{bmatrix} \boldsymbol{u_L^s} \\ \boldsymbol{f_L^s} \end{bmatrix} = \lambda \begin{bmatrix} -\boldsymbol{D_{LR}} & \boldsymbol{0} \\ -\boldsymbol{D_{RR}} & -\boldsymbol{I} \end{bmatrix} \begin{bmatrix} \boldsymbol{u_L^s} \\ \boldsymbol{f_L^s} \end{bmatrix} \tag{2-74}$$

Prescribe the Sign Convention of the Eigenmodeshapes

Since the eigenvectors are not unique, the sign of the modal displacements/stresses can be scaled differently across frequencies.

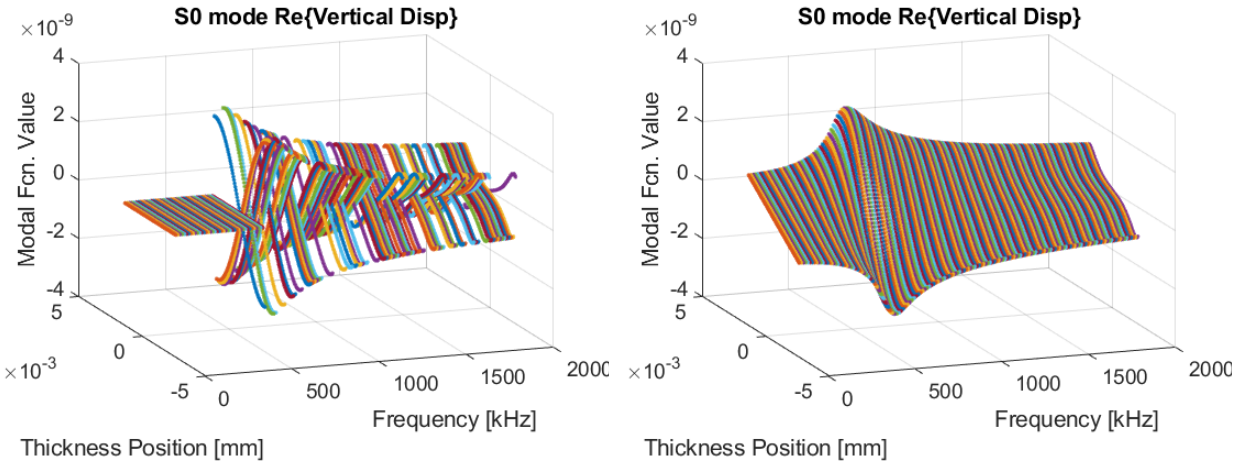

(a) without prescribing a sign convention (b) with a prescribed sign convention

Figure 2-11 WFE Eigenmode shapes for S_0 mode vertical displacement across frequencies

The consequence is that when the inverse Fourier time transform is done, the frequency domain solution has inconsistent phases between frequencies. To ensure the eigenvectors are consistent across frequencies, the top surface vertical displacement for every Lamb mode is multiplied by a scalar such that it is real and positive. For example, if the eigenvalue problem returns the nodal displacement of the top left node to be a negative imaginary quantity, the entire eigenvector $\begin{bmatrix} \boldsymbol{u}_L^s \\ \boldsymbol{f}_L^s \end{bmatrix}$ is multiplied by *i*, such that the resulting top surface displacement is a positive real number. Figure 2-11 shows the difference between the modal functions without and with the common sign convention. When the sign and phase of the modal function are prescribed, the modal functions have a common phase across frequencies for the numerical calculations of the inverse Fourier transform.

2.2.3 Theoretical Validation of WFE Model

In the previous sections, GMM and WFE are introduced to model the free wave response in multilayered plates, each have their advantages and disadvantages. In this section, the analytical GMM is used to validate the dispersion curves and the modal functions calculated from WFE. Furthermore, since both methods are capable of modeling multilayered material

systems efficiently, they are used to study the free wave response of several polymer adhesive systems. The baseline plate considered is a 3-layer aluminum skin panel of 1 mm skin thickness with different isotropic core materials that are 2 mm thick.

Validation of the WFE Dispersion Curves and Mode Shape using GMM

The aluminum-titanium laminate is chosen for comparing WFE results with those obtained from GMM. Figure 2-12 shows the dispersion data obtained from GMM, represented by the black crosses are identical to the WFE results (solid lines).

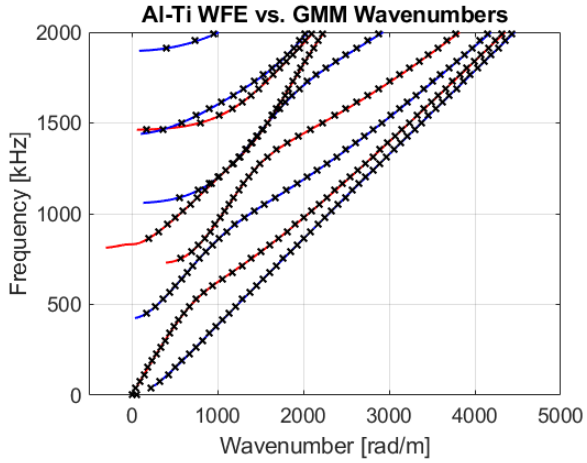

Figure 2-12 Wavenumber comparison between the WFE (solid blue lines denoting antisymmetric mode, and solid red lines denoting symmetric modes) and the GMM (denoted by black crosses) for the Al-Ti laminate

It is worth to mention that for the "backward" wave mentioned above, the GMM data would require the calculation of $\frac{\partial \omega}{\partial k}$ to identify the modes with negative group velocity (not shown). For the modes that have a negative derivative of $\frac{\partial \omega}{\partial k}$, $-k$ should be used instead.

Lamb Wave Propagation in Laminates with a Soft Core

The bulk wave velocities of some common of polymer adhesive materials are collected in Table 2-1. To down select the number of core materials being considered, the materials with more unusual bulk wave velocities in terms of c_1/c_2 and $c_1 - c_2$ are chosen using Figure 2-13. The baseline structure, highlighted in gray in the table, is the aluminum-titanium hybrid which is

characterized by the c_1 of the titanium is greater than the c_2 of the aluminum and the respective $c_1$and c_2 are relatively similar between the skin and core materials. 5505 Epoxy and P3-319 Epoxy, highlighted green, are characterize as the extremum cases in $c_1 - c_2$ whereas KT-820 PEEK and R-5100 PPSU, highlighted in yellow, are characterized as unusual in c_1/c_2. Finally, highlighted in orange is the high-density foam in which the elastic properties and the density are extremely low when compared to the aluminum skin.

Table 2-1 Material properties of some core materials being considered

ID	Material Name	E [GPa]	G [GPa]	ν	ρ [kg/m^3]	c_1[m/s]	c_2[m/s]
1	3506-1 Epoxy	4.20	1.567	0.34	1300	2230	1098
2	5250-4 RTM	4.62	1.71	0.35	1246	2439	1172
3	5505 Epoxy	7.24	2.68	0.35	1265	3030	1455
4	8551-7 Epoxy	4.08	1.478	0.38	1273	2449	1077
5	BSL914C Epoxy	4.00	1.48	0.35	1265	2252	1082
6	CETEX PEI	3.28	1.204	0.36	1270	2081	973
7	Coors Tek PEKK	4.40	1.57	0.4	1310	2683	1095
8	KT-820 PEEK	3.50	1.316	0.33	1300	1997	1006
9	KT-880 PEEK	3.70	1.35	0.37	1300	2244	1019
10	LY556 Epoxy	3.35	1.24	0.35	1273	2055	987.0
11	MY750 Epoxy	3.35	1.24	0.35	1273	2055	987.0
12	Polyester	3.24	1.17	0.38	1163	2284	1005
13	PR-319 Epoxy	0.95	0.35	0.35	1273	1094	526.0
14	R-5100 PPSU	2.34	0.824	0.42	1300	2144	796.0
15	Vinyl ester	3.44	1.172	0.38	1265	2256	993.0
16	High Dens. Foam	0.30	0.110	0.364	249.9	1433	663.4
17	Aluminum	68.9	26.5	0.3	2700	5861	3132
18	Titanium	100.0	37.59	0.33	4760	5579	2810

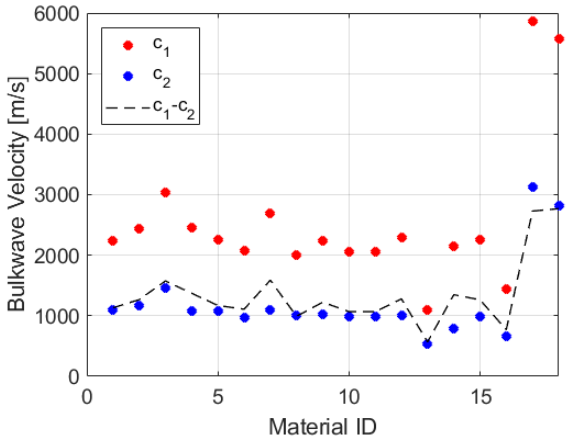

(a) Longitudinal, shear wave velocities, and their differences for different core materials

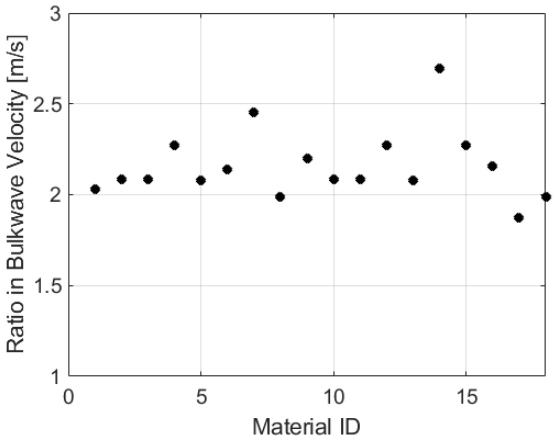

(b) The ratio between the longitudinal and shear wave velocities

Figure 2-13 Bulk wave velocities for material selection

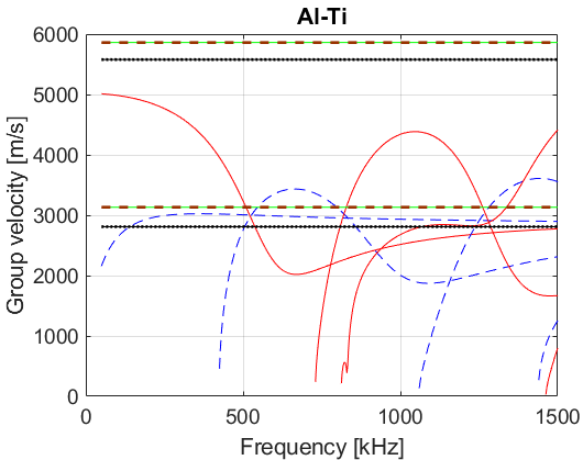

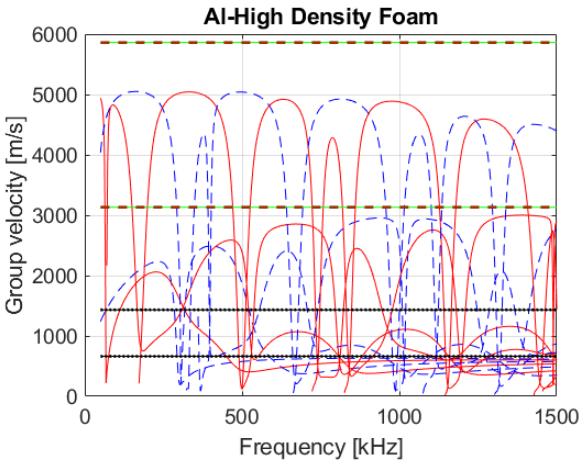

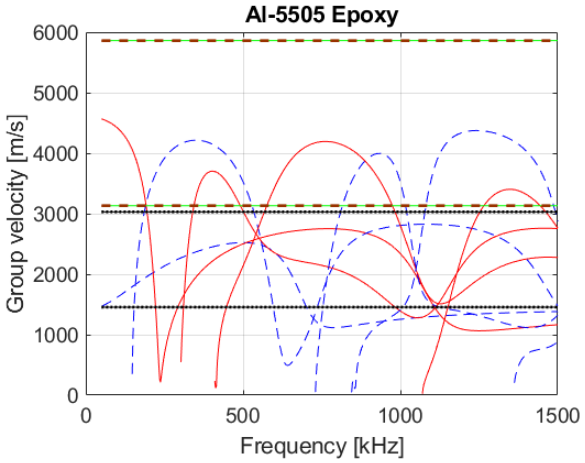

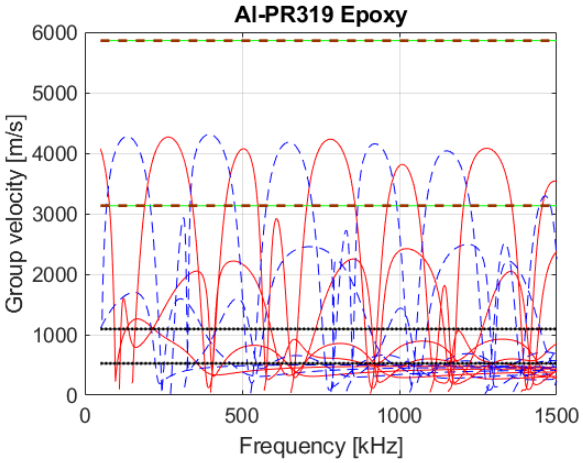

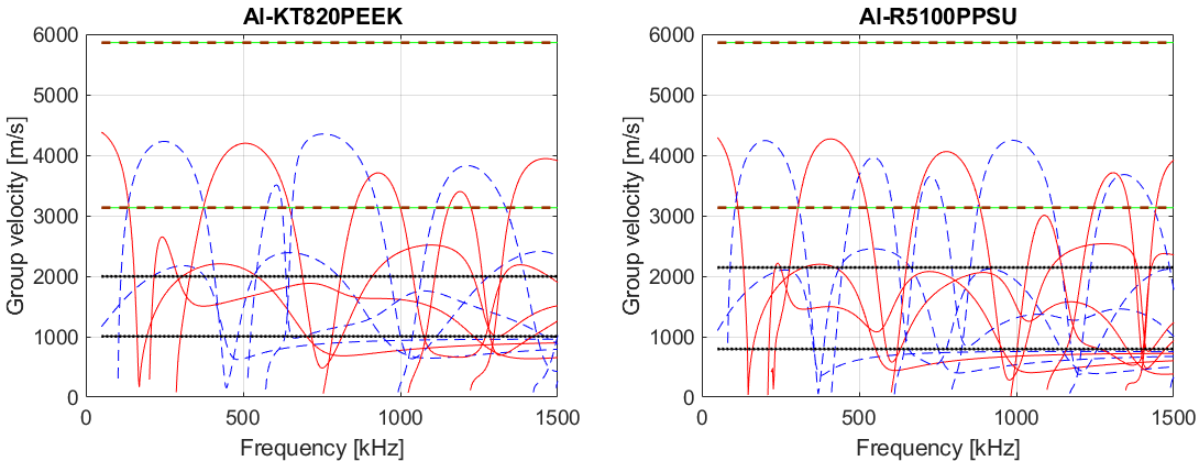

Figure 2-14 Group velocities and the bulk wave velocities for various hybrid laminates. The brown dashed lines are the c_1 and c_2 of the aluminum skin, whereas the black dotted lines are those for the core materials

The group velocity curved presented in Figure 2-14 show that more higher modes will appear when a material has slow bulk wave velocities. Furthermore, the group (and phase) velocities converges to the lowest shear wave velocity among the different laminated materials. This could be explained by the fact that Lamb wave modes are formed by the consecutive reflections of bulk waves, the slower velocities induce a smaller reflection angle so that more Lamb modes can be formed.

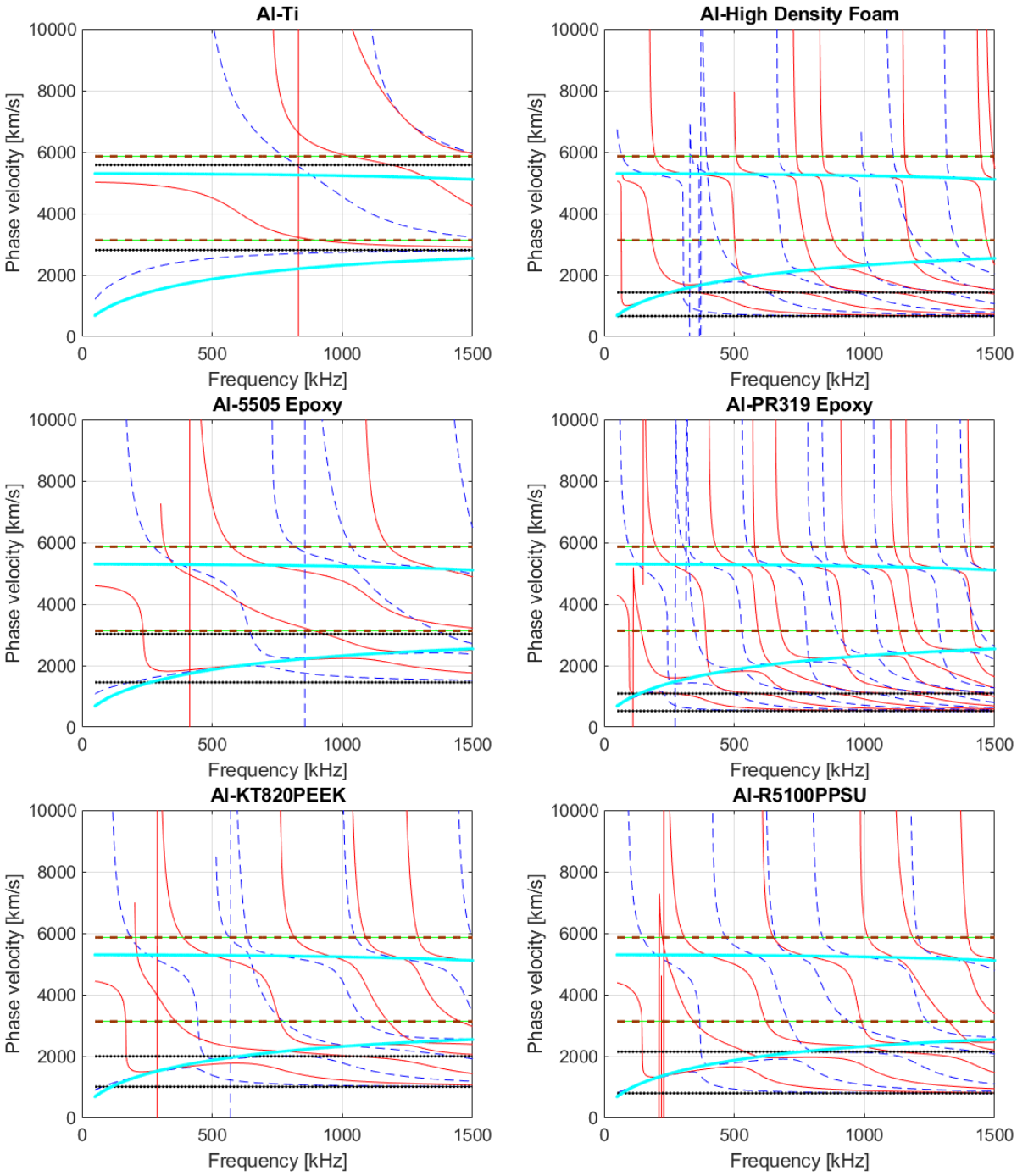

Figure 2-15 Phase velocities and the bulk wave velocities in various hybrid laminates. The brown dash lines are the c_1 and c_2 of the aluminum skin, the magenta lines are the A_0 and S_0 mode phase velocity of a 1mm thick aluminum plate, whereas the black dotted lines are those for the core materials

The phase velocity of the laminated materials shown in Figure 2-15 exhibits some remarkable features. When the core material has slower longitudinal and shear wave velocities than those of the skin (aluminum), the dispersion curves for the entire laminate would converge to the aluminum skin (magenta lines). Furthermore, as the frequency increases, the phase velocity would converge to the slowest shear wave velocity which is of the core material. It is worth mentioning that the "vertical lines" in the phase velocity appear because of the "backward" wave mentioned in section "Lamb Wave Mode Identification Based on Wavenumbers." For those wave modes to have a forward propagating power flow (with a positive group velocity), the phase velocity transitions from negative to positive, hence the vertical line.

The discussion of the nature of the dispersion curves pointed out some distinct differences between the nature of the wave propagation in a laminated material with a very slow core versus that of comparable bulk wave velocities. To better understand the underlying wave propagation mechanism, the wave motion across different layers is investigated. For the remainder of this section, the aluminum-titanium laminate, representing a stiffer core, and the aluminum-high density foam laminate, representing a softer core are studied. Figure 2-16 and Figure 2-17 show the displacement eigenvectors for the A_0 and S_0 modes, respectively across frequencies for the aluminum-titanium laminate and the aluminum-high density foam laminate. The eigenvector is multiplied by a scalar such that the vertical displacement is always a real number, and therefore the horizontal displacement is an imaginary quantity. As expected, the displacement in the soft foam core material is significantly larger than the stiffer aluminum skin whereas the Al-Ti laminate has barely visible slope change in the displacement. An important feature in the eigenvector is that below a certain frequency, the mode shapes exhibit a monotonic change with respect to thickness and above that frequency, the shapes display a sinusoidal

variation. The displacement magnitude often changes significantly around that frequency. In the case of a single layer isotropic plate, that frequency correspond to when $\eta_2 = \sqrt{k^2 - k_2^2}$ changes from a real to an imaginary quantity. For multilayer media, it appears that the eigenvectors behave similarly, but it is difficult to determine whether the same changes in the numerical characteristics of η_2 occurs.

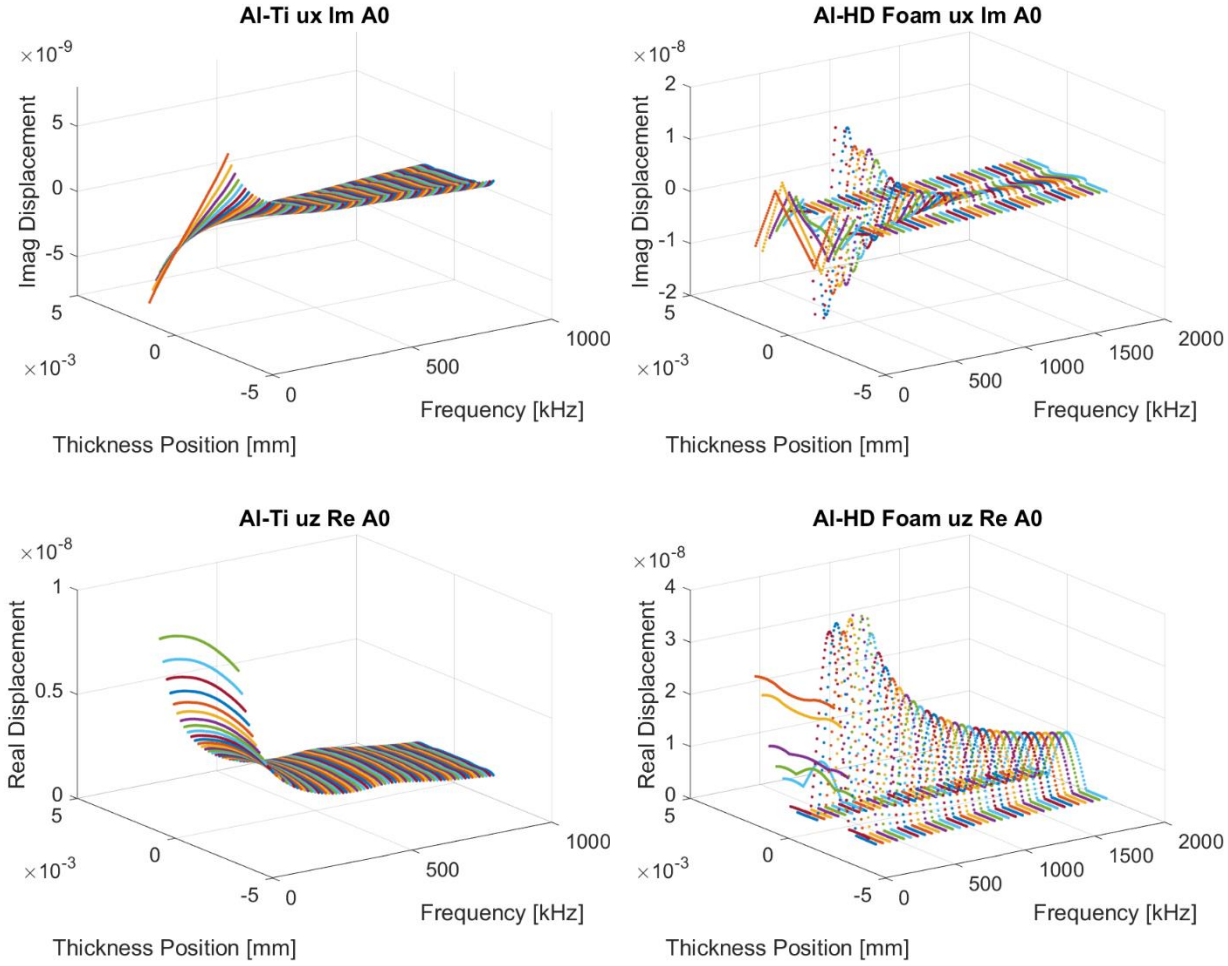

Figure 2-16 A_0 mode horizontal (u_x) and vertical (u_z) displacement eigenvector comparing Al-Ti and Al-High Density Foam laminates

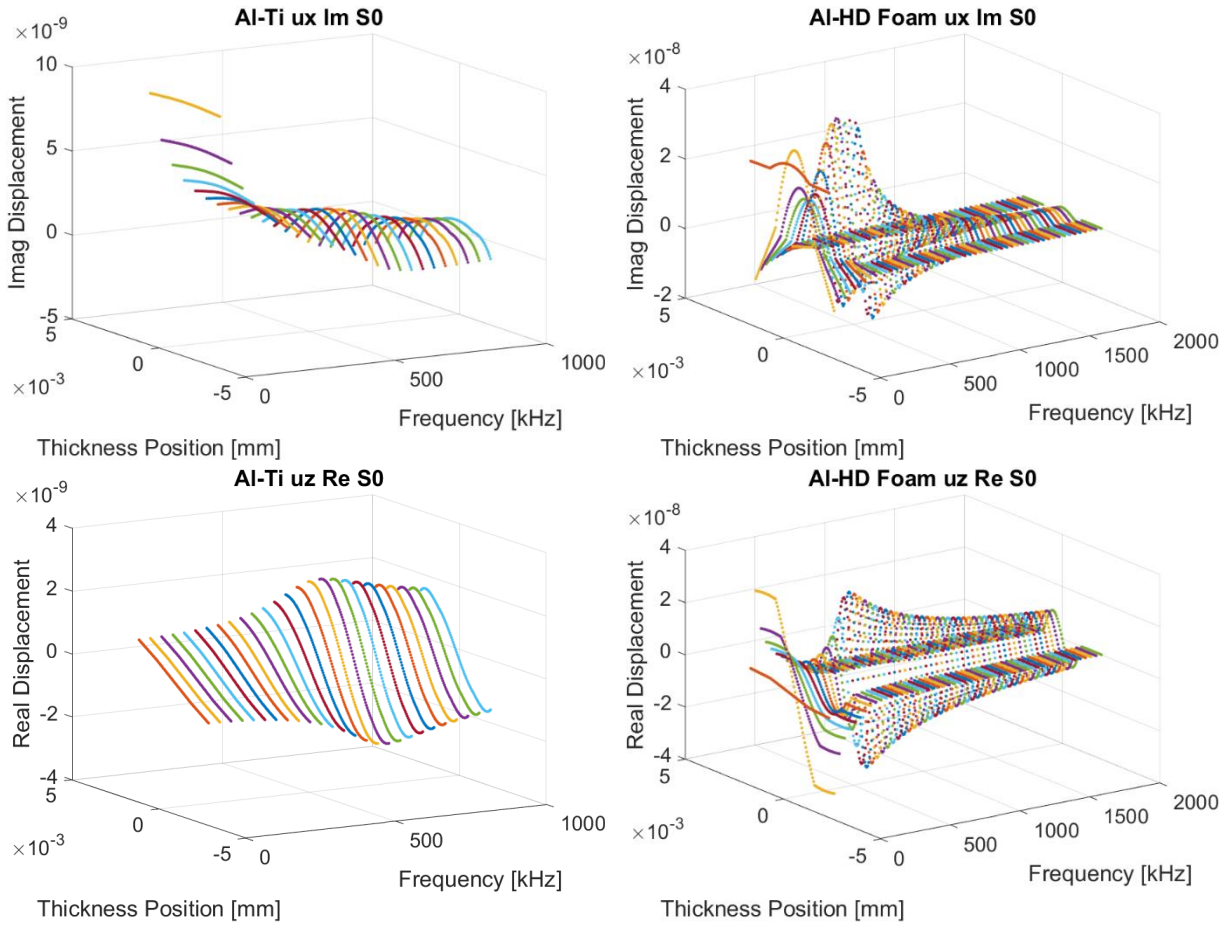

Figure 2-17 S_0 mode horizontal (u_x) and vertical (u_z) displacement eigenvector comparing Al-Ti and Al-High Density Foam laminates

The displacement vectors show the wave motion in different layers but not indicative to the wave characteristics in the stiffer aluminum skin because of the relatively low amplitude of the displacements. The elastic energy associated with the nodal displacements and forces, represented by the Poynting vector, $p_j^{(n)} = \frac{1}{2} Re\{i\omega f_j^* q_j\}$, (where f^* is the complex conjugate of the nodal force components, and the subscript $_j$ refers to the *x* or *z* component) is indicative of the stress state in the layers. Figure 2-18 shows the Poynting vectors for the A_0 and S_0 modes across frequencies for the two material systems.

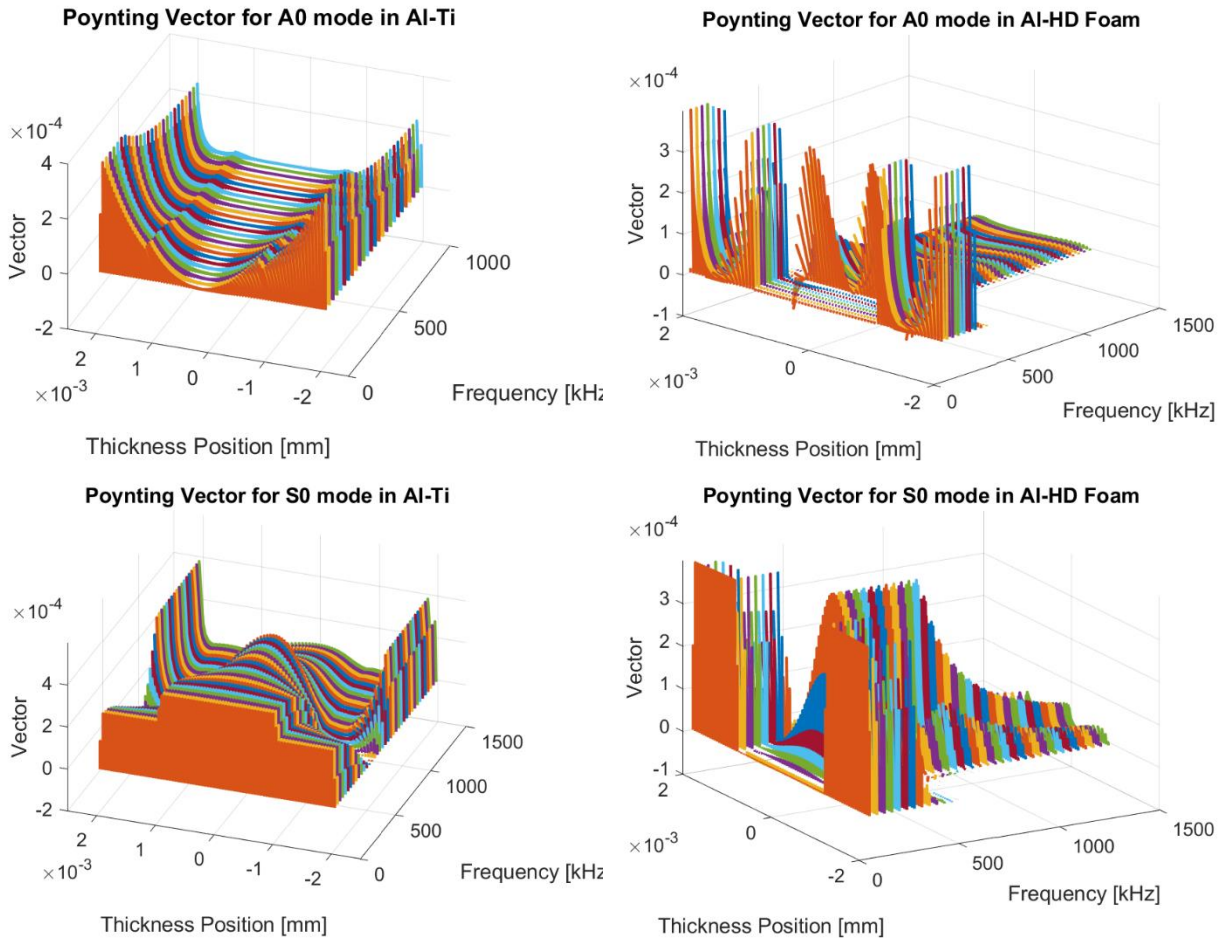

Figure 2-18 The Poynting vector of the A_0 and S_0 modal eigenvectors for Al-Ti and Al-High Density Foam for different nodal positions through the thickness at various frequencies

For the Al-Ti laminate, the elastic energy distribution in the aluminum skin does not change across frequencies for the A_0 mode whereas the S_0 mode has more energy concentrated in the titanium core in the lower frequencies and at the top and bottom surfaces in the aluminum skin for higher frequencies. For the aluminum-foam core laminate, the A_0 mode exhibits a different behavior where the elastic energy is concentrated on the plate's surfaces and at the interlaminar interfaces at lower frequencies. At higher frequencies, the elastic energy is concentrated almost exclusively in the soft core. The S_0 mode is similar in that the elastic energy is primarily in the skin at lower frequencies and in the core at higher frequencies. Figure 2-19 shows the selected frequencies depicting the distinctions at lower and higher frequencies.

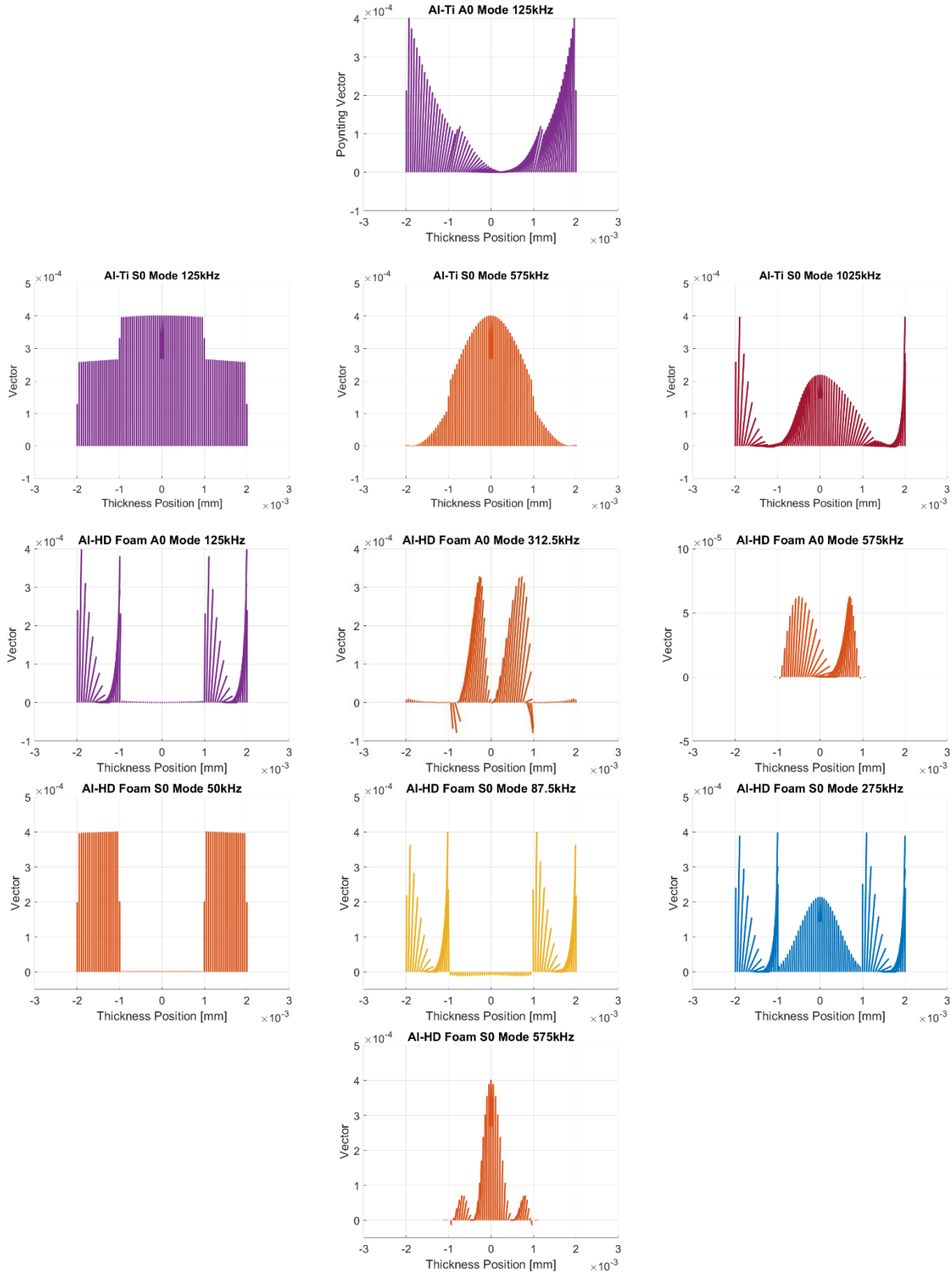

Figure 2-19 The Poynting vector of Al-Ti and Al-High Density Foam for A_0 and S_0 modes at various frequencies

Figure 2-19 highlights the differences in the energy distribution through the thickness between Al-Ti and Al-Foam laminates, where in the Al-Ti case, the elastic energy carried by the skin and core is relatively even as opposed to the Al-Foam, where the energy is either carried by the skin or the core. Furthermore, there are some frequencies such as at 87.5kHz and 312.5kHz, at which the direction of the Poynting vector is opposite to each other between the skin and the core, indicating the elastic energy is leaking across the interface.

2.2.4 Experimental Validation of the WFE Model

Quasi-isotropic laminates are often used in the design of composite structures and are often modeled as a homogenized material with the effective properties of the laminate. In practice, the manufacturing errors of those laminates could weaken the validity of the quasi-isotropic assumption but could still be sufficient for the purpose of structural analysis when a safety factor is employed. For guided ultrasonic wave based nondestructive testing methods, these deviations may cause a directional dependency of the propagation velocities that could lead to error in the time-of-flight analysis. In this section, the dispersion curves calculated by WFE is compared with experimental measurements for two carbon composite plates that one of them has the quasi-isotropic layup while the other does not.

Composite Modeling

A waveguide segment is modeled in ABAQUS CAE with dimensions $2H$ x 50 μm x 50 μm is created where $2H$ is the plate thickness. The waveguide is subjected to a periodic boundary conditions in the x_2 direction. For composite laminates, the model is partitioned such that each ply is modelled explicitly. A sufficiently large number of elements per ply thickness (element size less than 20 μm) is used to minimize any numerical dispersion artifacts, and to ensure convergence of the results. For the individual plies with various orientations, the lamina stiffness

properties are calculated through a matrix rotation. Figure 2-20 shows the convention for 3D WFE used in this work in which the 0° ply aligns with the global x_1 axis and a positive ply angle is rotated counterclockwise about x_3 axis. The lamina used is this study is a 2x2 twill woven fabric with T300 fibers of 3K tow embedded in CYCOM970 epoxy. It is worth noting that most manufacturers report only a subset of the elastic constants. In this case $G_{13}, G_{23}, \nu_{13}, \text{and } \nu_{23}$are obtained from composite handbooks with similar in-plane properties, and the complete list of the lamina properties is given in Table 2-2.

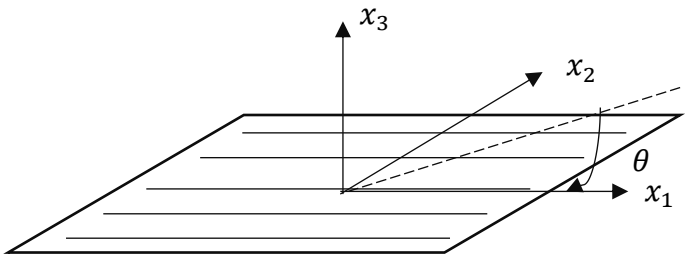

Figure 2-20 Illustration of the 3D ply rotation for stiffness properties calculations

Table 2-2 Lamina properties for the studied composite plate with T300/CYCOM970 (ρ = 1543 kg/m^3)

E_{11}[GPa]	E_{22}[GPa]	E_{33}[GPa]	G_{12}[GPa]	G_{13}[GPa]	G_{23}[GPa]	ν_{12}	ν_{13}	ν_{23}
57.25	55.5	13.5	5.20	4.08	3.28	0.06	0.5	0.37

Although there are serval software tools to calculate the overall elastic constants for different ply orientations, most of the tools would only accept real numbers. In preparation for modeling material attenuation with complex elastic properties, the well-known procedure is summarized below for completeness. First the compliance matrix is calculated through equation (2-75) below and the stiffness matrix $\boldsymbol{D}$ is evaluated from its inverse.

$$\begin{bmatrix} \frac{1}{E_{11}} & -\frac{\nu_{12}}{E_{11}} & -\frac{\nu_{13}}{E_{11}} & 0 & 0 & 0 \\ & \frac{1}{E_{22}} & \frac{-\nu_{23}}{E_{22}} & 0 & 0 & 0 \\ & & \frac{1}{E_{33}} & 0 & 0 & 0 \\ & & & \frac{1}{G_{23}} & 0 & 0 \\ & sym & & & \frac{1}{G_{13}} & 0 \\ & & & & & \frac{1}{G_{12}} \end{bmatrix}$$

(2-75)

To obtain the components of $\boldsymbol{D'}$, the stiffness matrix in the new orientation, evaluate the matrix transformation from equation (2-76) where the rotation matrix $\boldsymbol{T}$ is defined in equation (2-77) with $m = \cos(-\theta)$, $n = \sin(-\theta)$ and θ is the ply orientation relative to the propagation axis x_1 which would be positive when rotated counterclockwise as illustrated in Figure 2-20.

$$\boldsymbol{D'} = \boldsymbol{TDT}^T$$

(2-76)

$$\boldsymbol{T} = \begin{bmatrix} m^2 & n^2 & 0 & 0 & 0 & mn \\ n^2 & m^2 & 0 & 0 & 0 & -mn \\ 0 & 0 & 1 & 0 & 0 & 0 \\ 0 & 0 & 0 & m & -n & 0 \\ 0 & 0 & 0 & n & m & 0 \\ -2mn & 2mn & 0 & 0 & 0 & m^2 - n^2 \end{bmatrix}$$

(2-77)

The rotated elastic property for each ply can then be written into a .csv file and be read into ABAQUS CAE directly in the form of equation (2-78).

$$\begin{Bmatrix} \sigma_{11} \\ \sigma_{22} \\ \sigma_{33} \\ \sigma_{12} \\ \sigma_{13} \\ \sigma_{23} \end{Bmatrix} = \begin{bmatrix} D_{1111} & D_{1122} & D_{1133} & D_{1112} & D_{1113} & D_{1123} \\ & D_{2222} & D_{2233} & D_{2212} & D_{2213} & D_{2223} \\ & & D_{3333} & D_{3312} & D_{3313} & D_{3323} \\ & & & D_{1212} & D_{1213} & D_{1223} \\ & sym & & & D_{1313} & D_{1323} \\ & & & & & D_{2323} \end{bmatrix} \begin{Bmatrix} \varepsilon_{11} \\ \varepsilon_{22} \\ \varepsilon_{33} \\ 2\varepsilon_{12} \\ 2\varepsilon_{13} \\ 2\varepsilon_{23} \end{Bmatrix}$$

(2-78)

Note that for ABAQUS, the stress vector convention has a slight change to the standard Voigt notation, instead of $\{\sigma_{11} \quad \sigma_{22} \quad \sigma_{33} \quad \sigma_{23} \quad \sigma_{13} \quad \sigma_{12}\}^T$, it is $\{\sigma_{11} \quad \sigma_{22} \quad \sigma_{33} \quad \sigma_{12} \quad \sigma_{13} \quad \sigma_{23}\}^T$. Therefore, some row and column changes are necessary to convert the matrix from equations (2-76) to (2-78).

Furthermore, in the case of preparing dispersion data and modal functions, a 2D model is needed since ABAQUS would only allow the plane-strain problem to be modeled on the x_1-x_2 plane. The ply stiffness matrix rotation must be done about the x_2 axis as shown in Figure 2-21.

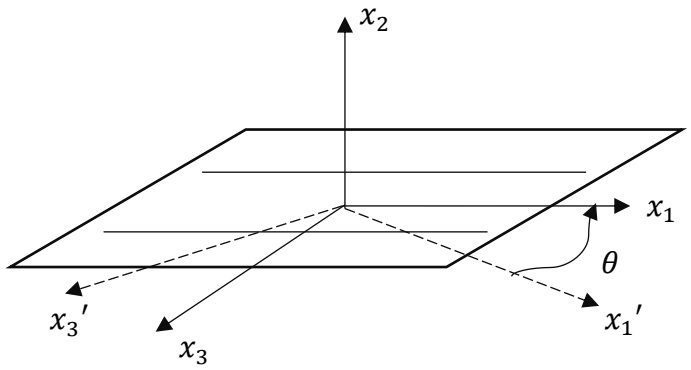

Figure 2-21 Illustration of the ply rotation about $x_2$axis

Although the angled plies are not strictly in plane-strain condition, it is determined that when the laminate has a balanced and symmetric layup, the plane-strain assumption is a fair approximation and further details are presented in Figure 2-26b. For such 2D case, the rotational matrix in equation about the x_2 axis is

$$\boldsymbol{T} = \begin{bmatrix} c^2 & 0 & s^2 & 0 & 2cs & 0 \\ 0 & 1 & 0 & 0 & 0 & 0 \\ s^2 & 0 & c^2 & 0 & -2cs & 0 \\ 0 & 0 & 0 & c & 0 & -s \\ -cs & 0 & cs & 0 & c^2 - s^2 & 0 \\ 0 & 0 & 0 & s & 0 & c \end{bmatrix}$$

(2-79)

Note that a change of direction for the elastic constants is made when entering the 0° properties listed in Table 2-2 where the left-hand side of the equations are written for the lamina in the $x_1 - x_3$ plane. The right-hand side of the equation is written for which the lamina is in the $x_1 - x_2$ plane instead

$$E_{22} = E_{33} \qquad E_{33} = E_{22} \qquad \nu_{12} = \nu_{13} \qquad \nu_{13} = \nu_{12} \qquad \nu_{23} = \nu_{32}$$

$$G_{13} = G_{12} \qquad G_{12} = G_{13} \tag{2-80}$$

Finally, for calculating the dispersion curves for different propagation directions, the global coordinate system is rotated through a clockwise angle θ from the layup 0° orientation about the off plane axis.

Experimental Procedure

Two composite plates are manufactured: plate A) with an anisotropic stacking sequence $[60/0/60/60/0/60]_s$ and plate B) with a quasi-isotropic stacking sequence $[-60/0/60/60/0/-60]_s$. It should be noted that both plates were supposed to be manufactured to the specifications of plate B, however, due to a misinterpretation, the angled layers for plate A were cut incorrectly. Both specimens are manufactured with the T300/CYCOM970 system mentioned in Table 2-2. The two plates are trimmed to a size of 440 mm by 440 mm and the cured laminate thickness to be 2.71 mm. To measure the group velocities of Lamb waves, a 10 V_{pp} Hann-windowed sine signal of 5 cycles with center frequency varying from 50 kHz to 300 kHz in steps of 25 kHz is generated by a waveform generator (NI 5402). The source and receiving piezoelectric transducers are identical (Digital Wave B225) and are positioned with the use of a Plexiglass template. The receiving transducer is connected to a signal conditioner (Digital Wave FM-1), which with a 20 kHz high-pass filter and 12 dB gain. The conditioned signal is captured by an

oscilloscope (Agilent 54624A) with a 5 MHz sampling frequency and a 400 μs recording time. Results from serval repeated wave bursts are averaged to achieve a higher signal-to-noise ratio. The receiving transducer is placed at serval distances from the source for each investigated direction (0°, 30°, 60°, and 90°), as shown in Figure 2-22.

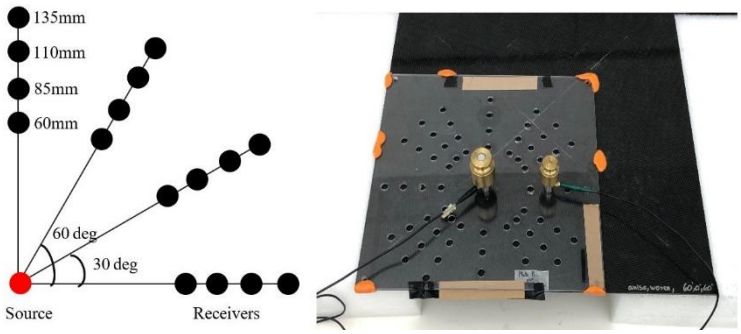

Figure 2-22 Experimental setup for measuring group velocities at different orientations. The source location is denoted by the red dot, while receivers are denoted by the black dots.

In order to determine the group velocity from the recorded signals, the time of arrival of the waveform corresponding to the center frequency is needed. Since Lamb waves are dispersive, the time domain waveform is subjected to a short time Fourier transform (STFT). An example for a source with center frequency of 200 kHz, measured at 0° and 135mm from the source is shown in Figure 2-23a. instead of using the waveform's peak times, the more robust time of the STFT peak amplitude at the center frequency is determined, as shown in Figure 2-23b. This process is repeated for measurements taken at 60 mm, 85 mm, 110 mm, and 135 mm separation distances for each investigated angle, as shown in Figure 2-22. The average group velocity for each frequency and orientation can then be determined by fitting a line through the data points of peak times vs. propagation distance as shown in Figure 2-23c.

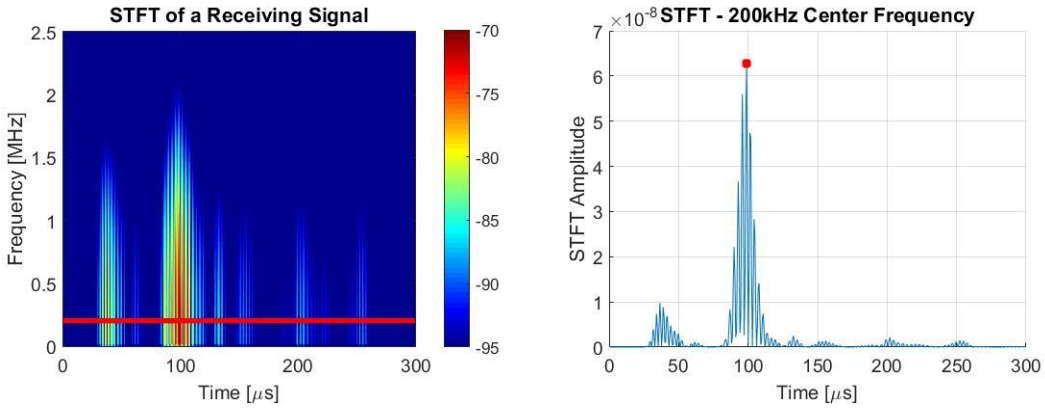

(a) Complete STFT of the signal (b) STFT result at center frequency

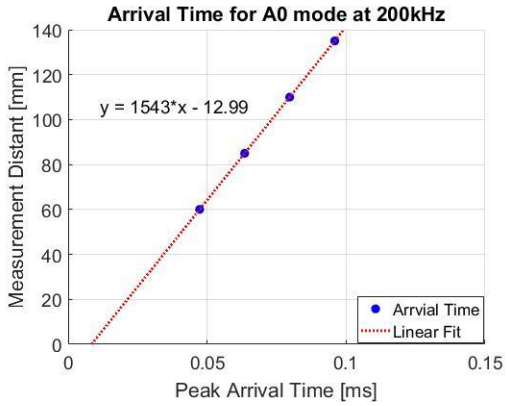

(c) The linear fit obtained from STFT peak times for the 4 locations

Figure 2-23 Time-of-flight evaluation of a sample signal using STFT

Comparison between WFE Dispersion Curves and Experimental Results

Figure 2-24 shows the numerical and experimentally derived dispersion curves for plate A with the anisotropic layup. The red lines denote the symmetric modes, and blue lines are used for the antisymmetric modes. The WFE model explicitly accounts for each ply in the laminate. It is evaluated for different propagation orientations, and the resulting dispersion curves are shown in Figure 2-24a.

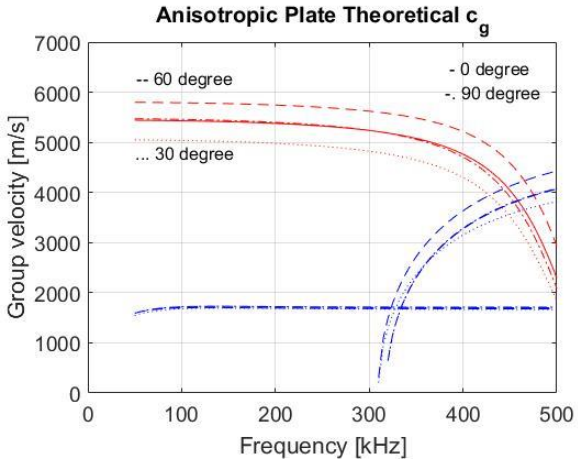

(a) WFE results for 0°, 30°, 60°, and 90°

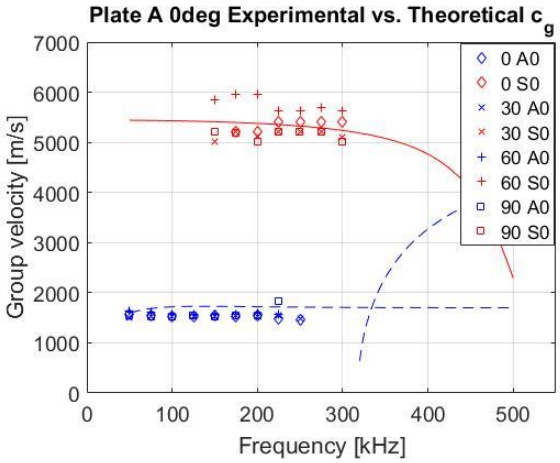

(b) Comparison of experimental group velocities to WFE 0° results

Figure 2-24 Dispersion results for plate A with the anisotropic stacking sequence

The model predicts that the A_0 mode is orientation-insensitive and non-dispersive in the investigated frequency range of 50-500 kHz. On the other hand, for the S_0 mode, it can be seen that waves propagating along the 60°-direction are predicted to be the slowest. These observations can be explained with having most fibers aligned with the 60°-orientation, and the least in the 30°-direction. Moreover, the WFE results suggest that the S_0 mode has almost the same propagation speed along 0° and 90°. Similar trends are observed from the experimentally derived group velocities as shown in Figure 2-24b. Overall, numerical and experimental results match reasonably well. Furthermore, despite the obvious variations in the results, S_0 waves along the 60°-direction are consistently observed to be the fastest. The experimental measurements of the group velocity for different orientations also show no significant change in A_0 mode group velocities across the measured frequency range.

For the quasi-isotropic plate B, the WFE prediction of the group velocity using an explicit model of the laminate's stacking sequence and the comparison with experimental results are shown in Figure 2-25.

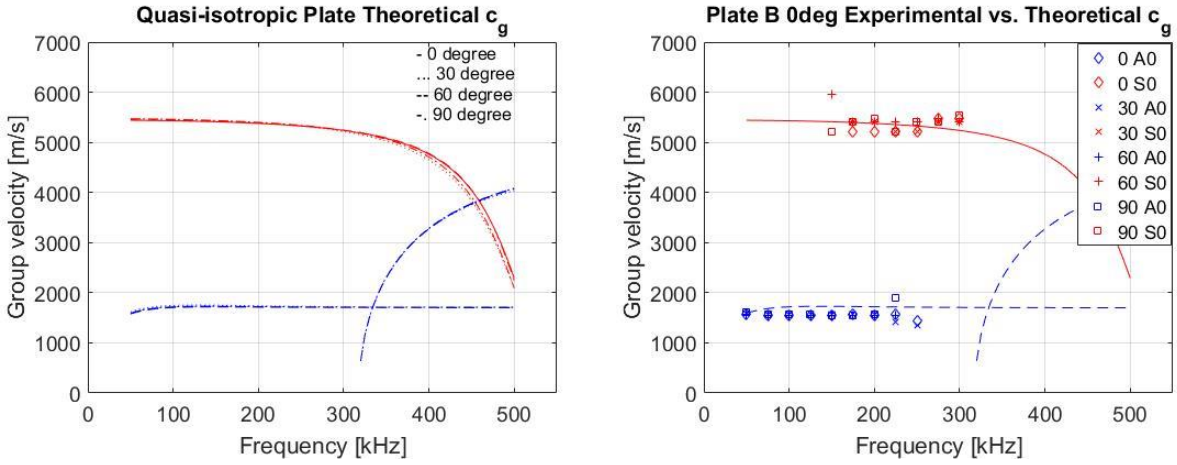

(a) WFE results for 0°, 30°, 60°, and 90°

(b) Comparison of experimental group velocities to WFE 0° results

Figure 2-25 Dispersion results for plate B (quasi-isotropic stacking sequence)

There is almost no difference between the different orientations for both the A_0 and S_0 modes. Despite some noise, the experimental results confirm that the A_0 and S_0 modes in the quasi-isotropic laminate are invariant with respect to the propagation direction. Since virtually no differences between the different orientations are observed, a transversely isotropic model is developed using the homogenized elastic properties for plate B which is presented in Table 2-3. The homogenized elastic properties are calculated using classical laminate theory [26].

Table 2-3 Effective Properties when Plate B is Homogenized into One Layer (ρ = 1543 kg/m^3)

E_{11}[GPa]	E_{22}[GPa]	E_{33}[GPa]	G_{12}[GPa]	G_{13}[GPa]	G_{23}[GPa]	ν_{12}	ν_{13}	ν_{23}
44.4	44.4	13.5	17.2	4.60	4.60	0.29	0.33	0.33

For the homogenized model, the analytical dispersion equation is available in equation (2-44), and the dispersion curves are compared to those obtained by the WFE ply-by-ply model in Figure 2-26a.

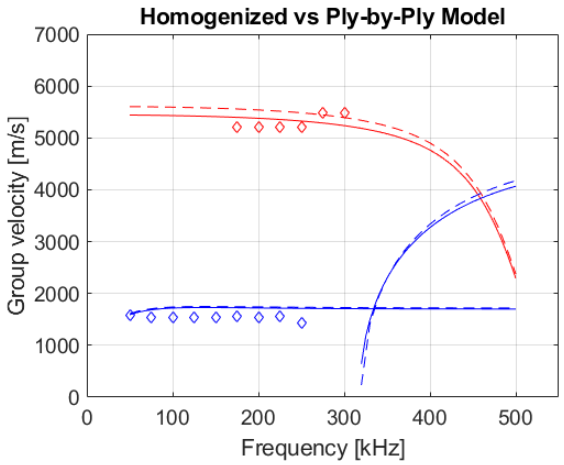

(a)) Dispersion curves calculated from WFE ply-by-ply model for waves propagating in 0° direction (solid line) vs. homogenized transversely isotropic model (dashed line)

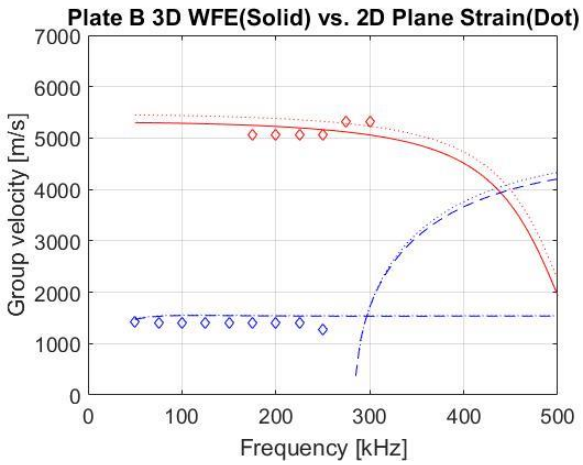

(b) Dispersion curves calculated from WFE ply-by-ply model with 3D elements for waves propagating in 0° direction (solid line) vs. the result calculated from 2D plane-strain ply-by-ply model (dotted line) and the experimental measurements

Figure 2-26 Dispersion curves for homogenized models

While the A_0 mode has a negligible difference between the two modes, for S_0, the homogenized model seems to predict a group velocity about 100 m/s slower than the 12-ply model. It should be noted that the solutions obtained by the WFE method have been compared with analytical solutions for isotropic and transversely isotropic plates in section 2.2.3, confirming their numerical convergence. Furthermore, a validity check for the 2D WFE implementation is made. Using an explicit ply-by-ply modeling for plate B with the use of plane-strain element where the ply constants are calculated by using the transformation equation in equation (2-79), the 2D vs. 3D dispersion curves for 0° propagation orientation is shown in Figure 2-26b. Comparing the dashed and dotted lines from Figure 2-26a and b, the results for the homogenized transversely isotropic analytical dispersion equation can be seen to be almost identical to the 2D plane strain ply-by-ply WFE results. This is likely because when the layup is balanced and symmetric, the effects of the non-zero stiffness constants that violate plane-strain would cancel out with those of for the matching plies.

2.2.5 On the Assumption of Transverse Isotropy of Honeycomb Sandwich Structure

Honeycomb Cell Model

Honeycomb sandwich composite structures, consists of thin composite skins enclosing a thick cellular core with honeycomb cells, has high bending stiffness and can be found in some aerospace structures. Traditionally, the honeycomb core layer is modeled with equivalent homogenized properties derived from structural theories for predicting the bulk material load-displacement response [39]. However, the use of homogenized layer with equivalent properties in wave propagation have yet been analyze in greater depth. With the use of WFE, waveguides with complex shapes can be handled by the FE discretization allowing the honeycomb cells geometry to be modeled. The 3D model of the honeycomb core has a cell size of $t = 0.0762$ mm, $L = 2.7568$mm according to Figure 2-27.

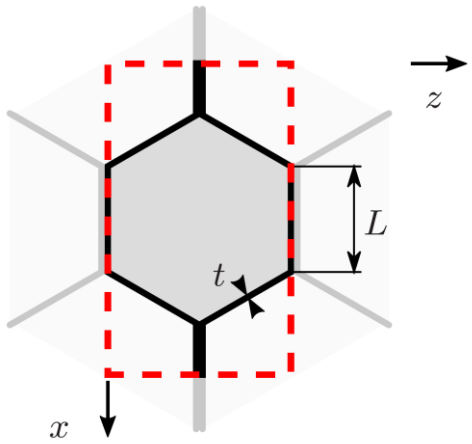

Figure 2-27 Honeycomb cell model in WFE (top view), representing one unit cell in the periodic structure

Utilizing the symmetry of the problem, this model is sufficient to represent a honeycomb core layer of infinite lateral dimensions with periodic boundary conditions. The material properties are given as follows: Young's modulus $E = 70.3$ GPa, Poisson's ratio $\nu = 0.33$, density $\rho = 2680$ kg/m^3 (aluminum 5052). The geometry is meshed in the FE software package Abaqus with about 40 elements in the plate thickness direction ($2H = 12.7$ mm). Mass and stiffness matrices

are extracted, and the equations of WFE are implemented and solved in MATLAB. The resulting dispersion curves for the honeycomb core model for waves propagating in the *z*-direction are shown in Figure 2-28.

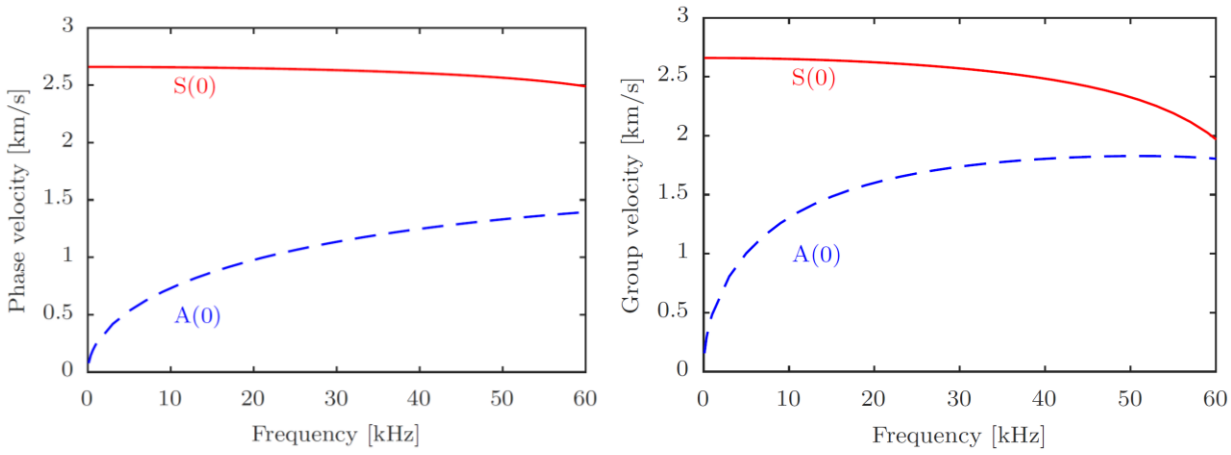

(a) Phase velocity (b) Group velocity

Figure 2-28 Dispersion curves for waves propagation in the honeycomb core in the z-direction (0°). Solid lines denote symmetric waves whereas antisymmetric waves are shown as dashed lines

It can be seen that in the considered frequency range, only the two fundamental modes, S_0 and A_0, are propagating. It should be noted that higher order modes are not investigated as the accuracy of the results at higher frequencies cannot be guaranteed due to the increased mesh requirements. In addition to the dispersion curves, mode shapes are investigated to conform symmetric and anti-symmetric wave motion. The determined mode shapes for the S_0 and A_0 waves are shown in Figure 2-29(a), (b), respectively.

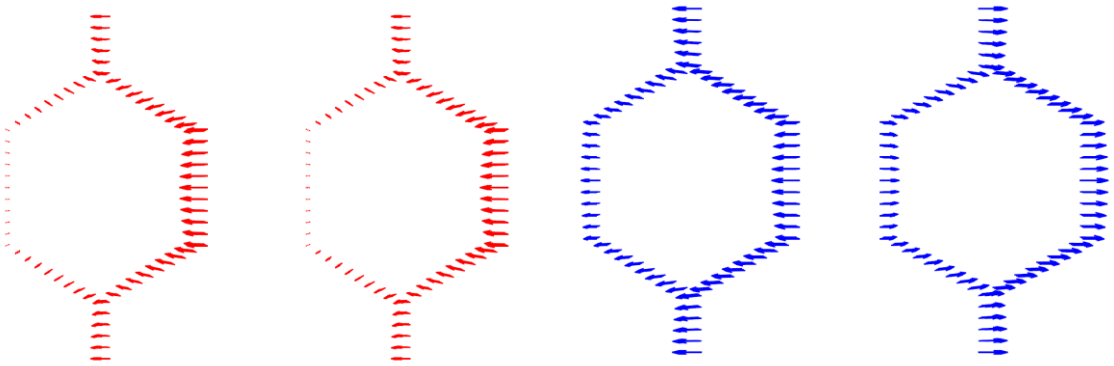

(a) S_0 at top (left) and at bottom (right) (b) A_0 at top (left) and at bottom (right)

Figure 2-29 In-plane displacements of fundamental modes in the *xz*-plane for the 0° model at 40 kHz

It can be seen that the in-plane displacement field of the S_0 wave is the same at the top and bottom of the core. On the other hand, the displacements of the A_0 wave are of the same magnitude but opposite sign at the top and bottom of the core. These results are in accordance with the theory and results for isotropic and transversely plates.

In a second step, the 3D model of the honeycomb core cell is rotated by 90˚ Keeping all other parameters (material properties, mesh) constant, and implementing corresponding symmetry and periodicity conditions for this case, the WFE method is again applied. The resulting dispersion curves are compared to the ones from the previous (0°) model in Figure 2-30.

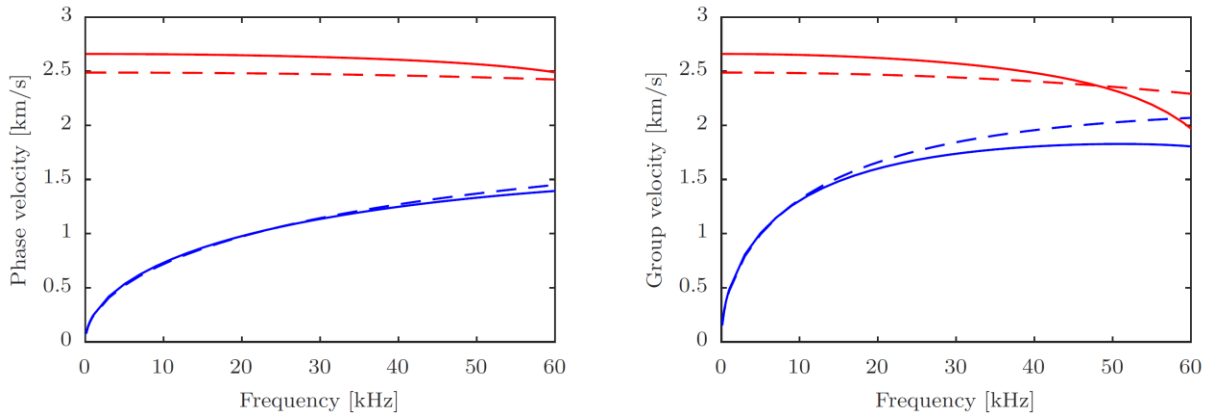

(a) Phase velocity (b) Group velocity

Figure 2-30 Dispersion curves in the honeycomb core. Solid lines denote results from the 0° model, results from the 90° model are shown as dashed lines

It can be seen that while the phase velocities for the A_0 wave are very similar between the two cases, the plots reveal noticeable differences for the S_0 wave. As in the previous case, also the mode shapes are analyzed for the 90° model. The mode shapes for both the S_0 and A_0 waves are shown Figure 2-31. For the sake of brevity, only the shapes at the top of the core are shown here.

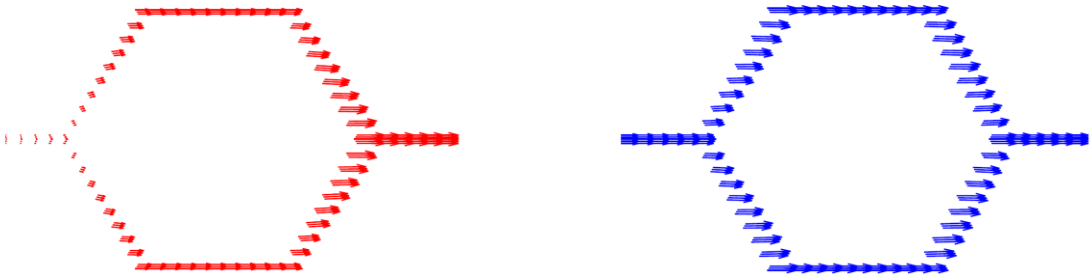

(a) S_0 at top (b) A_0 at top

Figure 2-31 In-plane displacements of fundamental modes in the *xz*-plane for the 90° model at f = 40 kHz

The equivalent behavior at the bottom of the core is evident. Compared to the mode shapes from Figure 2-29, it can be seen that in this configuration, the stiffness of the model is distributed differently, causing (slight) bending in different regions of the cell. This confirms that differences in the dispersion curves are to be expected.

Comparing 3D and Transversely Isotropic Homogenized Layer Model

In this subsection, results for a simplified model are derived in an effort to compare the results from the novel 3D model of the honeycomb cells with the established practice of modeling the core as a homogeneous transversely isotropic layer. In this case, the transversely isotropic core later is modeled with equivalent properties and the plane strain assumptions. The material properties are calculated using the mixture theory in [39] and are summarized in Table 2-4.

Table 2-4 Geometry and material parameters for the aluminum honeycomb core

Thickness [mm]	E_{11}[GPa]	E_{33}[GPa]	G_{13}[GPa]	ν_{12}	ν_{13}	ρ [kg/m^3]
12.7	3.43×10^{-3}	2.99	0.413	0.997	3.79×10^{-4}	0.33

The WFE is applied and the dispersion curves for waves propagation in this homogeneous layer are determined. Due to the reduced complexity of the geometry in the homogenized model, a smaller element size of about 50 μm is chosen for this study. The resulting dispersion curves (dashed lines) are compared with those from the 3D 0° model (solid lines) and are presented in Figure 2-32.

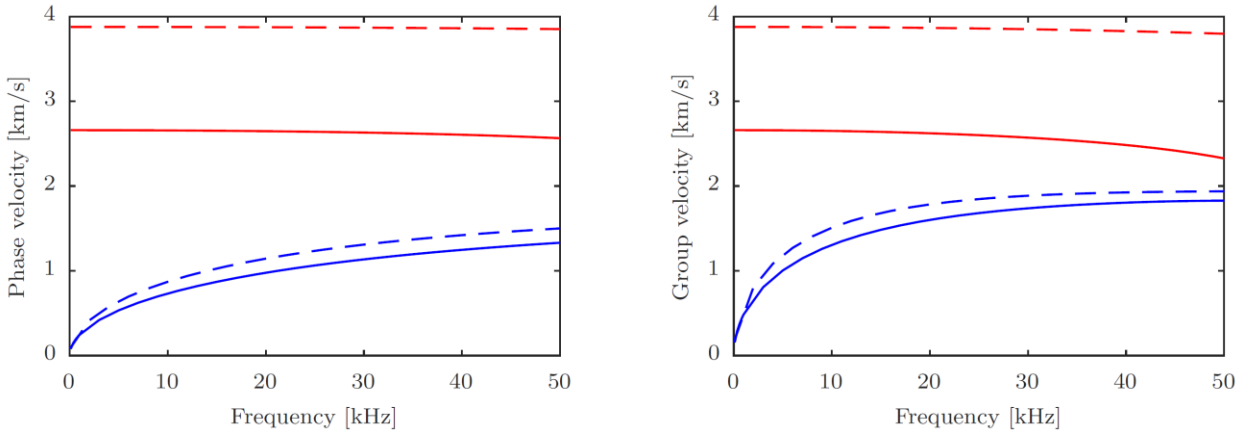

(a) Phase velocity (b) Group velocity

Figure 2-32 Dispersion curves for honeycomb core. Solid lines denote 3D model, dashed lines represent results from homogenized transversely isotropic core layer

It can be seen that both the S_0 and A_0 waves are significantly different. The effect is particularly strong for the S_0 wave. However, it should be noted that the equivalent material properties are based on simplified mixture theory, and more accurate predictions might reduce the differences.

Chapter 3 The Global Local Method

3.1 A Review of the Global Local Method

In Chapter 2, the mathematical description of Lamb wave propagation in various plate structures are presented. However, in NDE applications, the knowledge of the elastic waves generated by sources and scattered by defects in their path of propagation are also important. The equations governing Lamb waves for these problems are typically solved analytically for specific cases using integral (e.g. Fourier) transform techniques. For surface corrosion defects, solution for surface waves with varying plate thickness is available in [40]. Green's function approach is used to solve the scattering problem of Rayleigh waves at a corner and a step [41] [42]. Solution of a limited number of source problems exists as well, such as to the dislocation source response in an elastic plate [43], and the response to various types of surface loads [29]. The response of a unidirectional composite laminate subjected to concentrated surface load is given in [44] [45]. These analytical solutions often involve numerical evaluation of difficult integrals of complex value functions. Alternatively, some scattering of plate discontinuity problems can be solved by the least-square method of matching the displacement and stresses at the boundary of the discontinuity. The solutions for step discontinuity and delamination-like discontinuity are presented in [46] [47].

For the goal of developing a library of waveforms associated to different types of defects, a more general source and wave scattering modeling tool is required, and numerical methods could provide solution for such problem. Conventional transient time-domain dynamic analysis is computationally intensive to model a large structure requiring small time step and mesh sizes when the wavelength is small, or the frequency is high. With the use of the boundary element

method (BEM) [48], the amount of computation is reduced to the size of the plate boundary. Cho et. al. uses the BEM method with the elastodynamics fundamental solutions in the frequency domain and specialize the method to solve Lamb reflection at a free-edge in an efficient manner. The elastodynamics equations, instead of being solved with BEM, a variant of the finite difference (FD) approach known as Local Interaction Simulation Approach (LISA) is proposed by Delsanto et. al. [49]. The method is applied to solve scattering problems, such as a crack under normal incidence [50], in conjunction with local FE and global LISA to study a composite plate with delamination and stiffeners [51]. These methods are formulated quite differently from the finite element method, and thus could be difficult to take advantage of the existing utilities developed for FE, such as user defined material laws, solvers, etc. The semi-analytical FE method used in [52] is a good illustration of the flexibility to simulate elastic wave response in plates with defects. The spectral element method (SEM) is a time-domain FE for wave propagation analysis [53]. The Spectral Finite Element Method (SFEM), on the other hand, is a frequency domain method that derives the dynamic stiffness matrix exactly form the governing differential equations [54]. A demonstration of the method on infinite and semi-infinite half space indicates the efficiency of the method [55]. An extension of the SFEM suitable to model short waveguide is the wavelet spectral finite element (WSFE) [56].

The numerical methods mentioned previously can model wave propagation in many types of waveguides efficiently. When there is an anomaly in the waveguide (such as a defect), these methods could provide a numerical efficient solution in the far field, but a local description is still required for the defect. This is the idea of the global-local method is a higher fidelity local description satisfying the continuity conditions with the far-field solution. Early use of global local FE analysis is on axisymmetric scattering problems using Bessel functions in the far field

description [57]. Koshiba et. al. developed a framework for plates, in which the fields in the FE region are represented by the sum of normal Lamb modes and solved a series of notch scattering problems [58]. Another approach provided by Al-Nassar et. al. describes the far field with a sum of Lamb modes and enforcing continuity between the local FE region (that contain the scattering source) and the far field [59]. The formulation given in [59] is well suited for plates, because the Lamb wave modal functions are separated from the equations in the FE region. Chang et. al. formulated the scattering problem differently than [59], in which the modal amplitudes are the unknowns to be solved for [60]. Under this formulation, the least-square nature of matching a smaller number of Lamb modes with a larger number of FE boundary degree of freedom is clearer. Chang also describes the important requirements on the far field Lamb mode selection. He notes that the proper selection of non-propagating and backward propagating modes is important for energy conservation consideration.

The global local method shown before is applied to wave scattering problems where only one incident mode is considered (usually the A_0 or S_0 mode). However, in some cases the complete wavefield generated by a surface source would create multiple incident modes. The complex wavefield near a source can be represented by FE discretization, and the outgoing wavefield in the far field can be described by the sum of propagating Lamb modes. Schaal et. al. applies the global local method to study the energy loss of a surface mount resonator [61] [62]. A time varying force is applied to the resonator in the FE region, and the frequency response of the resonator tip is calculated. The far field Lamb modes would transport energy away from the FE region. The NDE source problem is similar to the resonator problem. Instead of minimizing the energy lost to substrate in the form of Lamb wave propagation, the NDE source could be modelled and optimized for maximum energy transport by the desired mode(s).

The global local method has been applied for modeling scattering and source problems separately. However, for practical NDE situations, the two aspects are combined. Therefore, a global-local framework that can combine the two types of problem is developed to simulate an NDE inspection procedure.

3.2 The Global Local (GL) Problem Formulation

The GL model for the problem is shown in Figure 3-1. The plate is subjected to a specified surface traction, representing an ultrasound source, and contains a defect at some distance away. Figure 3-1 illustrates that the region in the proximity of the surface load and the region around the defect are modelled by FE discretization and the elastodynamics fields in the regions outside are described by global functions. Plane strain conditions in the x-z plane are assumed throughout this work.

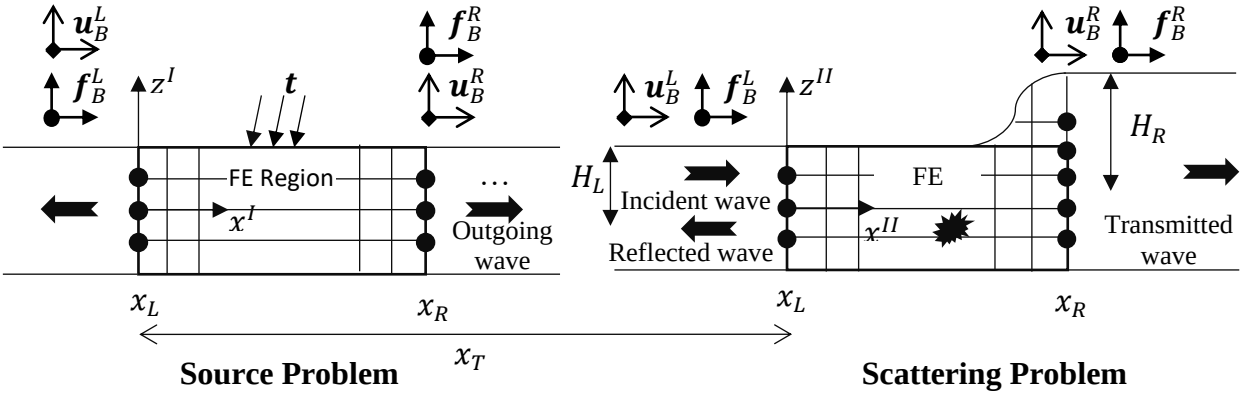

Figure 3-1 Illustration of the coupled source-scatterer problem in the global-local method. Subscript $_B$ refers to the FE boundary, and the superscript ^{L,R} refers to the left and right side of the boundary respectively

The coordinate system (x^I, z^I) is used in the source region and the scattering region is described by the coordinate system (x^{II}, z^{II}) separated by a distance x_T as shown in Figure 3-1. The equation of motion in the discretized zones is of the form:

$$\boldsymbol{M\ddot{u} + Ku = f}$$

(3-1)

where $\boldsymbol{K}$ and $\boldsymbol{M}$ are the stiffness and mass matrices that can be obtained from commercial FE software such as ABAQUS. Assuming time harmonic motion of the form $e^{-i\omega t}$, where ω is the circular frequency, equation (3-1) can be written in frequency domain in terms of the dynamic stiffness matrix $\boldsymbol{D}$ as

$$\begin{bmatrix} \boldsymbol{D_{LL}} & \boldsymbol{D_{LI}} & \boldsymbol{D_{LR}} \\ \boldsymbol{D_{IL}} & \boldsymbol{D_{II}} & \boldsymbol{D_{IR}} \\ \boldsymbol{D_{RL}} & \boldsymbol{D_{RI}} & \boldsymbol{D_{RR}} \end{bmatrix} \begin{Bmatrix} \boldsymbol{u_B^L} \\ \boldsymbol{u^I} \\ \boldsymbol{u_B^R} \end{Bmatrix} = \begin{Bmatrix} \boldsymbol{f_B^L} \\ \boldsymbol{f_I} \\ \boldsymbol{f_B^R} \end{Bmatrix}$$

(3-2)

where $\boldsymbol{D} = \boldsymbol{K} - \omega^2 \boldsymbol{M}$ and the superscripts *L, I, R* refer to the left, interior, and right degrees of freedom (DOFs) respectively.

3.2.1 The Source Problem

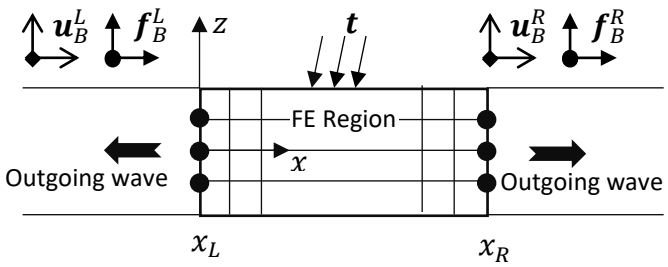

Figure 3-2 Illustration of the source problem. The FE region enclose the vicinity of the applied traction $\boldsymbol{t}$

For the source problem, the interior DOFs in equation (3-2) are further partitioned into either free (^{I0}) or subjected to applied traction (^{IF}).

$$\begin{bmatrix} \boldsymbol{D_{LL}} & \boldsymbol{D_{LIF}} & \boldsymbol{D_{LI0}} & \boldsymbol{D_{LR}} \\ \boldsymbol{D_{IFL}} & \boldsymbol{D_{IFIF}} & \boldsymbol{D_{IFI0}} & \boldsymbol{D_{IFR}} \\ \boldsymbol{D_{I0L}} & \boldsymbol{D_{I0IF}} & \boldsymbol{D_{I0I0}} & \boldsymbol{D_{I0R}} \\ \boldsymbol{D_{RL}} & \boldsymbol{D_{RIF}} & \boldsymbol{D_{RI0}} & \boldsymbol{D_{RR}} \end{bmatrix} \begin{Bmatrix} \boldsymbol{u_B^L} \\ \boldsymbol{u^{IF}} \\ \boldsymbol{u^{I0}} \\ \boldsymbol{u_B^R} \end{Bmatrix} = \begin{Bmatrix} \boldsymbol{f_B^L} \\ \boldsymbol{f_{app}} \\ \boldsymbol{0} \\ \boldsymbol{f_B^R} \end{Bmatrix}$$

(3-3)

where f_{app} is the Fourier time transform of the time dependent nodal force that created by the surface mounted transducers. The nodal displacements and the nodal forces on the FE boundaries

at $x = x_L$ and $x = x_R$ are expressed as a summation of the generated Lamb modes (e.g. A_0, S_0, …) with unknown amplitudes B_n in the forms,

$$\{\boldsymbol{u}_{\boldsymbol{B}}^{\boldsymbol{L}}\} = [\overleftarrow{\boldsymbol{Q}}]\{B_n^L e^{i\overleftarrow{k_n}x_L}\} \qquad \{\boldsymbol{f}_{\boldsymbol{B}}^{\boldsymbol{L}}\} = -[\overleftarrow{\boldsymbol{F}}]\{B_n^L e^{i\overleftarrow{k_n}x_L}\} \tag{3-4}$$

$$\{\boldsymbol{u}_{\boldsymbol{B}}^{\boldsymbol{R}}\} = [\overrightarrow{\boldsymbol{Q}}]\{B_n^R e^{i\overrightarrow{k_n}x_R}\} \qquad \{\boldsymbol{f}_{\boldsymbol{B}}^{\boldsymbol{R}}\} = [\overrightarrow{\boldsymbol{F}}]\{B_n^R e^{i\overrightarrow{k_n}x_R}\} \tag{3-5}$$

In equations (3-4) and (3-5) the modal displacements and nodal forces are denoted by $[\overrightarrow{\boldsymbol{Q}}]$ and $[\overrightarrow{\boldsymbol{F}}]$, respectively. For a homogeneous isotropic plate, the analytical expressions for the modal functions can be found in [63] [47]. For a multilayered plate, the WFE method [32] is used to determine the wavenumbers and the modal functions. Further details regarding the calculation of the modal functions are described in section 2.2.2. The upper arrows indicate the propagation direction with respect to the x direction. In equations (3-4) and (3-5), the columns of the matrices $[\overrightarrow{\boldsymbol{Q}}]$ and $[\overrightarrow{\boldsymbol{F}}]$ correspond to each Lamb mode, n, with wavenumber, k_n that should be chosen appropriately as described in [64] and in section 3.5.1. The rows are the x and z components evaluated at different z positions corresponding to the FE boundary nodes. Thus, $[\overrightarrow{\boldsymbol{Q}}]$ and $[\overrightarrow{\boldsymbol{F}}]$ have a number of rows equal to two times the number of boundary nodes on the left (or the right) side, and the number of columns equal to the number of symmetric and antisymmetric modes at a given frequency ω. Note that the minus sign on the nodal force in equation (3-5) is due to the negative direction of the normal on the FE boundary at x_L. Solving for B_n from the displacement expressions in equations (3-4) and (3-5), and substituting into the nodal force expressions in equation (3-4) and (3-5), respectively, the boundary nodal forces are expressed in terms of $[\overleftarrow{\boldsymbol{Q}}]$ and $[\overrightarrow{\boldsymbol{F}}]$. It should be noted that $[\overleftarrow{\boldsymbol{Q}}]$ is not a square matrix, and $[\overleftarrow{\boldsymbol{Q}}]^{-1}$ is its Moore-Penrose pseudoinverse. Finally, the augmented dynamic stiffness matrix, as shown on

the left-hand side of equation (3-6), is obtained by substituting the nodal force expressions into equation (3-3). Note that, this step ensures that the continuity conditions are satisfied across the boundary between the FE and global regions. The displacements in the FE region can then be obtained from equation (3-6). Furthermore, the outgoing wave amplitude coefficients, B_n^R are calculated and used as inputs for the coupled scattering problem.

$$\begin{bmatrix} \boldsymbol{D_{LL}} + \left[\overleftarrow{\boldsymbol{F}}\right]\left[\overleftarrow{\boldsymbol{Q}}\right]^{-1} & \boldsymbol{D_{LIF}} & \boldsymbol{D_{LI0}} & \boldsymbol{D_{LR}} \\ \boldsymbol{D_{IFL}} & \boldsymbol{D_{IFIF}} & \boldsymbol{D_{IFI0}} & \boldsymbol{D_{IFR}} \\ \boldsymbol{D_{I0L}} & \boldsymbol{D_{I0IF}} & \boldsymbol{D_{I0I0}} & \boldsymbol{D_{I0R}} \\ \boldsymbol{D_{RL}} & \boldsymbol{D_{RIF}} & \boldsymbol{D_{RI0}} & \boldsymbol{D_{RR}} - \left[\overrightarrow{\boldsymbol{F}}\right]\left[\overrightarrow{\boldsymbol{Q}}\right]^{-1} \end{bmatrix} \begin{Bmatrix} \boldsymbol{u_B^L} \\ \boldsymbol{u^{IF}} \\ \boldsymbol{u^{I0}} \\ \boldsymbol{u_B^R} \end{Bmatrix} = \begin{Bmatrix} \boldsymbol{0} \\ \boldsymbol{f_{app}} \\ \boldsymbol{0} \\ \boldsymbol{0} \end{Bmatrix}$$

(3-6)

The nodal force in the FE region and FE boundary can be solved from the nodal displacements:

$$f_L = \boldsymbol{D_{LL}} u_B^L + \boldsymbol{D_{LIF}} u^{IF} + \boldsymbol{D_{LI0}} u^{I0} + \boldsymbol{D_{LR}} u_B^R$$

$$f^{I0} = \boldsymbol{D_{IFL}} u_B^L + \boldsymbol{D_{I0IF}} u^{IF} + \boldsymbol{D_{I0I0}} u^{I0} + \boldsymbol{D_{I0R}} u_B^R$$

$$f_R = \boldsymbol{D_{RL}} u_B^L + \boldsymbol{D_{RIF}} u^{IF} + \boldsymbol{D_{RI0}} u^{I0} + \boldsymbol{D_{RR}} u_B^R$$

(3-7)

3.2.2 The Coupled Scattering Problem

In the 2D scattering problem of Lamb waves, an incident wave propagating from the left far field interacts with the scatterer in the finite element region as shown in Figure 3-1. The scatterer (e.g. a surface dent, a crack, etc.) would generate reflected waves to its left, and transmitted waves to its right.

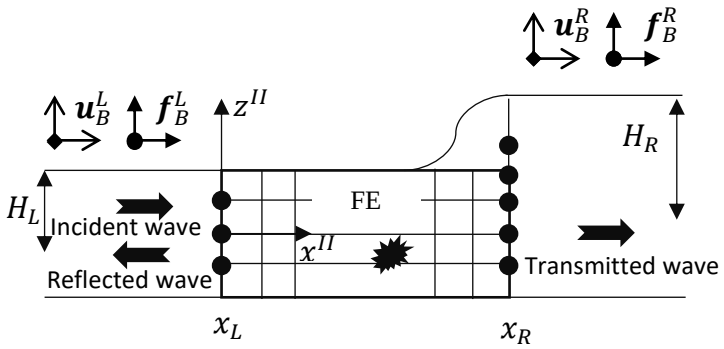

Figure 3-3 The sketch of a scattering problem, showing the scatterer in the FE region interacting with the incident wave from the left far field.

The equations for the coupled scattering problem are written in the coordinate system (x^{II}, z^{II}) and the superscript ^{II} will be omitted in the following sections. The displacements, $\boldsymbol{u}_B^L$ and nodal forces $\boldsymbol{f}_B^L$ at the left boundary nodes consist of the incident waves from the source problem and the reflected waves from the scattering region. The incident amplitude coefficient A_m is equal to the right going Lamb mode amplitude coefficients B_n^R of the source problem with a phase change due to the propagation distance x_T. The reflected displacement has the unknown amplitude coefficients B_n^L for each mode n:

$$\{\boldsymbol{u}_B^L\} = \left[\overrightarrow{\boldsymbol{QL}}\right]\{A_m e^{i\overrightarrow{kL_m}(x_L+x_T)}\} + \left[\overleftarrow{\boldsymbol{QL}}\right]\{B_n^L e^{i\overleftarrow{kL_n}x_L}\} \quad (3\text{-}8)$$

$$\{\boldsymbol{f}_B^L\} = -\left[\overrightarrow{\boldsymbol{FL}}\right]\{A_m e^{i\overrightarrow{kL_m}(x_L+x_T)}\} - \left[\overleftarrow{\boldsymbol{FL}}\right]\{B_n^L e^{i\overleftarrow{kL_n}x_L}\} \quad (3\text{-}9)$$

With the modal function matrix $[\overleftarrow{\boldsymbol{Q}}]$ and $[\overleftarrow{\boldsymbol{F}}]$, the left-hand field can be described by summing the contributions of incident mode *m* with known amplitude A_m and reflected mode *n* with unknown amplitude $B_n{}^L$. Note that the minus sign on the nodal force expressions is due to the negative face normal. The left-hand displacements and nodal forces at the boundary nodes consist of an incident field of Lamb mode *m* (e.g. A0) and a reflected field with unknown amplitude coefficients $B_n{}^L$ for each propagating Lamb mode *n* at a given frequency (e.g. S_0, A_1, …). The

modal displacement functions for isotropic material are listed in the appendix section 2.1. The nodal force functions for each mode are obtained by integrating the modal stresses with shape functions by following standard FE approach (as described in section 3.3). The modal displacement and nodal force functions are stored in the matrix $[\overleftarrow{\boldsymbol{Q}}]$ and $[\overleftarrow{\boldsymbol{F}}]$ respectively, where the columns corresponding to each Lamb mode, and the rows are the x and z degree of freedom for FE boundary nodes at different thickness positions, as shown in equation (3-10).

$$[\overleftarrow{\boldsymbol{Q}}] = \begin{bmatrix} q_x^{(m=1)} & q_x^{(2)} & \cdots & q_x^{(N)} \\ q_z^{(m=1)} & q_z^{(2)} & \cdots & q_z^{(N)} \\ \vdots & \vdots & \cdots & \vdots \\ q_x^{(m=1)} & q_x^{(2)} & \cdots & q_x^{(N)} \\ q_z^{(m=1)} & q_z^{(2)} & \cdots & q_z^{(N)} \end{bmatrix}_{2j*N} \quad [\overleftarrow{\boldsymbol{F}}] = \begin{bmatrix} f_x^{(m=1)} & f_x^{(2)} & \cdots & f_x^{(N)} \\ f_z^{(m=1)} & f_z^{(2)} & \cdots & f_z^{(N)} \\ \vdots & \vdots & \cdots & \vdots \\ f_x^{(m=1)} & f_x^{(2)} & \cdots & f_x^{(N)} \\ f_z^{(m=1)} & f_z^{(2)} & \cdots & f_z^{(N)} \end{bmatrix}_{2j*N}$$

(3-10)

where j is the number of nodes on the left or right boundary, and N is the number of propagating modes at a specific frequency. The modal displacement and stress functions are evaluated with the wave number for mode n, $\overleftarrow{k_n}$, for $[\overleftarrow{\boldsymbol{Q}}]$, and $[\overleftarrow{\boldsymbol{F}}]$, and $\overrightarrow{k_n}$ for $[\overrightarrow{\boldsymbol{Q}}]$, and $[\overrightarrow{\boldsymbol{F}}]$. The arrow above indicates the propagation direction with respect to the x direction. For continuity, the choice of wavenumber corresponding to the left or right propagation will be described later.

Similarly, the displacements and nodal forces at the right boundary nodes consist of the incident waves from the source with a phase shift of $(x_R + x_T)$, and the scattered waves with unknown amplitude coefficients B_n^R for each mode n:

$$\{\boldsymbol{u}_B^R\} = [\overrightarrow{\boldsymbol{QR}}]\{B_n^R e^{i\overrightarrow{kR_n}x_R}\}$$

(3-11)

$$\{\boldsymbol{f}_B^R\} = [\overrightarrow{\boldsymbol{FR}}]\{B_n^R e^{i\overrightarrow{kR_n}x_R}\}$$

(3-12)

Note that the wavenumbers kR_n are calculated with plate thickness equals to $2H_R$. Furthermore, for the right boundary nodes, the nodal coordinate z for evaluating the modal functions must be shifted to z' with the expression ($z' = z - shift$) where

$$shift = \frac{(z_{Rmax} + z_{Rmin})}{2} - \frac{(z_{Lmax} + z_{Lmin})}{2}$$

(3-13)

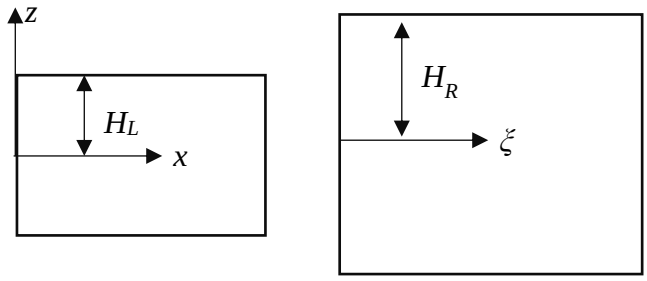

Figure 3-4 Illustration of the coordinate shift due to a change in the plate thickness

The next step is to use the displacement $\{\boldsymbol{u}_B^L\}$ in equation (3-8) to solve for the unknown amplitude coefficients $\{B_n^L e^{i\overleftarrow{k_n} x_L}\}$ and substitute them into the expressions for the nodal forces $\{\boldsymbol{f}_B^L\}$ from equation (3-9) to obtain the system of equations with the unknown displacements in the FE region. Using equation (3-8):

$$\left\{B_n^L e^{i\overleftarrow{kL_n} x_L}\right\} = \left[\overleftarrow{\boldsymbol{QL}}\right]^{-1}\{\boldsymbol{u}_B^L\} - \left[\overleftarrow{\boldsymbol{QL}}\right]^{-1}\left[\overrightarrow{\boldsymbol{QL}}\right]\{A_{mm} e^{i\overrightarrow{kL_{mm}}(x_L + x_T)}\}$$

(3-14)

Substituting into the left-hand nodal force given in equation (3-9),

$$\{\boldsymbol{f}_B^L\} = -\left[\overleftarrow{\boldsymbol{FL}}\right]\left[\overleftarrow{\boldsymbol{QL}}\right]^{-1}\{\boldsymbol{u}_B^L\} - (\left[\overrightarrow{\boldsymbol{FL}}\right] - \left[\overleftarrow{\boldsymbol{FL}}\right]\left[\overleftarrow{\boldsymbol{QL}}\right]^{-1}\left[\overrightarrow{\boldsymbol{QL}}\right])\{A_m e^{i\overrightarrow{kL_m}(x_L + x_T)}\}$$

(3-15)

For the right boundary, the nodal forces can be expressed in the form of equation (3-12) by solving for the amplitude coefficient from equation (3-11) as

$$\{\boldsymbol{f}_B^R\} = \left[\overrightarrow{\boldsymbol{FR}}\right]\left[\overrightarrow{\boldsymbol{QR}}\right]^{-1}\{\boldsymbol{u}_B^R\}$$

(3-16)

Substituting the nodal force into equations (3-2), the final system of equations for the displacements in the FE region is obtained:

$$\begin{bmatrix} \boldsymbol{D_{LL}} + [\overleftarrow{\boldsymbol{FL}}][\overleftarrow{\boldsymbol{QL}}]^{-1} & \boldsymbol{D_{LI}} & \boldsymbol{D_{LR}} \\ \boldsymbol{D_{IL}} & \boldsymbol{D_{II}} & \boldsymbol{D_{IR}} \\ \boldsymbol{D_{RL}} & \boldsymbol{D_{RI}} & \boldsymbol{D_{RR}} - [\overrightarrow{\boldsymbol{FR}}][\overrightarrow{\boldsymbol{QR}}]^{-1} \end{bmatrix} \begin{Bmatrix} u_B^L \\ u^I \\ u_B^R \end{Bmatrix} = \begin{Bmatrix} -\left([\overrightarrow{\boldsymbol{FL}}] - [\overleftarrow{\boldsymbol{FL}}][\overleftarrow{\boldsymbol{QL}}]^{-1}[\overrightarrow{\boldsymbol{QL}}]\right)\{A_m e^{i\overrightarrow{kL_m}(x_L+x_T)}\} \\ 0 \\ 0 \end{Bmatrix}$$

(3-17)

Representation of the Wave Field

One of the advantages of using GLM is that the modal contribution in the global regions from different Lamb modes can be separated. In this section, the expressions for the modal displacements and the power flow are defined so that they can be used for the analysis presented in the later sections of the paper.

Reflected Field

The reflected displacement is the absence of the incident field in the total field given in equation (3-8)(3-9)(3-11)(3-12), thus the reflected fiends are,

$$\{u_B^{ref}\} = [\overleftarrow{\boldsymbol{QL}}]\left\{B_n^L e^{i\overleftarrow{kL_n}x}\right\} = \sum_{n=0}^{N} B_n^L \{\overleftarrow{\boldsymbol{qL}_n}\} e^{i\overleftarrow{kL_n}x}$$

(3-18)

where $x_R^I < x < x_L^{II}$

The modal displacement is then

$$\{u_B^{ref_n}\} = [\overleftarrow{\boldsymbol{Q}}]diag\left\{B_n^L e^{i\overleftarrow{k_n}x}\right\} \qquad x < x_L$$

(3-19)

The modal amplitude coefficient B_n^L is

$$\{B_n^L\} = \left\{[\overleftarrow{\boldsymbol{QL}}]^{-1}\{\boldsymbol{u}_B^L\} - [\overleftarrow{\boldsymbol{QL}}]^{-1}[\overrightarrow{\boldsymbol{QL}}]\left\{A_m e^{i\overrightarrow{kL_m}(x_L+x_T)}\right\}\right\} * \left\{e^{-i\overleftarrow{kL_n}x_L}\right\}$$

(3-20)

Note that the modal amplitude coefficient should only be calculated for the propagating modes with real wave numbers.

Transmitted Field

The transmitted displacement field to the right of the FE region is

$$\{u_B^{tr}\} = \left[\overrightarrow{\boldsymbol{QR}}\right]\left\{B_n^R e^{i\overrightarrow{kR_n}x}\right\} = \sum_{n=0}^{N} B_n^R \{\overrightarrow{\boldsymbol{qR}_n}\} e^{i\overrightarrow{kR_n}x} \qquad \text{and } x > x_R^{II}$$

(3-21)

The modal transmitted field is then

$$\{u_B^{tr_n}\} = B_n^R e^{i\overrightarrow{kR_n}x}\{\overrightarrow{qR_n}\} \qquad \text{and } x > x_R^{II}$$

(3-22)

The modal scattering coefficients for the propagating modes are

$$\{B_n^R\} = \left\{\left[\overrightarrow{\boldsymbol{QR}}\right]^{-1}\{u_B^R\}\right\} * \{e^{-i\overrightarrow{kR_n}x_R}\}$$

(3-23)

Power Flow Associated to the Scattering Problem

The power flow is a useful quantity as a measure of the energy carried by the transmitted and reflected waves propagating in the plate. The general definition of power flow *P* through a cross-section *A* of a waveguide with unit normal $\boldsymbol{n} = \boldsymbol{e_1}$

$$P = -\int_A \sigma_{ij} n_j \dot{u}_\iota \, dA = -\int_A \sigma_{i1} \, \dot{u}_\iota dA$$

(3-24)

The time-average power flow over one period $T = \frac{2\pi}{\omega}$ expressed in the frequency domain is then given by

$$\langle P \rangle = \frac{1}{T}\int_0^T P \, dt = -\frac{\omega}{2}\int_A imag(\hat{\sigma}_{11}^* \hat{u}_1 + \hat{\sigma}_{21}^* \hat{u}_1 + \hat{\sigma}_{31}^* \hat{u}_3)\, e^{-2imag(k)x_1} dA$$

(3-25)

where * denotes the complex conjugate.

For a discretized cross-section, the time averaged power flow for a propagating wave is

$$P = -\frac{1}{2} Re\{\boldsymbol{f}^H \dot{\boldsymbol{q}}\} = -\frac{1}{2} Re\{-i\boldsymbol{\omega} \boldsymbol{f}^H \boldsymbol{q}\} \tag{3-26}$$

where ^{H} is the complex conjugate transpose, and $\boldsymbol{f}, \boldsymbol{q}$ are the nodal force and nodal displacement vector on the given cross section. The expressions for the transmitted modal power flow E_{tr}^n, reflected power flow E_{ref}^n for mode n, and the incident power flow E_{inc}^m are

$$E_{tr}^n = -\frac{1}{2} |B_n^R|^2 Re\left\{-i\omega \overrightarrow{\boldsymbol{f}\boldsymbol{R}_n}^H \overrightarrow{\boldsymbol{q}\boldsymbol{R}_n}\right\} \tag{3-27}$$

$$E_{ref}^n = -\frac{1}{2} |B_n^L|^2 Re\left\{-i\omega \overleftarrow{\boldsymbol{f}\boldsymbol{L}_n}^H \overleftarrow{\boldsymbol{q}\boldsymbol{L}_n}\right\} \tag{3-28}$$

$$E_{inc} = \sum_{mm=0}^{NL} -\frac{1}{2} \left| A_{mm} e^{i\overrightarrow{k_{mm}}(x_R + x_T)} \right|^2 Re\left\{-i\omega \overrightarrow{\boldsymbol{f}\boldsymbol{L}_{mm}}^H \overrightarrow{\boldsymbol{q}\boldsymbol{L}_{mm}}\right\} \tag{3-29}$$

where the $|\cdots|^2$ is the square of the modulus of a complex quantity.

If the FE region is not dissipative, the energy conservation principle dictates that the sum of the magnitude of the incident time averaged power flow should be equal to the sum of the transmitted and reflected power flows. Thus, equation (3-30) can be used to evaluate the numerical accuracy of the solution

$$Error = 1 - \frac{\sum_{all\ prop.\ modes\ NL} E_{tr}^n - \sum_{all\ prop.\ modes\ NR} E_{ref}^n}{E_{inc}} \tag{3-30}$$

Note that the power flow for the reflected waves calculated using the nodal force and nodal displacement vectors is negative in numerical value due to the definition of the normal to the cross section. Therefore, a negative sign is used in the reflected power flow in equation (3-30).

3.2.3 The Edge Excitation Problem

The formulation shown in the previous section can be modified with appropriate boundary conditions to model other types of Lamb wave propagation problems. In this section, we assume that a load is applied on the edge of the plate to model a transducer is being mounted on the edge of the plate.

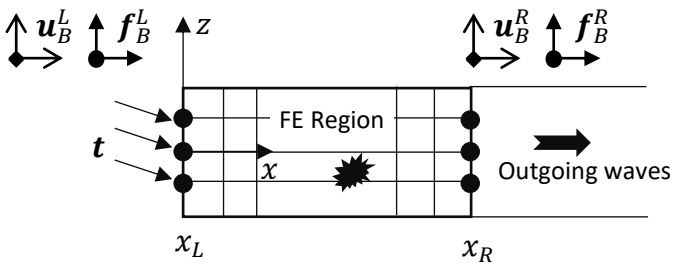

Figure 3-5 Illustration of the edge loading problem in which the left face of a plate is subject to an applied load

The nodes associated to the left edge in equation (3-2) is partitioned into F for those with applied traction f_{app}, and $L0$ for those that are traction free, I for the interior nodes and R for the right boundary nodes.

$$\begin{bmatrix} D_{FF} & D_{FL0} & D_{FI} & D_{FR} \\ D_{L0F} & D_{L0L0} & D_{L0I} & D_{L0R} \\ D_{IF} & D_{IL0} & D_{II} & D_{IR} \\ D_{RF} & D_{RL0} & D_{RI} & D_{RR} \end{bmatrix} \begin{Bmatrix} u_B^{LF} \\ u^{L0} \\ u^I \\ u_B^R \end{Bmatrix} = \begin{Bmatrix} f_{app} \\ 0 \\ 0 \\ f_B^R \end{Bmatrix} \quad (3\text{-}31)$$

In this case, the left-hand field does not exist, and only the right-hand field is represented by the Lamb wave modal expansion.

$$\{u_B^R\} = [\overrightarrow{Q}]\{B_n^R e^{i\overrightarrow{k_n} x_R}\}$$

(3-32)

$$\{\boldsymbol{f}_B^R\} = [\vec{\boldsymbol{F}}]\{B_n^R e^{i\vec{k}_n x_R}\}$$

(3-33)

By the substitution of $\{B_n^R e^{i\vec{k}_n x_R}\}$ from equation (3-33) into (3-32) , the following system of linear equations is obtained

$$\begin{bmatrix} \boldsymbol{D_{FF}} & \boldsymbol{D_{FL0}} & \boldsymbol{D_{FI}} & \boldsymbol{D_{FR}} \\ \boldsymbol{D_{L0F}} & \boldsymbol{D_{L0L0}} & \boldsymbol{D_{L0I}} & \boldsymbol{D_{L0R}} \\ \boldsymbol{D_{IF}} & \boldsymbol{D_{IL0}} & \boldsymbol{D_{II}} & \boldsymbol{D_{IR}} \\ \boldsymbol{D_{RF}} & \boldsymbol{D_{RL0}} & \boldsymbol{D_{RI}} & \boldsymbol{D_{RR}} - [\vec{\boldsymbol{F}}][\vec{\boldsymbol{Q}}]^{-1} \end{bmatrix} \begin{Bmatrix} \boldsymbol{u_B^{LF}} \\ \boldsymbol{u^{L0}} \\ \boldsymbol{u^I} \\ \boldsymbol{u_B^R} \end{Bmatrix} = \begin{Bmatrix} \boldsymbol{f_{app}} \\ \boldsymbol{0} \\ \boldsymbol{0} \\ \boldsymbol{0} \end{Bmatrix}$$

(3-34)

Benchmark Problem #1

The following problem demonstrates how the edge excitation model can be used to study the Lamb waves from a surface mounted transducer on an edge of a plate. The model considered here is a 20 mm thick steel plate ($E = 200$ GPa, $\nu = 0.33$, $\rho = 7960$ kg/m^3) with a left edge normal load of 1 MPa peak magnitude subjected to a Gaussian distribution to simulate a source transducer on the left edge as depicted in Figure 3-6. Within the plate, two models with a crack are simulated at the center of a 200 mm wide FE region with a 5 mm vertical crack or a 5 mm horizontal crack.

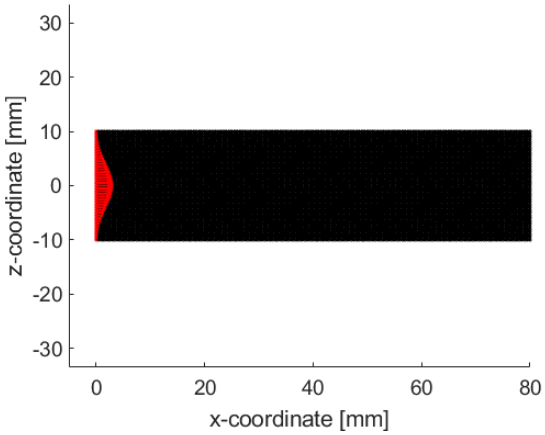

(a) A normal load with a Gaussian distribution applied on the left edge to represents a transducer

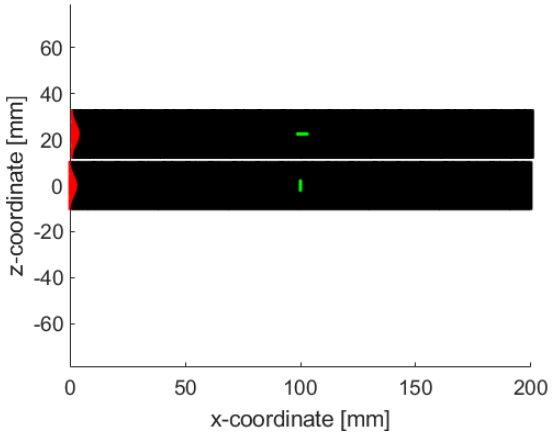

(b) the 5mm long horizontal and vertical crack cases

Figure 3-6 (a) The edge excitation problem representing the inspection of a leading edge

The displacement waveform at the origin for the two cases are compared with the defect free cases to mimic a pulse echo inspection. A 5-cycle tone burst of 400 kHz sine with Hann window is used as the excitation. Such excitation can be considered high frequency since the frequency thickness ratio would be 8 MHz · mm and thus a substantial higher mode contribution is expected. The waveforms for the simulated pulse-echo inspection are shown in Figure 3-7.

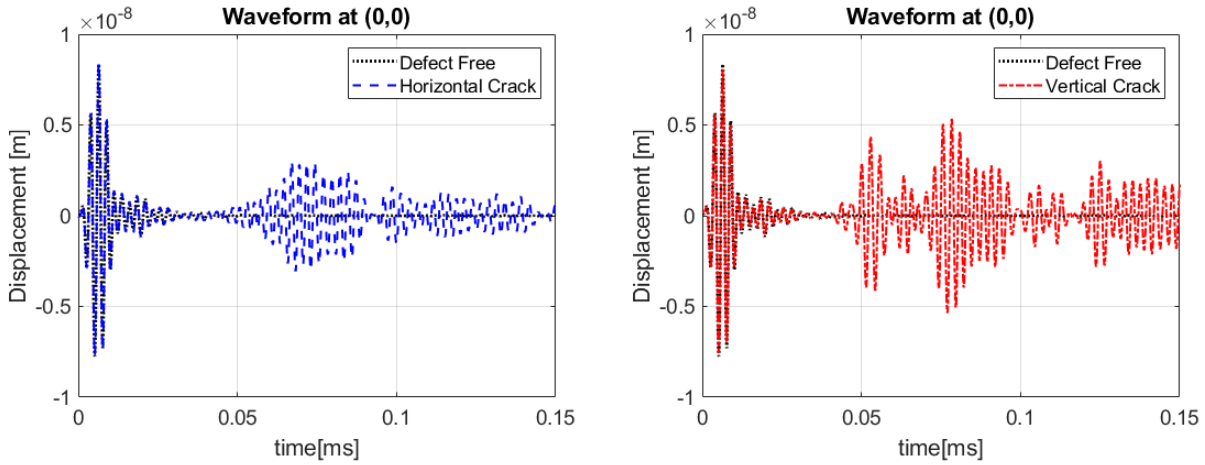

(a) The horizontal crack case (blue dash line) (b) The vertical crack case (red dash-dot line)

Figure 3-7 The horizontal displacement at the center of the transducer for the defect free (black dot line) case vs. the two defect cases

In the defect free case (black dotted line), the edge excitation only produces the incident packet and a small amount of surface vibrations but for the remainder of the period is free of signals. For the two crack cases, the echo is prominent whereas the vertical crack (the signal shown in red dash-dot line) produces distinct packets with the first reflection arriving earlier than the first reflection for the horizontal crack case. Upon inspecting the displacement field at various instances such as the ones shown in Figure 3-8, it is observed that the reflected waves are generated at the leading and the trailing edge of the horizontal crack continuously as the incident waves arrives. For the vertical crack case, most of the incident waves are reflected from the free edge thus producing more concise packets in the signal.

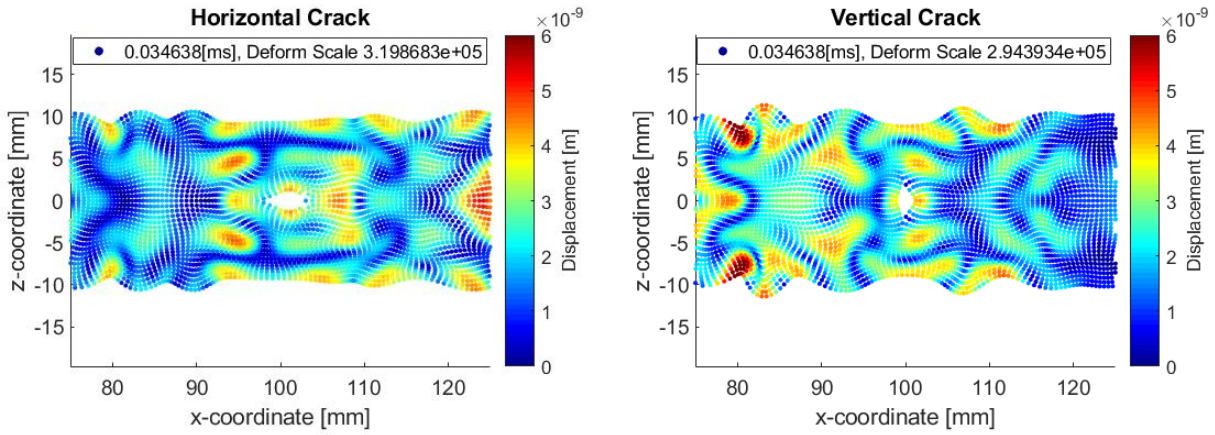

(a) horizontal crack case (b) vertical crack case

Figure 3-8 Magnitude of the displacement field around the crack at 0.035 ms

3.2.4 The Edge Reflection Problem

We next consider the free edge reflection problem as shown in Figure 3-9.

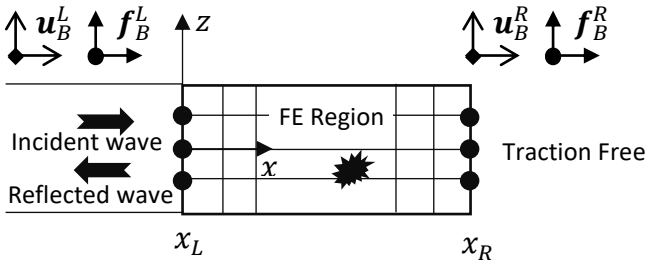

Figure 3-9 Reflection of Lamb waves at a free edge. Traction free boundary condition is applied at the free edge.

Since the right boundary is traction free to represent the plate edge, equation (3-2) becomes

$$\begin{bmatrix} \boldsymbol{D_{LL}} & \boldsymbol{D_{LI}} & \boldsymbol{D_{LR}} \\ \boldsymbol{D_{IL}} & \boldsymbol{D_{II}} & \boldsymbol{D_{IR}} \\ \boldsymbol{D_{RL}} & \boldsymbol{D_{RI}} & \boldsymbol{D_{RR}} \end{bmatrix} \begin{Bmatrix} \boldsymbol{u_B^L} \\ \boldsymbol{u^I} \\ \boldsymbol{u_B^R} \end{Bmatrix} = \begin{Bmatrix} \boldsymbol{f_B^L} \\ \boldsymbol{0} \\ \boldsymbol{0} \end{Bmatrix} \tag{3-35}$$

The right-hand displacements are unknown to be solved for, and the left-hand displacement and nodal force remains unchanged from the standard scattering problem. The final system of equations for the displacement in the FE region is then

$$\begin{bmatrix} \boldsymbol{D_{LL}} + [\overleftarrow{\boldsymbol{F}}][\overleftarrow{\boldsymbol{Q}}]^{-1} & \boldsymbol{D_{LI}} & \boldsymbol{D_{LR}} \\ \boldsymbol{D_{IL}} & \boldsymbol{D_{II}} & \boldsymbol{D_{IR}} \\ \boldsymbol{D_{RL}} & \boldsymbol{D_{RI}} & \boldsymbol{D_{RR}} \end{bmatrix} \begin{Bmatrix} u_B^L \\ u^I \\ u_B^R \end{Bmatrix} = \begin{Bmatrix} -(\{\vec{\boldsymbol{f}}_m\} - [\overleftarrow{\boldsymbol{F}}][\overleftarrow{\boldsymbol{Q}}]^{-1}\{\vec{\boldsymbol{q}}_m\})A_m e^{i\overrightarrow{k_m}x_L} \\ 0 \\ 0 \end{Bmatrix} \quad (3\text{-}36)$$

Benchmark Problem #2

As another benchmark problem, the reflection of an incident Lamb wave from a free end is compared with available results [44]. This problem is the edge reflection of an incident A_0 mode in a semi-infinite aluminum plate ($2H = 1.78$ mm, $E = 69$ GPa, $\nu = 0.33$, $\rho = 2700$ kg/m^3) as shown in Figure 3-10. The incident A_0 mode is assumed to have a unit power flow across the studied frequency range from 50 kHz to 2 MHz. The FE region of the GL model is 40 mm long and the elements are 4-node plane strain element of size 50 μm by 50 μm.

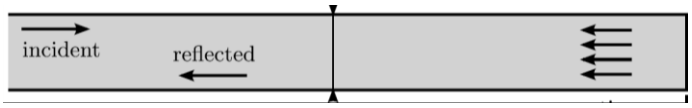

Figure 3-10 Illustration of the edge reflection problem

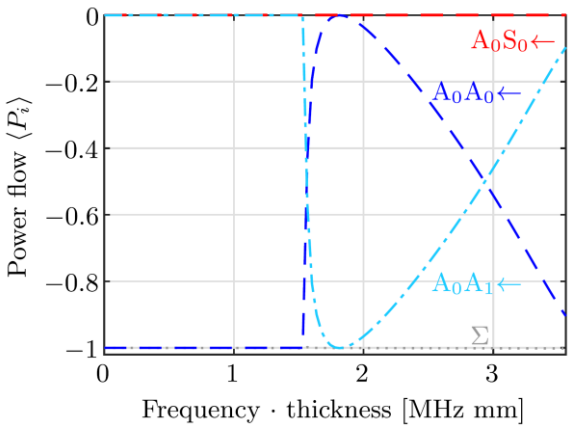

(a) The result given in [44]

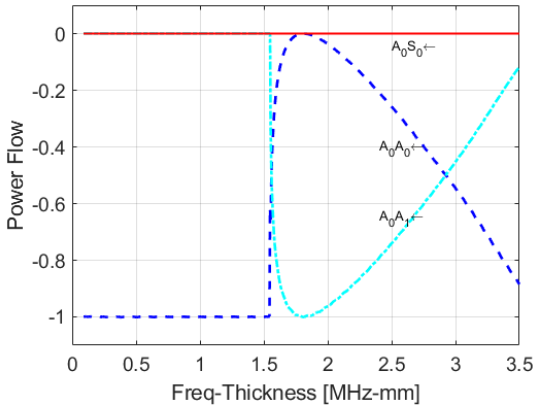

(b) The GL result showing that the scattering of the incident A0 mode into higher A modes is only possible at frequency thickness greater than 1.6 MHz-mm

Figure 3-11 Modal reflected power flow the scattering of an incident A_0 mode

Figure 3-11a shows the results calculated from satisfying the traction free boundary conditions in the least-square sense. Figure 3-11b shows the results using GLM. Both results agree with the

well-known behavior of the incident A_0 mode: there are no reflected S modes, and mode conversion to higher A modes are only possible above the first cut-off frequency.

3.3 Remark on Computing Nodal Force Vectors

For the source problems shown in section 3.2.1 and 3.2.3, the applied traction is required to be converted into the nodal applied force vector $\boldsymbol{f_{app}}$ per equations (3-6) and (3-31). This is done by integrating the traction components with the shape functions as in the standard FE approach. A brief review of computing the nodal force vector from traction using the isoparametric formulation is presented here. The nodal force vector is defined as

$$\boldsymbol{f} = \int_{\Gamma_t} \boldsymbol{N}\boldsymbol{t} ds = \int_{\Gamma_t} \boldsymbol{N}^{\boldsymbol{T}} \boldsymbol{N} \boldsymbol{t}_{\boldsymbol{node}} ds \tag{3-37}$$

where Γ_t is the boundary at which traction is applied, and $\boldsymbol{N}$ is the bi-linear shape functions. The nodal force at nodes, *i, j, k, l*, for the element shown in Figure 3-12 is obtained by integrating the products of the shape functions with the tractions evaluated at the boundary

$$\begin{Bmatrix} f_x^i \\ f_z^i \\ f_x^j \\ f_z^j \\ f_x^k \\ f_z^k \\ f_x^l \\ f_z^l \end{Bmatrix} = \int_{\Gamma_t} \begin{bmatrix} N_1 & 0 \\ 0 & N_1 \\ N_2 & 0 \\ 0 & N_2 \\ N_3 & 0 \\ 0 & N_3 \\ N_4 & 0 \\ 0 & N_4 \end{bmatrix} \begin{Bmatrix} t_x(x,z) \\ t_z(x,z) \end{Bmatrix} ds \tag{3-38}$$

Using isoparametric formulation, the boundary integral is expressed in natural coordinates (ξ, η).

$$\boldsymbol{f} = \int_{-1}^{1} \widehat{\boldsymbol{N}}^{\boldsymbol{T}} \widehat{\boldsymbol{N}} \boldsymbol{t}_{node} J_s d\xi \text{ or } d\eta$$

(3-39)

where $\widehat{\boldsymbol{N}}$ is the bilinear 2D shape functions in natural coordinates, that can be found in standard FE literature and in Appendix 3.1, evaluated at the boundary subjected to traction. J_s is the line Jacobian

$$J_s = \sqrt{\left(\frac{\partial x}{\partial \xi}\right)^2 + \left(\frac{\partial y}{\partial \xi}\right)^2} \; or \sqrt{\left(\frac{\partial x}{\partial \eta}\right)^2 + \left(\frac{\partial y}{\partial \eta}\right)^2}$$

(3-40)

As an example, if the edge between the nodes *k* and *l* is subject to traction, the shape functions are evaluated to η=1 and *J* is integrated for variable ξ from -1 to 1. With the use of the Jacobian matrix define below, the integration for (3-37) is done using Gaussian quadrature.

$$\boldsymbol{J} = \begin{bmatrix} \frac{\partial x}{\partial \xi} & \frac{\partial x}{\partial \eta} \\ \frac{\partial y}{\partial \xi} & \frac{\partial y}{\partial \eta} \end{bmatrix} = \left[\begin{bmatrix} \frac{\partial N_{1,2,3,4}}{\partial \xi} \\ \frac{\partial N_{1,2,3,4}}{\partial \eta} \end{bmatrix} \begin{bmatrix} x_i & z_i \\ x_j & z_j \\ x_k & z_k \\ x_l & z_l \end{bmatrix} \right]^T$$

(3-41)

For completeness, the procedure for Gaussian quadrature is described here. Consider a 2D integration over ξ-η domain as shown in Figure 3-12 which is the case in a 2D FE problem.

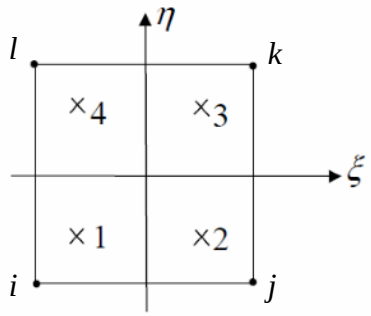

Figure 3-12 Integration domain with ξ-η limit from -1 to 1

The integral, evaluated by Gaussian quadrature is then

$$\iint_{-1}^{1} g(\xi,\eta)d\xi d\eta = \sum_{l_2=1}^{NINT2}\sum_{l_1=1}^{NINT1} g(\xi_{l_1},\eta_{l_2})\, w_{l_1} w_{l_2}$$

(3-42)

where l_1 l_2 are the integration points for ξ and η, respectively, and w_{l_1}, w_{l_2} are the integration weights. In other words, evaluate the integrand at $\xi = l_1$, and $\eta = l_2$ and multiply by w_{l_1}, w_{l_2} at each point and sum. The integration points for 2nd order rule are $l_{1,2} = -\frac{1}{\sqrt{3}}, \frac{1}{\sqrt{3}}$ with corresponding weight $w_{l_1}, w_{l_2} = 1$ for each point.

3.3.1 Nodal Force Vectors Evaluated from Modal Stress Expressions

GLM uses FE discretization to represent a source or a defect and the remainder of the plate by analytical global functions. Continuity of displacements and stresses across the global and the local regions are enforced. In the case of an isotropic plate, the symmetric and antisymmetric Lamb wave modes are the global functions and their analytical expressions can be found in the literature such as [63]. However, the procedure for converting the nodal stress expressions to the nodal force vector as required in equation (3-10) are often not explained. Therefore, a detailed implementation is given here. The modal stress functions in the frequency domain can be expressed in the form $\sigma(x,z,t) = A\hat{\sigma}(z)e^{i(kx-\omega t)}$ where A is an unknown constant. For the antisymmetric modes, the modal stress functions are

$$\hat{\sigma}_{xx} = \mu\left((2\eta_1^2 + k_2^2)\sinh(\eta_1 z) - \frac{(2k^2 - k_2^2)\sinh(\eta_1 H)}{\sinh(\eta_2 H)}\sinh(\eta_2 z)\right)$$

(3-43)

$$\hat{\sigma}_{zz} = -\mu(2k^2 - k_2^2)\left(\sinh(\eta_1 z) - \frac{\sinh(\eta_1 H)}{\sinh(\eta_2 H)}\sinh(\eta_2 z)\right)$$

(3-44)

$$\hat{\sigma}_{xz} = -i\mu 2k\eta_1\left(\cosh(\eta_1 z) - \frac{(2k^2 - k_2^2)^2\sinh(\eta_1 H)}{4\mathrm{k}^2\eta_1\eta_2\sinh(\eta_2 H)}\cosh(\eta_2 z)\right)$$

(3-45)

For symmetric mode, the modal stress functions are

$$\hat{\sigma}_{xx} = -\mu\left((2\eta_1^2 + k_2^2)\cosh(\eta_1 z) - \frac{(2k^2 - k_2^2)\cosh(\eta_1 H)}{\cosh(\eta_2 H)}\cosh(\eta_2 z)\right)$$

(3-46)

$$\hat{\sigma}_{zz} = \mu(2k^2 - k_2^2)\left(\cosh(\eta_1 z) - \frac{\cosh(\eta_1 H)}{\cosh(\eta_2 H)}\cosh(\eta_2 z)\right)$$

(3-47)

$$\hat{\sigma}_{xz} = i\mu 2k\eta_1\left(\sinh(\eta_1 z) - \frac{(2k^2 - k_2^2)^2\cosh(\eta_1 H)}{4\mathrm{k}^2\eta_1\eta_2\cosh(\eta_2 H)}\sinh(\eta_2 z)\right)$$

(3-48)

The nodal force induced by the propagating waves is exerted to the FE region boundary as shown in Figure 3-13 whre ***t*** is the traction resultant from the two stress components. Note that the element face normal is aligned with the *x* axis, thus, the relevant stress components are only $\hat{\sigma}_{xx}$ and $\hat{\sigma}_{xz}$. The applied modal stress functions ($\hat{\sigma}_{xx}$, $\hat{\sigma}_{xz}$) act on the left edge $\Gamma_{4\text{-}1}$, which are evaluated to the nodal forces t_{x1}, t_{z1} for node 1, at $z=z_i$ (bottom left) and $t_{x4}, t_{z4}$for node 4, at $z=z_l$ (at the top left), as shown in Figure 3-13. Since the stress distribution is known throughout the thickness, the nodal force integral in equation (3-38) can be calculated exactly without the use of isoparametric formulation.

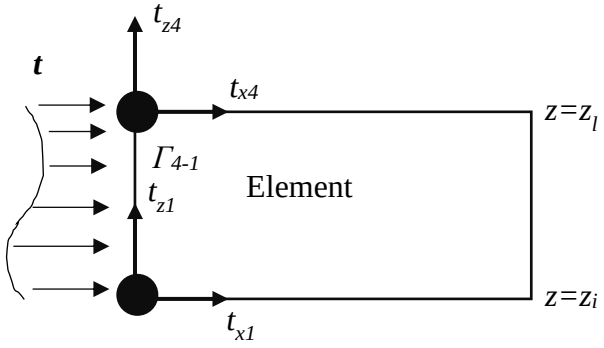

Figure 3-13 An element for nodal force integration from modal stress functions

The nodal force vector is

$$\begin{Bmatrix} t_{x1} \\ t_{z1} \\ t_{x4} \\ t_{z4} \end{Bmatrix} = \int_{\Gamma_{4-1}} \begin{bmatrix} N_1 & 0 \\ 0 & N_1 \\ N_4 & 0 \\ 0 & N_4 \end{bmatrix} \begin{Bmatrix} \hat{\sigma}_{xx} \\ \hat{\sigma}_{xz} \end{Bmatrix} dz$$

(3-49)

With the definition of edge length, $l_e = z_l - z_i$, the shape functions are

$$N_1 = \frac{z_l - z}{l_e} \qquad N_4 = \frac{z - z_i}{l_e}$$

(3-50)

The integrals can then be evaluated term by term with respect to the thickness coordinate, *z*. To simplify the expressions, some symbolic substitutions are made to highlight the functions' *z* dependence.

Antisymmetric Mode

Introducing the following symbols,

$$Å = 2\eta_1^2 + k_2^2 \qquad Æ = \frac{(2k^2 - k_2^2)sinh(\eta_2 H)}{sinh(\eta_2 H)} \qquad Ö = \frac{(2k^2 - k_2^2)^2 sinh(\eta_1 H)}{4k^2 \eta_1 \eta_2 sinh(\eta_1 H)}$$

(3-51)

The modal stress functions for anti-symmetric mode can be expressed as

$$\hat{\sigma}_{xx} = \mu[Å\sinh(\eta_1 z) - Æ\sinh(\eta_2 z)]$$

$$\hat{\sigma}_{xz} = -i\mu 2k\eta_1[\cosh(\eta_1 z) - Ö\cosh(\eta_2 z)$$

(3-52)

Multiplying the shape functions (3-50) with the modal stress functions in (3-52)

$$\begin{Bmatrix} t_{x1} \\ t_{z1} \\ t_{x4} \\ t_{z4} \end{Bmatrix} = \int_{z_i}^{z_l} \begin{bmatrix} \frac{z_l - z}{l_e} & 0 \\ 0 & \frac{z_l - z}{l_e} \\ \frac{z - z_i}{l_e} & 0 \\ 0 & \frac{z - z_i}{l_e} \end{bmatrix} \begin{Bmatrix} \mu[\text{Åsinh}(\eta_1 z) - \text{Æsinh}(\eta_2 z)] \\ i\mu 2k\eta_1[\cosh(\eta_1 z) - \text{Öcosh}(\eta_2 z)] \end{Bmatrix} dz$$

(3-53)

Note that the integrals would have the following four terms

$$\int_{z_i}^{z_l} sinh\,(\eta_j z)\,dz = \frac{\cosh(\eta_j z)}{\eta_j}\Big]_{z_i}^{z_l} \qquad \int_{z_i}^{z_l} cosh\,(\eta_j z)\,dz = \frac{sinh(\eta_j z)}{\eta_j}\Big]_{z_i}^{z_l}$$

$$\int_{z_i}^{z_l} zsinh\,(\eta_j z)\,dz = \frac{\eta_j z cosh(\eta_j z) - sinh(\eta_j z)}{\eta_j^2}\Big]_{z_i}^{z_l} \int_{z_i}^{z_l} zcosh(\eta_j z)\,dz = \frac{\eta_j z sinh(\eta_j z) - cosh(\eta_j z)}{\eta_j^2}\Big]_{z_i}^{z_l}$$

(3-54)

Carrying out the integrations the following nodal forces are obtained. Recalling that l_e is the element length in the thickness direction

$$t_{x_1} = \frac{\mu}{l_e}\left[z_l \text{Å}\left(\frac{cosh(\eta_1 z)}{\eta_1}\right)\Big]_{z_i}^{z_l} - \text{Å}\left(\frac{\eta_1 z cosh(\eta_1 z) - sinh(\eta_1 z)}{\eta_1^2}\right)\Big]_{z_i}^{z_l} - z_l\left(\frac{cosh(\eta_2 z)}{\eta_2}\right)\Big]_{z_i}^{z_l} + \text{Æ}\left(\frac{\eta_2 z cosh(\eta_2 z) - sinh(\eta_2 z)}{\eta_2^2}\right)\Big]_{z_i}^{z_l}\right]$$

$$t_{z_1} = \frac{-i\mu 2k\eta_1}{l_e}\left[z_l\left(\frac{sinh(\eta_1 z)}{\eta_1}\right)\Big]_{z_i}^{z_l} - \frac{\eta_1 z sinh(\eta_1 z) - cosh(\eta_1 z)}{\eta_1^2}\Big]_{z_i}^{z_l} - z_l\,\text{Ö}\left(\frac{sinh(\eta_2 z)}{\eta_2}\right)\Big]_{z_i}^{z_l} + \text{Ö}\left(\frac{\eta_2 z sinh(\eta_2 z) - cosh(\eta_2 z)}{\eta_2^2}\right)\Big]_{z_i}^{z_l}\right]$$

$$t_{x_4} = \frac{\mu}{l_e}\left[\text{Å}\left(\frac{\eta_1 z cosh(\eta_1 z) - \sinh(\eta_1 z)}{\eta_1^2}\right)\right]_{z_i}^{z_l} - z_i\text{Å}\left(\frac{cosh(\eta_1 z)}{\eta_1}\right)\Bigg]_{z_i}^{z_l}$$

$$- \text{Æ}\left(\frac{\eta_2 z cosh(\eta_2 z) - sinh(\eta_2 z)}{\eta_2^2}\right)\Bigg]_{z_i}^{z_l} + z_i\text{Æ}\left(\frac{cosh(\eta_2 z)}{\eta_2}\right)\Bigg]_{z_i}^{z_l}\Bigg]$$

$$t_{z_4} = \frac{-i\mu 2k\eta_1}{l_e}\left[\frac{\eta_1 z sinh(\eta_1 z) - cosh\,(\eta_1 z)}{\eta_1^2}\right]_{z_i}^{z_l} - z_i\frac{sinh(\eta_1 z)}{\eta_1}\Bigg]_{z_i}^{z_l}$$

$$- \text{Ö}\left(\frac{\eta_2 z sinh(\eta_2 z) - cosh(\eta_2 z)}{\eta_2^2}\right)\Bigg]_{z_i}^{z_l} + z_i\text{Ö}\left(\frac{sinh(\eta_2 z)}{\eta_2}\right)\Bigg]_{z_i}^{z_l}\Bigg]$$

(3-55)

Symmetric Mode

Similarly using the substitutions,

$$\text{Å} = 2\eta_1^2 + k_2^2 \qquad \text{æ} = \frac{(2k^2 - k_2^2)\cosh(\eta_2 H)}{\cosh(\eta_2 H)} \qquad \text{Ä} = \frac{(2k^2 - k_2^2)^2\cosh(\eta_1 H)}{4k^2\eta_1\eta_2\cosh(\eta_1 H)}$$

(3-56)

the modal stress functions become

$$\hat{\sigma}_{xx} = -\mu[\text{Å}cosh(\eta_1 z) - \text{æ}sinh(\eta_2 z)]$$

$$\hat{\sigma}_{xz} = i\mu 2k\eta_1[sinh(\eta_1 z) - \text{Ä}\,sinh(\eta_2 z)$$

(3-57)

The nodal force vector for symmetric mode is then evaluated using (3-54)

$$\begin{Bmatrix} t_{x1} \\ t_{z1} \\ t_{x4} \\ t_{z4} \end{Bmatrix} = \int_{z_i}^{z_l} \begin{bmatrix} \frac{z_l - z}{l_e} & 0 \\ 0 & \frac{z_l - z}{l_e} \\ \frac{z - z_i}{l_e} & 0 \\ 0 & \frac{z - z_i}{l_e} \end{bmatrix} \begin{Bmatrix} -\mu[\text{Å}cosh(\eta_1 z) - \text{æ}sinh(\eta_2 z)] \\ i\mu 2k\eta_1[sinh(\eta_1 z) - \text{Ä}\,sinh(\eta_2 z) \end{Bmatrix} dz$$

(3-58)

The nodal force components for the symmetric mode are then

$$t_{x_1} = -\frac{\mu}{l_e}\left[z_l \text{Å}\left(\frac{sinh(\eta_1 z)}{\eta_1}\right)\right]_{z_i}^{z_l} - \text{Å}\left(\frac{\eta_1 z sinh(\eta_1 z) - cosh(\eta_1 z)}{\eta_1^2}\right)\right]_{z_i}^{z_l}$$

$$- z_l \text{æ}\left(\frac{sinh(\eta_2 z)}{\eta_2}\right)\right]_{z_i}^{z_l} + \text{æ}\left(\frac{\eta_2 z sinh(\eta_2 z) - cosh(\eta_2 z)}{\eta_2^2}\right)\right]_{z_i}^{z_l}\Bigg]$$

$$t_{z_1} = \frac{i\mu 2k\eta_1}{l_e}\left[z_l\left(\frac{cosh(\eta_1 z)}{\eta_1}\right)\right]_{z_i}^{z_l} - \frac{\eta_1 z cosh(\eta_1 z) - sinh(\eta_1 z)}{\eta_1^2}\Bigg]_{z_i}^{z_l} - z_l \text{Ä}\left(\frac{cosh(\eta_2 z)}{\eta_2}\right)\Bigg]_{z_i}^{z_l}$$

$$+ \text{Ä}\left(\frac{\eta_2 z cosh(\eta_2 z) - sinh(\eta_2 z)}{\eta_2^2}\right)\Bigg]_{z_i}^{z_l}\Bigg]$$

$$t_{x_4} = -\frac{\mu}{l_e}\left[\text{Å}\left(\frac{\eta_1 z sinh(\eta_1 z) - cosh(\eta_1 z)}{\eta_1^2}\right)\right]_{z_i}^{z_l} - z_i \text{Å}\left(\frac{sinh(\eta_1 z)}{\eta_1}\right)\Bigg]_{z_i}^{z_l}$$

$$- \text{æ}\left(\frac{\eta_2 z sinh(\eta_2 z) - cosh(\eta_2 z)}{\eta_2^2}\right)\Bigg]_{z_i}^{z_l} + z_i \text{æ}\left(\frac{sinh(\eta_2 z)}{\eta_2}\right)\Bigg]_{z_i}^{z_l}\Bigg]$$

$$t_{z_4} = \frac{i\mu 2k\eta_1}{l_e}\left[\frac{\eta_1 z cosh(\eta_1 z) - sinh\,(\eta_1 z)}{\eta_1^2}\right]_{z_i}^{z_l} - z_i\left(\frac{cosh(\eta_1 z)}{\eta_1}\right)\Bigg]_{z_i}^{z_l}$$

$$- \text{Ä}\left(\frac{\eta_2 z cosh(\eta_2 z) - sinh(\eta_2 z)}{\eta_2^2}\right)\Bigg]_{z_i}^{z_l} + z_i \text{Ä}\left(\frac{cosh(\eta_2 z)}{\eta_2}\right)\Bigg]_{z_i}^{z_l}\Bigg]$$

(3-59)

3.3.2 Nodal Force Vector Evaluated from WFE Force Vector

In the previous section, the modal stress functions are given in the form of analytical expressions. Therefore, the nodal force for the FE region can be computed by integrating the product of the stress functions with the shape functions. However, for a ply-by-ply approach, the dispersion equation is solved by WFE and the global stress functions are instead embedded in the WFE nodal force vectors $\boldsymbol{f}_L^s$ in equation (2-66). In this section, the procedure to interpolate the

WFE nodal force for the GL nodal force is described. Consider the WFE elements shown in the left, and the GL elements at the left boundary shown in the right of Figure 3-14.

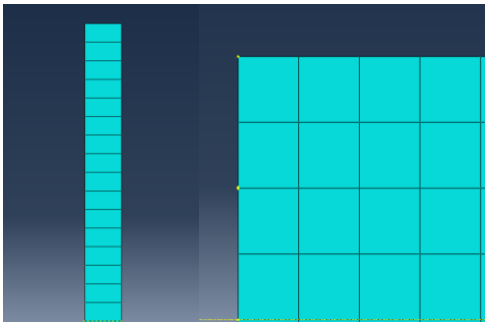

Figure 3-14 (L) WFE mesh and (R) Global local FE mesh

Typically, the element size through the plate thickness in the WFE mesh is smaller than the one in the GL mesh. Furthermore, the element size in the thickness direction may also change based on the individual ply thickness. The main idea behind the interpolation is to find a ratio between the GL element size and the WFE element size at the same thickness location. Then this factor is used to scale the WFE nodal force vector appropriately for the GL nodal forces. The first step in the procedure is to sort and find the nodal positions of the left boundary nodes for the WFE and GL meshes. These two vectors are used to compute the element size in the thickness direction for the two meshes. For illustration, they are plotted in Figure 3-15a as the red dot (WFE element size) and the blue diamond (GL element size). The next step is to interpolate the GL element size vector for all WFE nodes, shown as the black dots. Note that GL element size averaging is possible between element size variations through thickness. Finally, the ratio between the GL element size and the WFE element size is found by element-wise division of the the two vectors, and the results are shown in Figure 3-15b. Once the ratio is found for every WFE nodal point, the WFE nodal force vector is multiplied by this ratio to scale the GL nodal points. Finally, for each of the GL nodes, the nodal force vector is interpolated from this scaled WFE nodal force vector. It is worth mentioning that due to the numerical precision of the nodal coordinate, the GL nodal

points could be outside of the range of the WFE nodal points. In such cases, the GL nodal coordinate must be adjusted to fall in range for the interpolation to avoid errors.

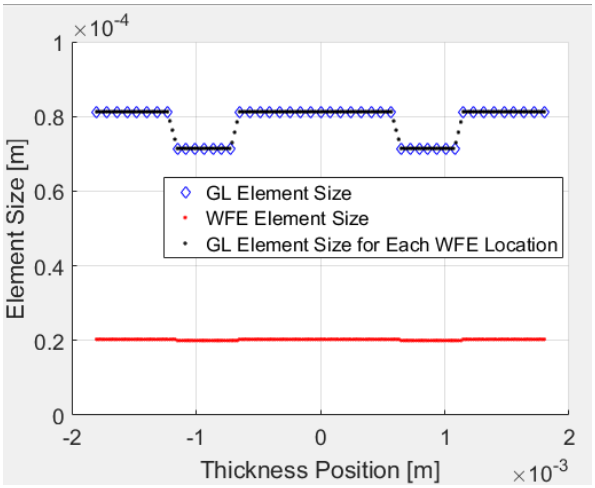

(a) the element size though thickness for WFE, GL mesh

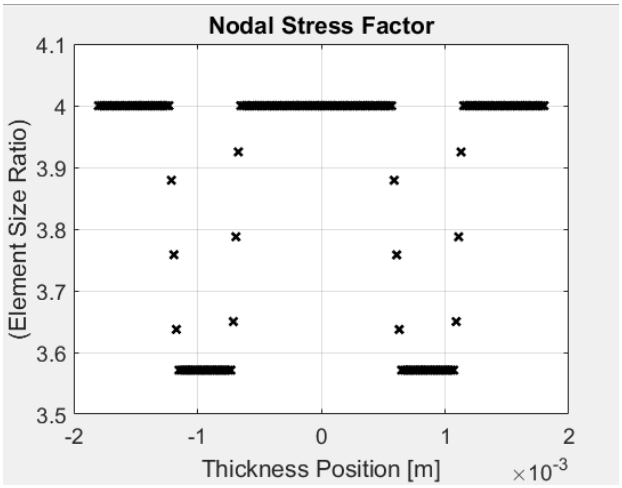

(b) the ratio between the WFE element size and the GL element size to compute the nodal stress factor

Figure 3-15 Example of the WFE element size and the GL element size, and the calculation of the nodal stress factor

3.4 Numerical and Modeling Considerations

3.4.1 Finite Element Discretization

Effects of the Local Region Size

One of the advantages of using GLM is that only a small region of the plate with irregularities is discretized to reduce the computational effort. However, a proper choice of the width of the local region is not immediately clear. A previous researcher has pointed out that the FE region boundary should be at least twice of the plate thickness away from the defect, where the contributions of the non-propagating modes can be ignored [65]. To further investigate the effects of the FE region width on the accuracy of the GL solution, a study with a stiffened aluminum plate (E = 68.9 GPa, ν = 0.3, ρ = 2700 kg/m^3), shown in Figure 3-16, with a 25 mm wide, 2.7 mm thickness increased section within the FE regions of 100 mm, 65 mm, 45 mm, and 40 mm in width is conducted. First the energy balance error, defined in equation (3-30), for both

A_0 and S_0 incident modes are considered. The incident wave amplitude is chosen such that the power flow of the incident mode is 1 at all frequencies.

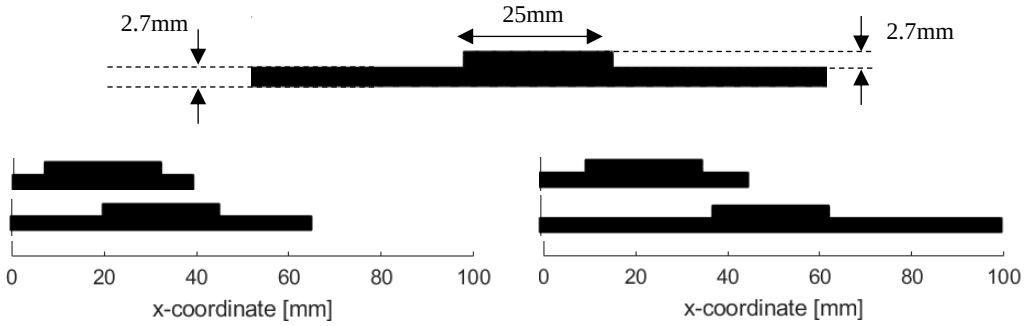

Figure 3-16 Geometry of the stiffned plate and the GL model with various FE region sizes

Figure 3-17 shows that as the FE region decrease in size, the lower frequencies have noticeable error in energy balance. Even with 20 mm spacing from the FE boundary to the step (65 mm FE region), at 50 kHz, the error can reach up to 6% in the case of A_0 incidence. It is, however, difficult to explain why the error for 40 mm FE region size is smaller than the 45 mm case. Despite this unusual result, one could conclude that if the error below the first cut-off frequency does not show an increasing trend towards the lower frequencies which is the case of 100 mm size, the FE region size is likely to suffice. Another interesting phenomenon is that the error is larger with A_0 incident mode than with S_0 incident. It is counterintuitive because the wavelength of A_0 mode is significantly smaller than that for the S_0 mode at lower frequencies (Figure 3-18b).

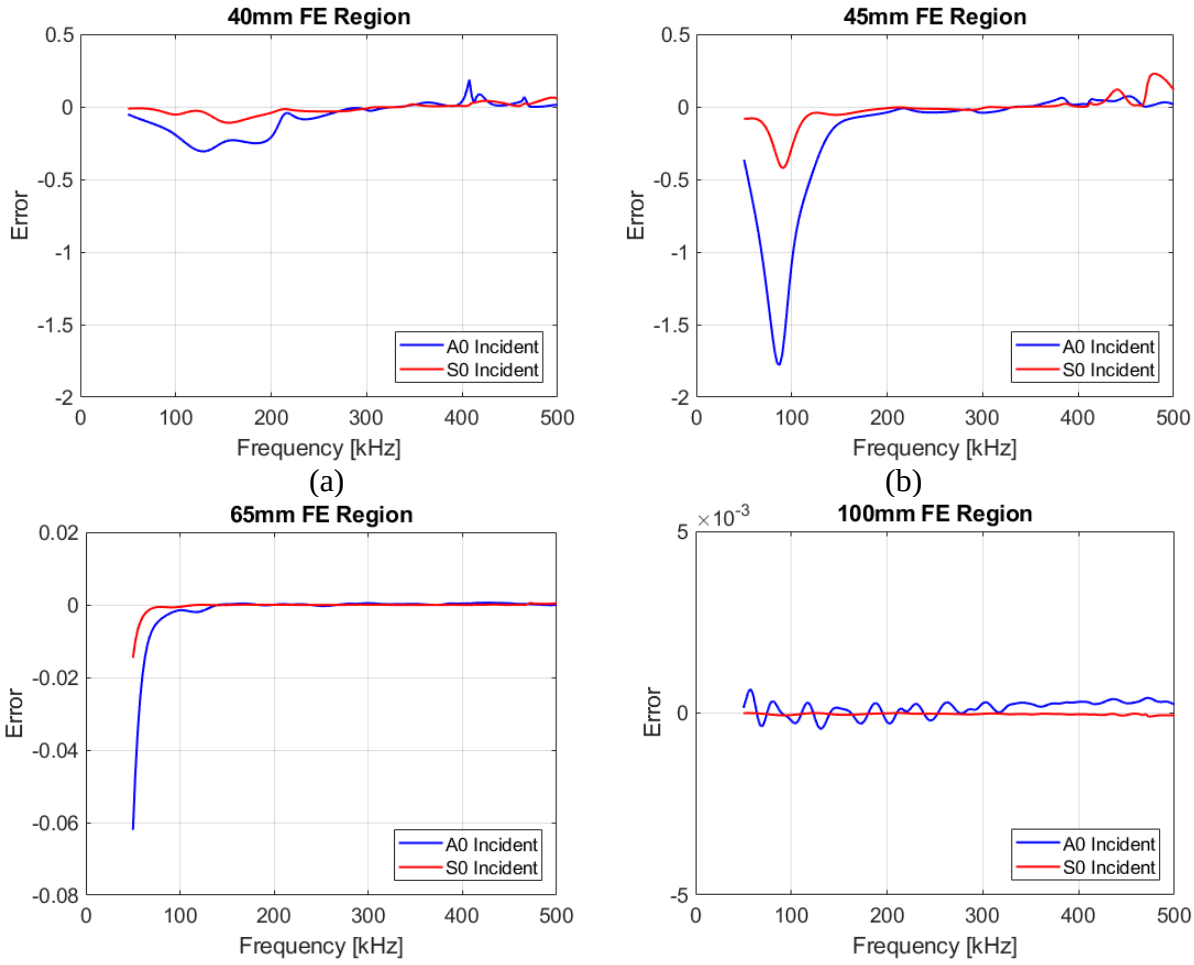

Figure 3-17 The energy balance error for the stiffened aluminum plate subjected to A_0 incidence (blue line) and S_0 incidence (red line) for FE region width of (a) 40 mm, (b) 45 mm, (c), 65 mm, (d) 100 mm

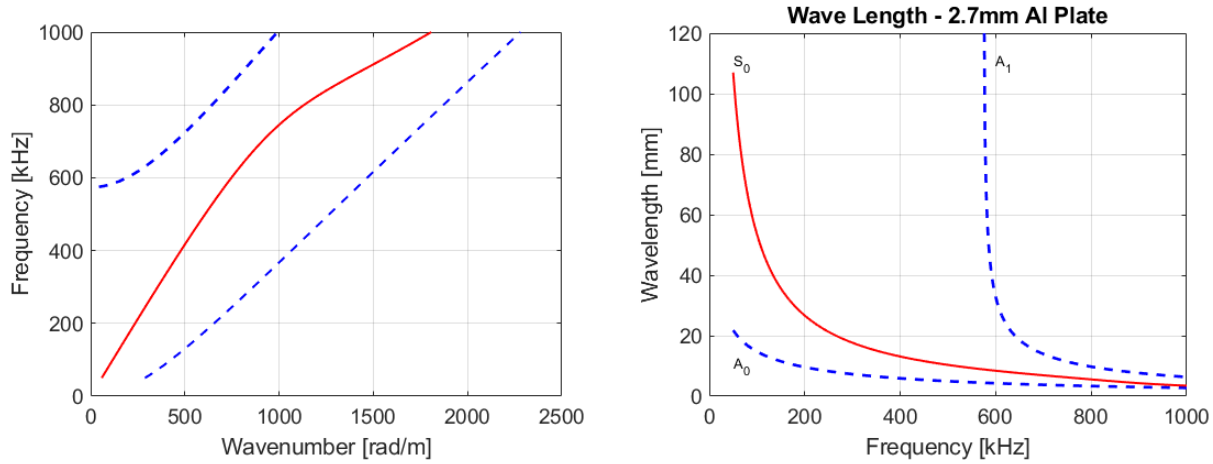

(a) the frequency wavenumber curves of the 1.6mm thick aluminum plate

(b) the coressponding wavelength-frequency relations

Figure 3-18 Dispersion curve for a 2.7 mm thick aluminum plate

Furthermore, at the cut-off frequencies, the wavelengths for the higher modes are theoretically infinite which is much longer than the FE region length. Figure 3-19 indicates that the energy balance has a noticeable "jump" in a narrow frequency range around the cut-off frequencies. For the rest of the frequencies, the error is much smaller than the transmitted and reflected power flow. It is worth to mention that the power flow variation as a function of frequency is smaller when the wavelength is longer. In other words, an incident S_0 mode has longer wavelength when compared to incident A_0 waves at lower frequencies, and the "dips" in the power flow spectrum at lower frequencies are not as numerous as for the S_0 incidence. This could be explained by the fact that wave scattering is most likely due to matching of the defect size with multiples of wavelengths.

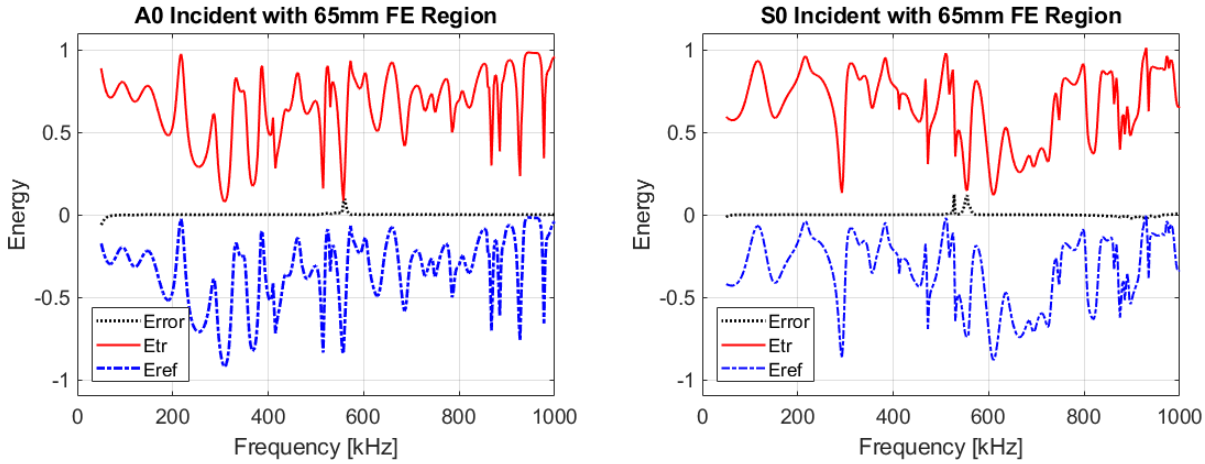

(a) A_0 incidence (b) S_0 incidence

Figure 3-19 The transmitted (red solid line) and reflected (blue dash-dot line) power flow for 65 mm FE region

Element Considerations

For some geometries or defects with complex shapes, it is necessary to use triangular elements in the FE discretization. Therefore, the computer algorithm that implements the GLM calculation described above should accept the mixed use of the 4-node bi-linear plane strain rectangular elements and the 3-node linear plane strain triangular elements. However, the nodal

force vector calculation outlined in 3.3, is only implemented for 4-node elements. Thus, the use of tri-element is not possible at the left or the right boundary, nor with applied traction loads. In contrast to rectangular elements, the shape functions for tri-elements lacks the product term of the two-dimensional coordinate, and thus can only represent a constant strain state, and be susceptible to shear locking. Therefore, an exercise is carried out to determine whether the use of mixed tri-rectangular element mesh would cause artificial stiffness change or affect the wavefield calculations. A model with a 2.7 mm thick aluminum plate free of defects is used to calculate the power flow of the scattered waves. Figure 3-20 shows the FE discretization where the local region is 50 mm long with a mesh that contains 26480 rectangular elements that are 68 μm by 68 μm, surrounding a region of 10 mm by 2 mm that is made up of 5920 triangular elements of the same edge lengths. The power flow results are then compared to those obtained from a mesh with only rectangular elements that are of the same edge length.

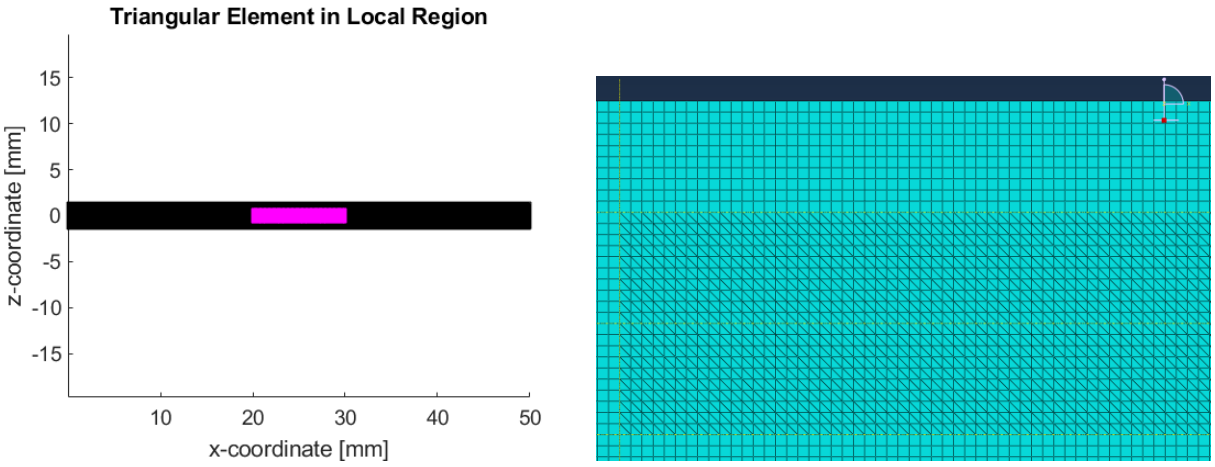

Figure 3-20 (a) the local region where the triangular elements are colored pink, (b) a magnified view of the mixed element mesh showing the orientation of the tri-elements

The power flow calculation is done for an incident A_0 mode with unit power flow across the studied frequency range. Figure 3-21a shows the energy balance error given in equation (3-30), which is the quantity that accounts for the difference between the power flows carried by the incident wave and the scattered waves.

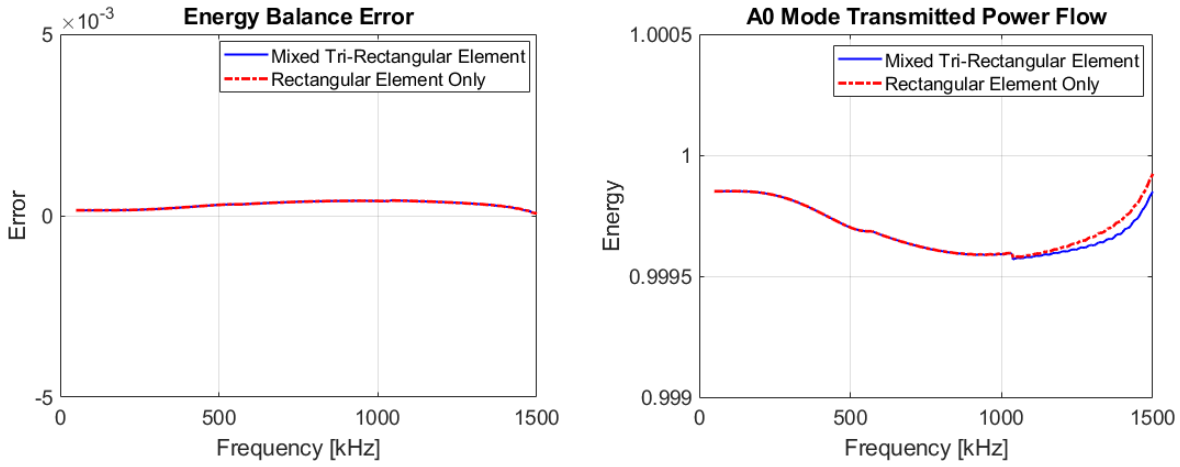

Figure 3-21 (a) Energy balance error, (b) transmitted A_0 mode power flow calculated using the two meshes

Since the local region has no energy dissipation mechanisms or defects, the incident power should be transmitted entirely as A_0 mode, which is confirmed with the results shown in Figure 3-21b. The numerical discrepancy between the rectangular element mesh and the mixed element mesh is almost indistinguishable at frequencies below 1 MHz, and for all practical problems negligible in the studied frequency range.

The FE discretization and the mass $\boldsymbol{M}$ and stiffness $\boldsymbol{K}$ matrices generation are done with ABAQUS/CAE. Like some commercial FE codes, ABAQUS has some modifications to the standard $\boldsymbol{M}$, and $\boldsymbol{K}$ calculations with (3-60) and the numerical integration rule in (3-42)

$$\boldsymbol{M} = \int_V \boldsymbol{N}^T \boldsymbol{\rho} \boldsymbol{N}\, dV \qquad \boldsymbol{K} = \int_V \boldsymbol{B}^T ¢ \boldsymbol{B}\, dV \tag{3-60}$$

where $\boldsymbol{\rho}$ is a diagonal matrix of density, ¢ is the elastic constant matrix, and $\boldsymbol{B}$ is the displacement gradient matrix containing the derivatives of the shape functions. In transient FE approach, the inverse of the mass matrix is computed regularly, thus it is common to diagonalize the mass matrix by row sum method as shown in the example of a single 4-node element of 1 m X 1 m with density 2700 kg/m^3 in (3-61).

$$\begin{bmatrix} 300 & 0 & 150 & 0 & 75 & 0 & 150 & 0 \\ & 300 & 0 & 150 & 0 & 75 & 0 & 150 \\ & & 300 & 0 & 150 & 0 & 75 & 0 \\ & & & 300 & 0 & 150 & 0 & 75 \\ & & & & 300 & 0 & 150 & 0 \\ & sym & & & & 300 & 0 & 150 \\ & & & & & & 300 & 0 \\ & & & & & & & 300 \end{bmatrix} \rightarrow \begin{bmatrix} 675 & 0 & 0 & 0 & 0 & 0 & 0 & 0 \\ & 675 & 0 & 0 & 0 & 0 & 0 & 0 \\ & & 675 & 0 & 0 & 0 & 0 & 0 \\ & & & 675 & 0 & 0 & 0 & 0 \\ & & & & 675 & 0 & 0 & 0 \\ & sym & & & & 675 & 0 & 0 \\ & & & & & & 675 & 0 \\ & & & & & & & 675 \end{bmatrix}$$

(3-61)

Moreover, when full integration is used for the bi-linear element, the stiffness matrix is calculated with the "selectively reduced-integration technique" with the order of integration reduced for selected terms for the purpose of preventing mesh locking [66]. Using the elastic property of aluminum, the 1m X 1m element $\boldsymbol{K}$ matrices calculated with the standard definition, the selectively reduced integration and the differences between the two are shown in (3-62).

ABAQUS $\boldsymbol{K}$

3.422916666666673e+10	1.656250000000000e+10	-2.097916666666673e+10	3.312500000000000e+09	1.214583333333327e+10	-3.312499999999998e+09	-2.539583333333328e+10	-1.656250000000000e+10
1.656250000000000e+10	3.422916666666673e+10	-3.312500000000000e+09	1.214583333333327e+10	3.312499999999999e+09	-2.097916666666673e+10	-1.656250000000000e+10	-2.539583333333327e+10
-2.097916666666673e+10	-3.312500000000000e+09	3.422916666666673e+10	-1.656250000000000e+10	-2.539583333333328e+10	1.656250000000000e+10	1.214583333333327e+10	3.312499999999999e+09
3.312500000000000e+09	1.214583333333327e+10	-1.656250000000000e+10	3.422916666666673e+10	1.656250000000000e+10	-2.539583333333328e+10	-3.312500000000000e+09	-2.097916666666673e+10
1.214583333333327e+10	3.312499999999999e+09	-2.539583333333328e+10	1.656250000000000e+10	3.422916666666673e+10	-1.656250000000000e+10	-2.097916666666673e+10	-3.312499999999999e+09
-3.312499999999998e+09	-2.097916666666673e+10	1.656250000000000e+10	-2.539583333333328e+10	-1.656250000000000e+10	3.422916666666673e+10	3.312500000000000e+09	1.214583333333327e+10
-2.539583333333328e+10	-1.656250000000000e+10	1.214583333333327e+10	-3.312500000000000e+09	-2.097916666666673e+10	3.312500000000000e+09	3.422916666666673e+10	1.656250000000000e+10
-1.656250000000000e+10	-2.539583333333327e+10	3.312499999999999e+09	-2.097916666666673e+10	-3.312499999999999e+09	1.214583333333327e+10	1.656250000000000e+10	3.422916666666673e+10

Standard $\boldsymbol{K}$

3.975000000000001e+10	1.656250000000000e+10	-2.650000000000000e+10	3.312499999999999e+09	-1.987500000000000e+10	-1.656250000000000e+10	6.624999999999998e+09	-3.312499999999999e+09
1.656250000000000e+10	3.975000000000001e+10	-3.312499999999999e+09	6.624999999999998e+09	-1.656250000000000e+10	-1.987500000000000e+10	3.312499999999999e+09	-2.650000000000000e+10
-2.650000000000000e+10	-3.312499999999999e+09	3.975000000000000e+10	-1.656250000000000e+10	6.624999999999998e+09	3.312499999999999e+09	-1.987500000000000e+10	1.656250000000000e+10
3.312499999999999e+09	6.624999999999998e+09	-1.656250000000000e+10	3.975000000000000e+10	-3.312499999999999e+09	-2.650000000000000e+10	1.656250000000000e+10	-1.987500000000000e+10
-1.987500000000000e+10	-1.656250000000000e+10	6.624999999999998e+09	-3.312499999999999e+09	3.975000000000000e+10	1.656250000000000e+10	-2.650000000000000e+10	3.312500000000000e+09
-1.656250000000000e+10	-1.987500000000000e+10	3.312500000000000e+09	-2.650000000000000e+10	1.656250000000000e+10	3.975000000000000e+10	-3.312499999999999e+09	6.624999999999998e+09
6.624999999999998e+09	3.312499999999999e+09	-1.987500000000000e+10	1.656250000000000e+10	-2.650000000000000e+10	-3.312499999999999e+09	3.975000000000000e+10	-1.656250000000000e+10
-3.312499999999999e+09	-2.650000000000000e+10	1.656250000000000e+10	-1.987500000000000e+10	3.312499999999999e+09	6.624999999999998e+09	-1.656250000000000e+10	3.975000000000000e+10

Difference ($\boldsymbol{K}_{\text{ABAQUS}} - \boldsymbol{K}$)

-5.520833333333271e+09	1.907348632812500e-06	5.520833333333271e+09	9.536743164062500e-07	3.202083333333327e+10	1.325000000000000e+10	-3.202083333333328e+10	-1.325000000000000e+10
1.907348632812500e-06	-5.520833333333271e+09	-1.430511474609375e-06	5.520833333333271e+09	1.987500000000000e+10	-1.104166666666729e+09	-1.987500000000000e+10	1.104166666666729e+09
5.520833333333271e+09	-9.536743164062500e-07	-5.520833333333279e+09	-1.907348632812500e-06	-3.202083333333328e+10	1.325000000000000e+10	3.202083333333327e+10	-1.325000000000000e+10
1.430511474609375e-06	5.520833333333271e+09	-1.907348632812500e-06	-5.520833333333279e+09	1.987500000000000e+10	1.104166666666721e+09	-1.987500000000000e+10	-1.104166666666729e+09
3.202083333333327e+10	1.987500000000000e+10	-3.202083333333328e+10	1.987500000000000e+10	-5.520833333333271e+09	-3.312500000000000e+10	5.520833333333271e+09	-6.624999999999998e+09
1.325000000000000e+10	-1.104166666666733e+09	1.325000000000000e+10	1.104166666666725e+09	-3.312500000000000e+10	-5.520833333333271e+09	6.624999999999998e+09	5.520833333333271e+09
-3.202083333333328e+10	-1.987500000000000e+10	3.202083333333327e+10	-1.987500000000000e+10	5.520833333333271e+09	6.625000000000000e+09	-5.520833333333271e+09	3.312500000000000e+10
-1.325000000000000e+10	1.104166666666733e+09	-1.325000000000000e+10	-1.104166666666733e+09	-6.624999999999998e+09	5.520833333333271e+09	3.312500000000000e+10	-5.520833333333271e+09

(3-62)

The difference of the two matrices shows which selected terms are subjected to the selective reduce integration. These numerical implementations appear to have negligible effects on the precision of the waveform prediction as the changes in the waveform prediction is often very small compare to changes in waveforms due defects.

Crack Tip Mesh Refinement

Delamination is a critical type of defect in laminated composites and the simplest way to model such defect is by separation of nodes. However, for fracture model, it is often required to have a fine mesh to converge to the high stress intensity at the crack tip. Therefore, a comparison of simple mesh is compared with another mesh that has a higher degree of mesh refinement. Figure 3-22 shows the two different meshes where the refined mesh has circular regions around the two crack tips with increased mesh density.

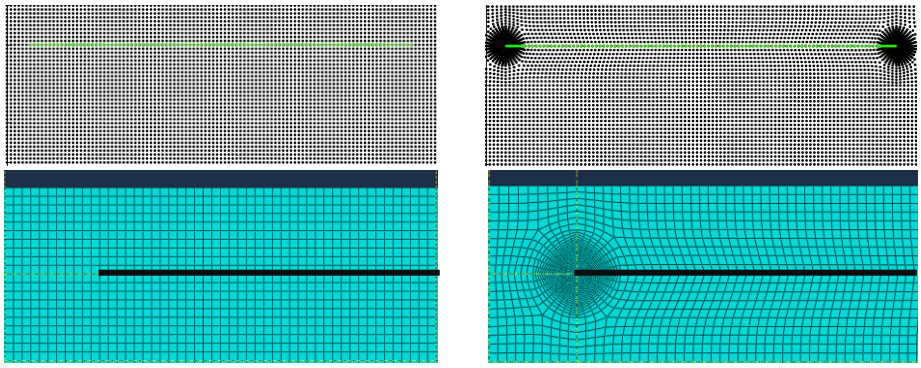

Figure 3-22 The nodal points around the crack, and the separation nodes are indicated by the green dots. The manifiying view of the mesh near the left crack tip for (a) the "regular" mesh, (b) the refined mesh

The physical problem considered here is a 4 mm thick aluminum plate (E = 68.9 GPa, ν = 0.3, ρ = 2700 kg/m^3), with a 10 mm long crack situated 1 mm below the top surface. The nominal element size is 100 μm by 100 μm, whereas for the refined mesh a circle of 1 mm diameter is drawn such that the element edge length is 25 μm in the radial direction (Figure 3-22b). To study the scattering effects of the two models, it is assumed that a single incident A_0 mode or S_0 mode is incident from the left boundary. For a better displacement waveform visualization, the incident wave is of 5 cycle Hann windowed sine pulse with a 300 kHz center frequency. Figure 3-23a shows that for an incident A_0 mode, both models predict the 300 kHz frequency content is not strongly transmitted with small differences in the power flows. The top surface vertical displacement at 216 mm to the right of the crack's leading edge in Figure 3-23b shows that the

scattered waves arrives in two main packets. For the displacements, the differences between the two models are not noticeable.

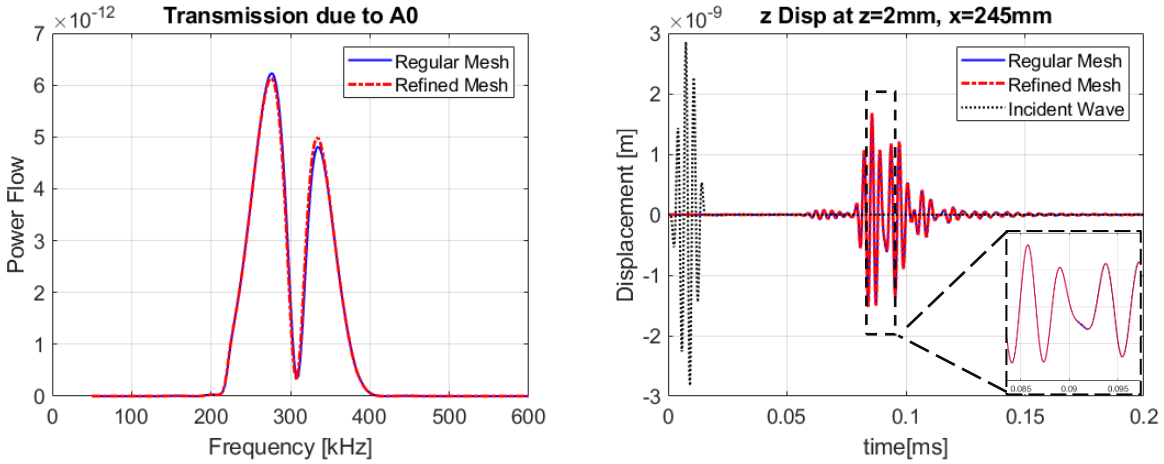

Figure 3-23 Comapring the result from the regular and the refined mesh for incident A_0 mode (a) the total transmitted power flow, (b) the top surface vertical displacement of the transmitted wave at 216 mm to the right of the crack leading edge

For incident S_0 mode, the transmission for 300 kHz frequency content is not as obstructive as A_0 mode. Figure 3-24a shows that the two models predict indistinguishable difference in transmitted power flow. The horizontal displacement waveform shown in Figure 3-24b indicates that the incident S_0 is strongly transmitted with smaller S_0 to A_0 packet trailing the main S_0 packet. Once again, the differences between the two models are negligible. When comparing the small amount of differences between the two models in Figure 3-23 and Figure 3-24, incident A_0 mode is more sensitive to the mesh refinement. This is likely due to the fact that the wavelength for A_0 mode (8 mm) is approximately 2 times less than that of S_0 mode (17 mm). Furthermore, it is believed that the dominating source of wave scattering in a discontinuity is that the guided waves above and below the crack travel at different speeds and when they reach the end of the trailing edge of the crack, a scattered wave must be induced to satisfy the continuity conditions when the waves arrive at the trailing edge and merge together.

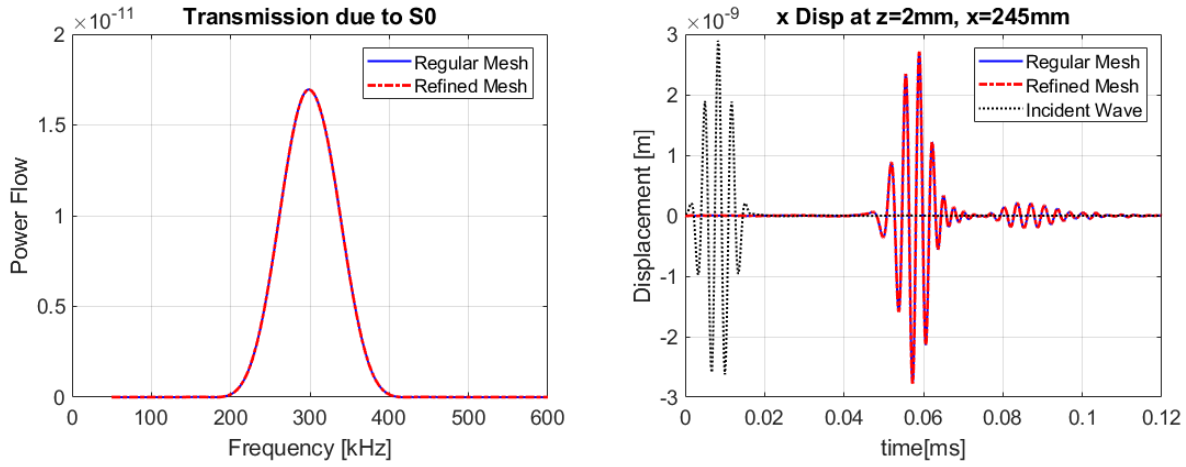

Figure 3-24 Comapring the results from the regular and the refined mesh for incident S_0 mode (a) the total transmitted power flow, (b) the top surface vertical displacement of the transmitted wave at 216 mm to the right of the crack's leading edge

3.4.2 Modeling Wave Attenuation with Complex Moduli

In modeling some composite structures with highly attenuative materials such as rich resin or adhesive polymer, it is necessary to introduce material attenuation to account for the reduction in the amplitude of the elastic waves with propagation distance and frequency. Furthermore, when the plate has a high frequency thickness ratio, a large number of higher modes are included in the global local analysis. The cutoff frequencies for the higher modes are the natural frequencies of the plate in which resonance occurs. Thus, for undamped models, the wave amplitude for the resonating mode is overpredicted in a small frequency range around the cutoff frequencies. By introducing a small amount of material damping, the global local model prediction for thick plates can be improved with the unrealistic plate motion due to resonance being suppressed.

The amplitude reduction of the waves as they propagate away from the source can be attributed to geometric spreading as shown in Figure 3-25, that is the increase in the perimeter of the wave front, and material dissipation. A comprehensive models of wave attenuation caused by the two effects in polymer matrix composites has been developed by Mal [65]. The main idea

behind the model is to assume that the stiffness constants in the frequency domain are complex with a small number of parameters that represent the energy absorbed by dissipated by the viscoelasticity of the polymers and the energy lost due to the scattering of the waves by the fibers. This model is used here with appropriate modifications to determine the effects of wave attenuation.

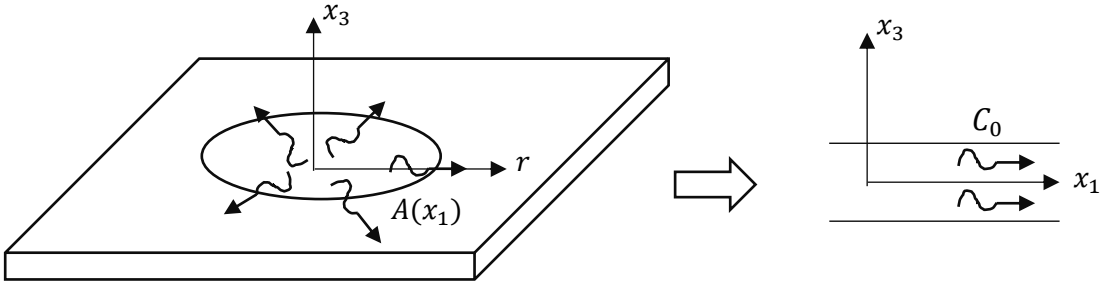

Figure 3-25 Elastic wave amplitude reduction due to geometric spreading

It should be noted that for isotropic solids, the moduli results in complex bulk wave velocities α and β of the form.

$$\alpha^2 = \frac{\hat{\alpha}^2}{1 + ip\left(\frac{\hat{\beta}}{\hat{\alpha}}\right)} \qquad \beta^2 = \frac{\hat{\beta}^2}{1 + ip} \tag{3-63}$$

where $\hat{\alpha}$, and $\hat{\beta}$ are the real bulk wave velocities, and p is a positive and dimensionless constant to be determined by experiment. It is worth to mention that [66] points out that Kelvin-Voigt and other spring-dashpot models fail to predict the wave amplitude as observed in viscoelastic solids.

Ply-by-Ply Implementation in a Layered Composite Plate

Assume that the lamina shown in Figure 3-26 is transversely isotropic with the symmetric axis aligned with the fiber direction and the damping parameter *p* is a known constant. The local stiffness matrix for a single ply along the fiber direction is first calculated using the inverse of

the compliance matrix shown in equation (2-75) with the real elastic properties. The local ply stiffness matrix is in the form

$$\begin{Bmatrix}\sigma_{11}\\ \sigma_{22}\\ \sigma_{33}\\ \sigma_{23}\\ \sigma_{13}\\ \sigma_{12}\end{Bmatrix}=\begin{bmatrix}C_{11} & C_{12} & C_{12} & 0 & 0 & 0\\ & C_{22} & C_{23} & 0 & 0 & 0\\ & & C_{22} & 0 & 0 & 0\\ & & & C_{44} & 0 & 0\\ & sym & & & C_{55} & 0\\ & & & & & C_{55}\end{bmatrix}\begin{Bmatrix}\varepsilon_{11}\\ \varepsilon_{22}\\ \varepsilon_{33}\\ 2\varepsilon_{23}\\ 2\varepsilon_{13}\\ 2\varepsilon_{12}\end{Bmatrix}$$

(3-64)

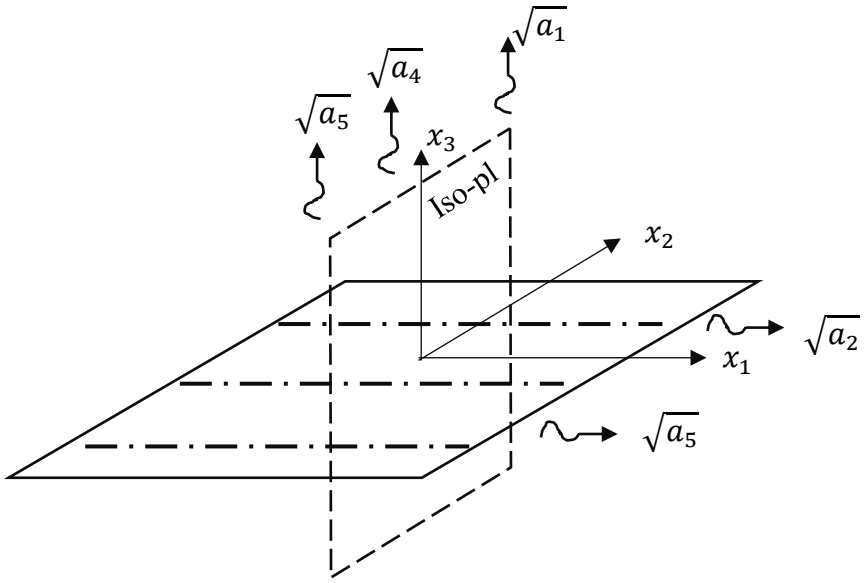

Figure 3-26 Sketch of a lamina showing the isotropic plane and plane wave velocities

$C_{11}, C_{12}, C_{22}, C_{23}, C_{55}$ are the five independent real material constants and $C_{44}=\frac{(C_{22}-C_{23})}{2}$. The associated constants are related to the bulk wave velocities, $\sqrt{\hat{a}}$, which can be determined from solving the Christoffel tensor equation

$$\hat{a}_1=\frac{C_{22}}{\rho},\hat{a}_2=\frac{C_{11}}{\rho},\hat{a}_3=\frac{C_{12}+C_{55}}{\rho},\hat{a}_4=\frac{C_{44}}{\rho},\hat{a}_5=\frac{C_{55}}{\rho}$$

(3-65)

It is worth mentioning that the longitudinal waves are related to $\hat{a}_2$, and $\hat{a}_1$, and the shear waves are related to $\hat{a}_4$ and $\hat{a}_5$. Extending the definition of the complex velocities for isotropic material in equation (3-63), the following complex stiffness constants *CC* are evaluated [65]

$$a_1 = \frac{\hat{a}_1}{1+ip\sqrt{\frac{\hat{a}_5}{\hat{a}_1}}} \quad \xrightarrow{yields} \quad CC_{22} = \rho a_1 \qquad a_2 = \frac{\hat{a}_2}{1+ip\sqrt{\frac{\hat{a}_5}{\hat{a}_2}}} \quad \xrightarrow{yields} \quad CC_{11} = \rho a_2$$

$$a_3 = \frac{\hat{a}_3}{1+ip\sqrt{\frac{\hat{a}_5}{\hat{a}_3}}} \quad \xrightarrow{yields} \quad CC_{12} = \rho a_3 - CC_{55} \qquad a_5 = \frac{\hat{a}_5}{1+ip} \quad \xrightarrow{yields} \quad CC_{55} = \rho a_5$$

$$a_4 = \frac{\hat{a}_4}{1+ip\sqrt{\frac{\hat{a}_5}{\hat{a}_4}}} \quad \xrightarrow{yields} \quad CC_{44} = \rho a_4 \qquad CC_{23} = -(2CC_{44} - CC_{22})$$

(3-66)

For transverse isotropy, the following relations hold between the stiffness constants

$$CC_{33} = CC_{22} \qquad CC_{66} = CC_{55} \qquad CC_{13} = CC_{12}$$

(3-67)

The complex stiffness matrix is then computed for different ply orientations using equation (2-76). In the calculation of the FE stiffness matrices, the complex elastic constants are then separated into the real and the imaginary part, such that $\boldsymbol{K} = \boldsymbol{K_{real}} - i\boldsymbol{K_{imag}}$ and are computed separately. Since $\boldsymbol{K_{real}}$ and $\boldsymbol{K_{imag}}$ are real valued matrices, they can be calculated by standard FE programs such as ABAQUS.

Homogenized and Transversely Isotropic Laminate

As pointed out in section 2.2.4, common composite laminates have a balance and symmetric layups so that a homogenized and transversely isotropic model is accurate for time-of-flight analysis at lower frequencies. The material damping with complex moduli implementation is similar to the ply-by-ply cases but with some differences in the bulk wave velocity definitions. For completeness, the equations are presented here.

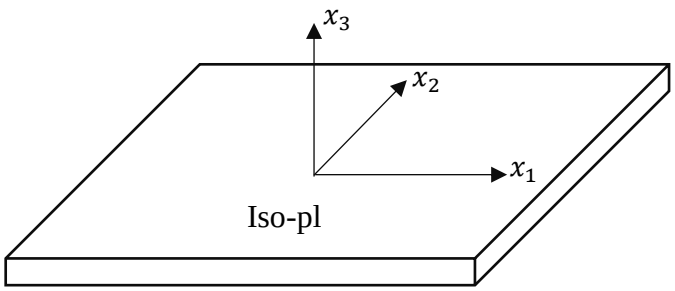

Figure 3-27 Homogenized laminate represented by transversely isotropic model

Assuming the five independent elastic constants $E_{11}, E_{33}, \nu_{12}, \nu_{13}$, and G_{13} are known, the derived elastic constants are

$$E_{22} = E_{11} \qquad \nu_{23} = \nu_{13} \qquad G_{23} = G_{13} \qquad G_{12} = \frac{E_{11}}{2(1+\nu_{12})}$$

(3-68)

Using equation (2-75), and calculating its inverse, the complex stiffness matrix is obtained:

$$\begin{Bmatrix} \sigma_{11} \\ \sigma_{22} \\ \sigma_{33} \\ \sigma_{23} \\ \sigma_{13} \\ \sigma_{12} \end{Bmatrix} = \underbrace{\begin{bmatrix} C_{11} & C_{12} & C_{13} & 0 & 0 & 0 \\ & C_{11} & C_{13} & 0 & 0 & 0 \\ & & C_{33} & 0 & 0 & 0 \\ & & & C_{44} & 0 & 0 \\ & sym & & & C_{44} & 0 \\ & & & & & C_{66} \end{bmatrix}}_{\boldsymbol{C}} \begin{Bmatrix} \varepsilon_{11} \\ \varepsilon_{22} \\ \varepsilon_{33} \\ 2\varepsilon_{23} \\ 2\varepsilon_{13} \\ 2\varepsilon_{12} \end{Bmatrix}$$

(3-69)

Upon calculating the stiffness matrix $\boldsymbol{C}$, the following quantities with the dimension of velocities squared are defined as follows [66]:

$$\hat{a}_1 = \frac{C_{11}}{\rho} \qquad \hat{a}_2 = \frac{C_{33}}{\rho} \qquad \hat{a}_3 = \frac{C_{13}+C_{44}}{\rho} \qquad \hat{a}_4 = \frac{C_{66}}{\rho} \qquad \hat{a}_5 = \frac{C_{44}}{\rho}$$

(3-70)

$\sqrt{\hat{a}_1}$ and $\sqrt{\hat{a}_5}$ are the velocities of the longitudinal and shear waves propagating in the x_1-x_2 plane respectively, whereas $\sqrt{\hat{a}_2}$ and $\sqrt{\hat{a}_5}$ are the velocities for the longitudinal and shear waves propagating in the x_3 direction. Unlike the ply-by-ply case, $\sqrt{\hat{a}_4}$ is the SH wave velocity in x_1-

x_2 plane. Subsequently, the complex velocities $\sqrt{a}$ are calculated using the real velocities with similar ratios of shear and longitudinal bulk wave velocity as in equation (3-63).

$$a_1 = \frac{\hat{a}_1}{1+ip\sqrt{\frac{\hat{a}_5}{\hat{a}_1}}} \quad \xrightarrow{yields} \quad CC_{11} = \rho a_1 \qquad a_2 = \frac{\hat{a}_2}{1+ip\sqrt{\frac{\hat{a}_5}{\hat{a}_2}}} \quad \xrightarrow{yields} \quad CC_{33} = \rho a_2$$

$$a_3 = \frac{\hat{a}_3}{1+ip\sqrt{\frac{\hat{a}_5}{\hat{a}_3}}} \quad \xrightarrow{yields} \quad CC_{13} = \rho a_3 - CC_{44} \qquad a_5 = \frac{\hat{a}_5}{1+ip} \quad \xrightarrow{yields} \quad CC_{44} = \rho a_5$$

$$a_4 = \frac{\hat{a}_4}{1+ip\sqrt{\frac{\hat{a}_5}{\hat{a}_4}}} \quad \xrightarrow{yields} \quad CC_{66} = \rho a_4$$

(3-71)

The transversely isotropic model yields the following relations

$$CC_{22} = CC_{11} \qquad CC_{55} = CC_{44}$$

(3-72)

and $CC_{12} = -(2CC_{66} - CC_{11})$. However, the resulting CC_{12} would result in a unrealistic negative stiffness constants for the imaginary parts in most homogenized materials. To overcome this issue, an additional complex quantity a_6 is defined such that an admissible CC_{12} can be calculated as

$$\hat{a}_6 = \frac{C_{12}}{\rho} \quad \rightarrow \quad a_6 = \frac{\hat{a}_6}{1+ip\sqrt{\frac{\hat{a}_5}{\hat{a}_6}}} \quad \rightarrow CC_{12} = \rho a_6$$

(3-73)

Determining the Damping Coefficients

The parameters should be determined from experiments. To determine the appropriate model damping parameter *p*, the imaginary part of the wavenumbers derived from experimental measurements are compared with the predicted imaginary wavenumbers in an interactive manner. The procedure is explained in this section with an example. Since the elastic wave amplitude decreases with increasing distance, multiple ultrasound measurements are taken to

determine the amplitude reduction and the parameters can be determined with a least square fit as shown in Figure 3-29a.

$$\ln\big(A(x_n)\big) = \ln(C_0) - 0.5\ln(x_n) - \alpha(x_n) \quad (3\text{-}74)$$

Consider a carbon fiber reinforced plate (890 mm by 890 mm by 2.7 mm) with a layup of $[0/\pm45/90]_s$ build up from HEXCELL AS-4/NEWPORT 301 plain weave 3K tow lamina as shown in Figure 3-28. Ultrasound signals are taken with the receiver being placed at a distance range from 50.8 mm to 533 mm to the source in 25.4 mm increments. Those distances are denoted as $x = x_1, x_2, \ldots x_n$ with the associated amplitude measurement $A(x_n)$. For this problem the wave function can be expressed in the form

$$A(x_1) = \frac{C_0}{\sqrt{x_1}} e^{-\alpha x_1} \quad (3\text{-}75)$$

where α is the damping parameter and C_0 is a constant.

These measurements are also taken at excitation frequency range from 50 kHz to 250 kHz in 10 kHz increments.

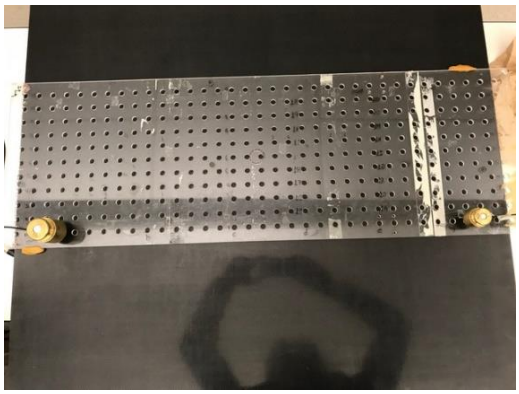

Figure 3-28 Composite plate used in the experiment for damping parameter estimation

With the measurements at various distances substituted into equation (3-74), the system of equations is rewritten into the form of $\boldsymbol{Ax} = \boldsymbol{b}$ where

$$\boldsymbol{A} = \begin{bmatrix} -x_1 & 1 \\ -x_2 & 1 \\ \vdots & \vdots \\ -x_n & 1 \end{bmatrix} \qquad \boldsymbol{x} = \begin{bmatrix} \alpha \\ \ln\,(C_0) \end{bmatrix} \qquad \boldsymbol{b} = \begin{bmatrix} \ln\big(A(x_1)\big) + 0.5\ln\,(x_1) \\ \ln\big(A(x_2)\big) + 0.5\ln\,(x_2) \\ \vdots \\ \ln\big(A(x_n)\big) + 0.5\ln\,(x_n) \end{bmatrix}$$

(3-76)

Since $\boldsymbol{A}$ is not square matrix, the system of equation is over determined and a least square solution is obtained by minimizing the second norm of the system of equations, i.e.

$$min\|\boldsymbol{Ax} - \boldsymbol{b}\|_2$$

(3-77)

The amplitude measurement $A(x_n)$ can be carried out in different ways from the measured ultrasound signals. Here, an envelope of the signal is obtained utilizing the Hilbert transform, and the peak value of the envelope is used. Care must be taken to ensure the amount of couplant, and the transducer contact remain relatively unchanged for measurements taken at various locations. For higher frequencies, it is possible to excite multiple Lamb modes. The determination of the amplitude $A(x_n)$ should be made by selecting the local peak in a time window for each Lamb mode. In order to determine the correct time window, the theoretical dispersion curves are used to determine the estimated time of arrival of the corresponding modes. This process is more robust when the theoretical dispersion curves are validated with the procedure discussed in section 2.2.4. The time window is then selected around the time of arrival with time period equal to that of the excitation signal. Figure 3-29a shows the relation between the amplitude of the A_0 mode excited at 150 kHz center frequency with the propagation distance. The calculated damping constant α is 0.1127. Figure 3-29b shows damping constants of the A_0 and S_0 modes for the remaining tested frequencies. The results conform with the observation from other researchers that the A_0 mode is more attenuative than the S_0 mode, and the damping

effect is more severe as the frequency increases. Furthermore, the results confirm than the damping effect is linearly proportional to frequency in this frequency range.

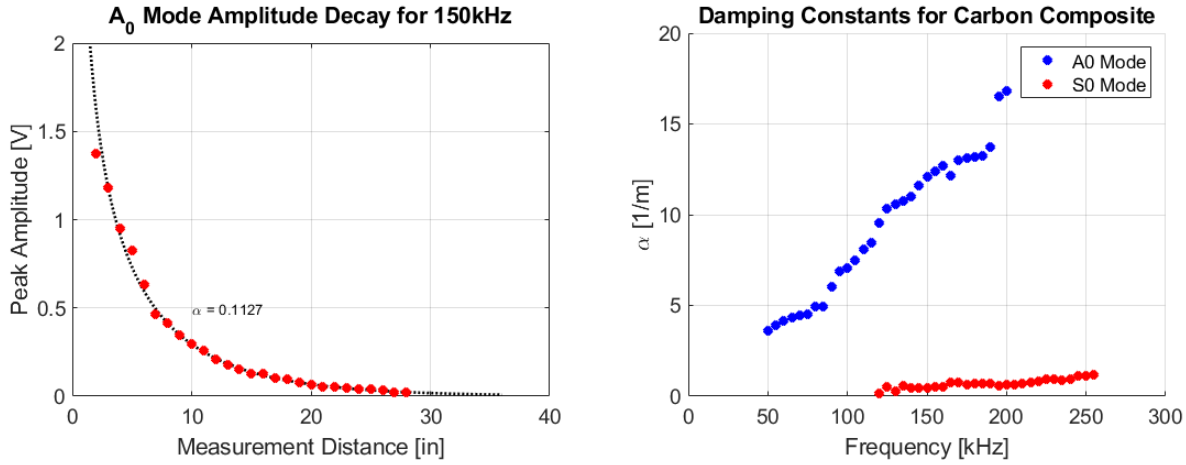

Figure 3-29 (a) Example of the A_0 mode amplitude decay for 150kHz center frequency, (b) damping constant α as a function of frequency for A_0 and S_0 mode

The next step is to develop a calibrated numerical model to simulate the elastic wave propagation with material attenuation. Since the layup is balance and symmetric, the WFE model used to calculate the theoretical dispersion curves is modeled as a transversely isotropic plate with the homogenized elastic properties as shown in Table 3-1.

Table 3-1 Effective Properties when composite plate is Homogenized into One Layer (ρ = 1570 kg/m^3)

E_{11}[GPa]	E_{33}[GPa]	G_{13}[GPa]	ν_{12}	ν_{13}
40.0	8.20	2.60	0.30	0.29

In order to determine the damping parameter p for the model, a single experimental damping coefficient α is chosen as an initial guess. In this case, the experimental value of α for the A_0 mode is 0.1127 for 150kHz is chosen, and by changing the model parameter p iteratively such that the imaginary wavenumber, k_I for the A_0 mode matches with sufficient agreement with that α value, that p value becomes the calibrated model damping parameter. It is determined that p = 0.035 gives the best match to the experimental damping parameter α. With this p value, the WFE and the GL models' complex stiffness matrices are calculated using

equation (3-71) and (3-73). For reference, the real and the complex stiffness matrices, denoted as $\boldsymbol{C}$ and $\boldsymbol{CC}$, respectively, in gigapascal, are presented in (3-78). The changes in the real part of the stiffness values are in the 1/100th , and the imaginary parts of the stiffness constants are about 3 orders of magnitude smaller than the real parts.

$$\boldsymbol{C} = \begin{bmatrix} 45.44 & 14.67 & 3.57 & 0 & 0 & 0 \\ & 45.44 & 3.57 & 0 & 0 & 0 \\ & & 8.62 & 0 & 0 & 0 \\ & & & 2.60 & 0 & 0 \\ & & & & 2.60 & 0 \\ & & sym & & & 15.38 \end{bmatrix}$$

$$\boldsymbol{CC} = \begin{bmatrix} 45.43 - 0.38i & 14.66 - 0.22i & 3.57 - 0.05i & 0 & 0 & 0 \\ & 45.43 - 0.38i & 3.57 - 0.05i & 0 & 0 & 0 \\ & & 8.62 - 0.16i & 0 & 0 & 0 \\ & & & 2.59 - 0.09i & 0 & 0 \\ & & & & 2.59 - 0.09i & 0 \\ & & sym & & & 15.38 - 0.22i \end{bmatrix}$$

(3-78)

Figure 3-30a shows the comparison between the imaginary part of the wavenumber calculated by WFE with element size of 20 µm by 25 µm, and the damping coefficient α calculated from the amplitude reduction in the signals.

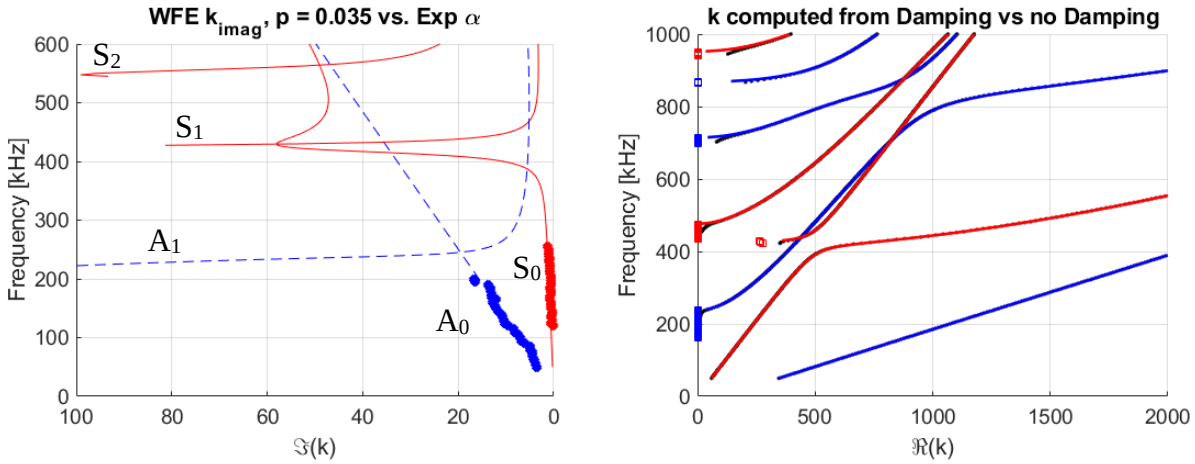

Figure 3-30 (a) Comparing experimental damping coefficient α (dots) with the imaginary part of the theoretical wavenumber (lines), (b) Wavenumber evaluated from WFE model without material attenuation (solid red/blue line), vs. with damping using p = 0.035 (black dot)

In spite of the fact that only the A_0 mode's damping coefficient α at 150kHz is used to calibrate the theoretical damping parameter p, the imaginary wavenumbers for both the S_0 mode and A_0 mode agree well with the experimentally derived wavenumbers. It is worth mentioning that, near the cutoff frequencies, the wavenumbers for the higher modes generally have larger imaginary parts even though the real parts remain largely unchanged when compared to the undamped model. This implies that the imaginary part of the wavenumber is critical to suppress the resonance behavior as discussed earlier. Moreover, Figure 3-30b shows that the real part of the wavenumber has insignificant difference in the damped and undamped models. Thus, by comparing the experimentally measured group velocity and the WFE predicted group velocity, the full material model in WFE can be validated experimentally. Figure 3-31 shows the dispersion curves calculated with the homogenized effective material properties listed in Table 3-1 and the group velocity measured from the experiment. The two results agree well thus validating the real elastic properties.

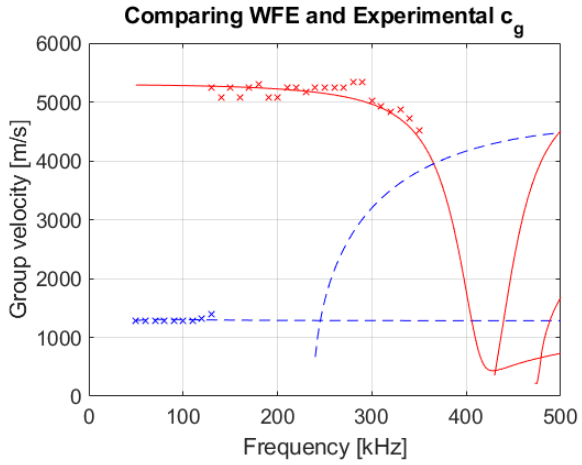

Figure 3-31Comparison between experimental group velocity (crosses) and WFE group velocity

Remarks on the Displacement Prediction using Material Attenuation

As pointed out in the previous section, the use of material damping is essential to suppress resonance in model predictions. A discussion is presented here to illustrate the changes

to displacement prediction with and without the use of damping. Consider the transversely isotropic model of the composite plate discussed in the previous section with the same damping parameter p =0.035. A GL model is used to simulate a surface mounted transducer exciting elastic wave with an 8 mm wide uniform normal load of 1 MPa magnitude applied on the top surface, and the results with and without the use of damping are compared. Since the cutoff frequencies are the resonance frequencies of the plate, the displacements are calculated for excitation frequencies that are in one case close to the first cutoff frequency at 250 kHz while the other case is below the first cutoff frequency at 175 kHz. The time dependence of the input signal is shown in Figure 3-32.

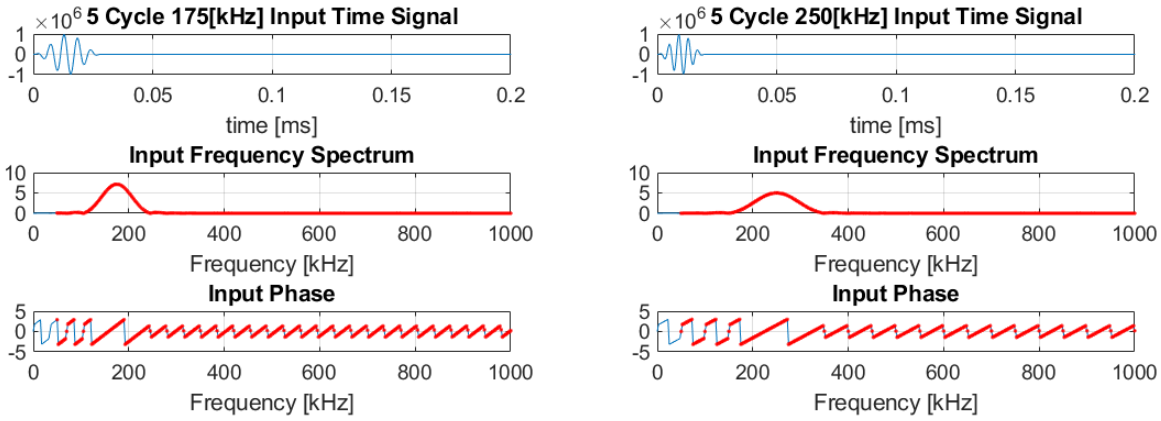

Figure 3-32 Hann windowed sine burst of 5 cycle is used for excitation (left) with center frequency at 175kHz below the first cutoff frequency (right) at 250kHz which is close to the first cut off frequency

Figure 3-33 shows the vertical displacement for the damped and the undamped models on the top surface 200 mm from the source. Comparing the spectra in (a) and (b) for the undamped and damped models, the resonance for the S_1 mode causes the peak value to surpass the main excitation, whereas the damped model has no "spikes" in the spectrum. It can be seen from Figure 3-33c, that "spike" introduces an oscillation in the waveform for all time, which suggests that resonance is occurring in which motion is present everywhere in the plate continuously. Near the cutoff frequencies, the condition number for the matrix inverse for the system of

equations in (3-17) increases, indicating that the dynamic stiffness matrix is close to singular. By introducing damping, the modal functions would have some complex parts such that the matrix determinant is not close to zero. Figure 3-33d shows that not only there is no resonance in the damped model, the faster traveling dispersive S_0 packet has a larger amplitude that the slower traveling A_0 packet as suggested by the higher damping coefficient for the A modes than for the S modes. The use of complex moduli damping model is essential to capture the relative amplitude between different wave modes for an attenuative material. Figure 3-34 confirms that close to the source at 30 mm, the damped and undamped solutions have similar A_0 to S_0 amplitude ratios in spite the resonance.

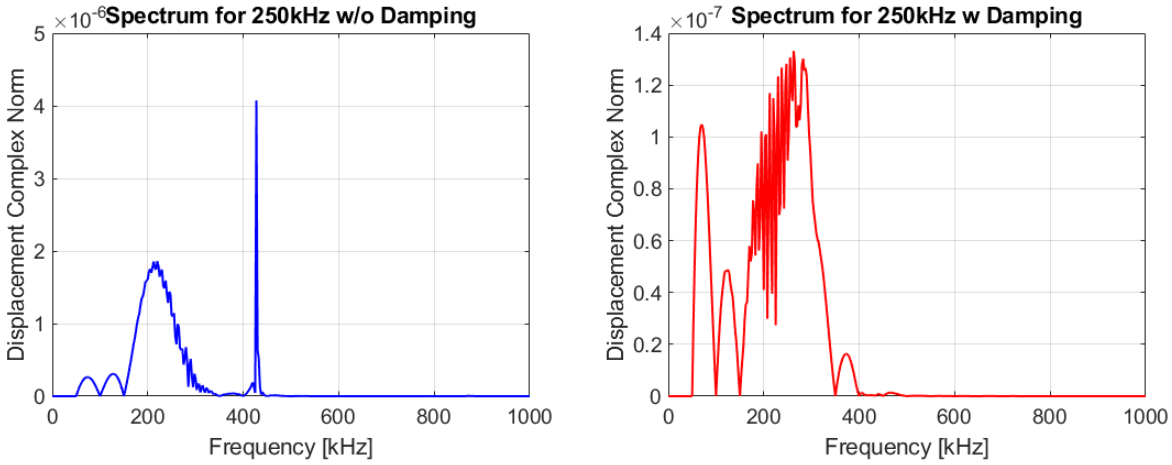

(a) Undamped model spectrum

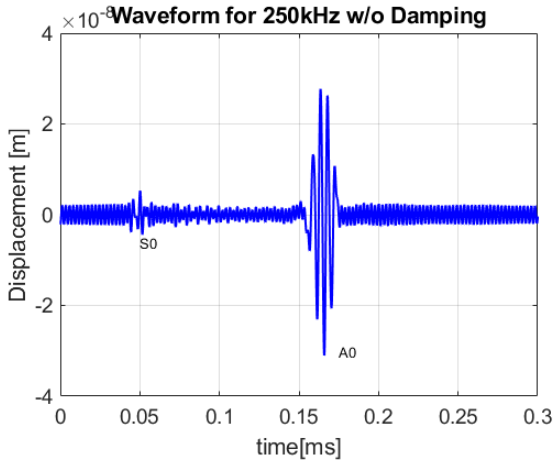

(b) Damped model spectrum

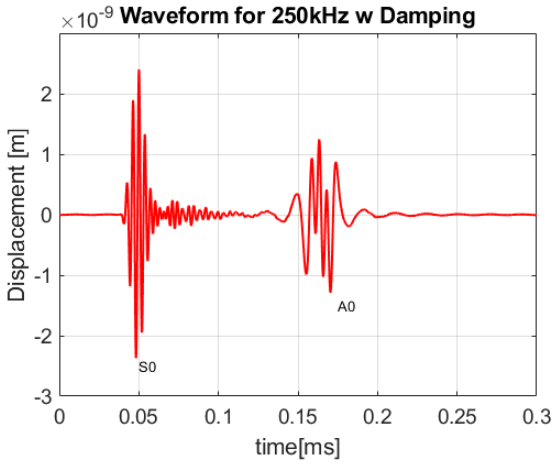

(c) Undamped model-vertical displacement

(d) Damped model-vertical displacement

Figure 3-33 Displacement results for 250kHz excitation for the resonance prone case, measured at 200mm to the right of the source on the top surface

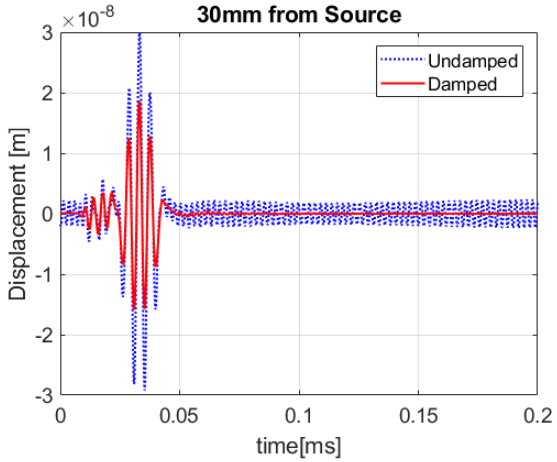

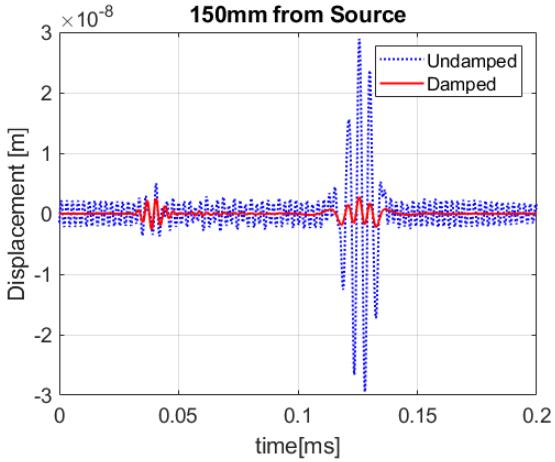

Figure 3-34 Top surface vertical displacement comparison between the damped and undamped model (a) 30 mm away from source, (b) 150 mm away from source

To confirm that the undamped model does not produce resonance when the excitation frequency is relatively far from the cutoff frequency, an input with 175 kHz center frequency is used and the displacement predictions are presented in Figure 3-35.

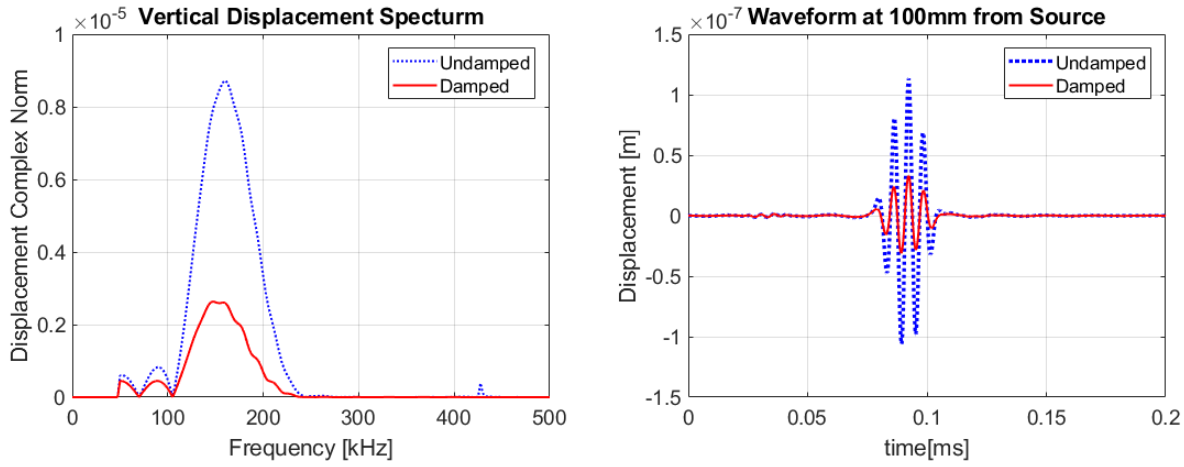

Figure 3-35 Top surface vertical displacement comparison between the damped and undamped model measured at 100mm from the source, using a 175kHz input (a) frequency spectrum, (b) waveform

Unlike the result from 250 kHz excitation, the "spike" near the cutoff frequency of S_1 around 425 kHz is not influential due to a lower frequency of excitation. Therefore, the time waveforms have similar shapes in the damped and undamped models, and the same time of arrival for the excited Lamb modes. In such instances, the undamped model is sufficient to predict the source response.

3.5 Global Local Method Verification and Validation

3.5.1 Validation of the Source Problem Against Analytical Solution

In this section, the GL modeling of the source problem is validated against analytical solution. Two problems, one with a linearly varying surface load on a single layer plate, and the other one with a uniform load on a multilayer plate, are studied.

Single Layer Plate Subjected to Dynamic Surface Load using Wavenumber Integral Approach

Consider the problem sketched of a plate with thickness $2H$ = 4 mm in Figure 3-36, where the normal load applied on a region with width equals to $2a$ varying linearly with peak intensity p_0.

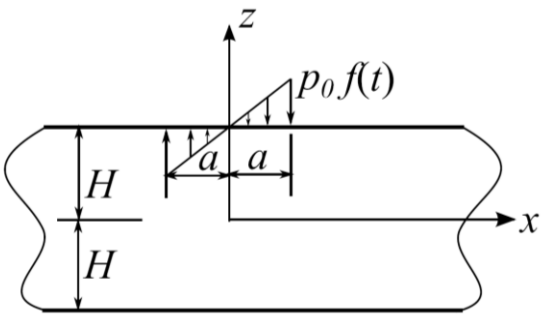

Figure 3-36 Sketch of the rocking load problem

The analytical solution is obtained by evaluating the wavenumber integral using residue theorem [29], and a brief review is given here. Assuming the plate is isotropic, perfectly elastic and in a state of plane strain, the displacements $u_i(x,z,t)$ and the stresses $\sigma_{ij}(x,z,t)$ are expressed using Fourier time transforms:

$$u_i(x,z,t) = \frac{1}{\pi} real\left(\int_0^\infty \bar{u}(x,z,\omega)e^{i\omega t}\,d\omega\right)$$

$$\sigma_{ij}(x,z,t) = \frac{1}{\pi} real\left(\int_0^\infty \bar{\sigma}_{ij}(x,z,\omega)e^{i\omega t}\,d\omega\right)$$

(3-79)

where $i,j = x,z$ and $\bar{u}$ and $\bar{\sigma}_{ij}$are the Fourier time transform of the displacements and stresses. Introducing another Fourier transform with respect to *x*, the frequency-wavenumber domain solution is in the form

$$\bar{u}_i(x,z,\omega) = \frac{1}{2\pi}\int_{-\infty}^{\infty} \hat{u}_i(k,z,\omega)e^{ikx}\,dk$$

$$\bar{\sigma}_{ij}(x,z,\omega) = \frac{1}{2\pi}\int_{-\infty}^{\infty} \hat{\sigma}_{ij}(k,z,\omega)e^{ikx}\,dk$$

(3-80)

Equation (3-80) is known as the wavenumber integral with the integration variable $k = \frac{\omega}{c}$ along the *x* direction. The double-transformed displacements $\hat{u}_i$ and stresses $\hat{\sigma}_{ij}$ satisfy a system of

ordinary differential equations (ODEs) in z, derived from the elastodynamic equations of motion. Appropriate boundary conditions must accompany the ODEs to solve the equations. The applied load $p_0 f(t)$ is transformed into the frequency-wavenumber domain as $\hat{P}_0(k,\omega)$. For the linear varying load,

$$\bar{P}_0(x,\omega) = \int_{-\infty}^{\infty} \frac{p_0 x}{a} f(t) e^{i\omega t} dt \qquad |x| \le a \tag{3-81}$$

$$\hat{P}_0(k,\omega) = \int_{-\infty}^{\infty} \bar{P}_0(x,\omega) e^{-ikx} dx = \int_0^{\infty} \left[\int_{-a}^{a} \frac{p_0 x}{a} e^{-ikx} dx \right] f(t) e^{i\omega t} dt$$

$$= \int_0^{\infty} \frac{2ip_0}{k} \left[\cos(ka) - \frac{\sin(ka)}{ka} \right] f(t) e^{i\omega t} dt \tag{3-82}$$

The solution to the ODEs in the frequency-wavenumber domain with the appropriate boundary conditions in the frequency-wavenumber domain is listed below [29]. For the antisymmetric mode,

$$\hat{u}_x(k,z,\omega) = -\frac{ik\hat{P}_0(k,\omega)}{2\mu R_a(k,\omega)} [(2k^2 - k_2^2)\sinh(\eta_1 z)\cosh(\eta_2 H) - 2\eta_1\eta_2 \cosh(\eta_1 H)\sinh(\eta_2 z)]$$

$$\hat{u}_z(k,z,\omega) = -\frac{\eta_1\hat{P}_0(k,\omega)}{2\mu R_a(k,\omega)} [(2k^2 - k_2^2)\cosh(\eta_1 z)\cosh(\eta_2 H) - 2k^2 \cosh(\eta_1 H)\cosh(\eta_2 z)] \tag{3-83}$$

where $R_a(k,\omega) = (2k^2 - k_2^2)^2 \sinh(\eta_1 H)\cosh(\eta_2 H) - 4k^2\eta_1\eta_2 \cosh(\eta_1 H)\sinh(\eta_2 H)$ which can be seen to be the right-hand side of the dispersion equation for the antisymmetric mode.

For the symmetric mode,

$$\hat{u}_x(k,z,\omega) = -\frac{ik\hat{P}_0(k,\omega)}{2\mu R_s(k,\omega)} [(2k^2 - k_2^2)\cosh(\eta_1 z)\sinh(\eta_2 H) - 2\eta_1\eta_2 \sinh(\eta_1 H)\cosh(\eta_2 z)]$$

$$\hat{u}_z(k,z,\omega) = -\frac{\eta_1 \hat{P}_0(k,\omega)}{2\mu R_s(k,\omega)}[(2k^2 - k_2^2)\sinh(\eta_1 z)\sinh(\eta_2 H) - 2k^2 \sinh(\eta_1 H)\sinh(\eta_2 z)]$$

(3-84)

where $R_s(k,\omega) = (2k^2 - k_2^2)^2 \cosh(\eta_1 H)\sinh(\eta_2 H) - 4k^2\eta_1\eta_2 \sinh(\eta_1 H)\cosh(\eta_2 H)$ which can be seen to be the right-hand side of the dispersion equation for the symmetric mode.

To evaluate the wavenumber integral as presented in equation (3-80) with the integrand (3-83) and (3-84), it is recognized that both the symmetric and antisymmetric modes have the same form:

$$\bar{g}(x,z,\omega) = \frac{\bar{P}_0(\omega)}{2\pi}\int_{-\infty}^{\infty} \frac{\hat{h}(k,z,\omega)}{R(k,\omega)} e^{ikx} dk$$

(3-85)

where $\hat{h}(k,z,\omega)$ is the part of the equation (3-83), (3-84) with the load $\hat{P}_0$ and R factored out. The denominator R=0 is the dispersion equation and it has a finite number of real roots and an infinite number of complex roots at a given frequency ω thus presenting singularities in the integral. In order to evaluate the integral, contour integration on the complex plane with the path C^+ shown in Figure 3-37 is used [34].

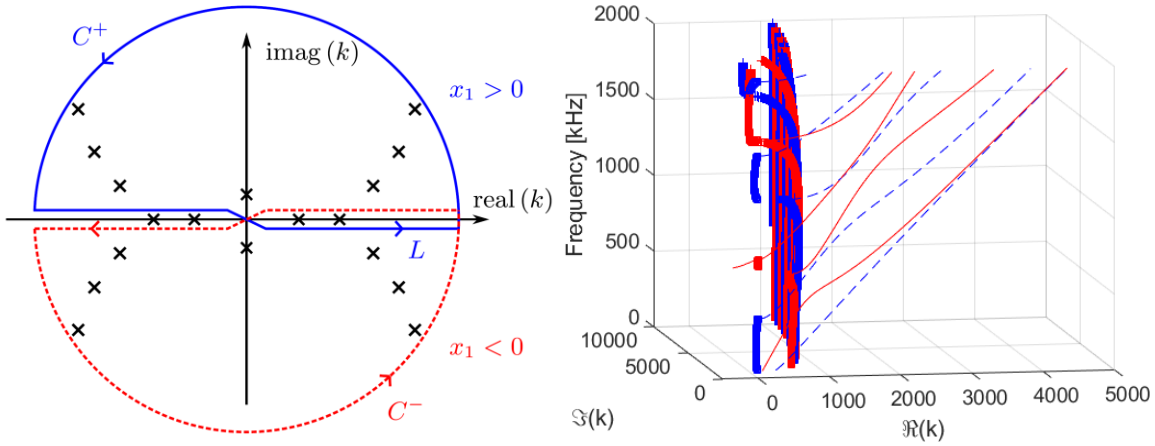

Figure 3-37 (a) Illustration of the path of contour integration and the roots of the dispersion equation, (b) the wavenumber for a 4[mm] thick aluminum plate

The path is chosen such that only the solution for the outgoing wave is retained. Since the integrands only have simple poles, and there are no branch points in the complex *k*-plane, the integral can be evaluated as the sum of the residues at the poles using Cauchy's theorem as shown below

$$\bar{g}(x,z,\omega) = \frac{\bar{P}_0(\omega)2\pi i}{2\pi}\sum_{n=1}^{\infty}\frac{\hat{h}(k_n,z,\omega)}{R'(k_n,\omega)}e^{ik_n x} \tag{3-86}$$

where $R'(k_n,\omega)$ is the derivative of $R(k,\omega)$ with respect to *k* evaluated at the root of the dispersion equation k_n, $R' = \frac{\partial R}{\partial k}\Big|_{k=k_n}$. The expressions for the vertical displacements in frequency domain for the antisymmetric and symmetric modes are given here; the remaining expressions for the displacements, stresses and $R^{'}$ are listed in appendix, section 3.2.

Anti-symmetric mode:

$$\bar{u}_z(\omega,x,z) = \sum_{k_a} -\frac{\eta_{1a}\bar{P}(k_a,\omega)}{2\mu R_a'(k_a)}[(2k_a^2 - k_2^2)\cosh(\eta_{1a}z)\cosh(\eta_{2a}H) - 2k_a^2\cosh(\eta_{1a}H)\cosh(\eta_{2a}z)]e^{ik_a x}$$

Symmetric mode:

$$\bar{u}_z(\omega,x,z) = \sum_{k_s} -\frac{i\eta_{1s}\bar{P}(k_s,\omega)}{2\mu R_s'(k_s)}[(2k_s^2 - k_2^2)\sinh(\eta_{1s}z)\sinh(\eta_{2s}H) - 2k_s^2\sinh(\eta_{1s}H)\sinh(\eta_{2s}z)]e^{ik_s x} \tag{3-87}$$

The GL solution is compared with the analytical solution calculated from the wavenumber integral evaluation for a 4 mm thick aluminum plate (E = 68.9 GPa, ν = 0.3, ρ = 2700 kg/m^3), subjected to a load with p_0 = 1 MPa and width $2a$ = 10 mm as shown in Figure 3-38a that has a time dependency of 5-cycle 300 kHz sine with a Hann window as shown in Figure 3-38b.

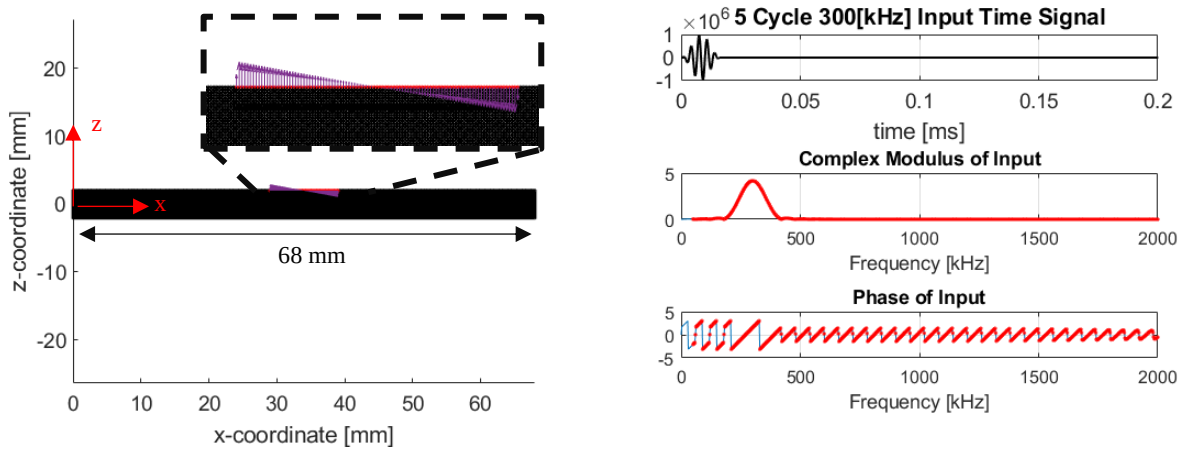

(a) (b)

Figure 3-38 (a) the geometry and the apply load of the aluminum plate, (b) the time varying input of 5 cycle Hann windowed tone burst

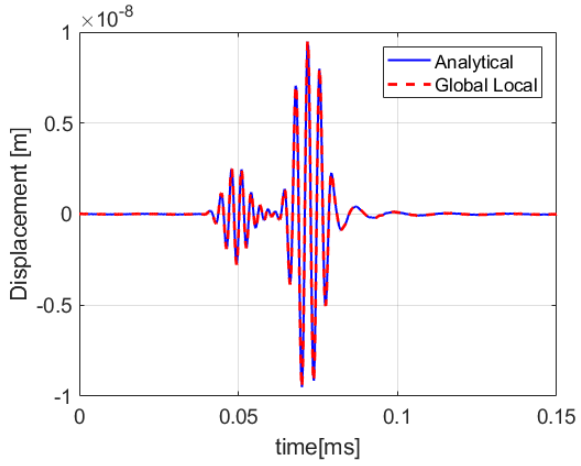

Figure 3-39 Comparing analytical solution and the GL solution for the vertical displacement at top surface, 200 mm away from the source

Layered Medium Subjected to Dynamic Surface Load using Matrix Approach

The global matrix method provides an analytical solution for the force response in a multilayered medium [70]. A brief review of the formulation is given here. In the frequency-wavenumber domain, the global matrix $\widehat{\boldsymbol{G}}$ is defined in equation (2-27) such that the system of equation is in the form

$$\widehat{\boldsymbol{G}}(k,z,\omega)\widehat{\boldsymbol{C}}(\omega) = \widehat{\boldsymbol{F}}(k,\omega)$$

(3-88)

where $\widehat{\boldsymbol{F}}(k,\omega)$ is the traction vector for every ply in the frequency-wavenumber domain. Thus, only the top surface normal traction component at the top surface is non-zero. To determine the unknown amplitude coefficients, the inverse of the global matrix is needed

$$\widehat{\boldsymbol{C}} = \widehat{\boldsymbol{G}}^{-1}\widehat{\boldsymbol{F}} \tag{3-89}$$

$$\widehat{\boldsymbol{C}} = \frac{adj(\widehat{\boldsymbol{G}})}{\det(\widehat{\boldsymbol{G}})}\widehat{\boldsymbol{F}} = \frac{\widehat{\boldsymbol{M}}\widehat{\boldsymbol{F}}}{\det(\widehat{\boldsymbol{G}})} \tag{3-90}$$

where $\widehat{\boldsymbol{M}}$ is the adjoint matrix of $\widehat{\boldsymbol{G}}$

$$\widehat{M}_{ji} = (-1)^{i+j}\det(\widehat{K}_{ij})$$

and $\widehat{\boldsymbol{K}}$ is the global matrix $\widehat{\boldsymbol{G}}$ matrix with the i^{th} row and the j^{th} column eliminated.

In a very similar fashion, the inverse Fourier transform from the frequency-wavenumber domain back to the frequency domain is carried out with the residue theorem.

$$\overline{\boldsymbol{C}}(\omega) = \frac{1}{2\pi}\int_{-\infty}^{\infty}\frac{\widehat{\boldsymbol{M}}\widehat{\boldsymbol{F}}}{\det(\widehat{\boldsymbol{G}})}dk = \frac{1}{2\pi}(2\pi i)\left(\sum_{k_n}^{\infty}\frac{\widehat{\boldsymbol{M}}\widehat{\boldsymbol{F}}}{\frac{\partial \det(\widehat{\mathbf{G}})}{\partial k}}\bigg|_{k_n}\right) \tag{3-91}$$

where k_n are the roots of the dispersion such that $\det(\widehat{\boldsymbol{G}}) = \mathbf{0}$, and $\det(\widehat{\boldsymbol{G}}) = \mathbf{0}$ is the dispersion equation (free wave response) for the layered medium. To calculate the derivative of the global matrix, the Jocobi Formula is used

$$\overline{\boldsymbol{C}}(\omega) = i\left(\sum_{k_n}^{\infty}\frac{\widehat{\boldsymbol{M}}\widehat{\boldsymbol{F}}}{\mathrm{tr}(\widehat{\boldsymbol{M}}\dot{\widehat{\boldsymbol{G}}})}\bigg|_{k_n}\right) \tag{3-92}$$

where tr() is the trace of matrix product($\widehat{\boldsymbol{M}}\dot{\widehat{\boldsymbol{G}}}$), and $\dot{\widehat{\boldsymbol{G}}}$ is the derivative of each of the elements in $\widehat{\boldsymbol{G}}$ with respect to k_n. Finally, the displacement and stress vectors for the m^{th} ply (as defined in section 2.1.2) in frequency domain is:

$$\overline{\boldsymbol{U}}(m) = \begin{Bmatrix} U_x^m \\ U_z^m \\ S_{xz}^m \\ S_{zz}^m \end{Bmatrix} = iQ(m)E(z,m)\,\{\overline{\boldsymbol{C}}(m)\} \tag{3-93}$$

where $\{\overline{\boldsymbol{C}}(m)\}$ is a sub-vector of $\overline{\boldsymbol{C}}(\omega)$ for the m^{th} ply.

As a benchmark problem, the predicted GL source response predicted is compared to the one obtained from the GMM. Because of the isotropic layer restriction in the current global matrix implementation, the structure is a 4-layer aluminum-titanium laminate with a thickness of 1 mm for each layer, which is used in the previous chapter in section 2.2.3. The material properties of the layers are given in Table 2-1. The source is a uniform traction load of 1MPa normal to the surface, with a width of 10 mm and the time dependency is a tone burst of 250 kHz center frequency. Since the 5 cycle Hann windowed sine excitation will be used multiple times in the remainder of this paper, it will be referred as the tone burst excitation. The FE region is 65 mm wide (Figure 3-40) with element size of 100 μm by 100 μm.

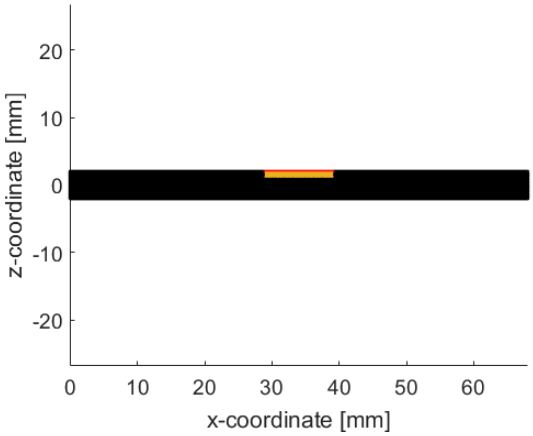

Figure 3-40. Uniform surface load on the Al-Ti laminate, and the black region indicate the size of the "local" region for the global local method

In both methods, the displacement is computed in the frequency domain, from 50 kHz to 2 MHz at every 2.5 kHz step. Since most signal processing hardware for physical experiments would have a high pass filter, the solution at lower frequencies is not needed. The time domain waveform is then obtained from IFFT. The displacement from both methods are compared in Figure 3-41 where the frequency spectrum and the time domain waveforms of the displacement at the top surface at 150 mm to the right of the surface load are shown.

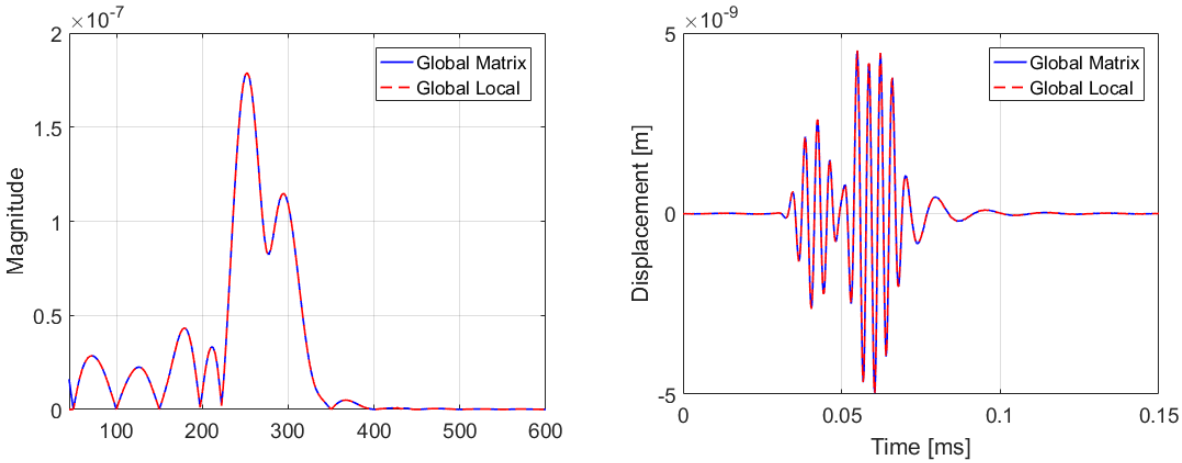

Figure 3-41. Vertical displacement on the top surface at 150mm to the right of the source. (a) frequency spectrum (b) time domain waveform

The two solutions give almost identical displacement prediction consisting of both S_0 and A_0 modes. The frequency spectrum also indicates serval frequencies that could not be excited with this specific load and plate configurations.

Experimental Validation of Source Modeling

In the previous section, the source transducer is modeled as a uniform distributed load, which is often not accurate enough to predict the waveform features as observed in experiments. The physical experiment to measure the ultrasound waveform is conducted on a hybrid titanium/carbon reinforced polymer specimen as shown in Figure 3-42. The plate has a stacking sequence of [0/45/Ti/-45/90]s (10 plies), where 0 degree is also the propagation direction. All composite plies (Woven fabric, HexForce 433) are 0.325 mm thick and the titanium plies (CP-Grade 2) are 0.5 mm thick with the material properties as shown in Table 3-2.

Table 3-2 Properties used in the FML models. $_{11}$ direction is along fiber direction

	E_{11} [GPa]	E_{33} [GPa]	G_{13} [GPa]	ν_{12}	ν_{23}	Density [kg/m^3]	Thickness [mm]
CFRP	77	13.8	5.1	0.06	0.37	1526.1	0.325
Ti	105			0.37		4510	0.5

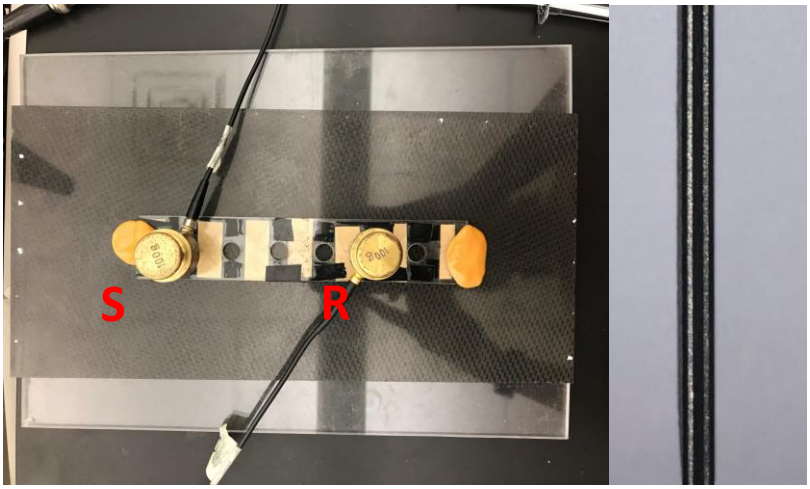

Figure 3-42 Experimental setup for measuring the waveforms on the FML specimen

Instead of modeling the electro-mechanical behavior of the transducer itself, two simple modifications can be used to improve the source response prediction and will be used for further damage detection studies. The first modification is to use a Gaussian windowed source distribution instead of the uniformly distributed surface source to model a more realistic transducer-plate contact condition. Since the source distribution is created numerically, any arbitrary traction distribution can be easily modeled with standard FE nodal force vectors. Thus, a large variety of transducers can be modelled without any modifications to the global-local theory or code implementation. The effects of using the Gaussian distribution is shown in Figure 3-43, in which the proportion and the waveform shape of the generated A_0 and S_0 modes are modified. Uniform loading would tend to generate an increased proportion of S_0 mode which is not observed in experiments when compared to a normal load with a narrower Gaussian window.

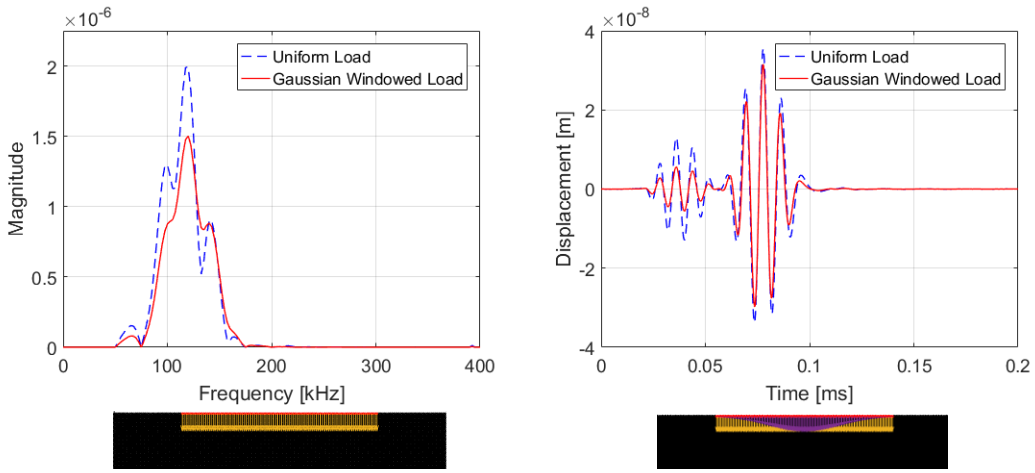

Figure 3-43 Comparing displacements at top surface, 100mm from source. Uniform vs. Gaussian windowed normal load (a) frequency spectrum (b) Waveform

The second modification is to use a face-to-face transducer response as the input to the GL model. The "face-to-face" response is the recorded signal when the source and receiving transducers are in direct contact, driven by the desired excitation (e.g. tone burst excitation at 125 kHz center frequency). The face-to-face response is subjected to Fourier transform and used as the GL model input term $\boldsymbol{f_{app}}$ in equation (3-3). This modification can capture the electrical

response of the measurement system and the vibrational behavior of that particular transducer pair. Figure 3-44a shows the desired source and the modified source obtained from the "face-to-face" response. Figure 3-44b shows the model prediction of the displacement waveforms between the two input sources. The face-to-face response has a small-time delay compared to the desired source because of the transducer face plate and the oscilloscope triggering time. The response also captures the extended tail that is due to ringing of the transducers.

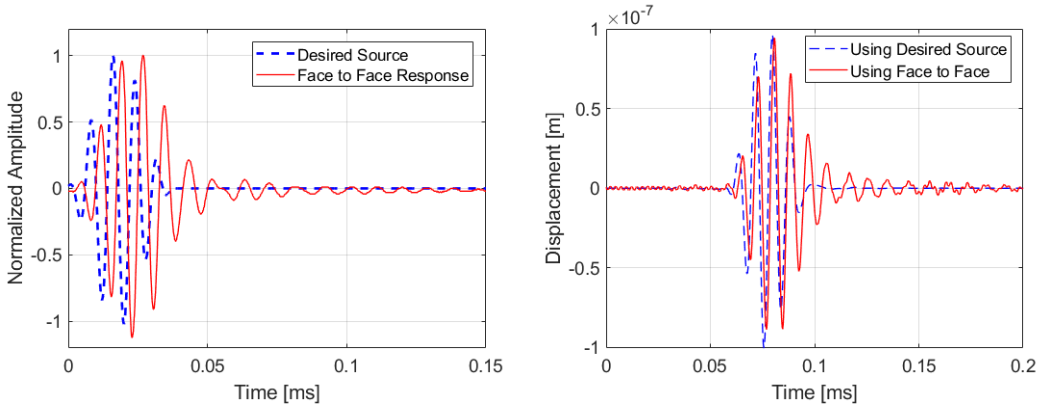

Figure 3-44 (a) The desired 5 cycle Hann windowed sine at 125 kHz center frequency source vs. the transducers' face-to-face response. (b) The GL displacement prediction under the desired driving source and the one with the modified source

Finally, using these two modifications, the predicted normalized waveform is compared with that obtained in the experiment (Figure 3-45). The GL prediction slightly underestimates the amplitude of the S_0 mode. For the A_0 main packet, the waveform prediction is significantly improved. Comparing the model prediction using the modified and the desired excitations, the former waveform matches more closely with the experimental measurement except the signal at the tail which is cause by the reflections from the edges.

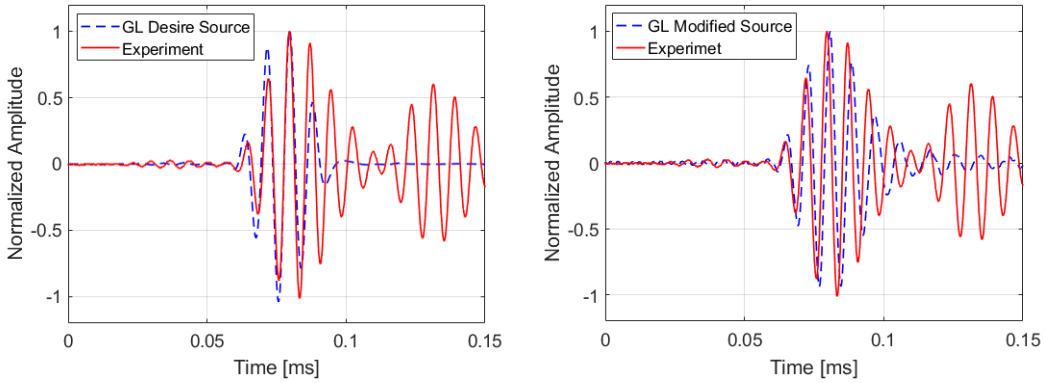

Figure 3-45 Measured waveform with the GL prediction using (a) the Hann windowed 5 cycle of sine at 125 kHz center frequency excitation (b) with the modified source which includes the system response. With the modified source, the GL result prediction agrees more closely with the measured waveform. The later arrivals are due to edge reflection

3.5.2 Validation of Combined Problem with ABAQUS

For Lamb wave problems, the analytical solution is often separated into the source and the defect problems, and it is not straightforward to combine them. Therefore, the more general transient FE method is used to validate the combined problem. The design of the FE problem is made with care such that a large enough portion of the plate for a short enough simulation time to mimic the elastic wave propagation in a large structure in which boundary reflections are of negligible influence. Two FE validations are presented in this section. The first problem is for an isotropic plate with a step increase in thickness, and the second one is a delamination within a hybrid composite.

Wave Scattering by a Step in an Aluminum Plate

The geometry of the FE problem is shown in Figure 3-46 which depicts a 500 mm section of the aluminum plate (E = 68.9 GPa, ν = 0.3, ρ = 2700 kg/m^3) subjected to a symmetric and uniform normal load of 1 MPa magnitude, at 200 mm to the left of the step that increases from 3.175 mm to 4.7625 mm. The distributed load is 8 mm wide, and due to the symmetric nature of the source and only the right propagating wave of interest, the right-half of the problem is

modeled. A symmetric boundary condition is used on the left end to ensure only vertical displacement is possible, and the bottom right node is pinned to avoid rigid body motions.

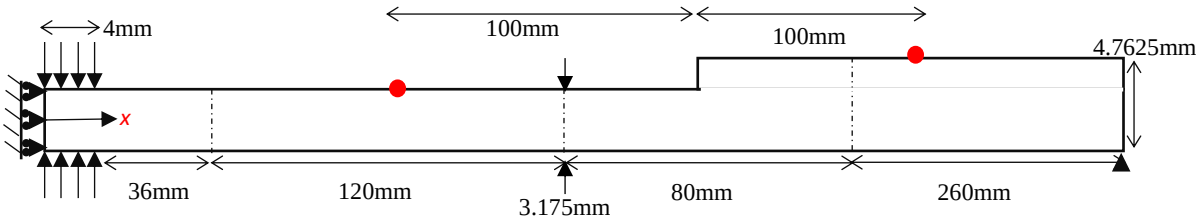

Figure 3-46 Geometry of the FE model of the step problem (not to scale). The rollers and the pin indicate the boundary conditions used for the FE model. The red dots indicate where the waveform is reported. The region bounded by the dashed line indicates where the 80 mm long local regions of the GL model.

The time domain FE model has a total simulation period of 0.175 ms to ensure no edge reflection to return to the displacement calculating points that are 100 mm before and after the step. Models with time steps varying from 0.5μs, 0.35μs, 0.25μs to 0.175μs are computed to ensure that the effect of numerical dispersion is negligible. As shown in Figure 3-47, the solution computed from 0.25μs and 0.175μs has negligible differences indicating time convergence. When time convergence is not achieved such as the case of 0.5μs step time, the predicted wave packets have a delayed arrival time, and a longer time period, hence it is described as numerical dispersion.

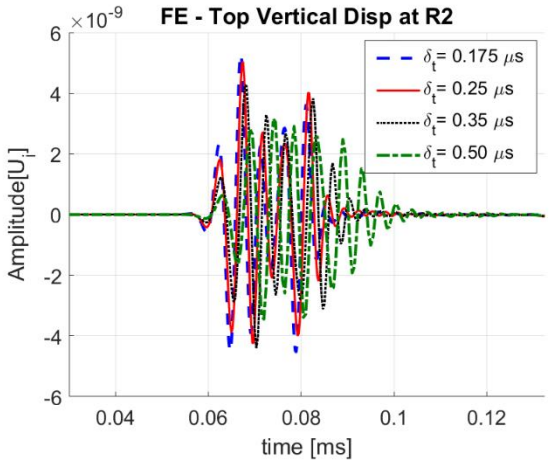

Figure 3-47 Vertical displacement at the top surface at 100 mm to the right of the step computed with different time steps using transient FEM. Convergence is achieved with 0.25μs

The 4-node plane strain elements that are used are 160μm by 160μm in size to ensure a large wavelength to element size ratio. The symmetric load is chosen to simplify the analysis by

generating predominately S_0 mode since the excitation (3 cycle Hann windowed sine burst) has a 200 kHz center frequency which is well below the cutoff frequency of either plate thickness. The group velocity presented in Figure 3-48 is used confirm whether the scattered wave is antisymmetric or symmetric with the appropriate time of arrival.

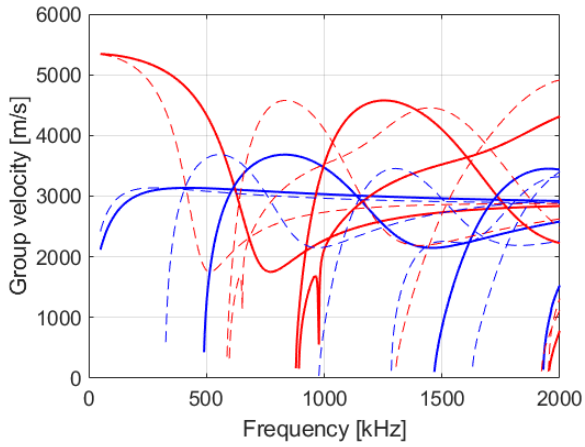

Figure 3-48 The group velocity for 3.175 mm thick (solid line) and 4.7625 mm thick (dash line) aluminum plate, where red lines are symmetric modes and blue lines are antisymmetric modes.

Figure 3-49 shows the displacement comparison between the ABAQUS transient solution and the GL solution for the reflected waves (100 mm to the left of the step) and the transmitted waves (100 mm to the right of step).

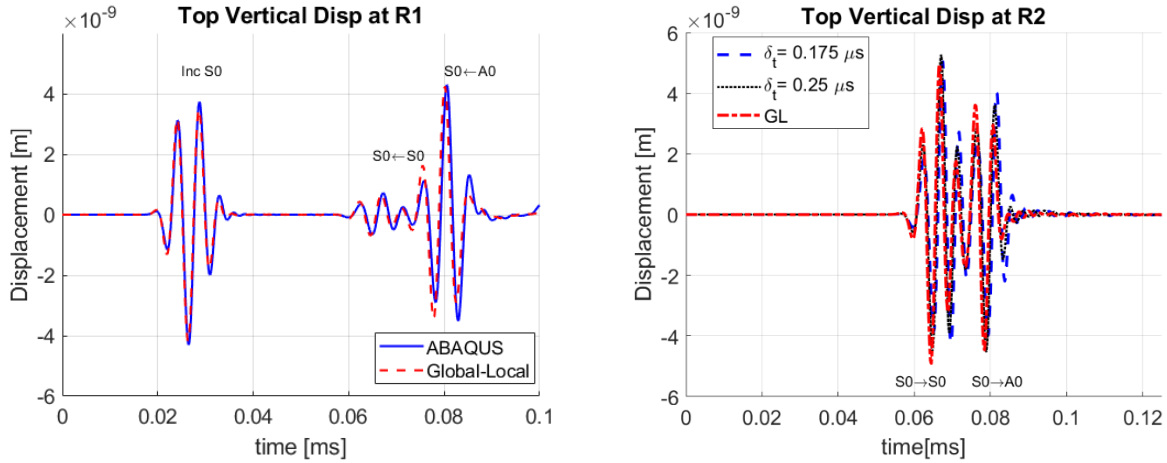

Figure 3-49 Top surface vertical displacement comparison between ABAQUS FE solution and the GL solution (a) 100 mm to the left of the step and (b) 100 mm to the right of the step

The top surface vertical displacement is calculated because that is the dominating displacement component that be measured by a surface mounted transducer. The left probing point shows the relatively non-dispersive S_0 mode that arrives shortly after 0.02 ms. The reflected waves consist on the faster returning S_0 mode ahead of the reflected A_0 mode arriving around 0.07 ms and 0.08 ms respectively. It is somewhat surprising that the reflected A_0 amplitude is larger than that of the reflected S_0 mode. For the transmitted waves, the scattered two modes have similar amplitudes and the group velocities have sufficient difference such that they are separated at that distance.

Wave Scattering in Hybrid Composites due to a Disbond

Both GLM and the conventional implicit time-stepping FE methods (ABAQUS) are used to model a disbond at the metal composite interface in the FML. Figure 3-50 shows the problem of the uniformly distributed sources, 8 mm wide with a tone burst excitation at 200 kHz center frequency, generating waves that interact with a 10 mm long disbond at a distance of 175 mm from the center of the source.

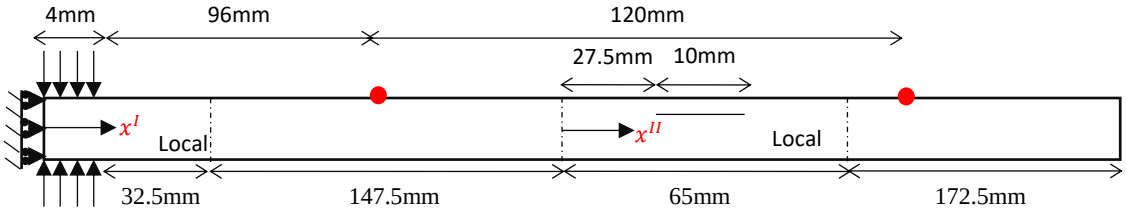

Figure 3-50. Sketch of the coupled problem. Only the right-half of the problem is shown. The dashed lines indicate the FE region in the Global Local model. The red dots indicate where the displacement is evaluated

For the GLM, each "local" region is 65 mm wide, which is 18 times the plate thickness. Both models have a mesh size of around 71 μm. Note that, for the conventional FE model, only the right half of the plate is modeled with the use of symmetric boundary conditions at the left end. This model has a total length of 385 mm in x-direction. A "crack seam," which allows the

separation of nodes is created to represent the disbond between the first 45/Ti interface in the upper half of the laminate. The faces of the disbond are assumed to be traction free. The time stepping FE model has a total simulation period of 0.1 ms using 1000 time-steps (with a time step of 0.1 μs). Figure 3-51 shows the vertical displacement from the conventional FE and GLM at 100 mm and 220 mm to the right of the source. The symmetric load generates only S_0 mode. At the left side of the disbond (at 100 mm), the reflected wave arrives at 0.06 ms, and at the right side of the disbond (at 220 mm), the scattered wave follows the main S_0 packet closely. The time snapshots of the displacement field (Figure 3-51c, d) show the disbond splits the incident wave into the waves above and below the disbond. Subsequently, part of the incident wave is reflected back and forth between the leading and trailing edges of the disbond creating the coda wave.

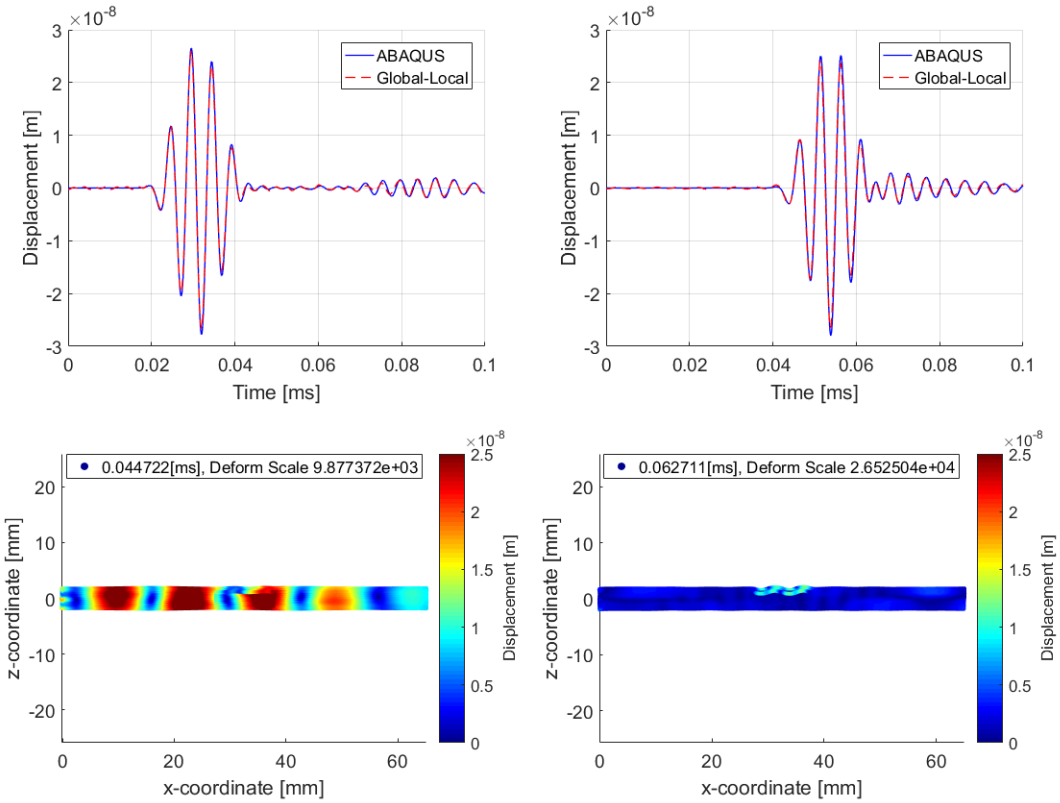

Figure 3-51. Comparison between the total vertical displacements obtained using GLM and FEM at (a) 100 mm, (b) 220 mm, to the right of the source, (c) Resultant displacement field in the vicinity of the delamination at 44.72 μs and (d) at 62.71 μs

Finally, it is worth mentioning that the time taken to calculate the transient FE solution is about 3 hours, while the GL solution requires around 10 minutes on the same desktop computer. The use of the GLM can significantly reduce computational time in the following ways. For a large plate, the source and defect regions are small. The rest of the global regions are represented by global functions thus eliminating the need for a large mesh. This is especially beneficial for FML because of the small through thickness mesh size requirement to model the different ply materials. Increasing the number of elements in thickness does not require a large increase in mesh size in the propagation direction. Furthermore, the frequency domain based GLM made it possible to use parallel computing directly using parallel for loop, because the solution at different frequencies are independent of each other. Finally, when the analysis involves the study of different defects, the GL solution of the source problem remains valid and can be coupled with different scattering problems without recomputing the source portion. The transient FE method would require modification to the entire model and be re-solved as a whole.

Chapter 4 Damage Characterization in Fiber Metal Laminate

The motivations of using FML in aerospace structure have been introduced in section 1.1.3 and in this chapter, a brief discussion of the different types of critical defects in FML is first given. These defects are modeled using GLM, for the purpose of determining the correlation between the ultrasound signal features and the defect characteristics. These models apply the extended GL framework developed in Chapter 3 in which the different source models are coupled with defects of various sizes in order to create a waveform library for the purpose of damage characterization. This library of waveforms is subsequently used to design damage indices to quantitatively describe the changes in the waveforms. Finally, the damage indices for serval simulated test signals with unknown defects are calculated and then compared to the defect library to illustrate a procedure to determine the nature of the unknown defects.

4.1 Mechanical Performance Considerations of Fiber Metal Laminate

The make-up of the polymer matrix composites and metal constituents, layup, ply thickness, and adhesion treatment at the metal-composite interfaces are some of the important factors in the overall mechanical performance and the nature of defects that could occur in FML. A brief review of the mechanics of FML is given here. For most design applications, the composite plies are modeled with anisotropic linear elastic material law based on classical laminate plate theory such as those given in [36] and [64] at the meso-level. A useful summary of the elastic properties of the different FML constituents is given in [68]. The meso-level approach is useful when the plate response of the laminate and the interface disbond failure is of interest. Such analysis can model part-level failure as in the case in [69]. Lind et. al. predicted

the FML failure near rivet holes of a 2-row rivet jointed specimen [69]. The meso-level analysis provides good insights into the composite ply angle designs, the linear response of the laminate and the onset of failure [70]. Beyond the linear region, composites begin to experience damage in contrast to metal that exhibit hardening behavior.

More advanced strength prediction and damage initiation criterion can be derived from the matrix crack initiation and the crack propagation energy, such as those suggested in [71]. Davila et. al. [72], and Hinton et. al [73] give good summaries of the failure (initiation) criteria for composite laminates. The Hashin criteria [74] is a popular failure criterion that takes into account the fiber and matrix tension-compression strength. This criterion assumes a quadratic interaction between the normal and shear stresses on the failure plane. Puck modifies the original Hashin criterion to include the calculation of the fracture plane to account for the transverse compression on the increase of shear strength [76]. In some instances, the stress state is 3 dimensional, for example, near a bearing hole, and a 3D damage initiation criterion is needed. Hundley et. al. analyzed the bearing strength of hybrid Ti/CFRP FML structures based on a 3D damage initiation criterion and a user defined damage model implemented in ABAQUS [77].

Beyond damage initiation, a damage evolution law is needed to describe the reduction in load carrying capability. A continuum damage model implies that the stiffness reduction, described by damage parameter(s) d_s, for the bulk materials without the need to model each defect and change in their morphology. The damage evolution law is usually derived from an energy potential. Maimi et. al. [78] [79], derived a continuum damage model that takes the longitudinal and transverse failure into account, and gave their numerical implementation. Another damage model proposed by Lapczyk et. al. [79], considers the energy dissipation from the formation of damages and this model is also being implemented in ABAQUS.

The interfacial strength is also important for the performance of FML structures. However, to quantify the inter-laminar capability is not a trivial task because asymmetric at the tested composite-metal interface, and the stress-state in each material would be complex. In addition, the interfacial strength also varies significantly on the bonding methods and curing conditions. In [80], Gan discusses the effects of interface structure on the mechanical properties of the composites. The residual stresses from bonding and curing steps make the prediction of the interface response difficult. The difference in the coefficient of thermal expansion between the composites and metal often causes buckling and disbond after cure. Fu et. al. proposed a higher order plate theory to describe the thermal stress induced buckling with interfacial slip [81]. Mechanical testing using existing composite test standards are often used to gain insights into the performance of the metal-composite interface. Lawcock et. al. conducts double-cantilever beam fracture tests, and three and four-point bending tests to characterize the interfacial fracture toughness [82]. The study compares two surface treatments to evaluate their influence on the fracture toughness of the interface. To overcome the asymmetry of the metal-composite interface, Carrillo et. al. suggests a single-cantilever beam test, in which only the bottom half is subjected to bending force and the top half is fixed to avoid out-of-plane deformations [84].

4.1.1 Design of FML Specimen

The hybrid composites of titanium and carbon fiber reinforced polymer analyzed in section 3.5 and in this chapter is designed to be representative of those being used in joining segments of launch vehicles. For such applications, the layup is designed to have a bearing failure mode. This section presents some simple models based on the classical laminate theory implemented in commercial software Helius Composites [84] to ensure that the sample design is

reasonable. The chosen FML design has lamina properties as shown in Table 4-2 and the layup is shown in Figure 4-20a. The laminate stiffness matrix calculated from classical laminate plate theory follows the convention as shown in Figure 4-1 with equation (4-1) relating the mid-plane strains and internal load. The ABD matrices are shown in the Appendix (Chapter 4).

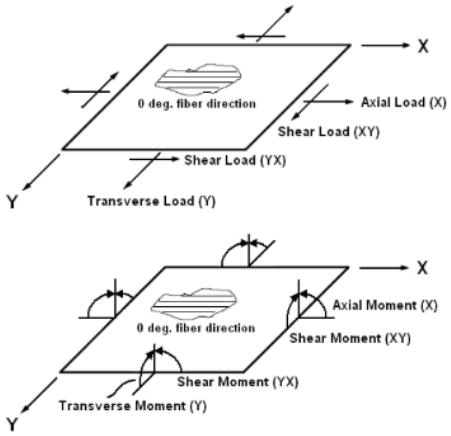

Figure 4-1 Laminate stiffness matrix sign convention

$$\begin{Bmatrix} N_{xx} \\ N_{yy} \\ N_{xy} \\ M_{xx} \\ M_{yy} \\ M_{xy} \end{Bmatrix} = \begin{bmatrix} A_{11} & A_{12} & A_{16} & B_{11} & B_{12} & B_{16} \\ A_{12} & A_{22} & A_{26} & B_{12} & B_{22} & B_{26} \\ A_{16} & A_{26} & A_{66} & B_{16} & B_{26} & B_{66} \\ B_{11} & B_{12} & B_{16} & D_{11} & D_{12} & D_{16} \\ B_{12} & B_{22} & B_{26} & D_{12} & D_{22} & D_{26} \\ B_{16} & B_{26} & B_{66} & D_{16} & D_{26} & D_{66} \end{bmatrix} \begin{Bmatrix} \varepsilon_{xx}^0 \\ \varepsilon_{yy}^0 \\ \gamma_{12}^0 \\ \kappa_{xx}^0 \\ \kappa_{yy}^0 \\ \kappa_{xy}^0 \end{Bmatrix} \tag{4-1}$$

The stress distribution for the individual plies is shown in Figure 4-2 where the laminate is subjected to a tensile load (stress) of 50 MPa in the *x* direction. The red, blue and green lines show the stress components σ_x σ_y σ_{xy} respectively, across the 10 plies.

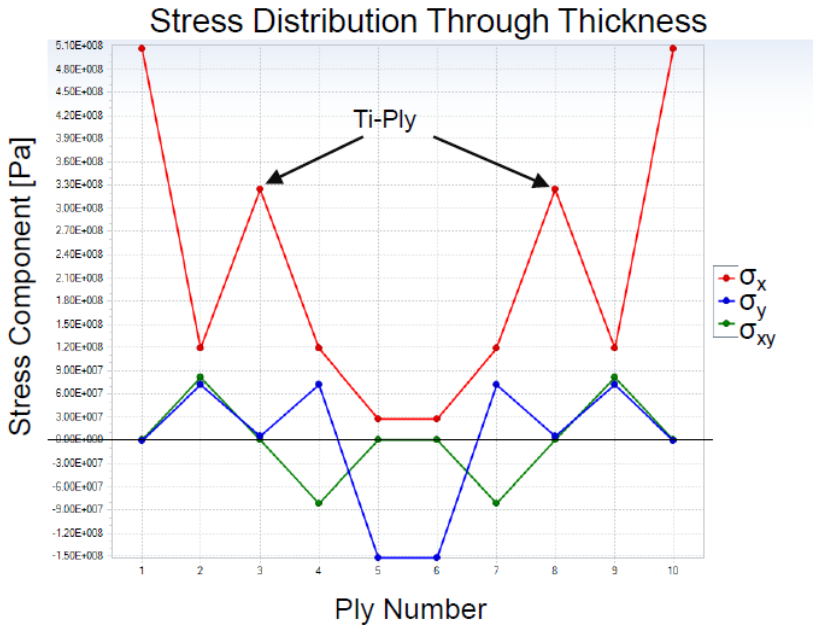

Figure 4-2 Stress distribution in each ply for a tensile load of 50 MPa

The 0-degree plies caries the most load with the highest tensile stress. It is ideal to have the composite plies carry the tension load and the Ti plies (ply 3 and 8) carry the shear load [85]. Similarly, in the transverse direction, the Ti plies are also subjected to less tensile stress than the neighboring composite plies.

The bearing capability of a bolted joint is evaluated by the bearing failure mode and the bearing margin. Typical design considerations are to modify the distance between the bolt holes (*W*), the pin diameter (*D*), and the edge distance (*e*) such that bearing failure is the failure mode. Figure 4-3 shows the different failure modes (shear out, bearing, and net tension failure) that can occur in a bearing test. If the bolt diameter is large compared to the width (or the pin holes are spaced in close proximity), net tension is the critical failure mode. Shear out is likely to happen if the bolt hole is placed close to the edge (i.e. *e* is small). Bearing failure is less catastrophic and can utilize the full bearing joint capability and thus is desirable. Figure 4-4 shows the final design of the bolted joint that would have a bearing failure. The FML sample (red) of 1 in width (*W*) is subjected to a 5 kN far field force. A hole with diameter (*D*) equals to 0.4 in with its

center located 1.25 in (*e*) away from the plate edge. Two steel plates are used to apply the far field load through a rigid pin.

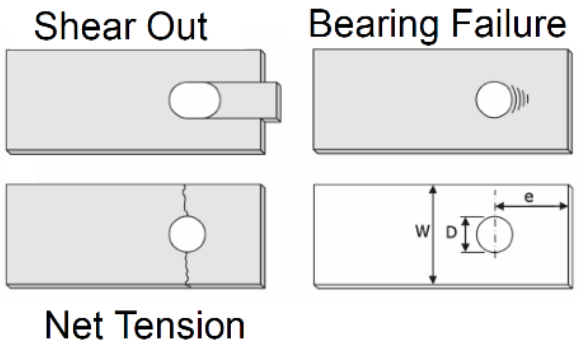

Figure 4-3 Bearing load failure modes. Bearing failure is ideal

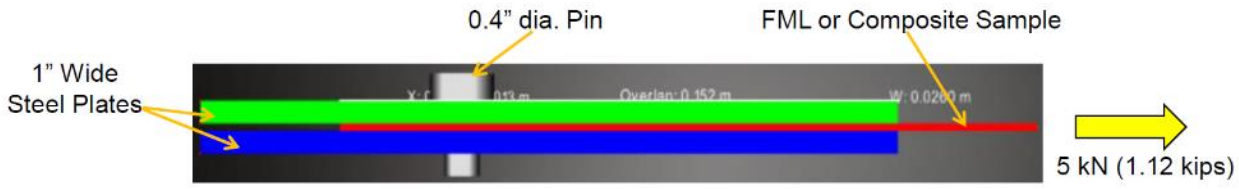

Figure 4-4 Bearing load modeling in Helius composite to evaluate FML bearing performance

Table 4-1 Bearing model result comparing the performance of an FML design and its composite counterpart

Sample	Critical Failure Mode	Bearing Margin	Shear Margin	Net Tension Margin
FML	Bearing	1.320	3.359	5.064
Composite	Bearing	0.243	1.620	2.457

Table 4-1 shows the bearing margin comparing the 10 ply FML sample and a composite plate with the Ti plies substituted with 90-degree plies. The bearing margin is defined by Margin = Factor of Safety – 1. In either case, bearing is the critical failure mode because of the design. The bearing margin is increased by almost 4 times in the FML sample when compared to the composite counterpart, thus confirming the motivation of using FML for pin bearing joints in launch vehicles. The less than 1 bearing margin suggests that the composite sample would have failed while the FML sample would be able to support a far field force of 5 kN. This design of

FML is manufactured for ultrasonic testing in the rest of this chapter. The details of the manufacturing process are shown in appendix 4.2

4.1.2 Ultrasonic Inspection in Mechanical Testing

In section 1.1.2, the advantages of using guided waves for NDE in qualification and acceptance tests for launch vehicle components are discussed. In this section, a proof of concept in the ultrasound monitoring experiment is presented. The hybrid composite specimen subjected to the bending test showcases the types of failure at the metal-composite interface. The experiment measures the load-displacement response from the Instron test frame, additional displacements and strains measurements are reported from Digital Image Correlation (DIC), and the ultrasound signals are captured from surface mounted piezoelectric patches (PZT). The FML sample used for this experiment consisted of 9 layers of titanium, and with overall dimensions of 153.21 mm X 19.43 mm X 8.59 mm. The supports are separated at 127 mm apart. A speckle pattern is applied to the front side of the sample for DIC measurement, and the images are processed by an open source DIC software, Ncorr [86]. For ultrasound measurements, PZTs were mounted on the top and bottom, with the source on the left side and the receivers on the right side, as shown in Figure 4-5.

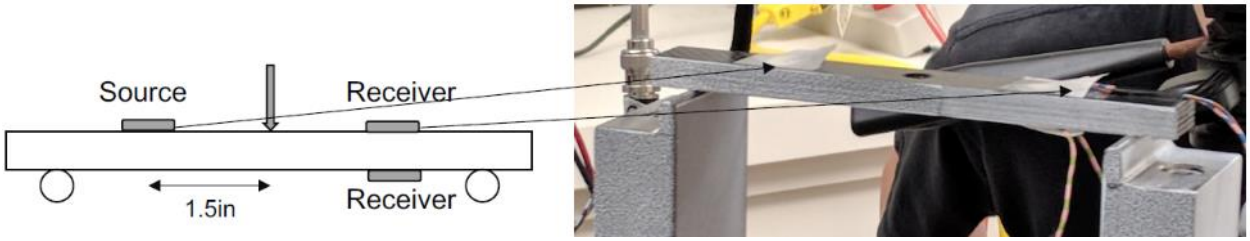

Figure 4-5 Specimen for three-point bending test is instrumented for DIC, and ultrasound measurement

The bending test is displacement controlled with compressing rate of 0.1 mm/s to reach the final displacement of 10 mm. The ultrasound inspection uses a source of 5 cycle Hann windowed sine

burst of 250 kHz center frequency. The ultrasound signals are taken every 1 mm of crosshead displacement, by pausing the load cycle.

Observations from the Mechanical Test

The force displacement response shows a peak load of 3.247 kN. The response also shows three significant unloading events during the test. Comparing the images taken at specific instances that correspond to the load drops shown in Figure 4-6, the first event is attributed to the delamination of the bottom plies, labelled as 1. The second unloading event corresponds to the disbond at a metal composite interface (MCI), labelled as 2. This disbond occurs near the mid-plane of the specimen and the force reading drops by approximately 2.5 kN. The third and final event is another disbond at an MCI, in the upper half of the specimen.

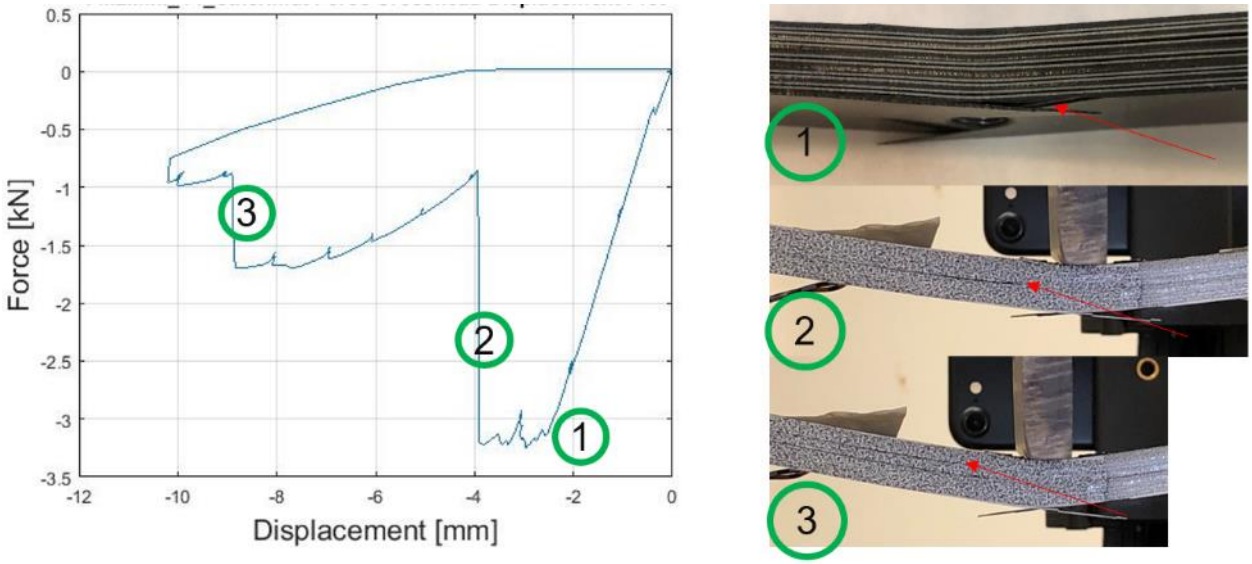

Figure 4-6 Load-displacement response and the defects associated to the unloading events

A close-up image of the disbonds is shown in Figure 4-7, revealing the locations of the defects. The image in the left-hand side a noteworthy damage feature where the disbond travelled through the composite plies, “shifting” from the titanium sheets positioned above to the one below.

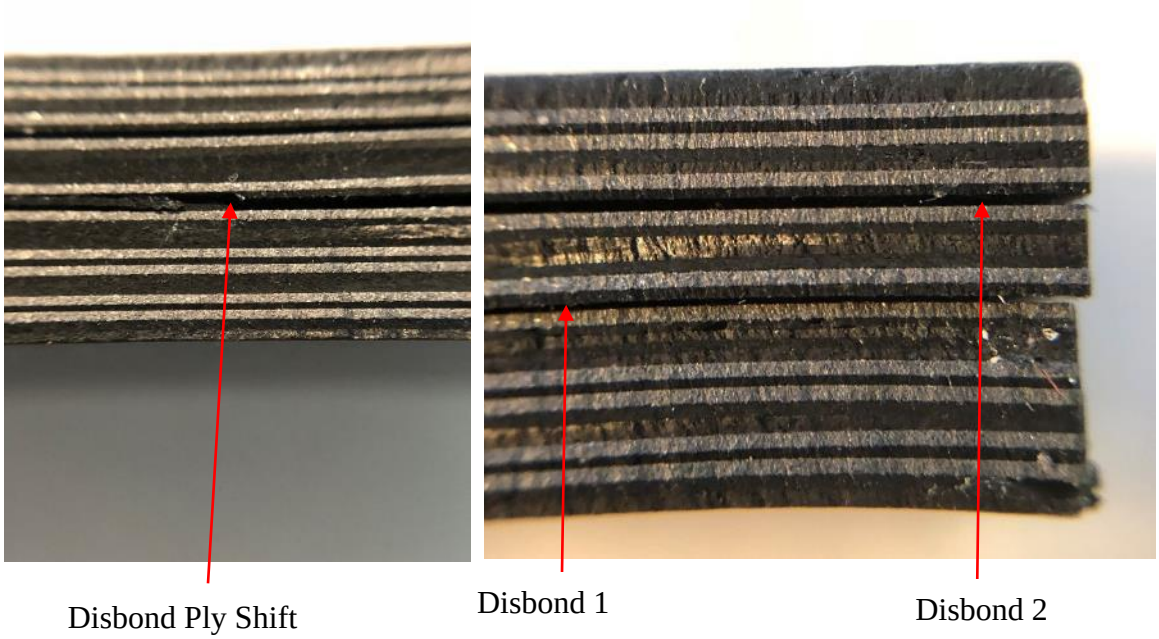

Figure 4-7 Detailed inspection of the disbands that cause the load drops

The displacement field measured from DIC is shown in Figure 4-8. The location of the first disbond can be determined where the horizontal displacement shows a change in sign. The interfacial displacement difference is determined to be 0.92 mm.

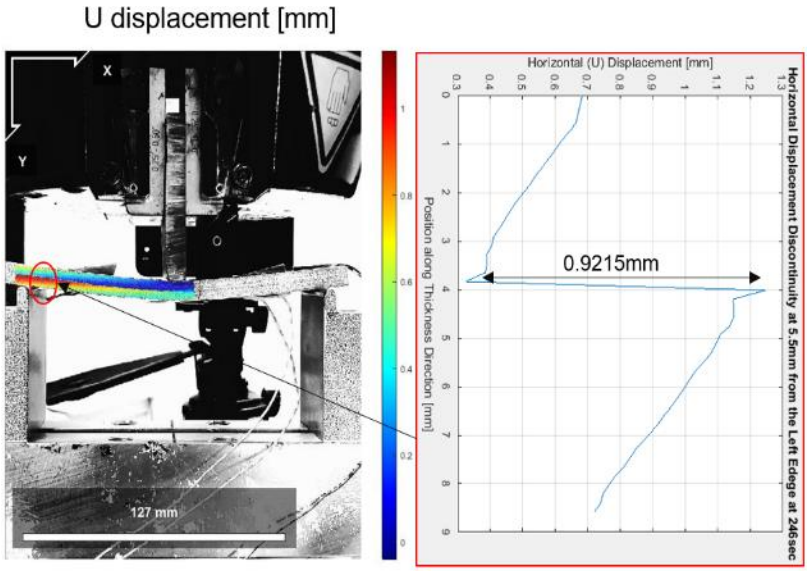

Figure 4-8 Horizontal displacement field shortly after the first disbond has occurred

In Figure 4-9, the second disbond can be observed upon close inspection. The smaller difference in the interfacial displacement indicates that the unloading for this event is smaller than that in first disbond, a fact mentioned previously in the force displacement response.

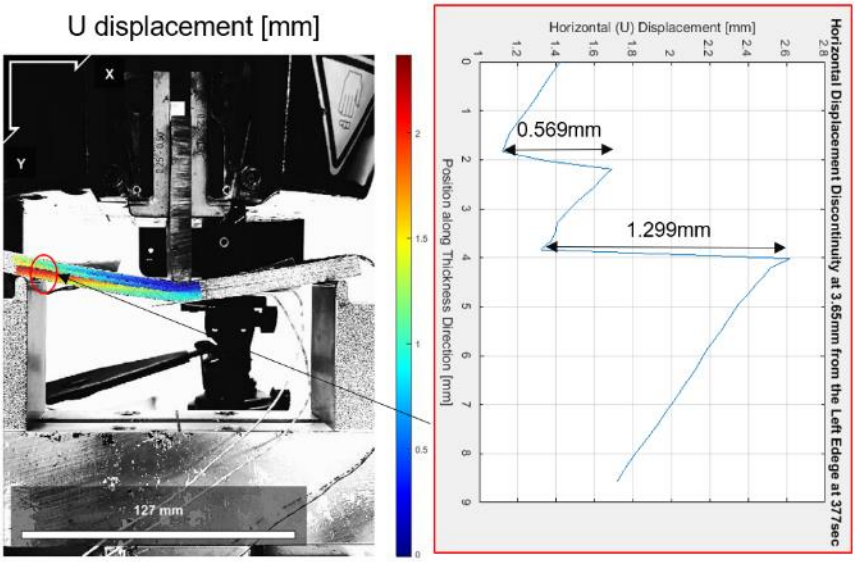

Figure 4-9 Horizontal displacement field after the occurrence of the second disbond

Ultrasound Results

The ultrasound waves are generated from the PZT at the left end of the specimen and travel to the receivers at the right end. Stressing the specimen causes a noticeable change in the observed signal as shown in Figure 4-10. Figure 4-10 shows the comparison between the signals taken at load magnitudes of 0.25 kN (red) and 1.25 kN (blue), respectively

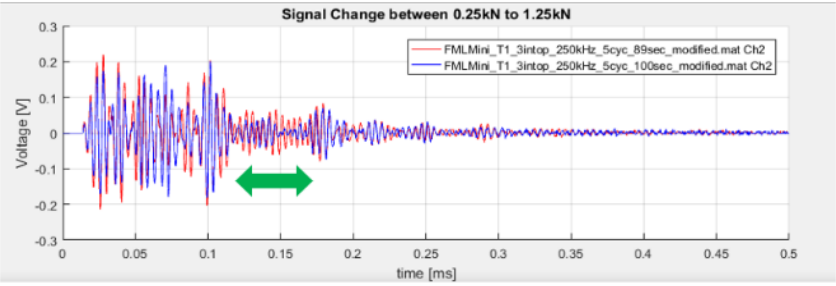

Figure 4-10 Measured ultrasound signals at load levels of 0.25 kN and 1.25 kN

The time period highlighted by the green arrows in Figure 4-10 shows the greatest change. After the first disbond, the same wave packet is also most influenced by the load changes as shwon in

Figure 4-11. It is worth mentioning that no waveform data was collected after the first disbond as shock of the failure caused the source PZT to separate from the specimen.

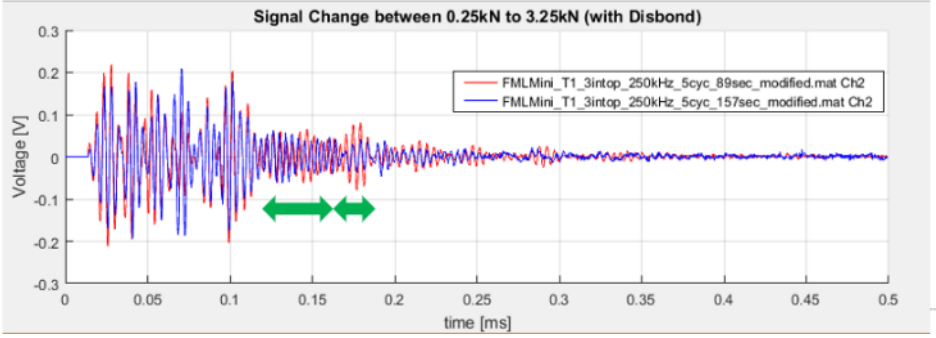

Figure 4-11 Specimen Signal after First Disbond

The frequency spectrum obtained by fast Fourier transform of the waveform as shown in Figure 4-12 shows an amplitude reduction, and a shift in peak frequency associated with the increase in applied load. In addition, a new frequency content began to appear after the first delamination, as seen in the right side of Figure 4-12.

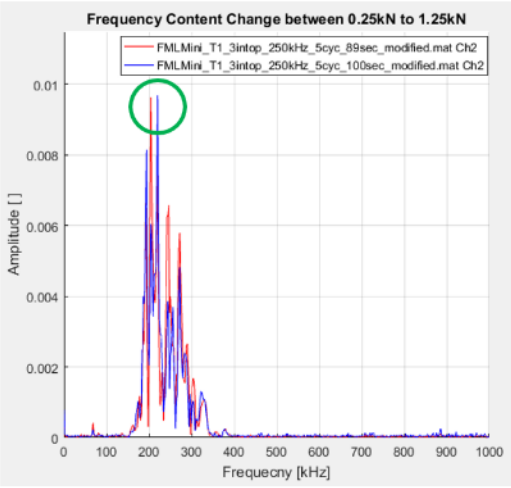

(a) at load level of 0.25 kN (red) and 1.25 kN (blue)

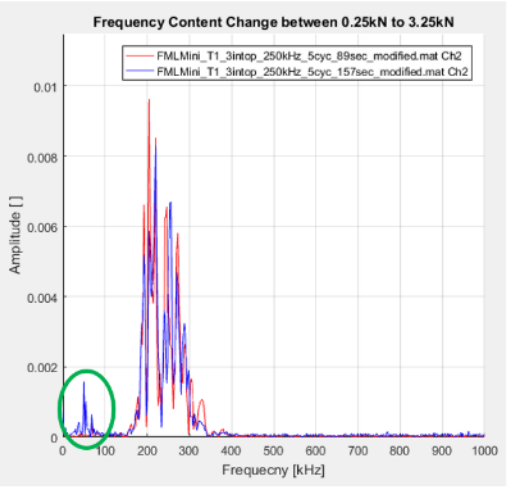

(b) before (red) and after the occurrence of first disbond (blue)

Figure 4-12 Frequency spectra of the ultrasound signals

4.2 Limitations of the Ultrasonic Transducers for Damage Detection

NDE using guided waves relies on the basic idea that Lamb waves are excited by the surface mounted transducers, and the nature of the defects can be inferred from the scattered waves. As a result, the frequency response of the transducers is an important factor in the sensitivity of the inspection. Since the combined GL approach takes into account the transducer excitation characteristics, and the measurement system response in the source portion of the problem, the modeling tool can be used to determine the frequency ranges that are sensitive to a different type of defects. This methodology is applied to different defects that could occur in FML structures during manufacturing or in service, specifically a gap that exists between two Ti sheets that are supposed to be continuous, henceforth referred to as the gap defect. The objective is to determine the frequencies of the ultrasonic waves that are more prone to scattering for various gap sizes.

4.2.1 Hybrid Composite Specimen and its GL Model

The model considered here is a hybrid titanium (Ti CP Grade 2) and carbon fiber reinforced polymer composite with 5H Satin weave woven plies (Hex433). The material constants used in the models are shown in Table 4-2. The hybrid composite plate has a stacking sequence of $[0/45/Ti/-45/90]_s$ in which the Ti plies are 0.5 mm thick and the cured ply thickness for the composites is assumed to be 0.325 mm. The local region representing the source transducer has an applied distributed load that is 8 mm wide with a Gaussian distribution. The FE region has a length (in the *x* direction) of 65 mm, whereas the FE region enclosing the defect has a length of 90 mm. Both FE meshes have an average element size of 75 μm × 75 μm of 4-node plane strain elements. The mesh size is well within $1/10^{th}$ of the smallest wavelength to ensure convergence. To mimic the measurements from experiments, the wave motion (vertical

displacements) on the top surface, at location 55 mm to the right of the center of the defect is shown, simulating a transmission test.

Table 4-2 Properties used in the GL models for Titanium CP Grade 2 and Hex433 CFRP. The $_{11}$ direction is along the fibers

	E_{11} [GPa]	E_{33} [GPa]	G_{13} [GPa]	ν_{12}	ν_{23}	Density [kg/m^3]	Thickness [mm]
CFRP	77	13.8	5.1	0.06	0.37	1526.1	0.325
Ti	105			0.37		4510	0.5

The ply gap is located at the top Ti ply (3rd ply from the top) and the gap spacing for different defect models varies from 0 mm (defect free) to 15 mm, at 1 mm increments (Figure 4-13). The width of the local region is many wavelengths larger than the largest gap size to ensure that the contributions of the propagating modes dominate at the boundary between the FE and the global regions. For the source model, a normal surface traction is applied only at the top surface with a Gaussian window of 8mm width to simulate a transducer.

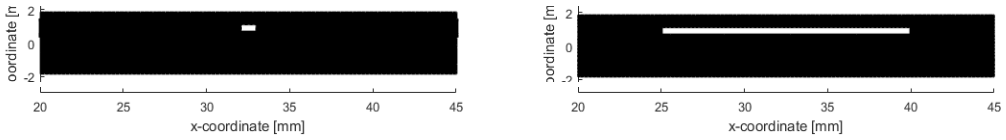

(a) 1 mm (b) 15mm wide

Figure 4-13 The geometry of the ply gap with width ranging from 1 to 15 mm

4.2.2 Sensitivity to Excitation Frequency and Minimum Detectable Size

To study the frequency response of the transducers (Digital Wave B-225), the physical transducer is subjected to a wideband excitation (0.1 ms chirp excitation with frequency increasing linearly from 20 kHz to 450 kHz), and the "face-to-face" response is recorded. Figure 4-14 shows the excitation signal and the frequency response of the transducer pair. The spectra indicate that the response is relatively weak at frequencies below 60 kHz, between 86 kHz to 96 kHz, and above 230 kHz. An amplifier is used in the measurement system so that the response spectrum can be greater than the source spectrum.

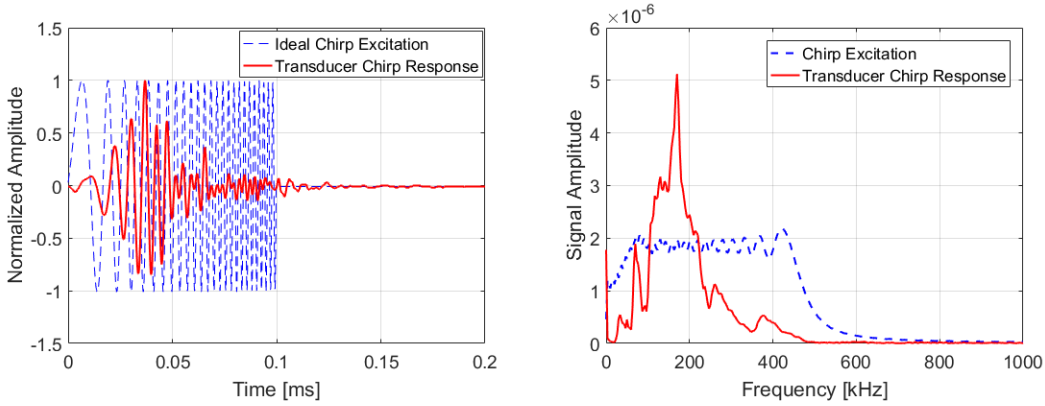

(a) source and reciever response in time domain (b) Frequency spectra for the two waveforms

Figure 4-14. Chirp (20 kHz to 450 kHz) signal is used to excite the transducer, and the face-to-face response

This "face-to-face" response is used as the time dependence of the source problem. The excited Lamb wave modes are then coupled with 16 different gap sizes. Figure 4-15 plots the transmitted and the reflected power flows due to all propagating Lamb modes for the various gap sizes as functions of frequency. The color in Figure 4-15 represents the strength of the power flow. As expected, for smaller gap size, wave scattering is less prone to occur, and the transmitted power flow follows the trend of the transducer frequency response spectrum closely. When the gap size is less than 4 mm, the reflected power flow is relatively insignificant for all frequencies. In contrast, for certain frequency and larger gap size combination, namely 172.5 kHz and 10 mm, the reflected power flow is significantly different from the transmitted power flow. Thus, those frequencies could be used in a reflection-based defect detection scheme for a particular gap size.

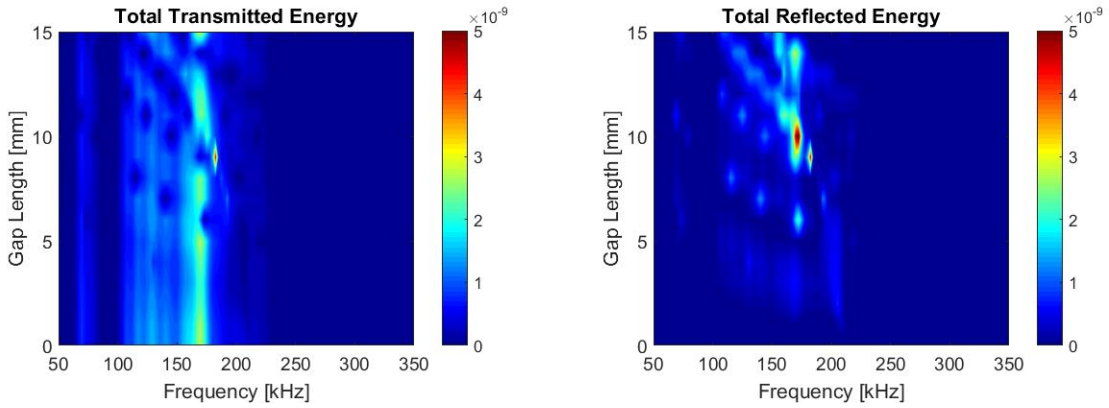

(a) Transmitted power flow from all Lamb modes, deep blue region indicates weak transmission,

(b) power flow of the reflected wave indicates gap size greater than 4mm has some stronger reflection for some specific gap size

Figure 4-15. Power flow spectrum of gap length vs. frequency

Figure 4-16 shows reflected power flow for A_0 and S_0 modes, respectively. Comparing the total power flow (Figure 4-15b) with the power flow of A_0 mode (Figure 4-16a), the results can be seen to be similar thus indicating there is very little mode conversion below 160 kH and above 200 kHz for a gap size less than 7 mm. Following similar observation, other frequency-gap size combination that produces stronger wave scattering can be determined, and it may be possible to select a sensitive Lamb mode.

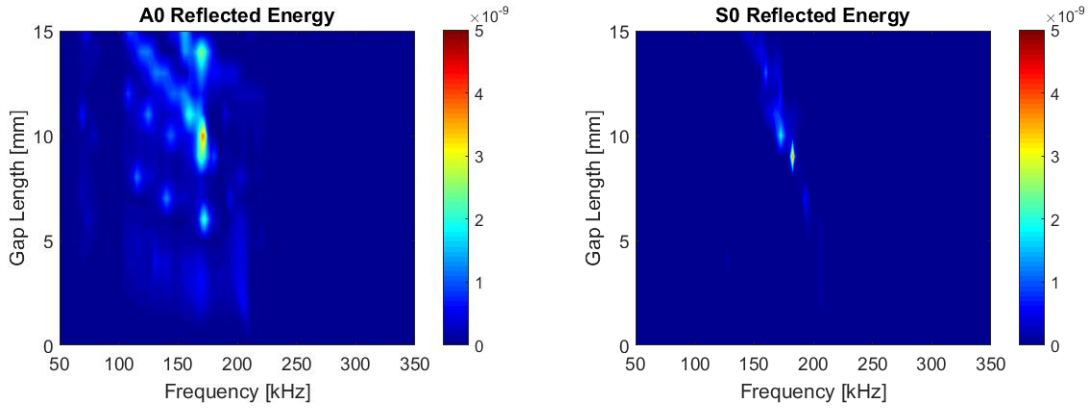

(a) A_0 mode (b) S_0 mode

Figure 4-16 Reflected power flow for various gap sizes

The power flow representation in Figure 4-15 - Figure 4-16 are informative in studying the gap defect scattering characteristics and source selection but may not be directly related to the ultrasonic measurement from surface mounted transducers. Power flow is a through-thickness averaged quantity and the FML material has distinct through-thickness variation in stiffness. In Figure 4-17, the top surface vertical displacement spectra at 65mm to the left, and to the right of the gap are presented.

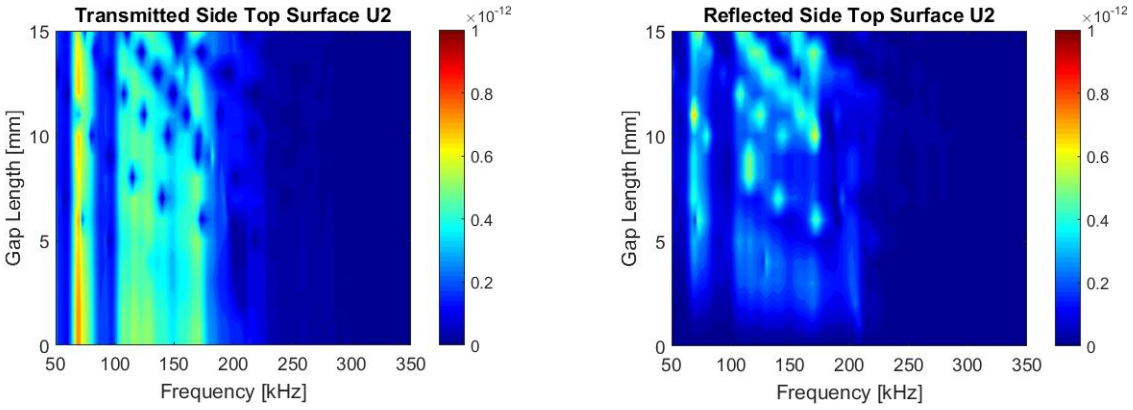

(a) 65mm to the right (b) 65mm to the left of the gap

Figure 4-17. Vertical displacement spectra at top surface

The results show that around 85 kHz to 100 kHz, the weak transducer response causes indistinguishable displacement amplitude changes for all gap lengths, making it difficult to identify the defect. At higher frequency ranges, namely between 110 kHz to 170 kHz, it is more likely for a specific gap size to cause strong reflections. Furthermore, the reflected displacement spectrum indicates that with a center frequency at around 170 kHz, the difference between 10mm and 8 mm gap size is quite pronounced. That is, despite the relatively small gap size difference, the 10 mm case causes more pronounced reflection, which is effective for detecting defects with high sensitivity.

For practical applications, it is necessary to inspect displacement time waveforms which are more directly comparable to experimental measurements. A source problem with the input of transducer "face-to-face" response subjected to a tone burst excitation with 175 kHz center frequency is created, and this source problem is coupled with the 8 mm and 10 mm gap scattering problems. Figure 4-18 shows the vertical displacement at the top surface 65mm to the left and to the right of the gap. For the transmitted side, the waveform for the less sensitive 8mm ply gap case (solid blue line) is similar to the defect free (dash black line) case with only a small amplitude reduction. However, the waveform for the 10 mm ply gap case (solid red line) shows a

significant amplitude change and increase in time duration on both the transmitted and reflected sides.

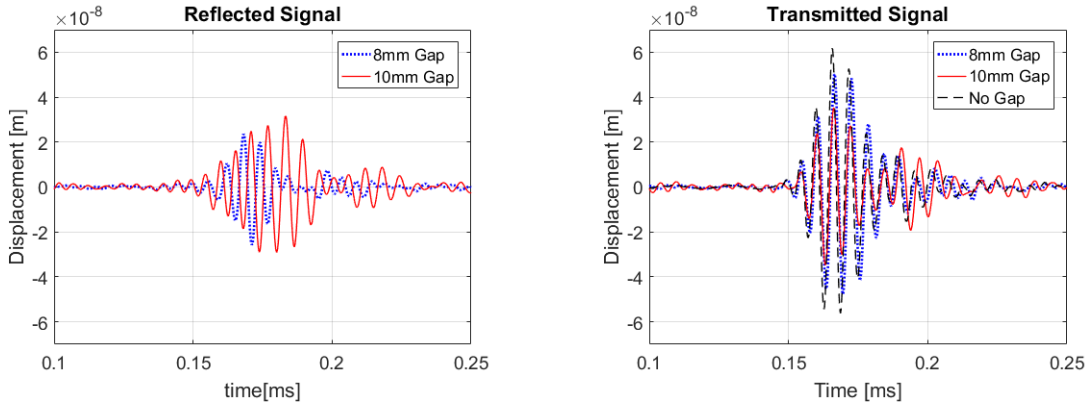

(a) at 65 mm to the left, (b) 65 mm to the right of the center of the gap

Figure 4-18. Vertical displacement for a narrow band excitation at the top surface for 8mm and 10 mm gap lengths. Results show that the 10 mm gap changes the incident wave significantly as compared to the 8 mm case

These features could be useful in developing a Lamb wave-based damage detection scheme. To inspect the scattering features at other locations, the surface displacement is presented in a spatial-temporal plot (Figure 4-19) where the horizontal axis is the arrival time of the waves, the vertical axis is the *x*-coordinate, and the colors represents the (vertical) displacement amplitude. The figures show the right (transmission) side of the gap for 8mm and 10mm gap size.

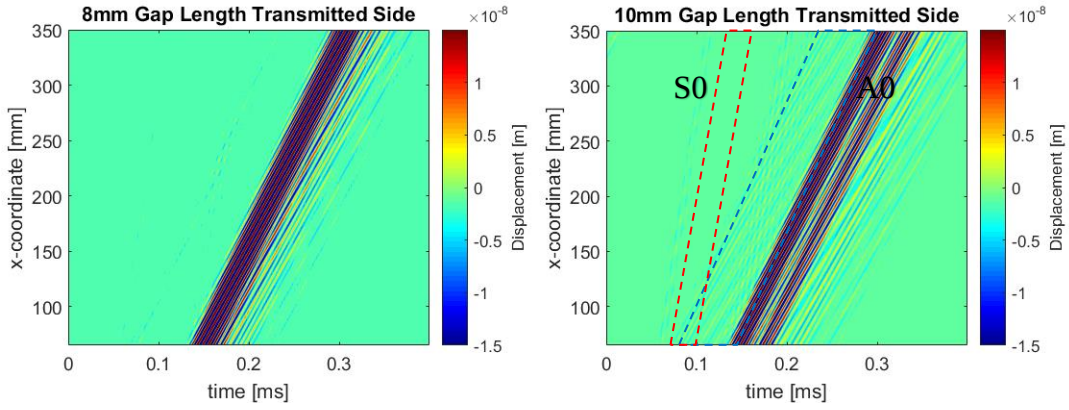

(a) 8 mm gap (b) 10 mm gap

Figure 4-19. Space-time representation of the surface displacement on the transmitted side. The 10mm gap shows a more significant mode conversion and distortion of the waveform than the 8mm gap case

The wave duration for 10 mm case is longer than that for the 8 mm case in the given distance range. Furthermore, the slope of the color band indicates that the dominant transmitted and reflected waves are A_0 mode Lamb wave without significant dispersion. Small mode conversion to S_0 can be seen for the 10 mm case in the transmission side because of band branching at a steeper slope from the A_0 mode.

4.3 Defect Characterization in FML

The complexity in the changes in guided wave characteristics associated to the wide range of defects means that inverse process to classify the damage type and to quantify the severity of the damage is difficult. No straightforward solution exists to the inverse problem and one possible method to approach the problem is with machine learning strategies. A substantially large amount of data, and a robust waveform data reduction scheme are needed to formulate the machine learning problem. The GL simulation tool is efficient in simulating a wide range of elastic wave propagation problems of composites with defects. It is used here to model different damages of various severity to demonstrate how the model can be used to design a damage characterization scheme for NDE.

4.3.1 Defect Study Matrix

Figure 4-20 describes the various defect cases included in this study. The FML material system considered in this section is identical to the one described in section 4.2.1. The plate in the vicinity of the surface loading is modeled by an FE mesh of 65 mm in length in the propagation direction, whereas in the vicinity of the defect, the plate is represented by a 100 mm wide mesh. Two types of defects are studied in this work (Figure 4-21), a gap in the Ti ply (Type 1), representing a manufacturing error in positioning the titanium sheets, and a disbond at the interface of the 45-degree composite ply and the Ti ply (Type 2). Both types of defects are

modeled with dimensions in the *x* direction varying from 0 mm to 35 mm in 1 mm increment. Furthermore, these defects are modeled in two different structural configurations, the first is the entire structure is hybrid composites (config. A), and the second is a transition from full carbon composite to hybrid composite (config. B).

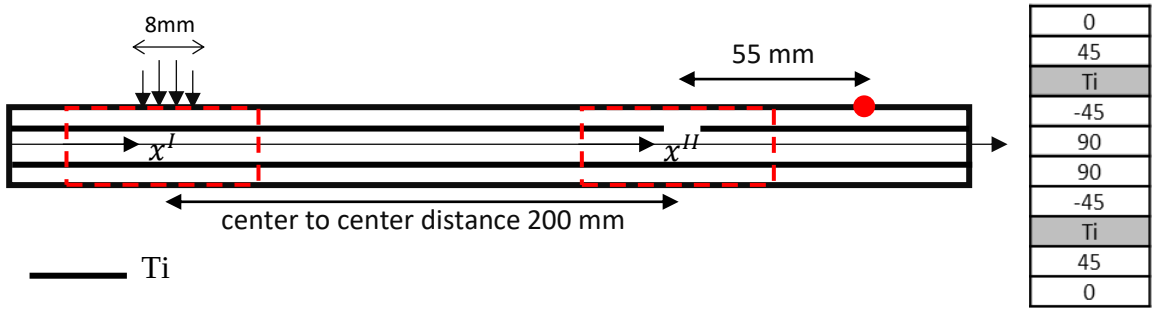

(a) Ti ply gap defect (Type 1) in full hybrid composite (Config. A)

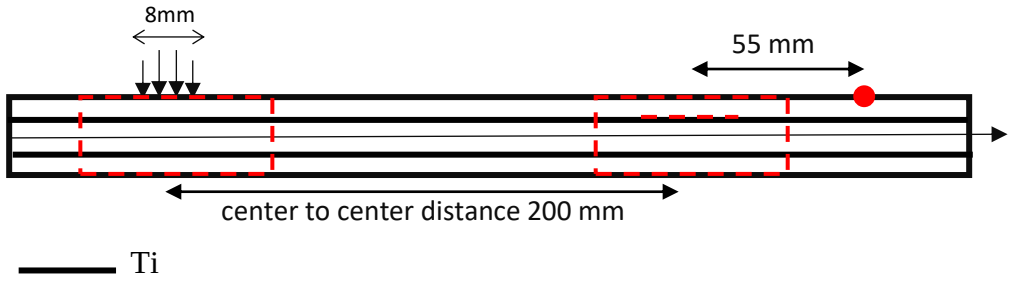

(b) Disbond at the Ti-composite interface (Type 2) in full hybrid composite (Config. A)

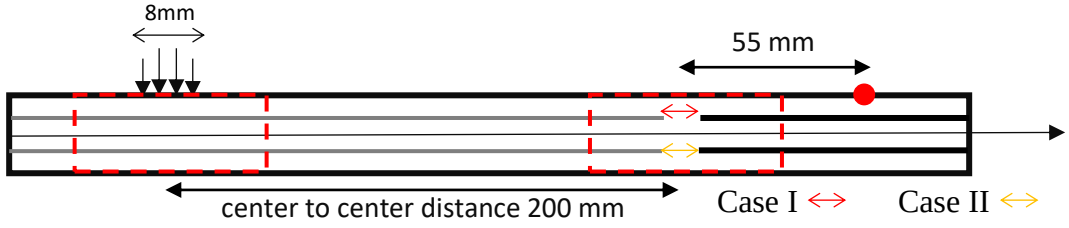

(c) Ti ply gap defect (Type 1) in transition region (Config. B) where the gap could either exist in the top Ti ply (Case I) or the bottom Ti ply (Case II)

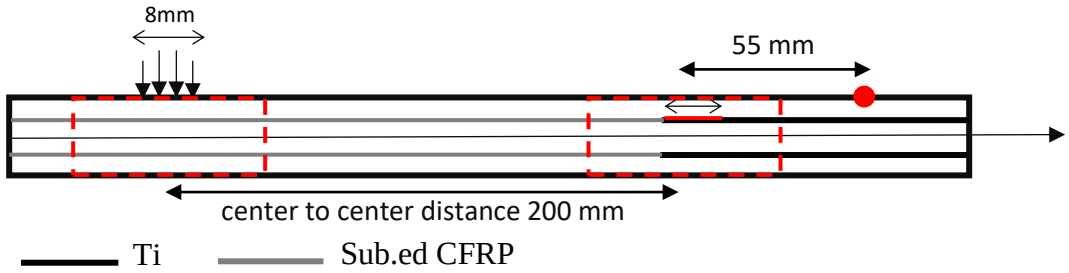

(d) Disbond at the Ti-composite interface (Type 2) in transition region (Config. B)

Figure 4-20 Geometry of the FML defect study matrix. The thick black lines and the thick gray lines represent the Ti plies and the substituting 90 deg plies. The displacement is reported at 55 mm to the right of the center of the defect indicated by the dot. The FE regions are outlined by the dash box, where x^I and x^{II} are the local coordinates of the source and scattering FE region, respectively

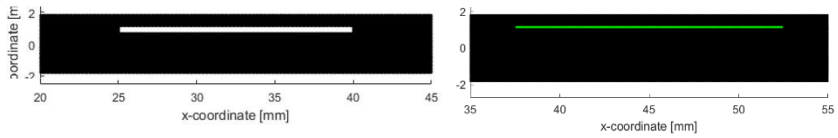

Figure 4-21 Illustration of the defect type (L) gap, representing the discontinuity in the Ti ply due to placement error, (R) disbond at the 45/Ti interface where the green line highlight the FE nodes that can be separated

Since the signal analysis for damage characterization would require amplitude comparisons, the effects of material attenuation are included in these models using the complex moduli procedure outlined in section 3.4.2. For the carbon composite lamina and the titanium plies, the parameter *p* have values of 0.035 and 0.0035, respectively. It is necessary to include a small *p* value for the titanium, estimated to be 1/10th of polymer matrix composite. Furthermore, the source transducer is represented by a 1 MPa normal load with a Gaussian distribution spanning 8 mm, in one case with excitation frequencies of 175 kHz and the other at 125 kHz (Hann windowed 5 cycle sine pulse, Figure 4-22). To better mimic the ultrasound measurements from a physical experiment, the transducer face-to-face responses at those frequencies are used as the model excitation.

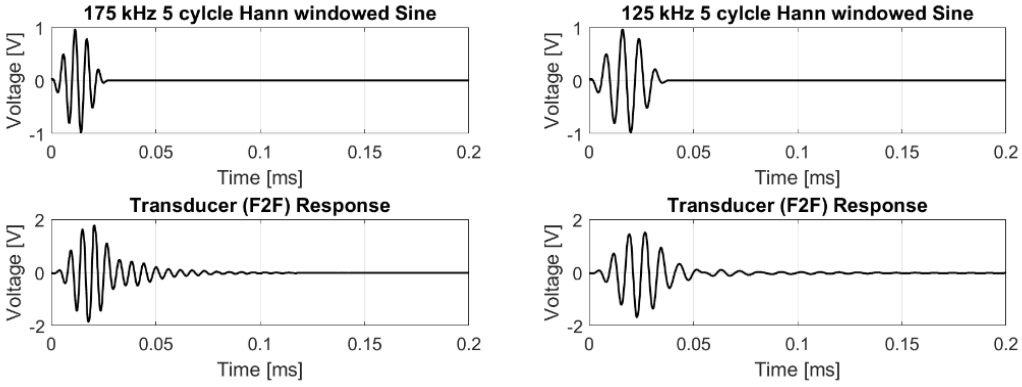

Figure 4-22 Excitation and transducer response for (L) 175kHz and (R) 125kHz

4.3.2 Global-Local Model Waveform Prediction

In this section, a survey of the waveform prediction for the various combinations as described in the defect study matrix is presented. The visual inspection of the waveform changes for different damage cases are used to design the damage indices in the subsequent steps.

Full Hybrid Composites

In the case of the entire plate is made with FML, the predicted vertical displacement with no defect measured at 255 mm to the right of the center of the source is shown in Figure 4-23. These two signals are considered as the "baseline" and by comparing these signals to those obtained from the damaged cases are used to design a damage index for damage characterization. Under both excitation frequencies, both S_0 and A_0 modes are generated but of different proportions. This is due to the fact that A_0 mode is more attenuative than S_0 mode, a trend that is stronger with increasing frequencies as discussed in section 3.4.2. Naturally, the amplitude of the received signal for 175 kHz is significantly smaller than the case of 125 kHz, at almost ¼ of the later. The signals also show that the effects of transducer vibrations and dispersion are different for the two fundamental modes. The trailing wave packet behind the S_0 mode is longer in the case of 175 kHz than that of 125 kHz, whereas the packet behind the A_0 mode is longer at 125 kHz. In the case of signals recorded from damaged cases, these trailing packets are often overlapped with the scattered waves.

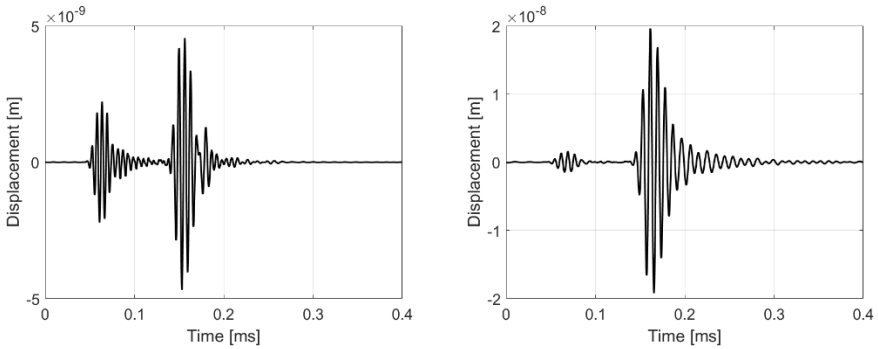

Figure 4-23 Signal predicted for no damage case at 55mm to the right of the would have existed defect (L) 175kHz and (R) 125kHz

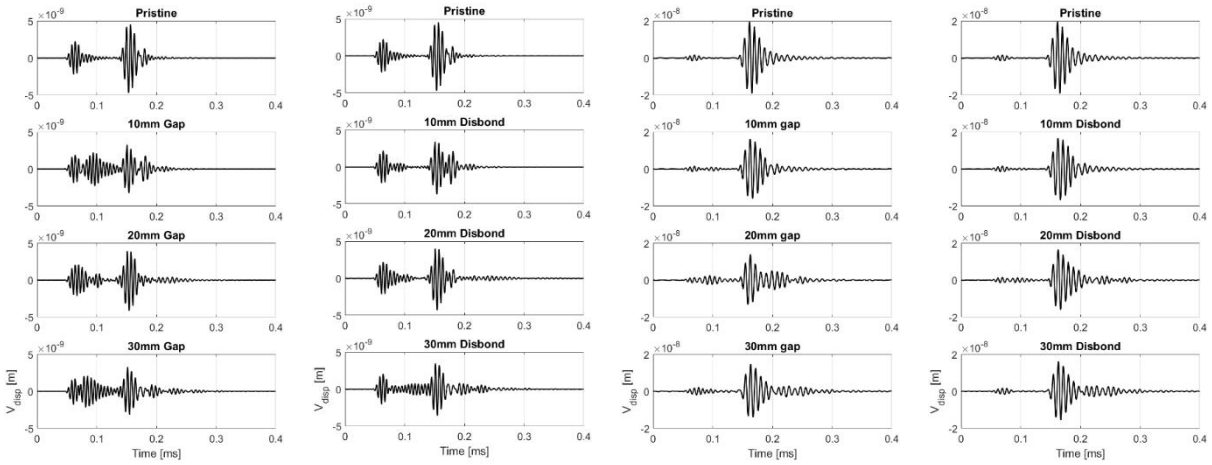

(a) (b) (c) (d)

Figure 4-24 Selected waveforms measured at 55 mm to the right of the defect for 175 kHz excitation for (a) gap defect, (b) disbond defect, and 125 kHz for (c) gap and (d) disbond defects

Figure 4-24 shows the predicted waveforms for the pristine cases and those from 10, 20, and 30 mm defect sizes. In the case of 175 kHz. Inspecting both excitation frequencies and at different defect sizes, the coda (packet tail) is longer for the case of gap defect than disbond defect. This is more evident at higher frequencies since the wavelength of the S_0 mode is more sensitive to the defect. The longer coda suggests that waves are more prone to scattering in the gap defect than the disbond defect. This can be attributed to the fact that the wave motion is more distorted by the gap defect since the stiffness changes more significantly than the disbond defect. As the length of the defect increases, the waveforms between the S_0 and A_0 modes exhibit the most changes when compared to the pristine signal. To examine the wave packets associated to the

scattered waves, Figure 4-25 plots are shown for the displacement contribution from A_0 mode, S_0 mode and the sum of all Lamb modes for the case of a 10 mm gap defect at 175 kHz excitation as an illustration. For all studied defect sizes, S_0 and A_0 signals tracks well with the total displacement, indicating that the mode conversion is mainly between the fundamental modes. Since the added wave packet arrives between the directly reached S_0 and A_0 modes, the scattered wave is effectively from S_0 to A_0 conversion.

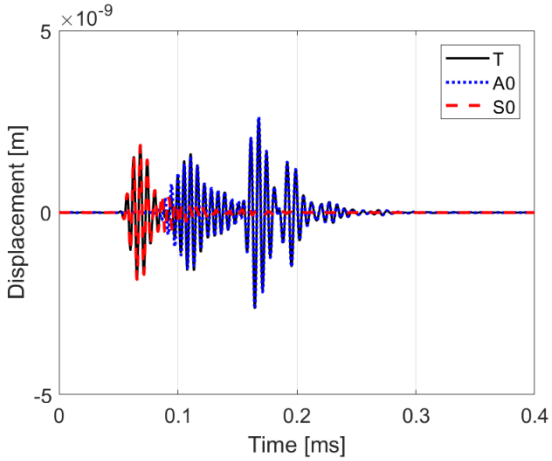

Figure 4-25 Waveform for 175 kHz, 10mm Gap defect, plotting the vertical displacement for A0 (dotted line), S0 modes (dash line) and the sum of all Lamb modes (solid line)

In order to better compare the waveforms for the various damaged cases, they are plotted in 3D plots in Figure 4-26 and Figure 4-27 where the *x*-*y* plane denote the time of flight and the defect sizes and the displacement amplitudes are represented by the height (z-axis) and the contour color. For both the disbond and the gap defect, visual inspection shows that below 5 mm, the waveform experiences negligible change from the pristine case, and the changes at the lower 125 kHz is even smaller. Therefore, it is difficult to distinguish between smaller damage sizes indicating 5 mm could be the minimum detectable size in a qualitative sense. At larger defect sizes, there are bands of scattered waves at the tail of the main packets with an increased phase delay as the defect size increases. The results make it possible to use the delay in the S_0 and A_0 codas to identify possible defect sizes. The challenge is that the delay is not unique to one defect

size. A process of elimination is needed with multiple source excitation frequencies to determine the most likely defect size. Figure 4-27 shows the amplitude variation between different defect sizes. As expected, if the defect that is prone to wave scattering, the main packet has a significant amplitude reduction and the amplitude of the coda wave increases.

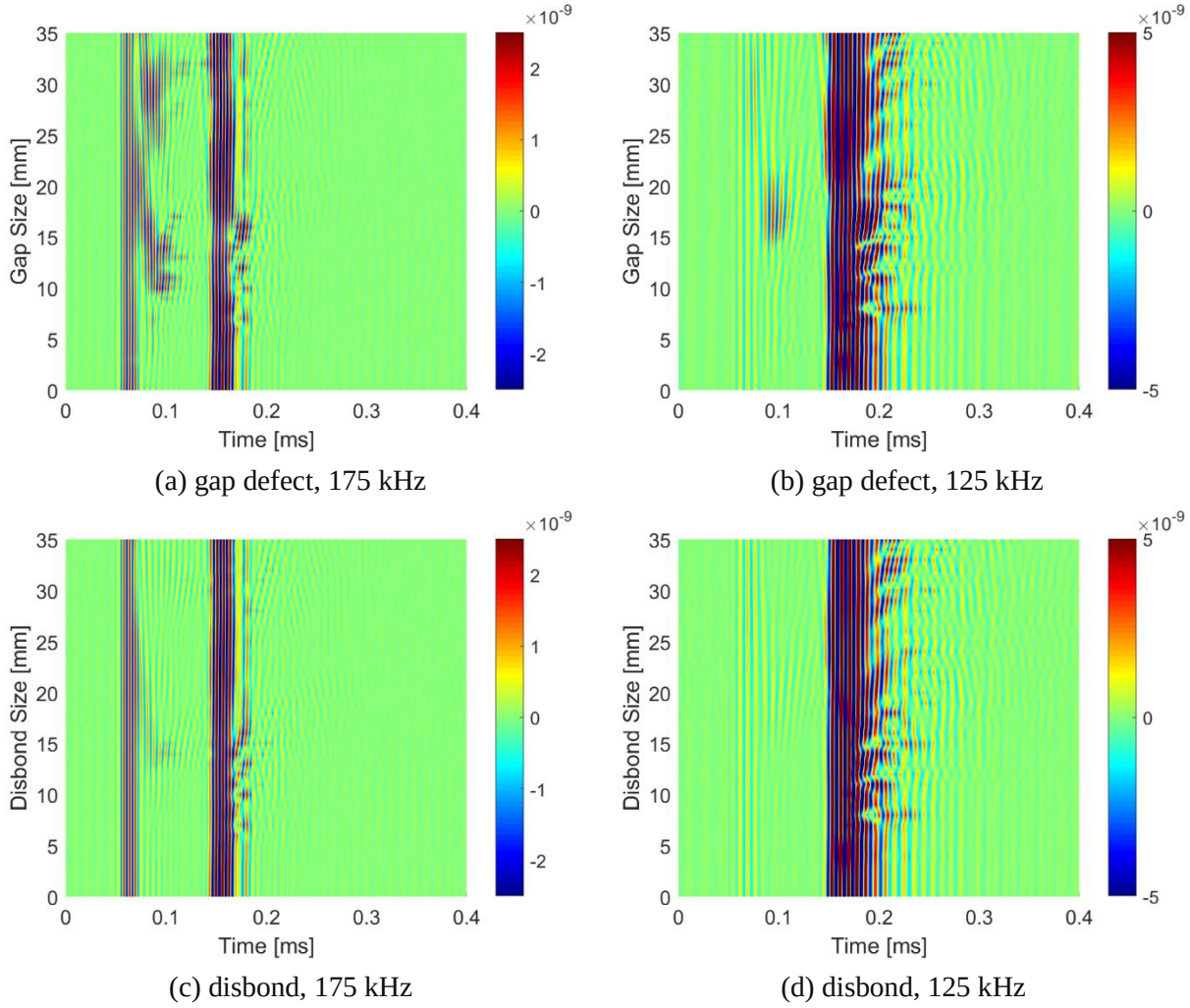

(a) gap defect, 175 kHz

(b) gap defect, 125 kHz

(c) disbond, 175 kHz

(d) disbond, 125 kHz

Figure 4-26 Waveforms for all defect sizes of Type 1 (Gap) and Type 2 (Disbond) subjected to 125 kHz, and 175 kHz excitation

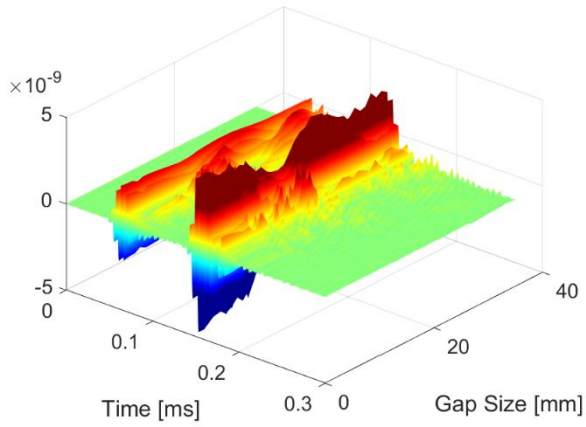

(a) gap defect, 175 kHz

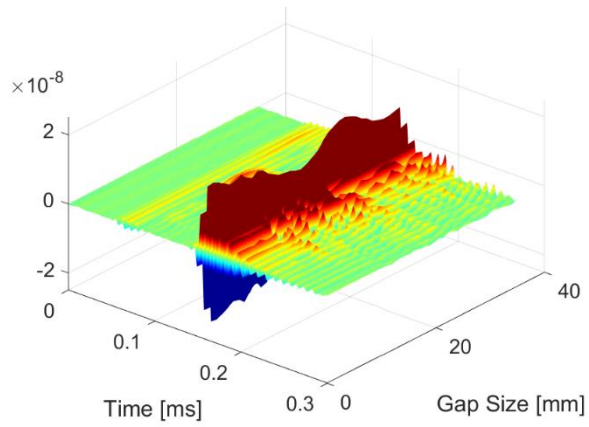

(b) gap defect, 125 kHz

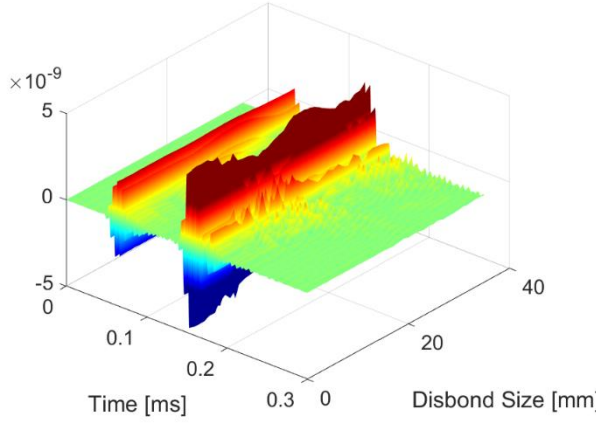

(c) disbond, 175 kHz

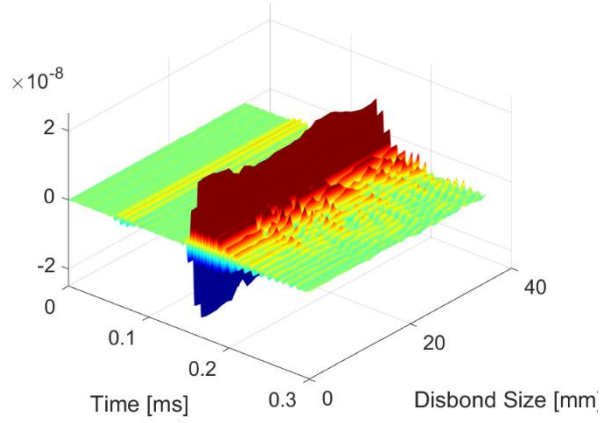

(d) disbond, 125 kHz

Figure 4-27 Waveform of all defect sizes of Type 1 (Gap) and Type 2 (Disbond) subjected to 125 kHz, and 175 kHz excitation. The contour color shares the same color code as Figure 4-26

Transition Region

To complete the dataset for the study matrix, the waveforms for the full composite to hybrid transition region (Config. B) is presented below. In spite of the difference in group velocity in a solid composite laminate and the hybrid composite as shown in Figure 4-28b, the time of arrival of the S_0 and A_0 are differ by approximately half a cycle at the measurement point. The full hybrid composite would yield a slow S_0 mode but a faster A_0 mode with similar amplitudes as shown in the pristine signal prediction in Figure 4-28a.

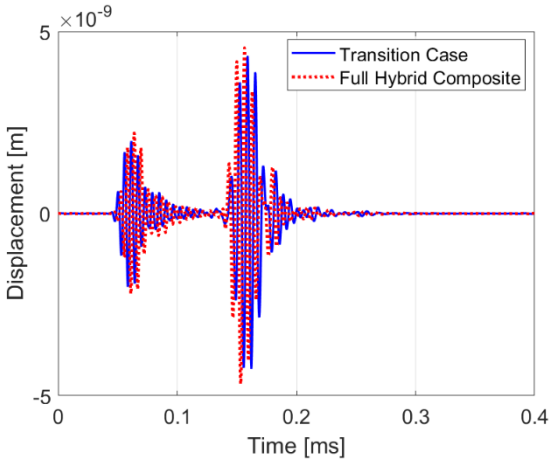

(a) predicted signals at 55mm to the right of the would have existed defect

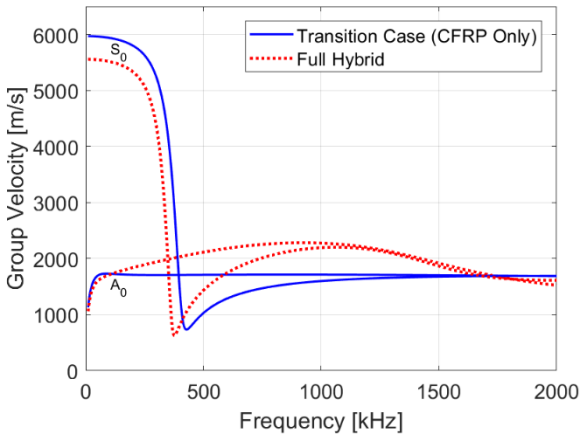

(b) group velocity for A_0 and S_0 mode

Figure 4-28 Comparison of the results for no damage case between the transition region (Config B) and the full hybrid composite (Config. A) under 175 kHz excitation

The waveform prediction for the transition region with gap and disbond defect are shown in Figure 4-29. An additional test case for this set of result is the comparison for a gap defect at the top Ti ply versus at the bottom Ti ply. Preliminary inspection of Figure 4-26 and Figure 4-29 shows that a similar amount of wave scattering occurs between the S_0 and A_0 modes if the defect types and the defect sizes are the same. In contrast, the scattered waves for disbond versus gap defect are different that can be observed between the S_0 and A_0 modes in Figure 4-26a, and c. The depth at which the gap defect occurs also produces some differences in scattered waves that can be deduced by comparing Figure 4-29a, and b. From the qualitative observation, the waveform changes produced by the different damage scenarios, at various severity (defect length) are a complex combination of amplitude, phase changes and the addition of new wave packets. Therefore, it is difficult to construct a simple way to characterize damage from a waveform (i.e. the inverse problem).

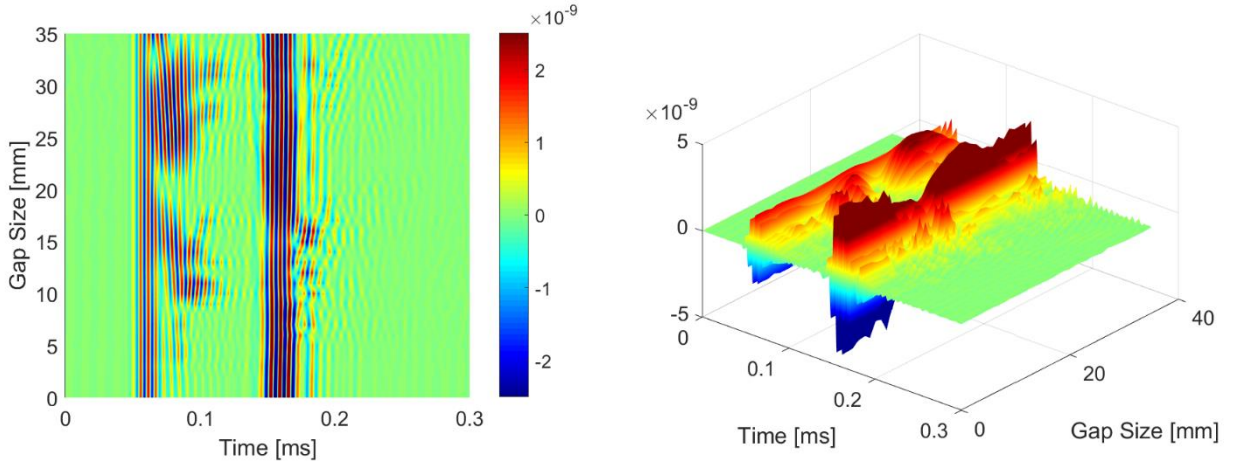

(a) Top Gap

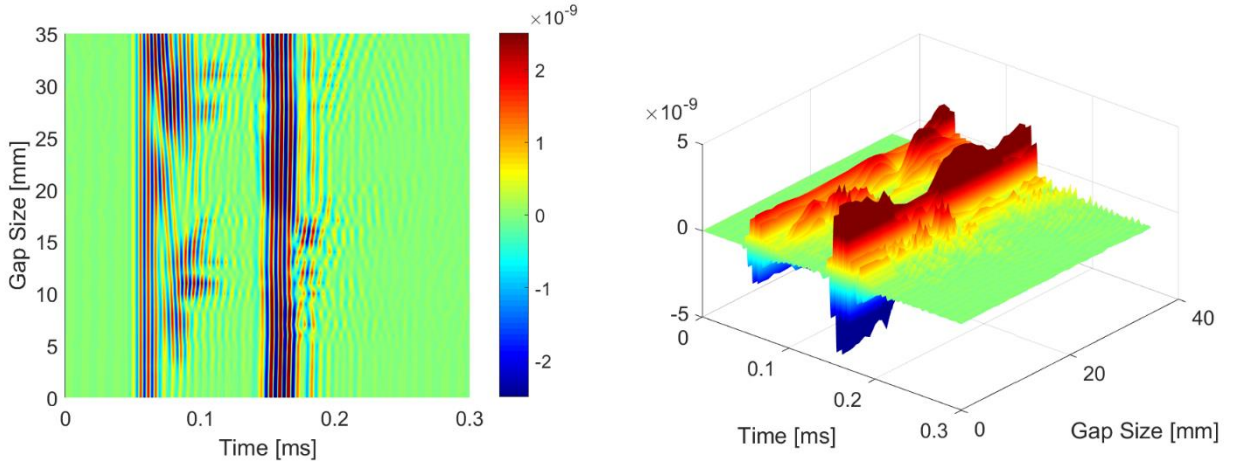

(b) Bottom Gap

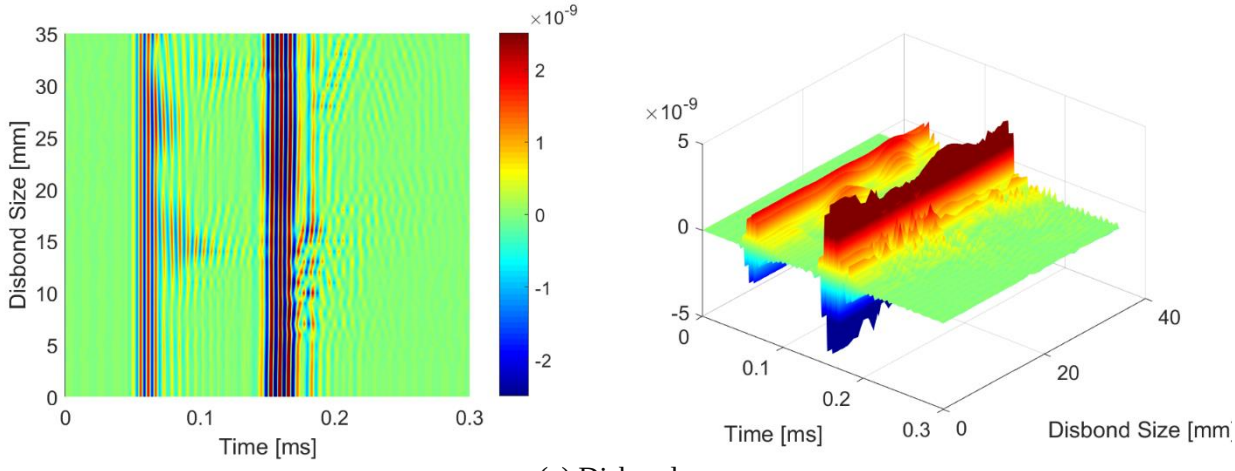

(c) Disbond

Figure 4-29 Waveforms for the transition region (Config. B) for all defect sizes of (a) Type 1 (Gap) at top (Case I) or (b) bottom Ti ply (Case II), and (c) Type 2 (Disbond) subjected to 175 kHz excitation

4.3.3 Damage Indices

The survey of waveforms in section 4.3.2 indicates that the signal changes are not monotonic variation of amplitude or phase delay across the full range of the defect sizes and time of flight, thus the inverse damage characterization process is ambiguous. Despite some monotonic trends of amplitude and/or phase can be found in a limited range of defect size or in a short time window, it is difficult to determine the domain of applicability for these reductions. The survey also lacks a quantitative measure of the amount of signal changes when compared to the pristine signal. The use of damage index (DI) naturally arises to reduce the information in a time signal (or in frequency) into a single scalar value. This DI reduction coincides with the need for various damage characterization inversion schemes, such as machine learning. In this section, serval DIs are used to process the GL predicted waveforms to examine their effectiveness.

The form of the DIs is motived by the nature of signal changes. Figure 4-30 shows the waveforms and their absolute values for the selected cases for a gap defect 55 mm to the right of the center of the defect, that is at $x^{II} = 100$ mm .

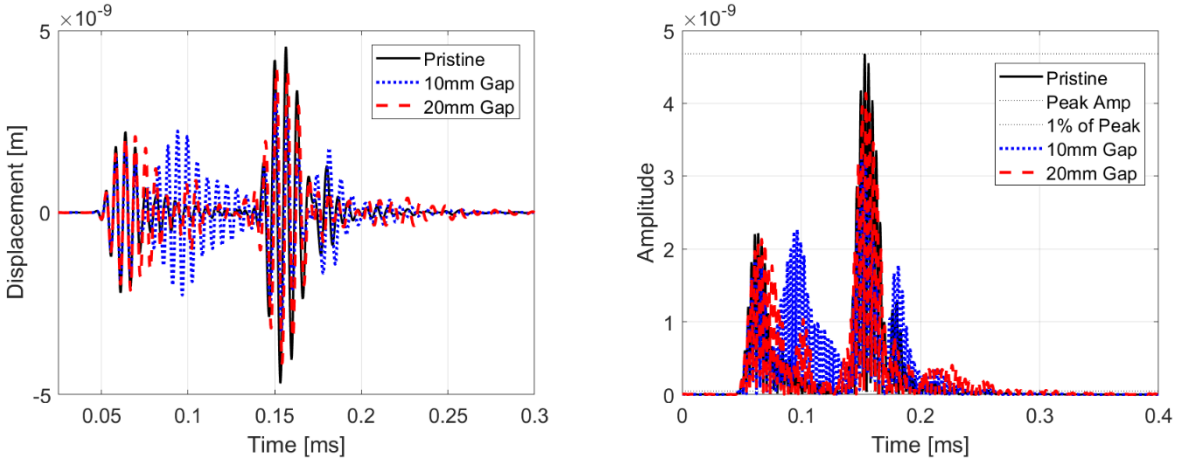

(a) Selected signals (b) Absolute value of the time signal

Figure 4-30 Comparison of the time signals between pristine and 2 gap defect sizes

The changes are complex in which a new wave packet appears between the main S_0 and A_0 mode, A_0 mode has a noticeable amplitude drop and phase delay, and the new packet tail appears

after the main A_0 mode. Despite the smaller defect size some of these changes seem to be more severe in 10 mm than in 20 mm gap size. This could be the result of different wave modes, originated from the scattering of different Lamb modes overlapping in time and the changes are diminished. Since the signals exhibit various degree of amplitude, phase and waveform changes, a combination of DIs based on these criteria are used and are described as the fundamental DIs.

Fundamental Damage Index Calculations

DI_1

DI_1 is an amplitude-based DI using the cross-correlation of the damage signal, $xcorr_{damage}$, with the pristine signal. The cross-correlation between two signals, $xcorr(R_2, R_1)$ can be graphically illustrated by Figure 4-31. As an example, both R_1 and R_2 are displacements for pristine case whereas $R_1$is taken 25 mm to the left of R_2. By time shifting the signal R_1 in Figure 4-31a, the sum the product of the signals, R_2 and $R_1$is calculated at each time shift to be the cross-correlation as shown in Figure 4-31b.

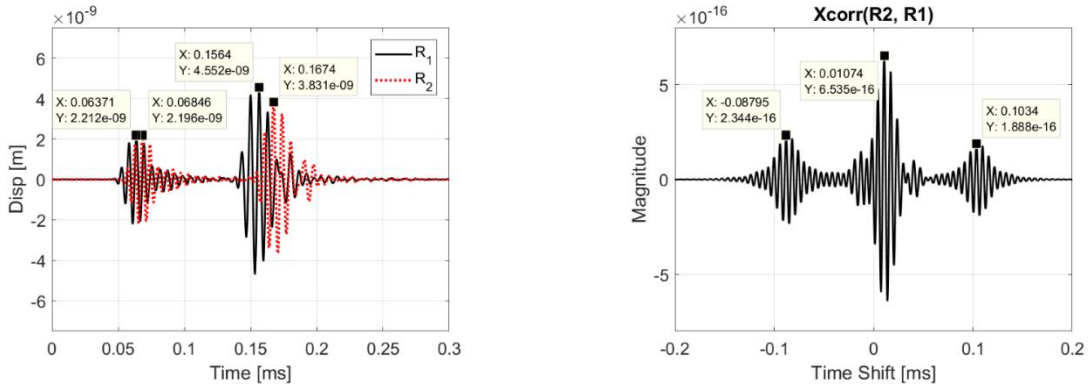

(a) R_1 is measured a location to the left of R_2 (b) $xcorr(R_2, R_1)$

Figure 4-31 Sample cross-correlation of two signals

The biggest peaks corresponding to the time shift of $R_1$to have the most overlap with R_2 namely, both the A_0 and S_0 modes are approximately overlapping. The left and right-side peaks of the cross-correlation are the overlapping of A_0 or R_1overlaps with S_0 of R_2 and S_0 of R_1overlaps with the A_0 of R_2. Equation (4-2) defines the DI in which the ratio between the peak of the

absolute value of the cross-correlation of damage signal being R_2 and the pristine signal being R_1. The autocorrelation, $auto\ corr_{prisinte}$, is the cross-correlation of the pristine signal with itself and is then used to describe the peak amplitude change.

$$DI_1 = 1 - \frac{\max\{|xcorr_{damage}|\}}{\max\{|auto\ corr_{prisinte}|\}} \tag{4-2}$$

Figure 4-32 shows the autocorrelation, and the cross correlation calculated from the 10 mm, and 20 mm gap defect signals. Since the peak is centered around time shift of 0 value, DI_1 is capturing the amplitude change of A_0 and S_0 modes, with the A_0 mode being more influential. Therefore, the variation of DI_1 appears in similar trend as the peak amplitude of A_0 mode with respect to damage size. This DI is unitless and is bounded between 0 and 1, thus it is straightforward to compare the DI values between measurements. However, as this DI is amplitude based, when applied to the physical measurement, extreme caution must be taken to control the amplitude to ensure a fair comparison between pristine and damage signals. This might not be always possible when multiple transducers are used, as the transducers and the measurement system could have difficulties in to quantifying the amplitude variations or their own. DI_1 is less effective to represent the appearance of new wave packets or phase delay because the peak value of the cross-correlation does not utilize the information contained in the lower amplitude parts of the time signal. Therefore, DI_1 is sometimes used with the windowing of time signal to compensate for these shortcomings. However, it is difficult to generalize a specific set of time windows to processing of other signals. This issue will be addressed in the discussion to follow.

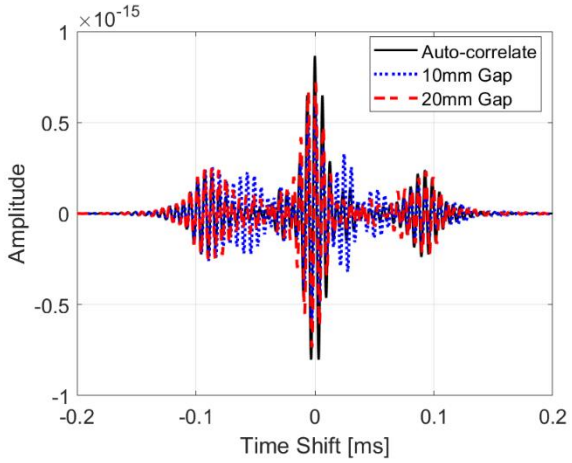

Figure 4-32 Auto-correlation (solid line), cross-correlation of 10 mm (dotted line), 20 mm gap (dash line) cases with pristine signal

DI_2

Based on the waveform observations, a DI is needed to account for the scattered wave packets in a signal. The formation of new wave packets associated to the scattered waves generally reduces the amplitude of the main wave packets. This is the case when a gap defect of 10 mm to 15 mm size under 175 kHz excitation as shown in Figure 4-26and Figure 4-27a. Therefore, DI_2 is designed to account for new wave packets when compared to the pristine case. For the calculations of DI_2, it is important to discount the small fluctuations due measurement noise in experiments, or the numerical error in model data. For the data presented in this section, the signals with amplitude less than 1% of the peak amplitude is set to 0. Then, the number of data points with non-zero values are counted for the DI calculation using Equation (4-3).

$$DI_2 = \frac{\text{num of dat pt} > 1\% \text{ peak in damage case} - \text{num of dat pt} > 1\% \text{ peak in pristine case}}{\text{num of dat pt} > 1\% \text{ peak amp in pristine case}}$$

$$= \frac{\text{num of dat pt} > 1\% \text{ peak in damage case}}{\text{num of dat pt} > 1\% \text{ peak amp in pristine case}} - 1 \quad (4\text{-}3)$$

The increase in the number of data points in the damage case would indicate the formation of new wave packets due to wave-scattering. Since the number of data points is used for the DI

calculations, it does not rely on the absolute magnitude of the signal and the entire signal is considered. The DI takes a positive value when additional scattered wave packets is present in the damage signal when compared to the pristine signal. However, when the waves are in destructive interference, this DI could be negative. Alternatively, the DI can be defined as:

$$DI_2 = \frac{|\text{num of dat} > 1\% \text{ peak in damage case} - \text{num of dat} > 1\% \text{ peak in pristine case}|}{\text{num of dat pt} > 1\% \text{ peak amp in pristine case}} \tag{4-4}$$

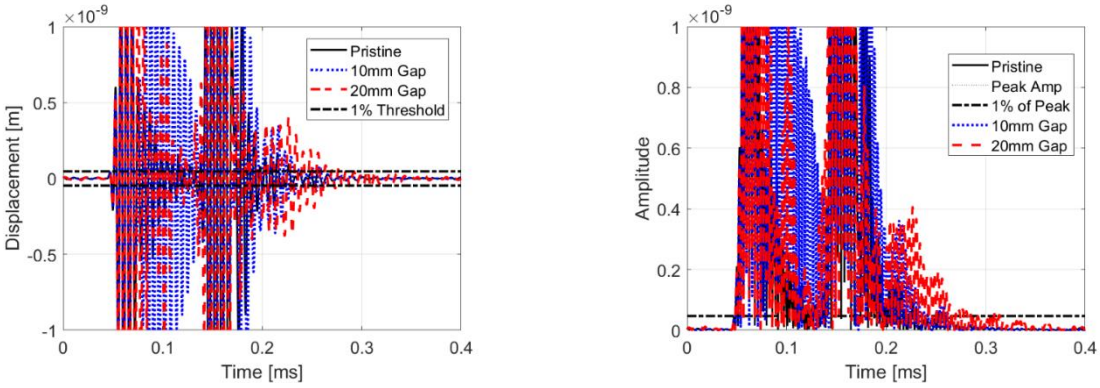

(a) Waveform (b) Absolute value of the waveform

Figure 4-33 Signals of the pristine and damage cases along with the 1% of the peak amplitude of the pristine case

Figure 4-33 shows the signals of the pristine and damage cases along with the 1% threshold. A drawback of DI_2 is the vaguely defined threshold. The 1% threshold is used here because of the numerical noise produced by the Fourier transform and other sources. Other thresholds should be determined under different experimental or numerical conditions.

DI_3

In some cases, the waveforms are not changed significantly in the transmitted region when compared to the incident waves. The scattered waves could be in interference with the main wave packets. By taking the difference of the damage signal with the pristine signal (see Figure 4-34), the waveform associated to the scattered waves can be made more visible.

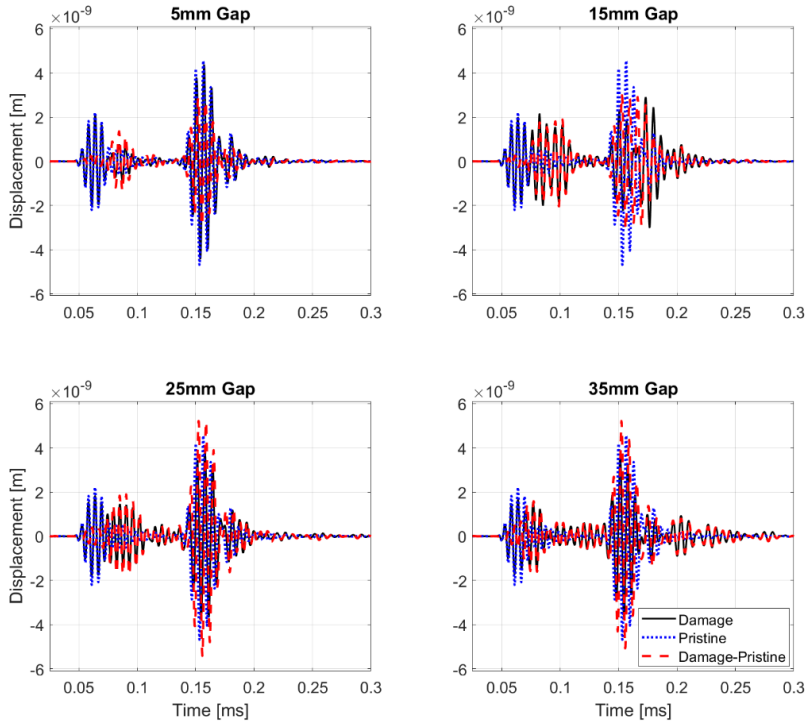

Figure 4-34 Selected cases of the damage (solid line), pristine (dotted line), and the difference (dash line) of signals

When a phase shift less than a period occurs between the pristine and the damage signals, the signal difference would sum the amplitude of the two waveforms and the phase change information is strongly retained. Based on the signal difference, DI_3 is then defined as:

$$DI_3 = \frac{\frac{1}{2}\int|\text{damage signal} - \text{pristine signal}|\text{dt}}{\int|\text{pristine signal}|\text{dt}} \tag{4-5}$$

DI_3 uses the area under the signal difference to quantify the amount of scattered waves and phase changes. To ensure the area is summed over the entire signal, the absolute value of the signal difference is used. For the DI to be unitless, the area of the signal difference is divided by the area under the pristine signal. Consider the case of a damage signal with exactly half a period phase shift with respect to the pristine singal, the maximum signal difference would result in two

times the amplitude of the original signal. Therefore, a factor of ½ is used to ensure the DI is bounded between 0 to 1. DI_3 accounts for both amplitude and phase changes. Since the amplitude is compared between the pristine and the damaged signal, it requires careful measurement to ensure proper signal cancelation between two signals. In experiments, it is difficult to ensure that two repeated measurement to be identical. Namely the contact between the transducers and the surfaces of the material or taking measurements with two different sets of transducers can produce some signal differences. In order to better compare the waveforms from different experimental measurements, it is typical to normalize each signal with the peak amplitude of the signal, which is often the A_0 mode. However, normalizing the signals with respect to the peak of S_0 mode could be advantageous for a number of reasons. Figure 4-35 shows the GL model predicted waveform for various gap sizes separating S_0 and A_0 mode. The changes in S_0 mode are less apparent than the A_0 mode. The main S_0 packet has small amplitude changes but with no visible phase changes. This is because S_0 mode has longer wavelength than A_0 mode at a given frequency and thus less sensitive. Assuming the primary contribution are the fundamental modes, the slower A_0 main packet is more likely to change due to interference of the scattered waves.

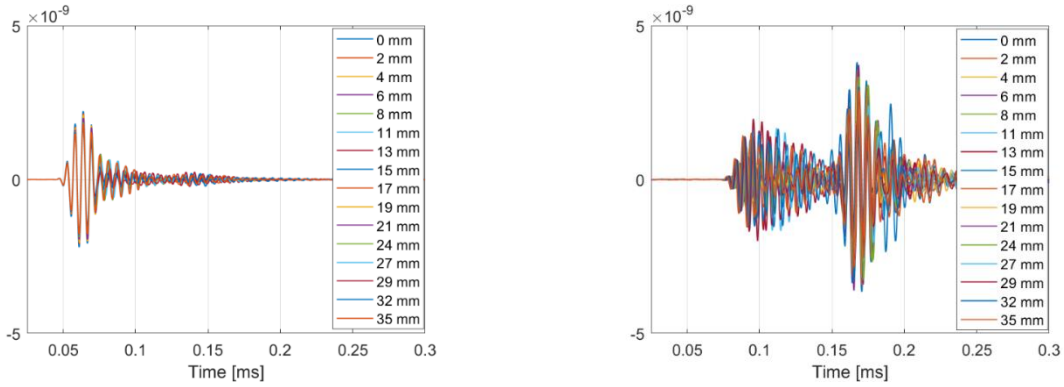

(a) S_0 mode (b) A_0 mode

Figure 4-35 Overlapping modal displacement for gap sizes with 175 kHz excitation

Since the changes of the primary S_0 packet is among the smallest due to damage, if the measured signals are normalized with the peak of the S_0 mode, the changes due to the transducer contact and response could be reduced. By doing so, DI_3 could be applied with greater effectiveness for experimental data.

DI_4

The previous DIs was, in some way, comparing the amplitudes of the damage and pristine signals. A DI that only considers the phase change information would be less affected by the amplitude changes due to measurement conditions. The analytical signal, in which the real part is the signal itself and the imaginary part is the Hilbert transform of the signal, is helpful in determining the phase information. Specifically, the following DI utilizes the (averaged) instantaneous frequency calculated from the analytical signals to capture the phase change due to waves scattering. The instantaneous frequency of a monocomponent signal can be estimated from the time rate of change of the phase angle of the analytical signal. If the signal is not monocomponent, the average of the instantaneous frequency is estimated instead. This DI is based on the fact that when waves scattering occurs, the mixing of wave modes would induce instantaneous frequency changes to the time signals. The converse is true, the instantaneous frequency sees smaller variation in the time period of the main packets. The line data in Figure 4-36 shows the instantaneous frequency between 0.04 ms and 0.3 ms for the selected gap sizes under a 175 kHz excitation.

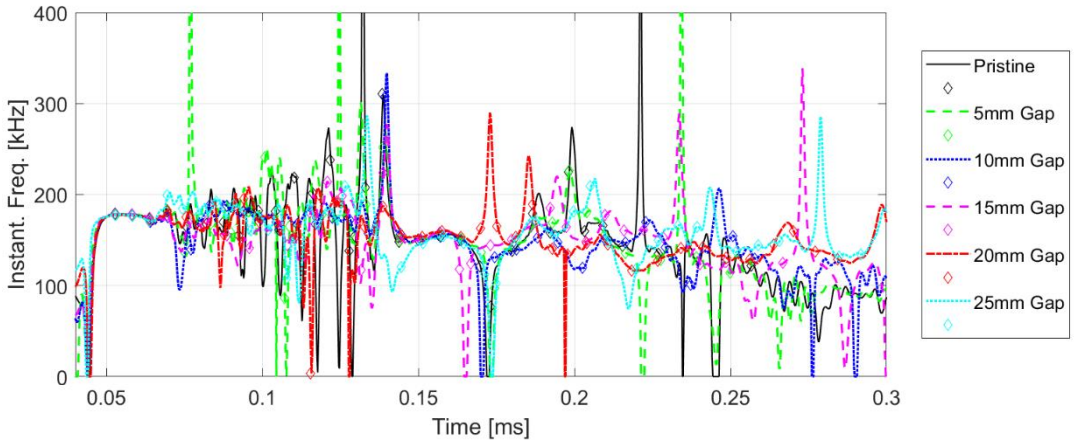

Figure 4-36 Instantaneous frequency of some gap damage cases with 175 kHz excitation. The diamonds are the data point correspond to the values at waveform peaks

In order to better capture the frequency changes due to mode mixing, the values of the instantaneous frequency that coincide with the waveform peaks and troughs are selected. The values at the peak times are shown in diamond in Figure 4-36. The time that corresponds to the extremum of the waveform is found by taking the difference of the consecutive values of the time series. Then use the sign change of the difference to indicate the time index at which the extremum occurs. Figure 4-37a, b shows the time signals, the difference of the consecutive values of the time series, and the extremum points for the pristine and 10 mm gap signals, respectively. Figure 4-37c, d shows the extremum points for all gap sizes. It can be seen that in the time period of the main wave packet, the extremum points are of regular pattern indicating little phase delay as the gap size increases.

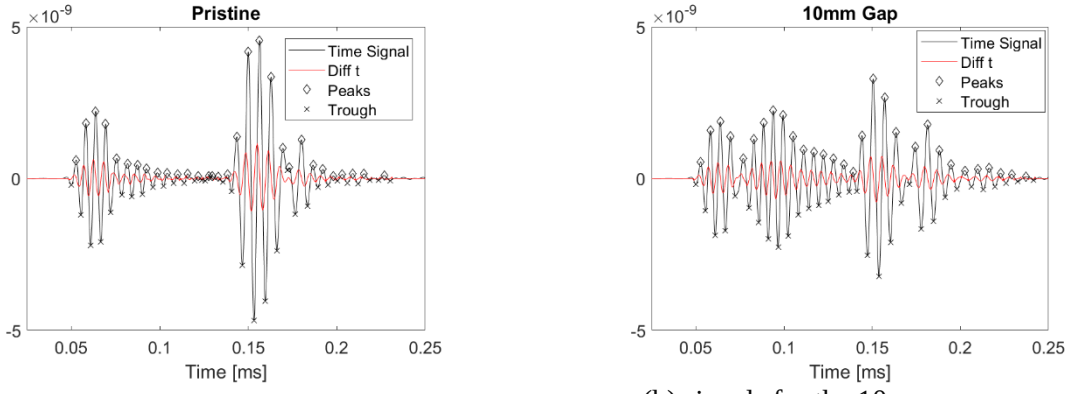

(b) signals for the 10 mm gap case

(a) Pristine signal, showing the signal itself, the difference of the entries, and the identified peak and trough

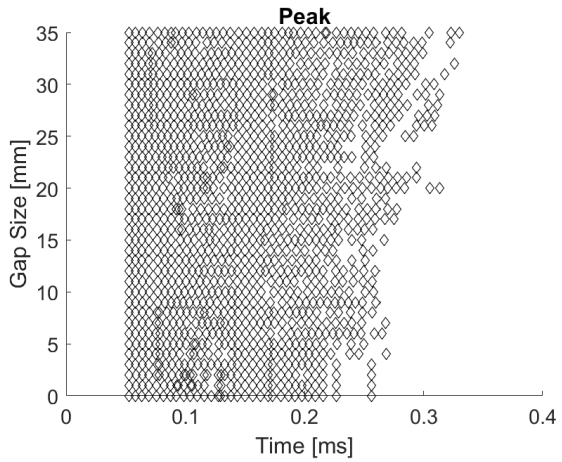

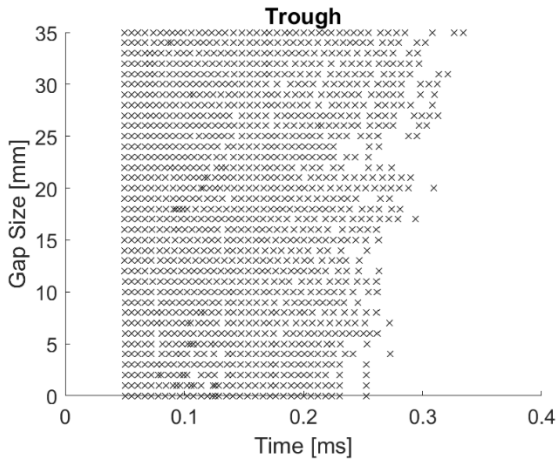

(c) Peaks of all the gap cases

(d) Trough of all the gap cases

Figure 4-37 Identifying the peaks and trough of the time signals for gap defect under 175 kHz excitation

Using the instantaneous frequency at the extremum points, DI_4 is defined as:

$$DI_4 = \frac{\sum(|\text{Inst. Freq of Damage} - \text{Inst. Freq. of Prisitne}|)\text{at damage case extremum}}{\sum(\text{Instant. Freq. of Pristine Signal })\text{at pristine case extremum}} \tag{4-6}$$

All the frequency changes are sum over the extremum points and then it is normalized by the instantaneous frequency calculated in the pristine case. Figure 4-38 shows the data points that are used to calculate DI_4.

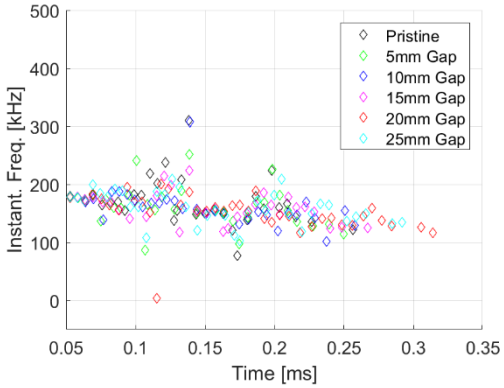

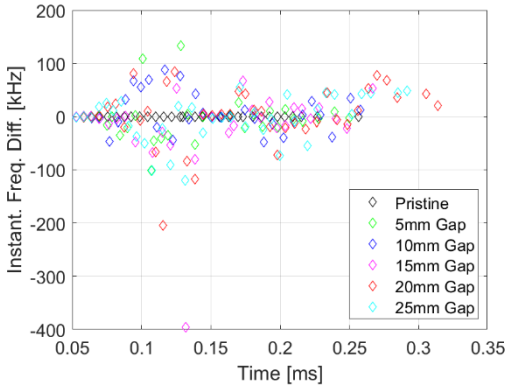

(a) Instantaneous frequency

(b) Difference of instantaneous frequency between the damage and pristine case

Figure 4-38 Data points at the peak points for various gap sizes

The instantaneous frequency is found to give a systematic way to determine a time window associated to the main wave packets. By taking the difference in consecutive entries of the instantaneous frequency, the time periods with smaller variations are those of the main wave packets. Figure 4-39a shows the absolute value of the difference in instantaneous frequency calculated from the pristine signal. The time periods with small amplitudes could be used to define the time windows for the main S_0 and A_0 modes (indicated by the red and blue arrows, respectively). The time window associated to the S_0 mode and the signals for the different damage cases are shown in Figure 4-39b. The windowed signal has the least of wave interference since it is the fastest traveling wave mode and thus the waveform changes are simpler for DI calculations. As an illustration, using the time window shown in Figure 4-39b and calculate DI_1 (peak of cross-correlation) for the signals measured at $x^{II} = 125$, the DI values are plotted in Figure 4-40b. This DI shows less fluctuation when compared to DI_1 that is calculated from the entire time signal as the defect size increases.

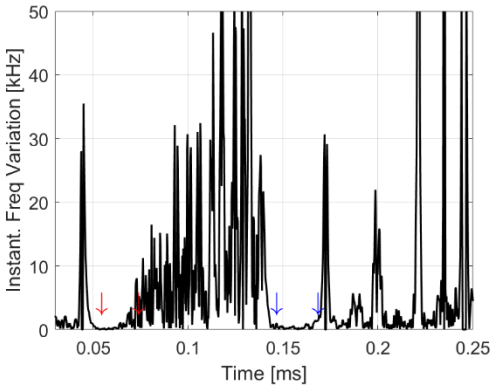

(a) Absolute value of the difference of the consecutive entries in the instantaneous frequency where red and blue arrows marks the main S_0 and A_0 modes, respectively

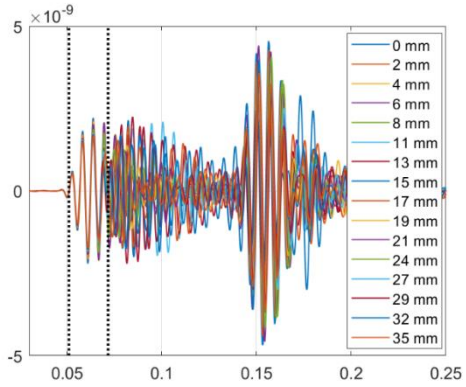

(b) Overlapping signals for different gap sizes, with the time window of S_0 mode shown in the vertical dotted lines

Figure 4-39 Time windowing of the main packets using instantaneous frequency determined to be 0.051 ms to 0.07 0ms for S_0 mode and 0.143 ms to 0.165 ms for A_0 mode for measurement taken at $x^{II} = 125$ mm

Evaluating the Performance of the Damage Indices

In this section, the results are presented for the DIs calculated from the waveforms obtained for all the damage cases. The relationships between the defect sizes and the DI values are plotted to evaluate their effectiveness in characterizing damages. The DIs results are used to determine if it is feasible to distinguish the two types of defects, to estimate the defect size or to determine if the defect is on the upper or lower half of the laminate.

First, the robustness of the DIs is evaluated. Figure 4-40 plots the four DIs for the gap defect (Type 1) in full hybrid composites (Config. A) using signals measured at different receiver locations (x^{II} = 100 mm, 125 mm, 150 mm, 175 mm). The line data are the calculated DIs using the signals associated to defect sizes of 0mm (pristine) to 35 mm, in 1 mm increment, which is being referred to as the training dataset. The cross points are additional data points calculated from the models with gap sizes of 3.5, 7.5, 14.5, 18.5, 21.5, 28.5, and 33.5 mm, which is being referred to as the validation dataset. The DIs are for the disbond defect is shown in Figure 4-41, whereas the validation dataset is calculated from models with disbond sizes of 4.5, 9.5, 12.5, 17.5, 22.5, 26.5, and 32.5 mm instead.

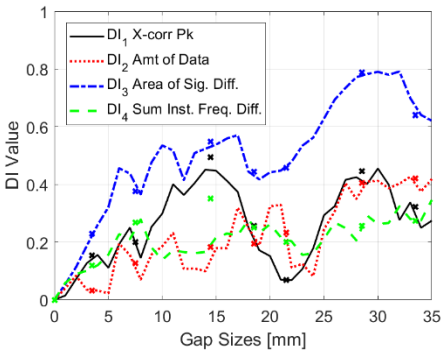

(a) x^{II} = 100 mm

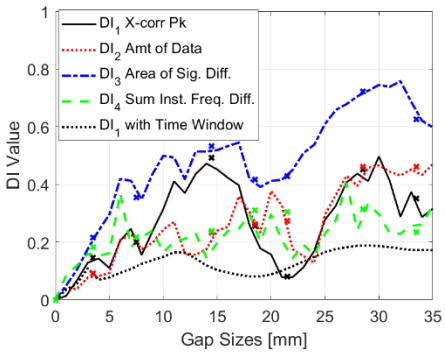

(b) x^{II} = 125 mm

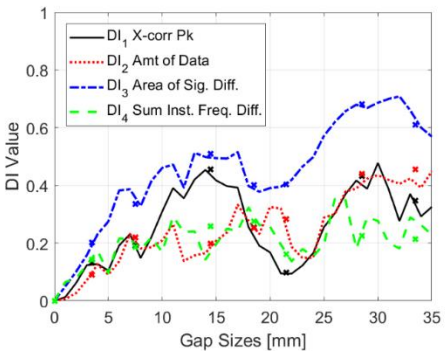

(c) $x^{II} = 150$ mm

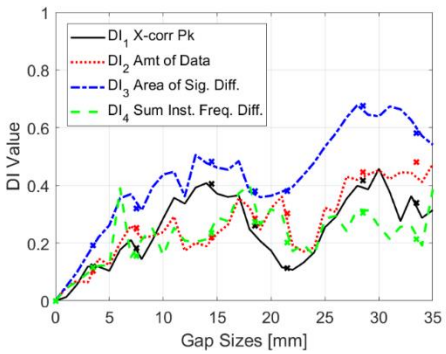

(d) $x^{II} = 175$ mm

Figure 4-40 DIs for gap defect with 175kHz excitation. Cross points are calculated from validation cases

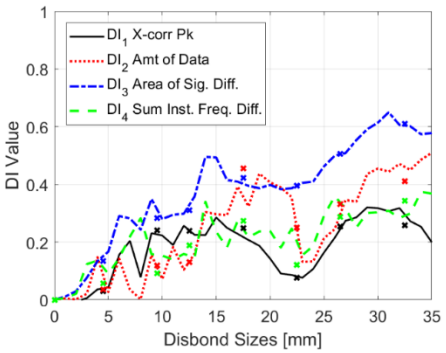

(a) $x^{II} = 100$ mm

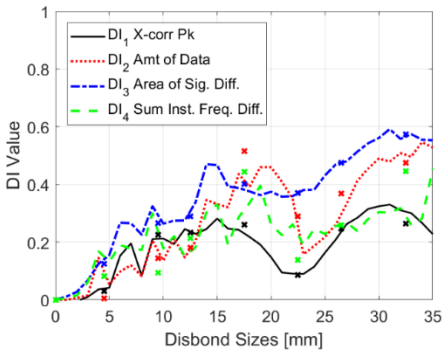

(b) $x^{II} = 125$ mm

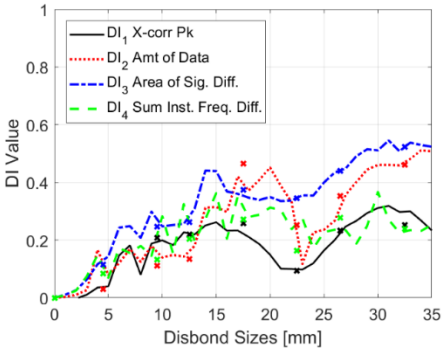

(c) $x^{II} = 150$ mm

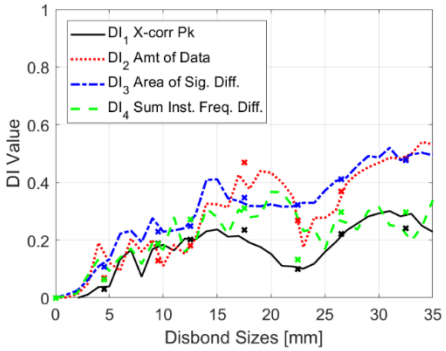

(d) $x^{II} = 175$ mm

Figure 4-41 DI for disbond with 175kHz excitation. Cross points are calculated from validation cases

Despite that the DIs are unitless, the theoretical upper bounds for each of the DIs may not be the same. Therefore, the sensitivity of the DIs may not be evaluated by the DI magnitude. Instead, a better performing DI should take a unique value for each damage case, and the value should not fluctuate in a small neighborhood of a given defect size. DI_1(solid black line) shows similar fluctuations as DI_3 (blue dash dot line) for both the gap and disbond defects. In particular, the

fluctuations above 10 mm defect size is qualitatively less than smaller defect sizes. The reason for the worse performance in the smaller defect sizes is that the peak amplitude changes in the A_0 and S_0 mode is small. Between the defect sizes of approximately 15 mm to 28 mm, DI_1 is not unique due to the fact that the A_0 mode amplitude increases to a peak near 21 mm. DI_2 and DI_4 perform poorly in terms of the fluctuations with respect to different defect sizes. This could be due to the complex interactions of the different wave modes. However, DI_2 and DI_4 could be used to compensate the decrease in DI_1 between 15 mm to 28 mm defect sizes. DI_3 is the best performing DI due to the fact that the DI show less fluctuations and has a monotonic trend in most of defect sizes. Almost all of the validation dataset (cross points) falls in between the data points of the training set, indicating that the increment of the defect size in the training set is sufficiently fine. The notable exceptions are DI_1, DI_2, and DI_4 with 17.5 mm disbond. The validation set consistently under predict the DI values. In practical applications, the transducer placement could vary for different inspections. Thus, the DI should perform similarly despite the waveform signals are measured at different locations. Figure 4-42 plots the four DIs for the gap defect at the four different receiver locations.

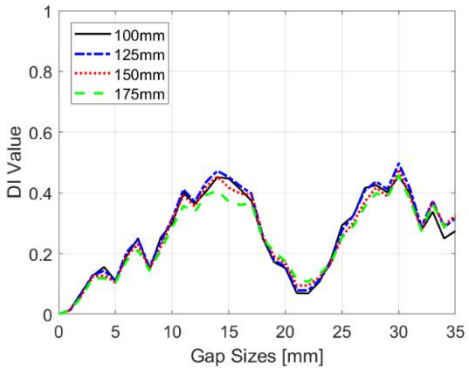

(a) DI_1 – Cross correlation peak

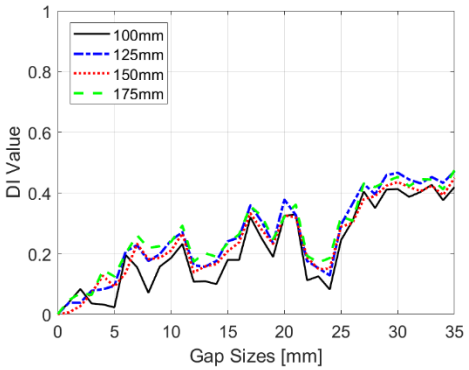

(b) DI_2 – Number of data points > 1%

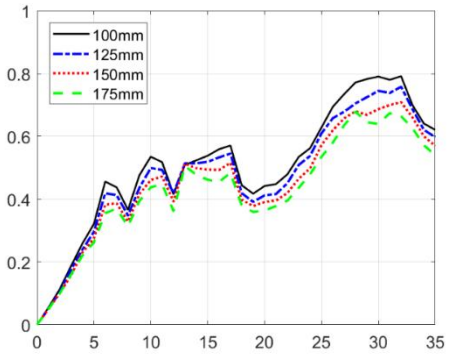

(c) DI_3 – Area of signal difference

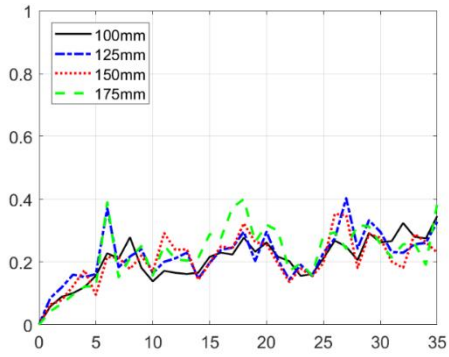

(d) DI_4 – Sum of instantaneous frequency change

Figure 4-42 DI changes using signals measured at $x^{II} = 100$ mm, 125 mm, 150 mm, 175 mm for gap defect at 175 kHz excitation

Among the four DIs, DI_1 is least affected by the location. This could be due to the fact that the peak amplitude of is normalized to the pristine signal and the effects of attenuation is accounted for. The influence of mode mixing is not as sensitive in DI_1 and it is another reason why it is less sensitive to measurement distance. In contrast, DI_3 is distant dependent and increasingly affected by measurement distance with larger defect sizes. This is likely due to the fact that the "signal of the scattered waves," calculated by taking the signal difference of the damage and the pristine signal, is larger with an increased phase change at longer distances. This dependency of measurement distance is not obvious in DI_2. It remains unclear how the addition of scattered wave packets varies at different distances. The performance of DI_4 is poor as the variation in distance is chaotic with respect to the increase in defect size. With the 175 kHz excitation, the ultrasonic wave is not sensitive to that size of defect and the waveform is similar to the pristine case. Base on this assumption, a set of study with 125 kHz excitation frequency is conducted, and the choice of 125 kHz is based on the result from Figure 4-14b that at this frequency, the transducers have a strong response. Figure 4-43 shows the four DIs calculated for 125 kHz and the performance of the DIs is similar to the case of 175 kHz. DI_4 and DI_1 has fewer fluctuations than the other DIs. DI_2 has perform noticeable much worse. This could be due to the fact that at

lower frequencies, S_0 mode is less excitable and thus the reduction of S_0 to A_0 conversion that contributes the most to the generation of new wave packets as in 175 kHz is diminished.

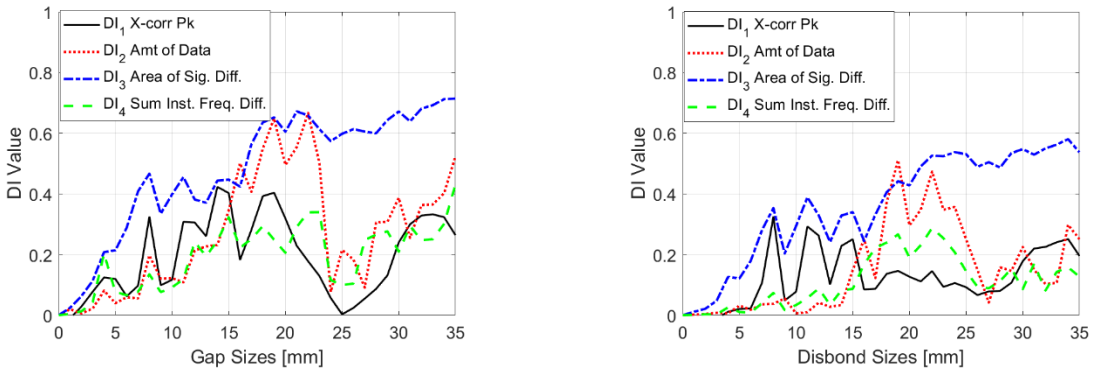

(a) Gap defect (b) Disbond defect

Figure 4-43 DI values for 125kHz excitation using time signals at $x^{II} = 125$ mm

To better compare the better performing DIs between the two frequencies, Figure 4-44 plots $DI_1$and DI_3 using signals measured at $x^{II} = 125$ mm for the gap and disbond defects. It can be seen that the increase of $DI_3$are similar in the two frequencies and when the DIs of the 175 kHz has a distinct minimum between 15 mm to 25 mm defect sizes, the DIs of the 125 kHz set has an approximate maximum. The difference in performance of the DIs at various frequency-defect size combination may suggest that using multiple frequencies DIs sets could a unique DI versus defect size relationship. DI_1 for 125 kHz preforms poorly as it has a stronger minimum between 18 mm to 32 mm in the gap defect case.

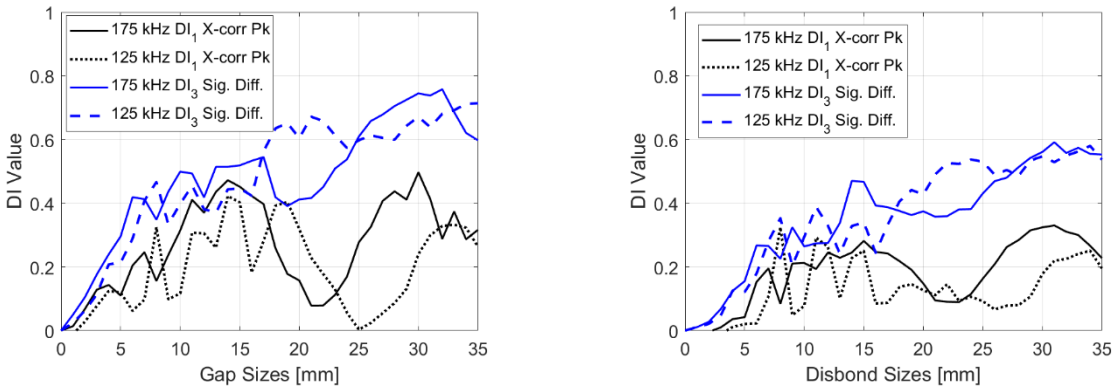

(a) Gap defect (b) Disbond defect

Figure 4-44 Comparing DI_1 and DI_3 for the two excitation frequencies

Another aspect to explore is to determine whether it is possible to differentiate the gap defect in the top or in the bottom Ti ply. Figure 4-45 shows the four DIs using signals with 175 kHz excitation measured at $x^{II} = 125$ mm for the top and bottom gap defect in the transition region (Config. B).

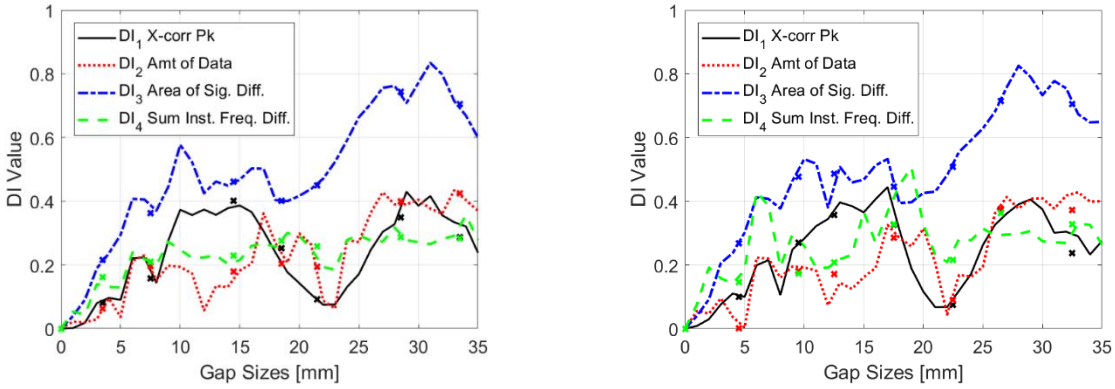

(a) Top Gap (b) Bottom Gap

Figure 4-45 DI values for gap defect at the transition region with 175kHz excitation using signals measured at $x^{II} = 125$ mm

All four DIs for are checked with validation set (plotted as crosses) with gap sizes 3.5, 7.5, 14.5, 18.5, 21.5, 28.5, and 33.5 mm for the top gap, and 4.5, 9.5, 12.5, 17.5, 22.5, 26.5, and 32.5 mm for the bottom gap cases. The DIs calculated from the validation sets are fall in the trendlines of the training set. DI_1 and DI_3 are the better performing DIs as in gap defects in the transition region as well. For these two DIs, DI_1 shows a distinct different trend between the top and bottom gap for gap sizes between 10 mm to 15 mm. However, visual inspection of the DIs shows no clear distinction between the top and bottom gap cases.

Finally, the DIs for the disbond damage in the transition region is compared to the disbond in a full hybrid laminate. Figure 4-46a plots the four DIs for the former case with 175 kHz excitation and calculated using signals measured as $x^{II} = 125$ mm. Thus, it should be compared to the DIs plotted Figure 4-41b for the full hybrid case. DI_1 and DI_4 have less fluctuation in disbond size greater than 15 mm. These two sets of DIs are compared to the full

hybrid cases in Figure 4-46b. The comparison shows that the DIs are not indicative whether the disbond is in a full hybrid or in the transition region, rather only the disbond size can be deduced with higher level of certainty.

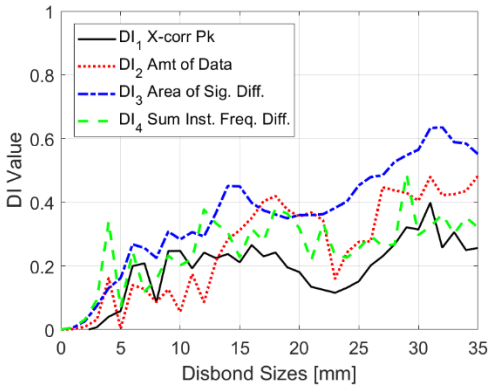

(a) DIs for disbond defect in transition region

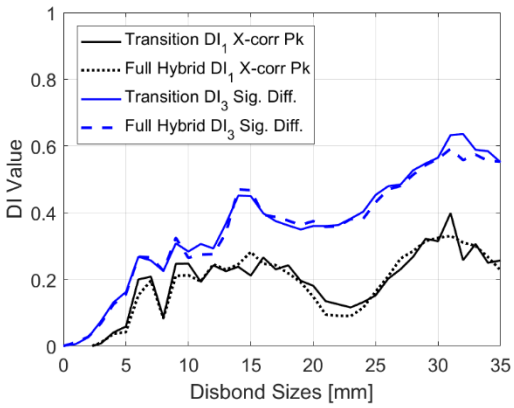

(b) Comparing DI_1 and DI_3 between disbond defect in transition region and in full hybrid

Figure 4-46 DIs of the disbond defects in transition region calculated from signals at $x^{II} = 125$ mm

4.3.4 Damage Characterization for Unknown Test Case

In this section, the DI library obtained from the training cases are being applied to characterize damage for two hypothetical damaged signals (test cases). The two signals are associated to a disbond damage of 24.4 mm long where one of them is simulated in the full hybrid composites (Config. A) and the other is in the transition region (Config. B). Assuming the only priori knowledge is the structure, the four DIs specified in section 4.3.3 are calculated using the newly obtained damage signals and the pristine signal. For the test signals, a single value is calculated for each DI for each structural configuration and the DIs are plotted against the DI library in Figure 4-47a, c and Figure 4-48 a, c, e. The horizonal lines are the DI values for the test cases and at the defect sizes cross the various DI library are the potential defect sizes. Since there is no prior knowledge of the defect type, the DIs calculated from the test case are compared to both the gap and disbond defect library. In order to identify the defect, the four DIs of the test cases should take the same value with the DI library at one defect size for one of the libraries. To

better identify the matching defect size, the test case DIs are subtracted with the DI library and are plotted Figure 4-47b, d, and Figure 4-48 b, d, f. The pink line indicates the difference between the test DIs and the DI library equals to 0.

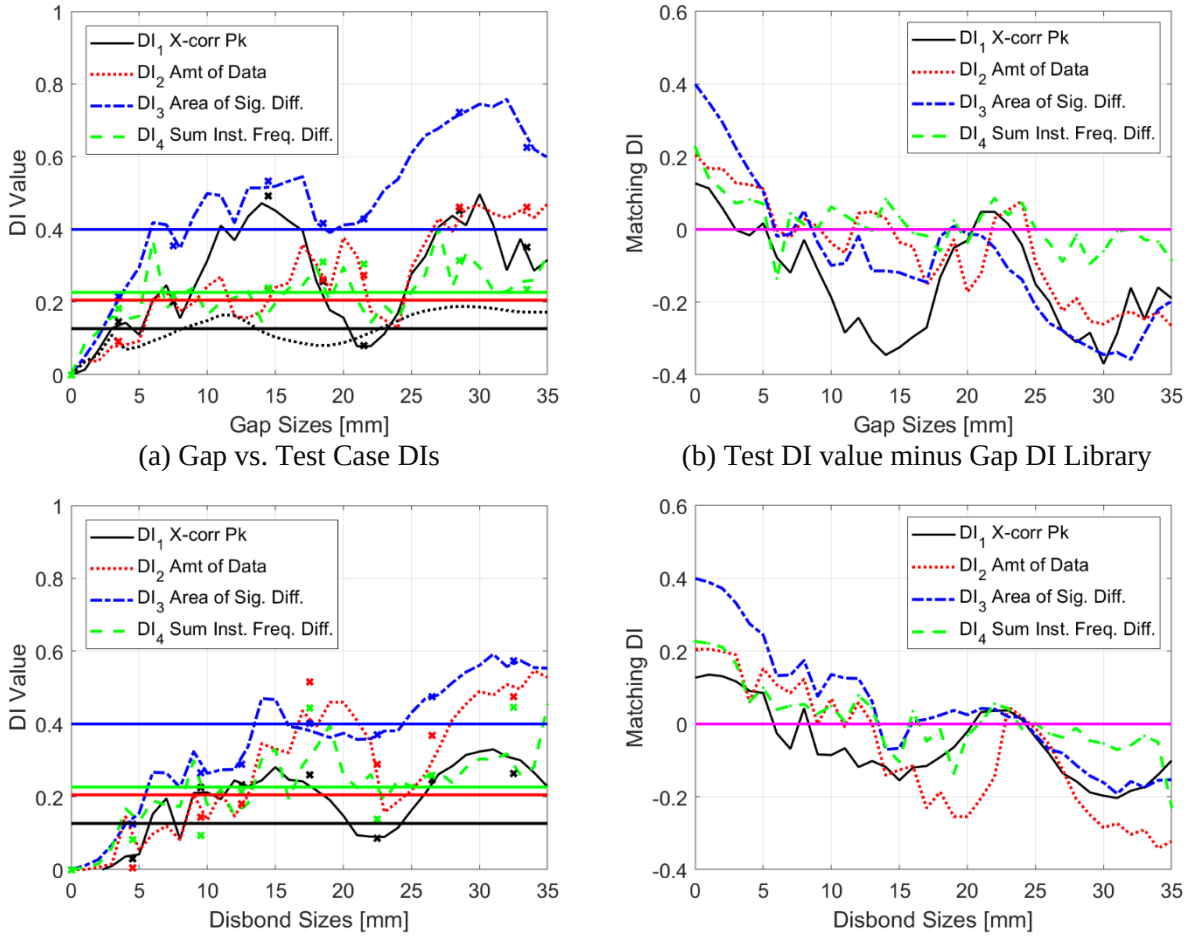

(a) Gap vs. Test Case DIs

(b) Test DI value minus Gap DI Library

(c) Disbond vs. Test Case DIs

(d) Test DI value minus Disbond DI Library

Figure 4-47 Comparing DI library with the DI calculated from the damage signal in the full hybrid composite structure (Config. A)

It can be seen that in Figure 4-47b for the full hybrid structure, no gap size at which the difference in the DIs is close to 0 at a given defect size. Whereas in Figure 4-47d, the difference in DIs approaches 0 at a disbond size just short of 25 mm. Since the disbond size increment in the library is 1 mm, the zero-crossing point could be between 24 mm and 25 mm. Furthermore, it is encouraging that the zero-crossing is unique in the range of studied disbond cases which implies that we can uniquely determine to be one disbond size for the test signal.

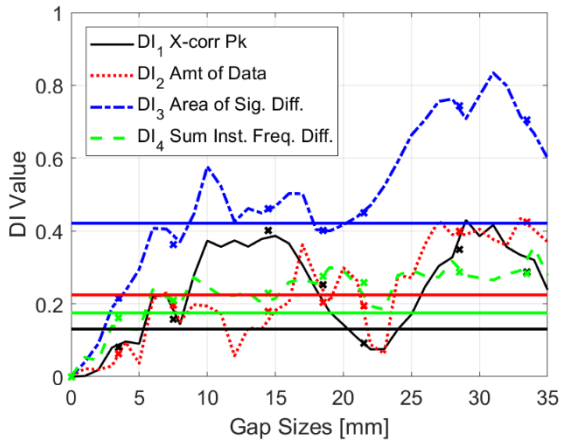

(a) Top Gap vs. Test Case DIs

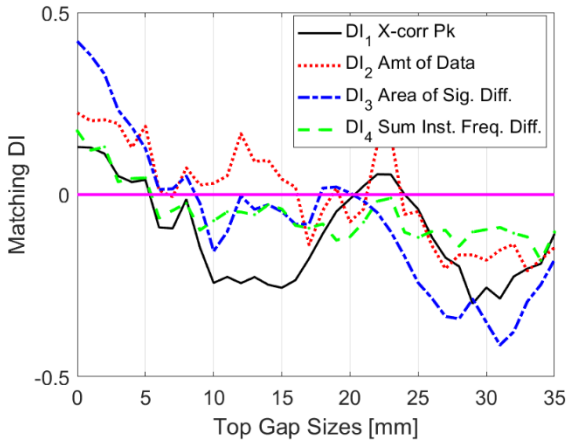

(b) Test DI value minus Top Gap DI Library

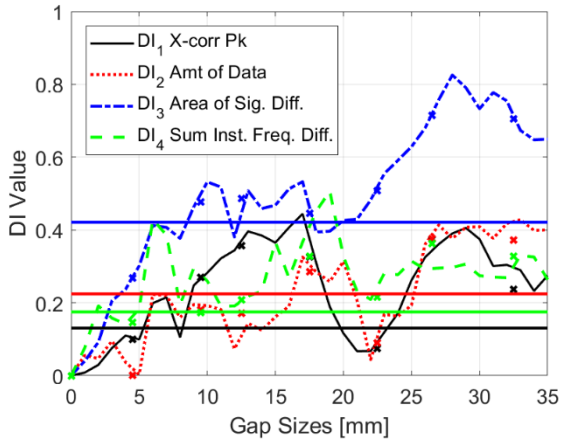

(c) Bottom Gap vs. Test Case DIs

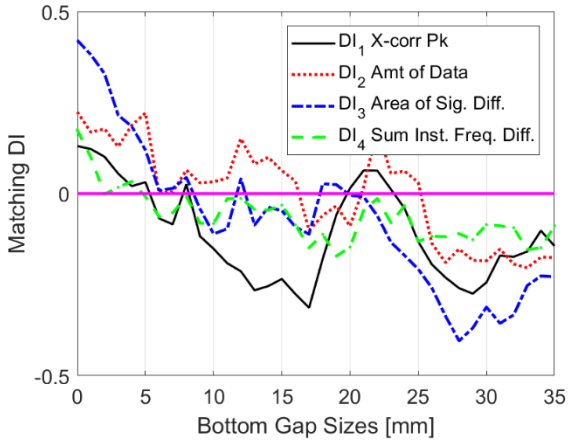

(d) Test DI value minus Bottom Gap DI Library

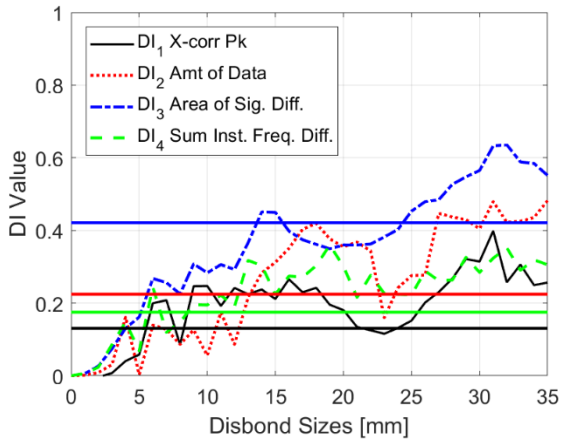

(e) Disbond vs. Test Case DIs

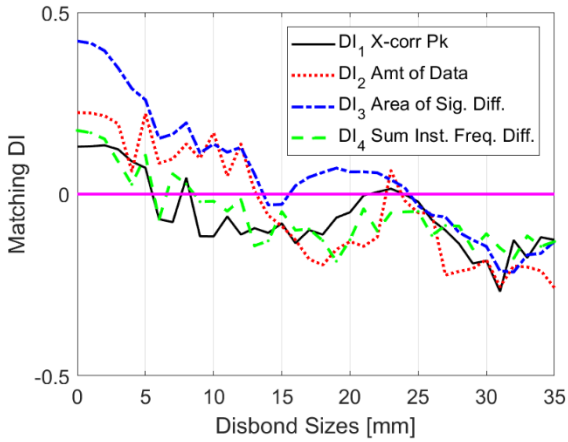

(f) Test DI value minus Disbond DI Library

Figure 4-48 Comparing DI library with the DI calculated from the damage signal in the transition region (Config. B)

Similar results for the transition region are presented in Figure 4-48 b, d, f. In this instance, the difference between the test DI and the DI libraries indicates that the defect could be top or

bottom gap of 8 mm long or a disbond at 24 mm. The sum of the difference between the test case and the library for all four DIs for the top gap is 0.1427, whereas for the bottom gap is 0.1614 and for the disbond base is 0.0861. The smallest of the difference indicates that disbond of 24 mm is the most likely defect associated to the test signal.

Chapter 5 Damage Characterization in Stiffened Composite Structures

Polymer matrix composites such as carbon fiber-reinforced polymers (CFRPs) have superior in-plane structural properties and are increasingly being used for advanced designs. The thin composites panels are often stiffened through a local thickness increase or with bonded stiffeners of different cross-sectional shapes to prevent excessive bending or buckling. These stiffened regions are prone to manufacturing defects, in particular delaminations/disbonds, since it is more difficult to maintain compaction and a uniform resin flow in these regions [36]. Defects in these stiffened regions are particularly detrimental to the structure and are often difficult to inspect with traditional through-thickness non-destructive evaluation (NDE) techniques since it is around irregular regions and testing access is restricted [87].

However, guided wave propagation phenomena in stiffened composites are complex and the wave forms can vary significantly due to the presence of the change in the geometry [88], [89]. Nonetheless, it has been shown that it is generally possible to identify the signal changes in the transmitted waves due to defects in the stiffener. In most aerospace structures, many stiffeners (e.g. ribs) are used and several of them could be present between the source and the receiving transducers when the inspection range is increased. Thus, it is of interest to determine whether it is still feasible to identify signal changes when the guided waves have propagated through several stiffeners. In order to design a guided wave-based damage detection scheme, the signal changes due to different defects, geometry and excitation must be analyzed.

In this work, the efficiency of the coupled formulation as described in section 3.2.2 is being further enhanced by considering multiple stiffeners in a number of local regions to study

their wave transmission characteristics. First, experimental measurements from a composite plate with a T-shaped stiffener are compared with the GL model predictions to gain insights into the guided wave characteristics. Different delaminations are considered in the stiffener to identify the signal changes using the GL model. Finally, the model with four stiffeners with an embedded defect is investigated to determine whether the predicted signal change is indicative of a damaged case when multiple stiffeners are present.

5.1 Flat Stiffener

5.1.1 Finite Element Models and Composite Specimen

Two CFRP plates, one with an added flat stiffener and one without, are cured with the CYCOM970 prepreg with T300 fiber of 3K tow and 2x2 twill. The lamina properties are given in Table 5-1. Both plates have an identical layup of $[60/\ 0/\ 60/\ 60/\ 0/\ 60]_s$ with a ply thickness is 0.225 mm for a total plate thickness of 2.71 mm. The stiffened plate with identical layup ($[60/\ 0/\ 60/\ 60/\ 0/\ 60]_s$) has an additional 12 plies added that is approximately 50 mm wide spanning the full length of the transverse direction (see Figure 5-1 and Figure 5-2 highlighted by the red box). The two plates are trimmed to an approximate size of $450\ \text{mm} \times 450\ \text{mm}$ as shown in Figure 5-2. The GL model of the flat stiffener is made with a local region width of 100 mm, with a nominal element edge length of 75 μm.

Table 5-1 Lamina properties of the stiffened composite panel (density ρ=1543 kg/m^3)

E_{11}[GPa]	E_{22}[GPa]	E_{33}[GPa]	G_{12}[GPa]	G_{13}[GPa]	G_{23}[GPa]	ν_{12}	ν_{13}	ν_{23}
57.25	55.25	13.50	5.20	4.08	3.28	0.06	0.5	0.37

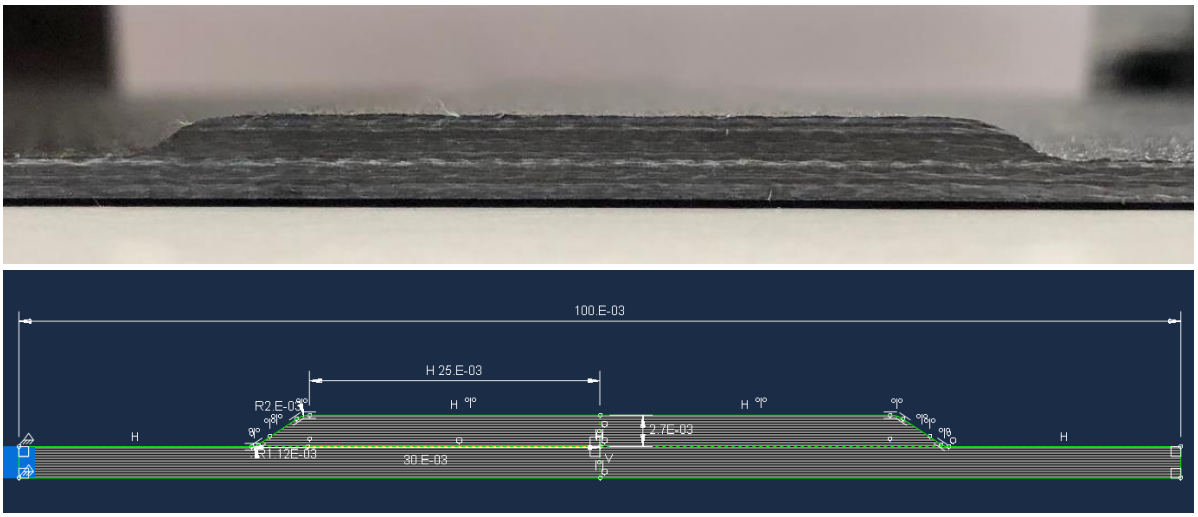

Figure 5-1 Geometry of the flat stiffener and the associated GL model of the local region

5.1.2 Experimental Setup

In this section, an experimental program is carried out to compare the waveform changes predicted by the GL model versus physical measurements between a composite plate with the flat stiffener and the one without it. Figure 5-2 shows the placement of the two plates with 0° aligned with the *x*-axis, and the placement of the various transducers.

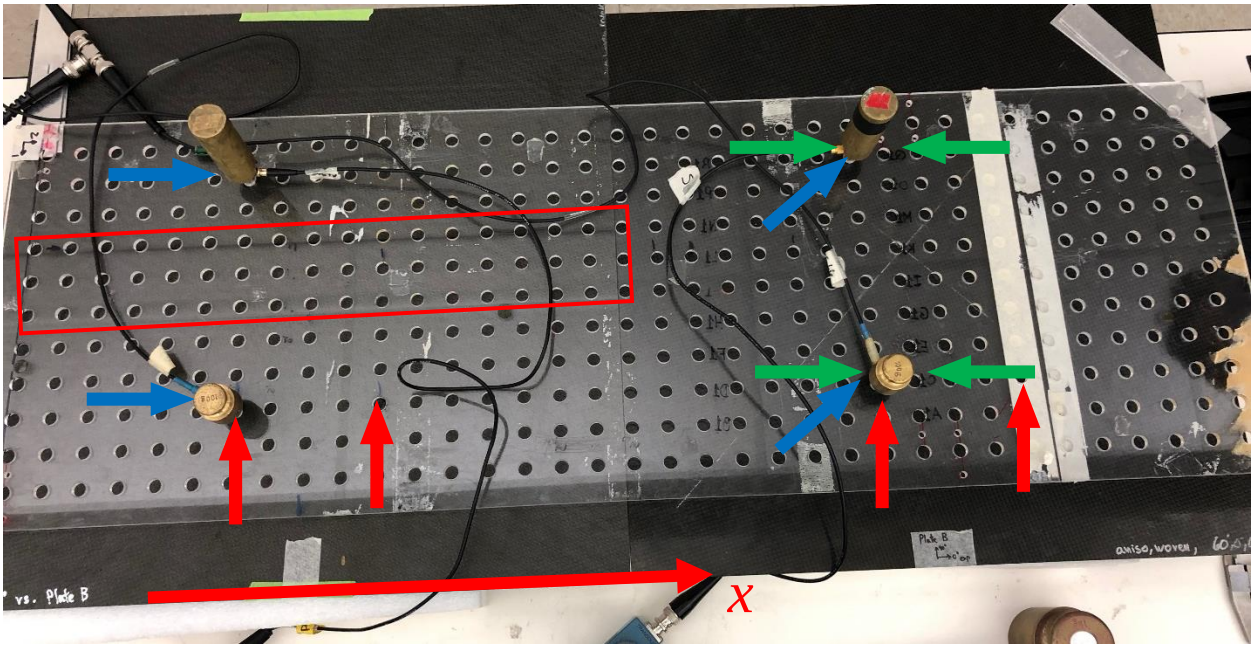

Figure 5-2 Experimental setup to measure the waveform changes between the plate with a flat stiffener and the one without. The colored arrows correspond to the 3 different measurement cases

In order to compare the two plates simultaneously, two pairs of identical models of transducers denoted by pair A-D and pair C-B (i.e. 4 Digital Wave B225) with the source transducer in each pair driving by the same 100 kHz, 5 cycle Hann windowed sine electrical input. Both receiving transducers are filtered and amplified through a signal conditioner (Digital Wave FM-1) and digitized by an oscilloscope (Agillent 54624A) using the same timing trigger. Four sets of signals are recorded, 1) direct (face-to-face) contact of transducer A to D, and C to B to measure the response of their paring, 2) as shown in green arrows in Figure 5-2, both pairs A-D and C-B are placed on the nominal plate (without stiffener) with source and receiver 178 mm apart in the same direction. These two signals are expected to be very similar, 3) shown as red arrows, pair A-D are placed on the plate with stiffener with a wave-path not crossing the stiffener, and pair C-B are placed on the nominal plate with 102 mm source-receiver separation distance in both pairs. Since both plates are manufactured from the same curing cycle, it is expected that the signals from these two measurements are similar. Finally, 4) as shown in blue arrows, pair A-D are measuring across the stiffener, whereas pair C-B are placed on the nominal plate with an identical 178 mm separation distance as pair A-D, with the purpose of showing the effects of the flat stiffener. These four measurements are repeated 3 times Despite some amplitude variations between sets, all three sets of results support the same conclusion and only the results from the first measurement are presented for brevity.

5.1.3 Experimental and Global-Local Model Results

Experimental Results

Figure 5-3 shows the measured waveforms from the four sets of experiments. By comparing the transducer response and the different wave paths, the effects of the stiffener can be isolated.

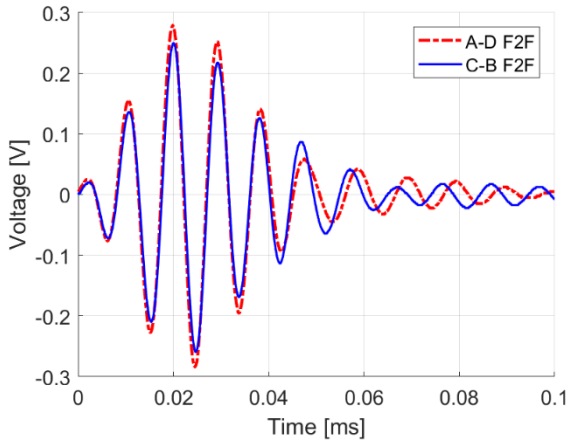

(a) Transducer pairs response

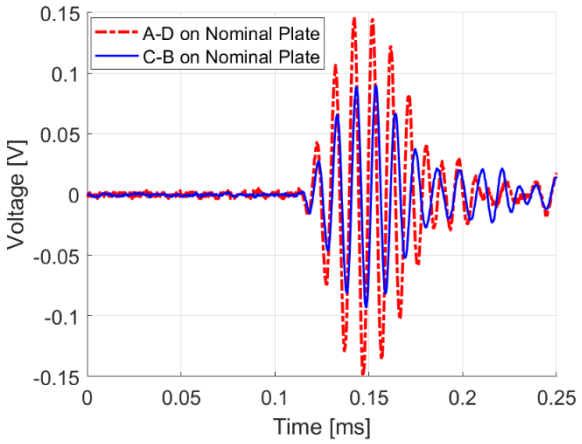

(b) Comparing transducer pairs on nominal plate (green arrow)

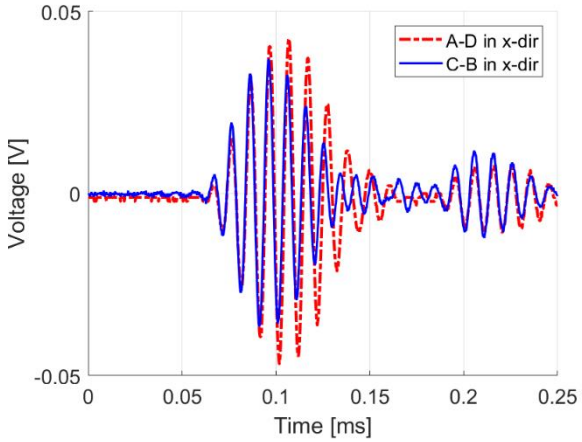

(c) Comparing the response between the two plates without the stiffener (red arrow)

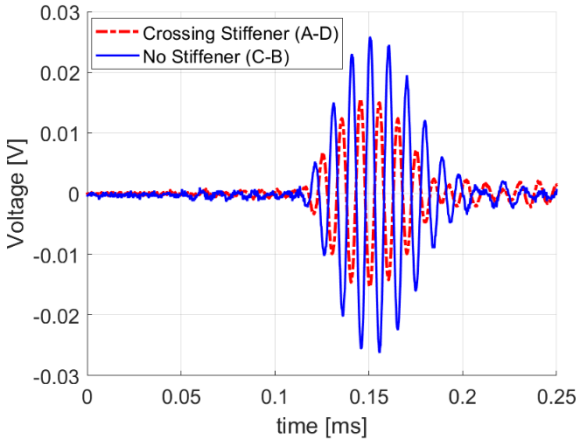

(d) Waveform change due to the stiffener (blue arrow)

Figure 5-3 Simultaneous waveform measurements between the nominal and the stiffened plates

Figure 5-3a shows that the two pairs of transducers have very similar amplitude response under the ideal contact condition. Noticeable ringing in the transducer can be observed, and larger difference in the waveform can be seen in the time period in which the piezo element is free from excitation. This suggests that under excitation, the transducer response, is highly comparable. Figure 5-3b shows the results when both transducer pairs are placed on the same place propagating in the same direction. Assuming reasonable homogeneity in the nominal plate, the two waveforms shall be similar. It can be seen that the phase of the two measurements is identical but there is a difference in amplitude. Since the face-to-face response report similar

amplitudes, this difference in Figure 5-3b is likely to be attributed to the contact conditions between the plate and the transducer. Therefore, only the time shift information shall be considered in the subsequent discussion. Figure 5-3c shows that the time difference between the waveforms measured on the two plates are not noticeable, despite the amplitude difference in the latter half of the packet after 0.1 ms. This is attributed to the difference in transducer ringing as pointed out in Figure 5-3a. Therefore, Figure 5-3c suggests that the time of flight in the nominal region of the two plates is highly comparable. Finally, Figure 5-3d shows that the waveform is delayed by half a period in the case of the passing the stiffener when compared to the wave path with the same distance and orientation in the nominal plate. This phase shift is certainly due to the change in group velocities as observed in the dispersion curves of the corresponding thickness.

Global Local Model Prediction

In order to mimic the experimental measurements, two GL models are used to simulate the wave path with the without the stiffener. Figure 5-4 shows the configuration of the two models. The source model is represented by a 54 mm wide local region subjected to 8 mm wide top surface load with a Gaussian distribution, and the time dependency is using the transducer pair C-B face-to-face measurement presented in Figure 5-3a. The red dot indicates the vertical displacement reporting point that is separated to the center of the source by 180 mm (~7 in) as in the experiment. For the model that represents the reading in the stiffened plate, the source model is coupled with the stiffener local model with the source time dependency using A-D pair transducer response.

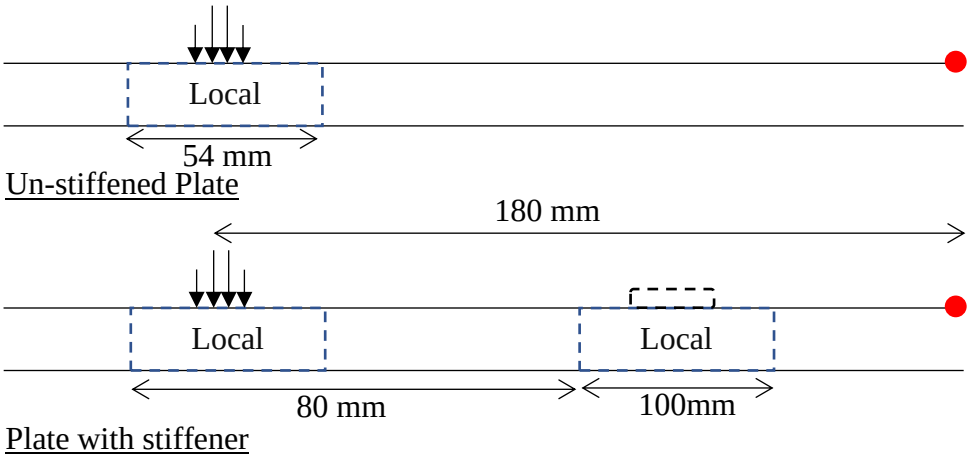

Figure 5-4 GL model configuration to represent the experiment with and without the stiffener

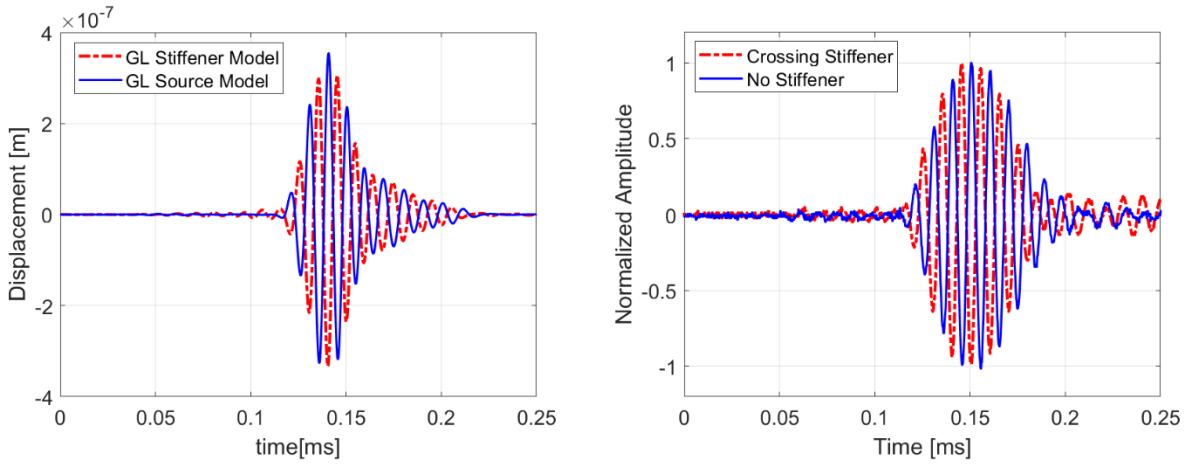

(a) GL model prediction of vertical displacement reported at red dot

(b) Normalized experimental measurement

Figure 5-5 Comparing the effects of stiffener reported by GL model and experiment

Figure 5-5 shows the comparison between GL model predicted waveforms and the experimental waveforms. Since the amplitude in the experimental measurement (Figure 5-3d) varies due to the transducer to plate contact condition, Figure 5-5b shows the waveform with peak amplitude normalized to unity. Figure 5-5a shows that the GL mode predicted waveforms indicate a half period delay if the wave has passed the stiffener, agreeing with the experimental observation. Furthermore, the time of arrival of the wave packet agrees between the predicted and the experimental result at around 0.15 ms. However, the packet shape in the model prediction has a larger reduction in the second half of the packet than that observed in the experiment.

5.2 T-Shape Stiffener

5.2.1 Finite Element Models and Composite Specimen

The composite structure studied in this work is a CFRP plate with a T-shaped stiffener on one side. The plate is manufactured with woven prepreg made with T300 fibers and CYCOM970 epoxy where the cured lamina properties are given in Table 5-1. Figure 5-6 shows the model of the stiffened region, where the base plate has a quasi-isotropic layup of $[-60/\ 0/\ 60/\ 60/\ 0/\ -60]_s$ and the 50 mm × 50 mm

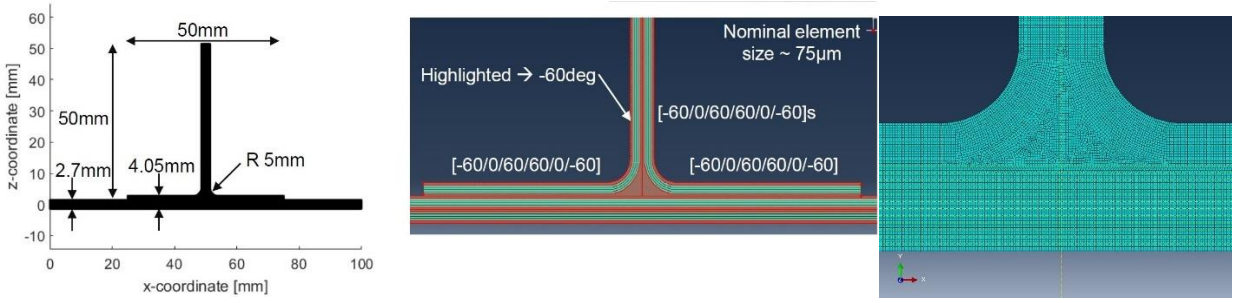

(a) Model Geometry and layup of T-stiffened area (b) FE mesh

Figure 5-6 The FE region of the T-shaped stiffener and CFRP panel for the global-local model

T-stiffener are co-cured by combining two L-shape stiffeners. In the local FE model, the stiffener is located at the center of a 100 mm wide segment of the base plate (440 mm × 440 mm) transverse to the 0° direction (*x*-direction). The nominal element size is 75 µm × 75 µm, and the mesh is comprised of linear quadrilateral and triangular elements Figure 5-6b. The width of the local region is verified to be sufficient such that the effects of the non-propagating mode at the left and right boundaries are negligible [94].

5.2.2 Experimental Observation

Prior to a detailed numerical analysis, experiments are carried out for the case of a single stiffener on a CFRP panel to determine a baseline for the global-local model. The general experimental setup is shown in Figure 5-7. The actuating transducer (Digital Wave B225) is

driven by a 5-cycle Hann-windowed sine burst with 175 kHz center frequency at 10 V_{pp}. An identical model (B225) transducer is used as a receiver and the receiving signal is filtered and amplified through a signal conditioner (Digital Wave FM-1) and is digitized by an oscilloscope (Agillent 54624A). Experimental measurements are conducted through the stiffener as well as parallel to it to capture a nominal wave signal. Note, due to the quasi-isotropic stacking sequence, the different wave propagation direction is not affected by the generally anisotropic nature of the composite.

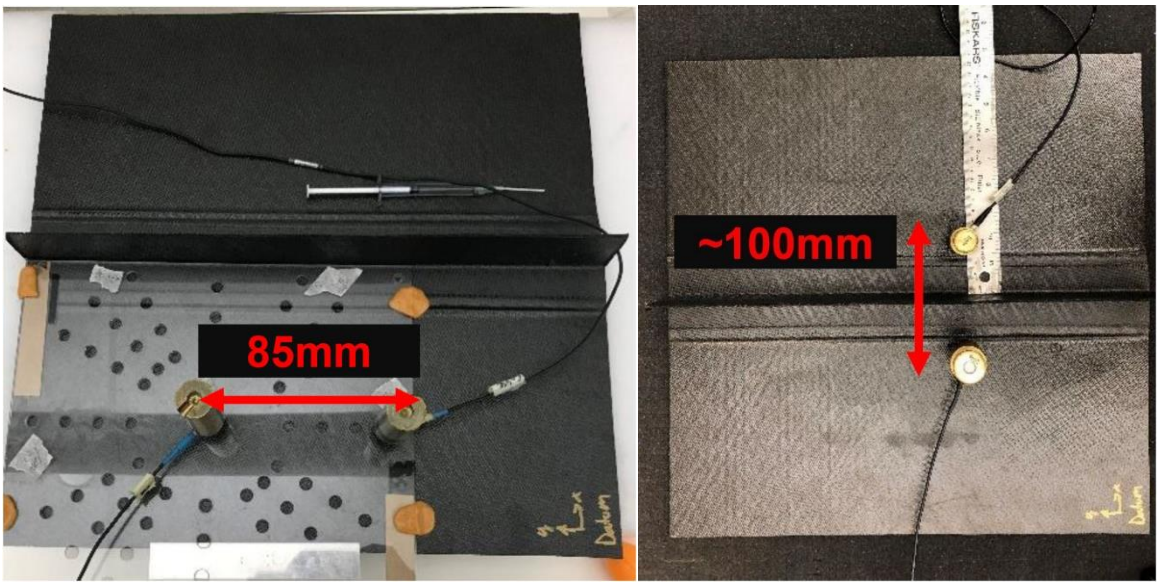

(a) Unstiffened wave path (b) Wave path through T-stiffener

Figure 5-7 Experimental setup for guided ultrasonic wave measurements on a stiffened CFRP panel

The measured waveforms, shown in Figure 5-8, indicate that the amplitude reduction and the waveform changes is significant. Furthermore, the tail of the wave packet behind the main packet is due to the ringing in the transducer, which can be seen more clearly for the unstiffened case, as shown in Figure 5-8a.

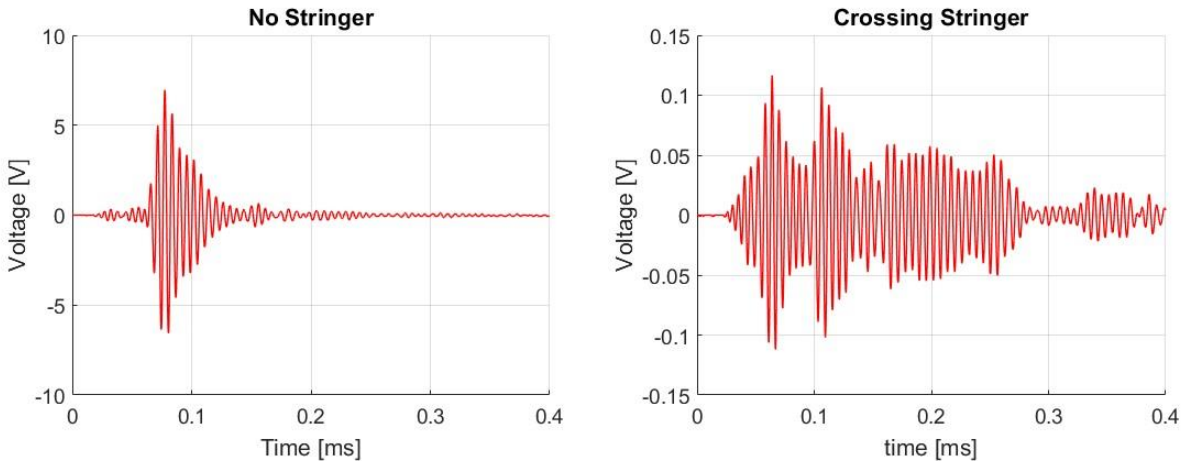

(a) Unstiffened wave path (see Figure 5-7a) (b) Wave path through T-stiffener (see Figure 5-7b)

Figure 5-8 Measured signals on CFRP specimen from unstiffened and stiffened region

The latter phenomenon is studied further: as shown in Figure 5-9, where the input tone burst signal is plotted as a solid blue line, and the transducer face-to-face response is plotted as a red dash line, the signal is substantially affected by ringing, despite the broadband nature of the transducers.

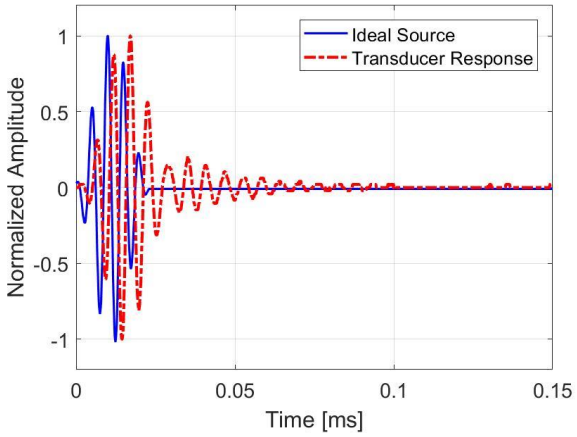

Figure 5-9 Measured signals from face-to-face experiment compared to the "ideal" source signal

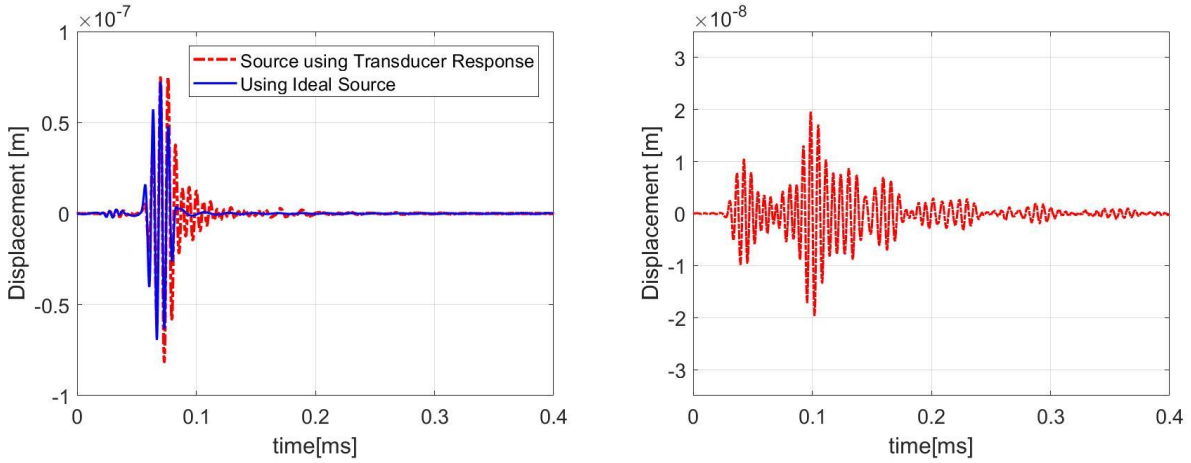

(a) at 85 mm from source (no stiffener) (b) at 100mm from source (50 mm after stiffener)

Figure 5-10 Vertical displacements from GL model with and without single T-shaped stiffener

In order to improve the waveform predictions of the global-local model, the transducer response is used as the input time signal instead of the original "ideal" tone burst. The waveform prediction in accordance with the experimental setup with such input is shown in Figure 5-10. In the case of no stiffener, the prediction using the transducer response reflects wave trail of the A_0 mode much better and is comparable to the experimental measurement. Furthermore, in the case of the waves crossing the stiffener, the model predicts two main wave packets followed by several scattered packets as in the experiment. However, the waveform from the global-local fails to predict the relative amplitudes of the two packets correctly.

5.2.3 Global Local Simulations with T-shaped Stiffeners

It is the interest of this work to investigate the feasibility of detecting damage in a more realistic situation where several stiffeners are in the path between the source and the receiving transducers. Figure 5-11 outlines the problem of interest with four T-shaped stiffeners that are 150 mm apart (center to center).

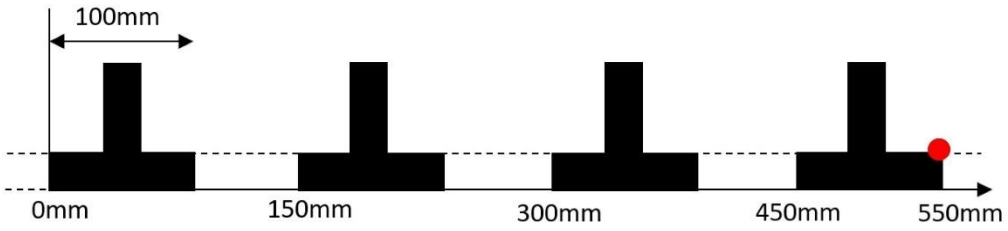

Figure 5-11 Sketch of the coupled GL problem with four T-shaped stiffeners in the wave propagation path

ach stiffener is modeled with the identical local FE model. Using the coupled GL formulation, the forward propagating waves' scattering is investigated, that is the right propagating waves from the upstream scattering problem is used as the incident waves for the next stiffener. Note that this formulation does not consider multiple reflections between the neighboring stiffeners. Since the reflected waves from a single stiffener has approximately one fourth of the transmitted waves peak amplitude, it is believed that the right going waves contributions from the secondary wave scattering is small, in particular for dissipative materials. Thus, the model is still indicative of the physical experiment. Here, the simplified source for the subsequent simulations is a 5-cycle Hann-windowed A_0 mode at 175 kHz and is excited at x=0 mm. This simplified source is used to ease the analysis of the scattered waves the stiffeners. To capture the response of the system and all scattered waves, the vertical displacement signal at x=550 mm (see Figure 5-11) is extracted, i.e., at the end of the forth stiffener (if present).

As seen from the experimental signals (see Figure 5-8), even the case of Lamb waves crossing a single T-shaped stiffener are complex. Therefore, the case of a single stiffener is first studied to identify important wave form features. That is, only the first stiffener remains in the GL model from Figure 5-11 for this study. Snapshots of the wave fields at the stiffener are shown in Figure 5-12.

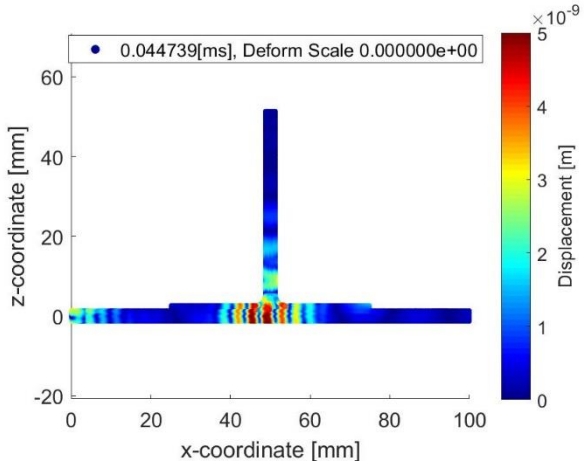

(a) t = 45 μs, incident wave splits at the vertical part of the stiffener

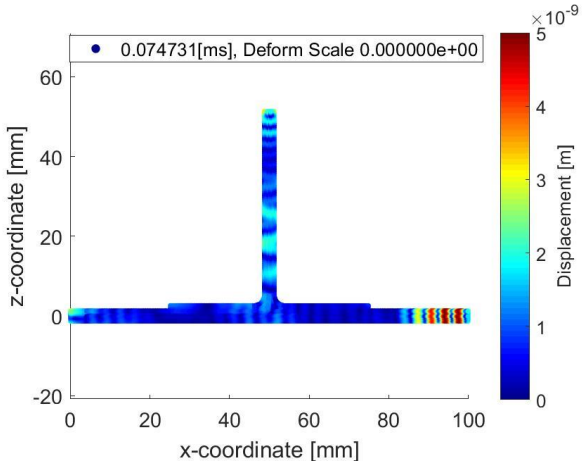

(b) t = 75 μs, first transmitted wave reaches end of local model and the scattered waves begin to return from the end of vertical part of the stiffener

Figure 5-12 Resultant displacement fields at the single stiffener subjected to an A_0 incident wave

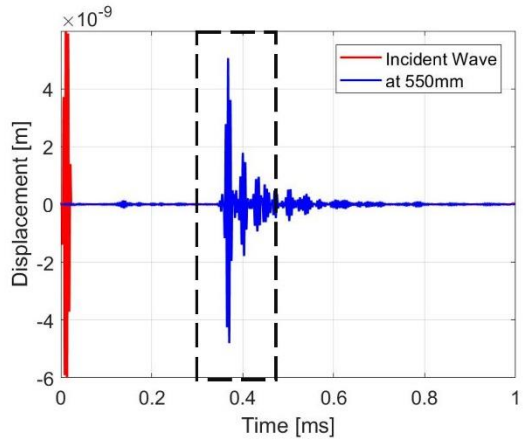

(a) waveform showing the directly reached wave and the subsequent scattered waves

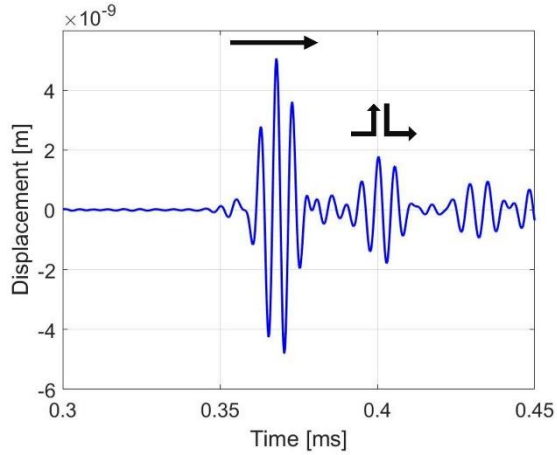

(b) in a shorter time window showing the directly reached wave and the wave packet that traversed the vertical stiffener

Figure 5-13 GL model vertical displacement for a single defect free stiffener at x=550 mm

At t = 45 μs, the incident A_0 has reached the root of the vertical stiffener, as shown in Figure 5-12a. The incident wave is splitting with the major portion of the energy traveling to the right, and another significant portion traveling upward into the vertical part of the stiffener. In the discussion below, the former is referred to as the directly transmitted wave, and the later waves is referred to as the vertical returned waves. Furthermore, the (small) reflection of the incident waves from the first thickness increase has begun to travel back and is leaving the local region to

the left. At a later time at t = 75 μs, as shown in Figure 5-12b, the directly transmitted wave is about to leave the local region forming the biggest packet as labeled with the right going arrow in Figure 5-13b, whereas the vertical returned waves continues to scatter in the stiffener, travel to the left and to the right leaving the stiffener. Furthermore, the wave field should be viewed in conjunction with the vertical displacement measured at the x=550 mm location, which is shown in Figure 5-13. It can be seen that the incident A_0 mode is minimally converted into the faster S_0 mode that arrives approximately 0.15 ms. The transmitted A_0 mode appears as many pulses of consecutively diminishing packets arriving after 0.35 ms. The right going portion of the vertical returned waves forms the second packet in the zoomed-in time signal shown in Figure 5-13b. These two packets are, in theory, the easiest to analyze and will be the focus for the remainder of this paper. The additional scattering forms a relatively continuous tail of waves as shown in Figure 5-13a. However, due to their relatively low amplitudes and complex superposition, these parts of the signal are difficult to analyze.

5.2.4 Effects of Multiple Stiffeners without Defects

In order to analyze the wave propagation when multiple stiffeners are present, the vertical displacements at x=550 mm are reported for every added stiffener. That is, stiffeners are "activated" from left to right in Figure 5-11, by using the "output" of the previous model as the input for the added stiffener model in the GL coupling scheme. The results are shown in Figure 5-14.

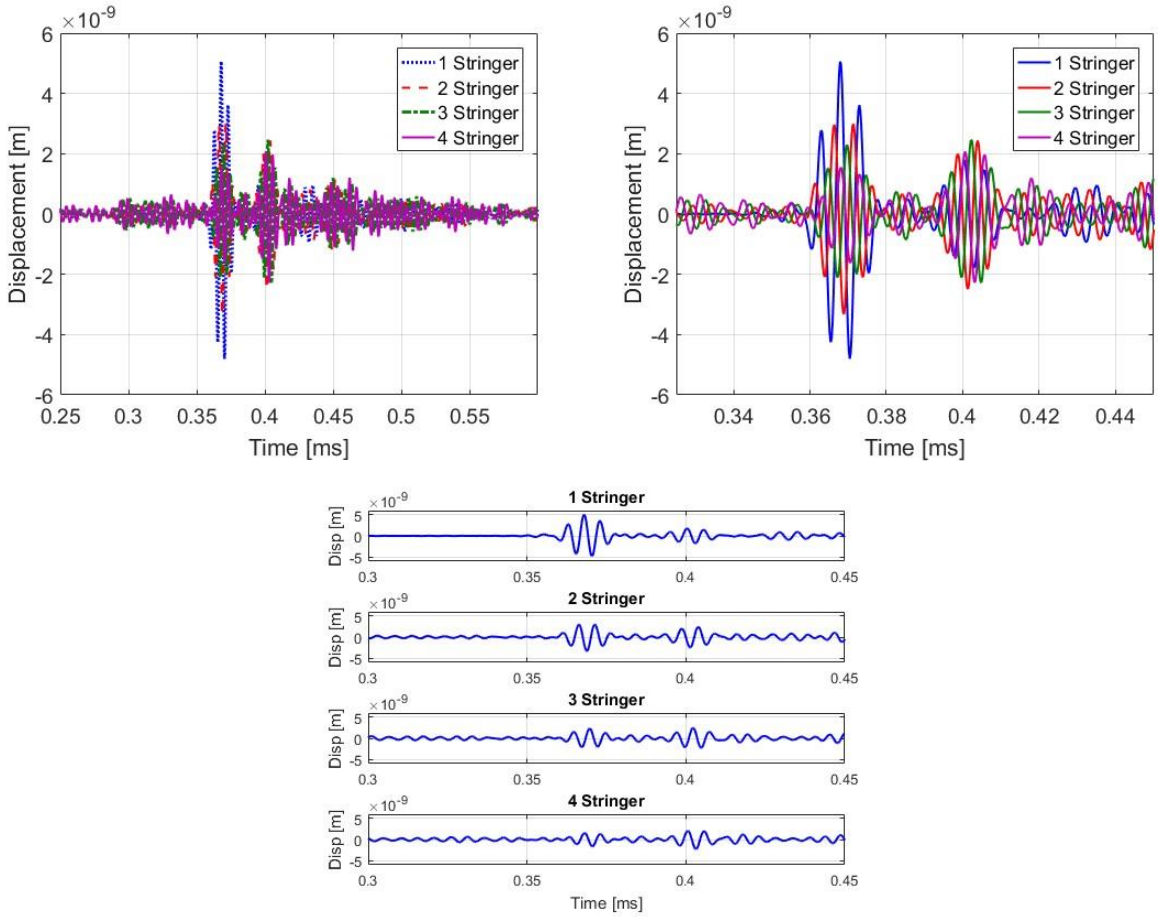

Figure 5-14 Vertical displacement at *x*=550 mm with different number of stiffeners with a longer and a shorter time window

It can be seen that the directly transmitted and the vertical returned waves are the dominant wave packets. Furthermore, the first dominant packet monotonically reduces in amplitude with an increasing number of stiffeners, whereas the amplitude of the second dominant packet remains relatively constant. A summary of these findings is given in Table 5-2.

Table 5-2 Summary of main effects (changes in amplitude of main wave packets) of multiple stiffeners in wave path

Case / Peak Amplitude	1st Packet [nm]	2nd Packet [nm]
1 Stiffener	5.064	1.786
2 Stiffeners	3.327	2.488
3 Stiffeners	2.300	2.463
4 Stiffeners	1.601	2.166

The continuous amplitude reduction of the first dominant packet is attributed to the consecutive conversion of the directly transmitted waves into vertical return waves (and other smaller scattered waves) in each passing of a new stiffener. For the second dominant wave packet, the different waves that have traveled only once into the vertical portion of a stiffener but are transmitted directly in the rest of the stiffeners superpose and thus the amplitude of the corresponding wave packet remains close to constant. In other words, since the wave paths are the same for the waves that a) are directly transmitted at the first stiffener and travel into the vertical region of the second stiffener and b) the vertical returned waves from the first stiffener travelling directly through the second stiffener etc. Thus, these waves all experience the same path length and superpose. The coda waves, i.e. those waves trailing the directly transmitted and the vertical returned waves, contain additionally scattered waves from the stiffeners. However, it is nearly impossible to identify the contributions from individual waves or stiffeners. Nonetheless, it should be noted that in the case of four stiffeners, the amplitude of the first packet is only slightly higher than the coda waves.

5.2.5 Effects of Damage in the Stiffener

Before the final investigation on the feasibility to detect damages in a multi-stiffener configuration, a few prototypical delamination cases are studied in a single stiffener configuration to observe for the waveform changes. The defect is designed at the joining locations of the left and right portions of the stiffener. That is, typically two L-shaped portions are merged to form a T, with additional (fiber) filling at the joint corner. Thus, this localized area is prone to small defects that may lead to a growing delamination in the stiffener and may require additional mitigation strategies in the manufacturing process [95]. Figure 5-15 shows the four

cases being considered, where two cases are 14.5 mm long delamination to the left and to the right of the root of the stiffener, a shorter 7.7 mm long delamination at the stiffener's root separating the base plate and the T-structure, and finally a 14.5 mm long vertical delamination at the mid-plane of the T-shape starting from the top of the base plate.

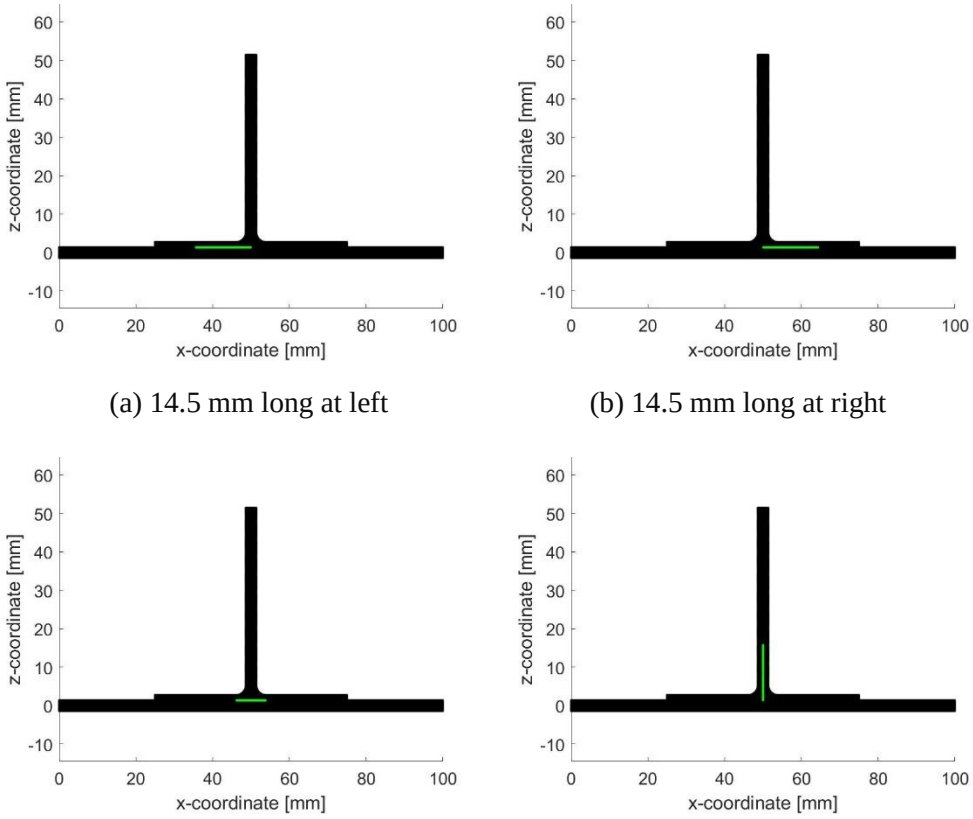

(a) 14.5 mm long at left (b) 14.5 mm long at right

(a) 7.7 mm long at base (b) 14.5 mm long vertically

Figure 5-15 Different delamination cases and their location (highlighted in green) in the T-shape stiffener

In this section, the wave propagation problem is a single A_0 incident (5 cycle Hann windowed sine) with 175 kHz center frequency enters at 50 mm to the left of the center of the T-stiffener, and the vertical displacements at 50 mm to the right of the center of the stiffener are compared. The left, and right base delamination is studied first, with the goal to determine whether it is

possible to determine the relative location of the defect w.r.t. the vertical region in the transmitted signal.

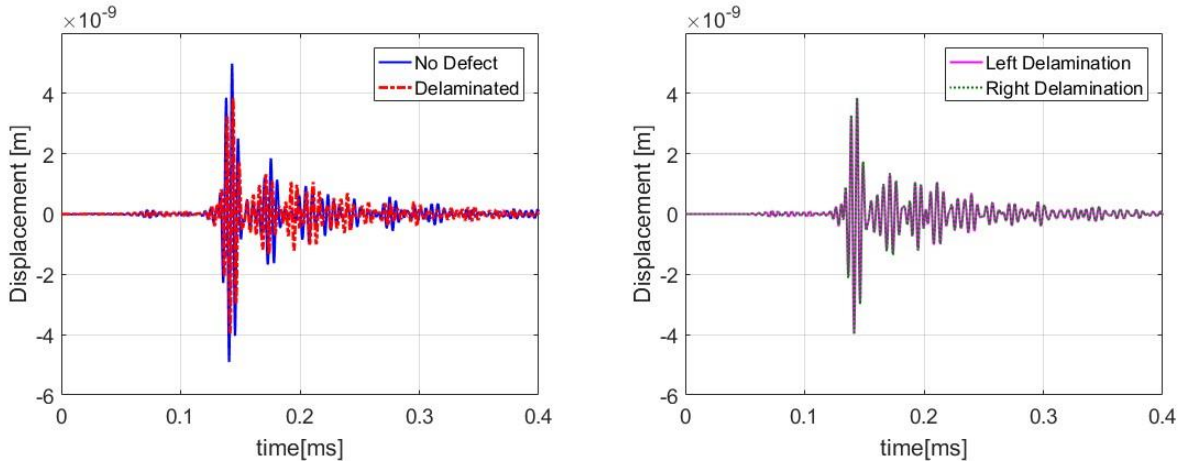

(a) Comparing defect free signal with left based delamination

(b) comparing left base delamination and right base delamination

Figure 5-16 Vertical displacement 50 mm to the right of the center of the stiffener

Figure 5-16a shows the waveform comparison between the defect free cases and the left base delaminated case. The changes in the directly reached and the vertical returned packets are relatively small with small amplitude reduction, and the phase change is small. In a realistic inspection scenario, it would be difficult to observe such small changes. By observing the wavefield animation, the small degree of waveform changes can be explained by the fact that the defect does not impede the path for the scattered waves to travel into the vertical region, which is the dominating waveform feature. Figure 5-15b shows a somewhat unexpected result in which the waveform for the left and the right base delamination has indistinguishable differences, despite the scattering due to the delamination occurs in one case before the vertical stiffener and the other case after. This would imply that with the transmitted waves, it is not possible to determine the two relative defect locations.

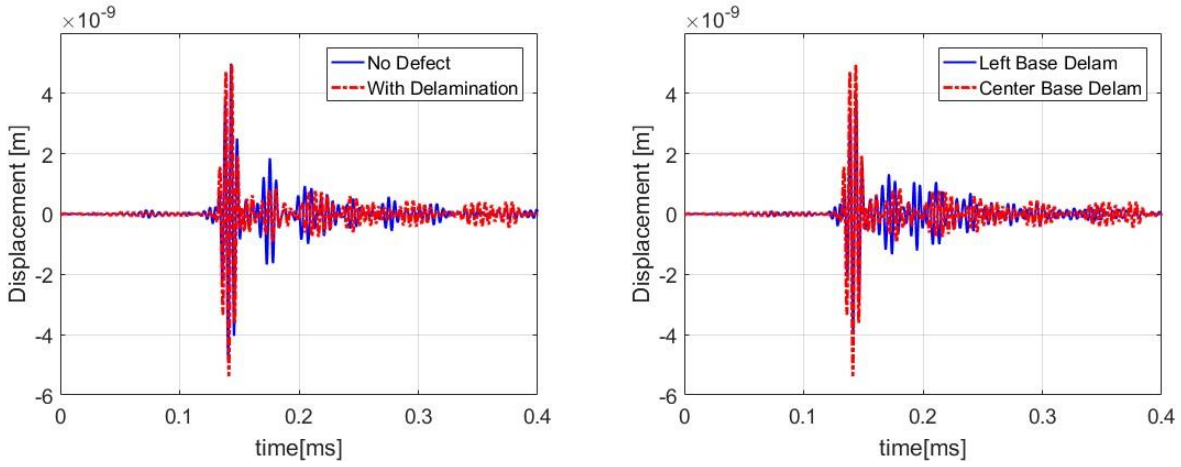

(a) Comparing defect free signal with center-based delamination

(b) comparing center base delamination and left base delamination

Figure 5-17 Vertical displacement 50 mm to the right of the center of the stiffener

Figure 5-17 concerns the 7.7 mm long delamination right beneath the vertical portion of the stiffener. Comparing the damaged and the pristine signals in Figure 5-17a, the directly reached waves has negligible amplitude drop whereas the vertical return waves has a significant amplitude reduction. From the wavefield animation (not shown), it is determined that the incident waves in the base plate is not as effective in propagating into the vertical region with the delamination spanning more of the root region. Thus, much of the incident waves are propagating through the base plate making the reduction in the amplitude of the vertical return waves a useful indicator in base delamination. Figure 5-17b shows the differences between the center base and the left base delamination, indicating the directly reached waves for the left base defected cases is noticeably smaller in amplitude than the center base case. Furthermore, due to the scattering in the left base delamination, the vertical returned waves form a more continuous packet with a larger amplitude. These distinctions make it possible to differentiate these two types of defects.

As for the case of a delamination in the vertical portion of the stiffener, the waveform shown in Figure 5-18 indicates that the differences between the defect free and the damaged cases is highly distinguishable.

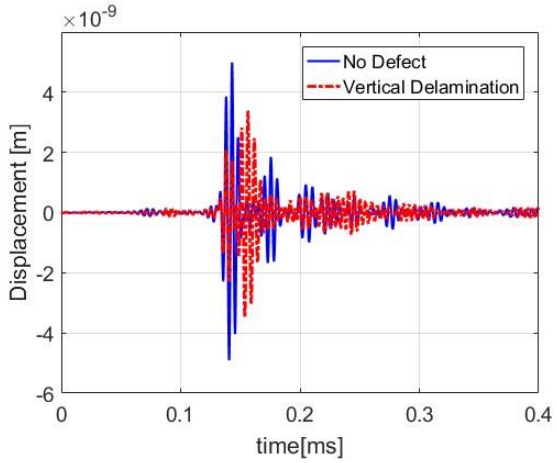

(a) Comparing defect free signal with the vertical delamination

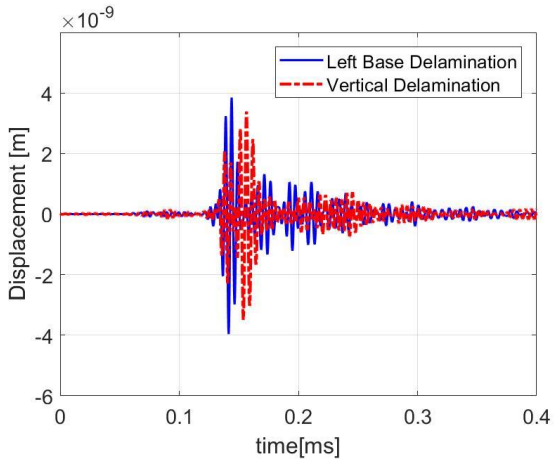

(b) Comparing vertical delamination and left base delamination

Figure 5-18 Vertical displacement 50 mm to the right of the center of the stiffener

The directly reached waves has a significant drop in amplitude and the vertical returned waves has a significantly earlier arrival time and an increased in amplitude compared to the defect free case.

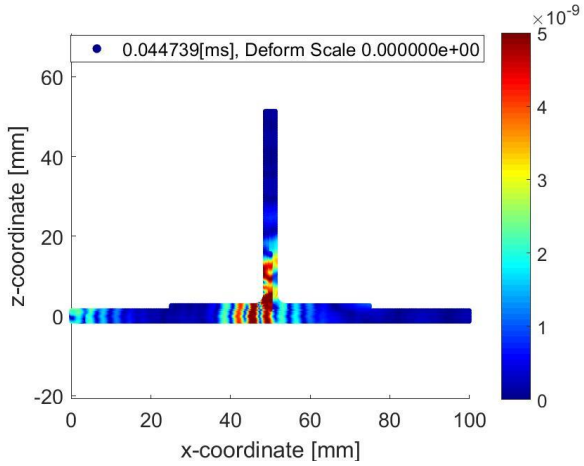

(a) t= 0.045 μs when the incident waves begin to split into the left portion of the vertical stiffener

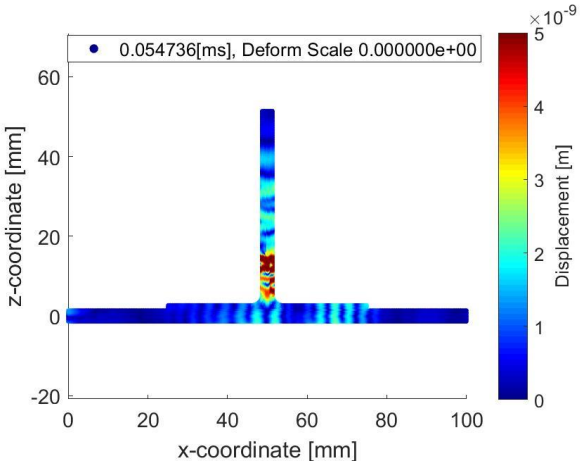

(b) t= 0.055 μs, at upper end of the delamination, the elastic waves are reflected back to the base plate

Figure 5-19 Resultant displacement field around the single stiffener subjected to A_0 incident

The wave fields shown in Figure 5-19 suggests that the incident waves are prone to travel on the left side of the delamination upward along the vertical stiffener. Once the waves reached the end of the delamination tip, the wave field mismatch causes a strong reflection returning to the base plate. Therefore, less waves are traveling into the vertical portion of the stiffener and an earlier arrival time for the vertical return waves. Figure 5-18a, b suggests that sufficient signal differences that can be appreciated to identify and distinguish this type of damage.

5.2.6 Feasibility to Detect Damage across Multiple Stiffeners

In an attempt to determine the likelihood of using Lamb waves to inspect for damages across several stiffeners, a vertical delamination (same location and extends as in the previous section) is introduced in the last of the four stiffeners, as shown in Figure 5-20. With equal spacing of 150 mm apart, the 4th stiffener has the 14.5 mm long vertical delamination, and the vertical displacement is reported for the pure A_0 incident at 175 kHz.

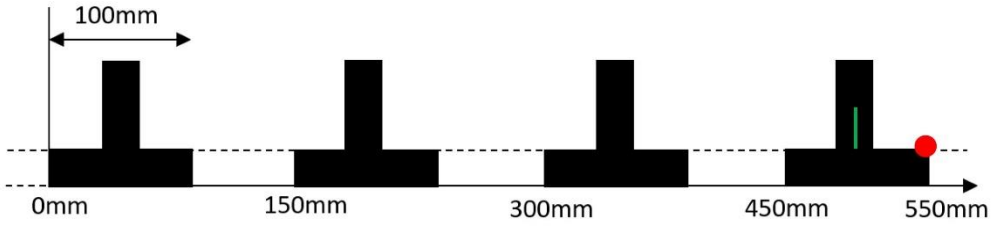

Figure 5-20 Embedded delamination, highlighted in green, in the last stiffener in a four-stiffener configuration

The vertical displacement is calculated with the GL methodology for a pure A_0 incident wave at 175 kHz. Since this model does not consider the material attenuation and the geometric spreading in circular wave fronts, it represents the best-case scenario in which the amplitude drops are only the result of the scattering of the stiffeners.

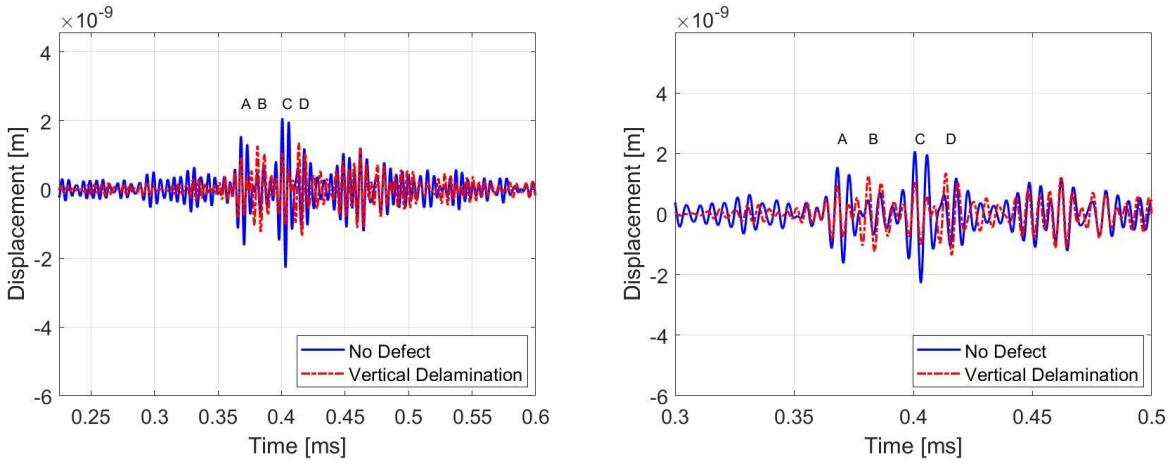

(a) signal between 0.2 ms to 0.6 ms (b) signal between 0.3 ms to 0.5 ms

Figure 5-21 GL model predicted vertical displacement reported at the red dot (top surface, 50 mm to the right of the center of the last stiffener). Solid blue line representing signal for no delamination in the last stiffener whereas the red dash line for the case with the delamination

The two main contribution from the pristine case of the initial incident A_0 are labeled *A* and *C*. At marker *A*, it can be seen that the defect causes a decrease in amplitude. Instead, in additional wave of significant amplitude can be observed at marker *B*. That is, it appears that the same waveform features (see Figure 5-18) for the vertical delamination in a single stiffener are present here as well. Similarly, marker *C* and *D* shows the same feature in which a packet with smaller amplitude is followed by a packet with larger amplitude when the delamination is present. Most likely, the directly transmitted and the vertical return waves, having the strongest amplitude, arrive at the fourth stiffener as separate wave packets, and thus each packet is scattered in a similar fashion as the single stiffener case. In summary, all of the four mentioned waves (*A*-*D*) may serve as an indicator of a delamination in one of the stiffeners, as all exhibit noticeable differences compared to the pristine case.

5.2.7 Summary

In this work, the well-known global-local method is modified such that multiple wave-scattering features can be studied simultaneously in combination with an arbitrary source problem. That is, the "outgoing" Lamb waves from the first GL problem are propagated as the

incident waves to the subsequent GL problem. The modeling method is demonstrated to be efficient in simulating one-way ultrasonic wave propagation in composite structures.

The modeling tool is applied to study the feasibility of detecting damage in a stiffened composite structure with four T-shaped stiffeners. First, a simpler case of a single T-stiffener is analyzed, and the waveform features are compared with experimental measurement. The ultrasonic Lamb waves entering the stiffener primarily split into the directly transmitted waves, which travel along the base plate, and the vertical return waves, which travels into and return from the vertical region of the stiffener. These two wave packets are the most noticeable waveform features and are trailed by a significant amount of additional scattered waves. When a vertical delamination is embedded into the stiffener, the first packet experiences a significant amplitude drop whereas the second packet appears to have an earlier arrival time.

In the multi-stiffener configuration, the waveforms for one to four pristine stiffeners are studied to show that the directly transmitted wave packet has a monotonic amplitude drop with an increase of the number of stiffeners, whereas the vertical return wave packet does not. In fact, after four stiffeners, the directly transmitted wave nearly diminishes and exhibits similar amplitude as the coda waves. Since the model represents the most ideal condition without geometric and material attenuation, in physical experiments, it would be difficult to observe this wave packet. Finally, a vertical delamination is embedded into the last of the four stiffeners, showing that both the directly transmitted and the vertical return waves show noticeable changes. These findings indicate that it could be possible to detect damage in a multi-stiffener configuration with those wave packets in NDE applications if the sensitivity problem is solved with adequate excitation amplitude.

Chapter 6 Concluding Remarks

This dissertation presents the fundamental research work for using ultrasonic guided wave for non-destructive evaluation on launch vehicles made with advanced composites. The complexity of Lamb wave interactions with hidden defects makes it difficult to infer the defect characteristics from the ultrasonic waveform changes. In this work, the existing global-local method (GLM) is extended to model Lamb wave propagation in composite structures with various defects and the extended method is validated through other analytical tools and laboratory experiment. The global local method is extended in the following aspects

- Using the global matrix method with appropriate boundary conditions, the matrix size for the modal function calculations is reduced by half for multilayered media with a balanced layup. The alternative form of the global matrix is analytically reduced to the well-known dispersion equation for a single layer medium with transversely isotropic properties
- Using the waveguide finite element (WFE) method, the free wave propagation characteristics for various multilayered plates are analyzed for time of flight analysis. The dispersion curves calculated using WFE are validated against analytical solution and experimental measurement. The dispersion curve and the modal functions are then used in GLM.
- The improved GLM couples the solution for the source problem and the scattering problem with dissimilar modal functions on either side. In addition, wave attenuation is implemented with complex material properties. These extensions can better represent the source transducers and to model defects in a more complex structure. The extended GLM is validated with analytical tools such as the conventional transient FEM, and the

global-matrix method, and experimental measurements. The numerical performance is also investigated in terms of different FE region size, and FE discretization.

- The validated GMM is then used to create damage signal library for various defects in fiber-metal laminate (hybrid composites) and stiffened composite structures.
- Using the waveform library for the hybrid composites, the effectiveness of serval damage indices is discussed and are used to process damage signals with unknown damage. The library is then used to successfully differentiate the type of damage and to estimate the defect size.

This work has presented the framework of using the global-local method as a numerically efficient model tool to create a waveform library for damage characterization in complex composite structures.

Appendix

Chapter 2 Lamb Wave in Thin Plates

2.1 Isotropic Plate

Consider an isotropic plate of thickness *2H,* have elastic constants *E*, and *v*, and density ρ.

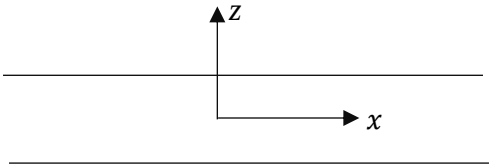

The longitudinal and shear wave velocities c_1 and c_2 are respectively,

$$c_1 = \sqrt{\frac{E(1-\nu)}{\rho(1+\nu)(1-2\nu)}} \tag{2-1}$$

$$c_2 = \sqrt{\frac{E}{\rho 2(1+\nu)}} \tag{2-2}$$

Define the wavenumber

$$k = \frac{\omega}{c} \qquad\qquad k_j = \frac{\omega}{c_j} \tag{2-3}$$

Such that

$$\eta_j = \sqrt{k^2 - k_j^2} \tag{2-4}$$

2.1.1 Symmetric Mode

Dispersion Equation

$$\frac{\tanh(\eta_1 H)}{\tanh(\eta_2 H)} = \frac{(2k^2 - k_2^2)^2}{4k^2\eta_1\eta_2} \tag{2-5}$$

Modal Displacement and Stress Functions

$$U_x(\omega, k, z) = iA_s\left[kcosh(\eta_1 z) - \frac{(2k^2 - k_2^2)^2\cosh(\eta_1 z)}{4k^2\eta_1\eta_2\cosh(\eta_1 H)}\cosh(\eta_2 z)\right] \tag{2-6}$$

$$U_z(\omega, k, z) = A_s\left[\eta_1 sinh(\eta_1 z) - \frac{(2k^2 - k_2^2)^2\cosh(\eta_1 z)}{4k^2\eta_1\eta_2\cosh(\eta_1 H)}\sinh(\eta_2 z)\right] \tag{2-7}$$

$$S_{xx}(\omega, k, z) = \mu A_s\left[(2\eta_1^2 + k_2^2)\cosh(\eta_1 z) - \left(\frac{(2k^2 - k_2^2)\cosh(\eta_2 z)}{\cosh(\eta_2 H)}\right)\sinh(\eta_2 z)\right] \tag{2-8}$$

$$S_{zz}(\omega, k, z) = \mu A_s(2\eta_1^2 + k_2^2)\cosh(\eta_1 H)\left[\frac{\cosh(\eta_1 z)}{\cosh(\eta_1 H)} - \frac{\cosh(\eta_2 z)}{\cosh(\eta_2 H)}\right] \tag{2-9}$$

$$S_{xz}(\omega, k, z) = i\mu A_s 2k\eta_1\sinh(\eta_1 H)\left[\frac{\sinh(\eta_1 z)}{\sinh(\eta_1 H)} - \frac{\sinh(\eta_2 z)}{\sinh(\eta_2 H)}\right] \tag{2-10}$$

2.1.2 Anti-Symmetric Mode

Dispersion Equation

$$\frac{\tanh(\eta_2 H)}{\tanh(\eta_1 H)} = \frac{(2k^2 - k_2^2)^2}{4k^2\eta_1\eta_2} \tag{2-11}$$

Modal Displacement and Stress Functions

$$U_x(\omega,k,z) = -iA_a\left[ksinh(\eta_1 z) - \frac{(2k^2-k_2^2)\sinh(\eta_1 H)}{2\mathrm{k}\sinh(\eta_2 H)}\sinh(\eta_2 z)\right] \tag{2-12}$$

$$U_z(\omega,k,z) = -A_a\left[\eta_1 cosh(\eta_1 z) - \frac{(2k^2-k_2^2)\sinh(\eta_1 H)}{2\eta_2\sinh(\eta_2 H)}\cosh(\eta_2 z)\right] \tag{2-13}$$

$$S_{xx}(\omega,k,z) = \mu A_a\left[(2\eta_1^2+k_2^2)\sinh(\eta_1 z) - \left(\frac{(2k^2-k_2^2)\sinh(\eta_2 z)}{\sinh(\eta_2 H)}\right)\sinh(\eta_2 z)\right] \tag{2-14}$$

$$S_{zz}(\omega,k,z) = -\mu A_a(2k^2-k_2^2)\sinh(\eta_1 H)\left[\frac{\sinh(\eta_1 z)}{\sinh(\eta_1 H)} - \frac{\sinh(\eta_2 z)}{\sinh(\eta_2 H)}\right] \tag{2-15}$$

$$S_{xz}(\omega,k,z) = -i\mu A_a 2k\eta_1\cosh(\eta_1 H)\left[\frac{\cosh(\eta_1 z)}{\cosh(\eta_1 H)} - \frac{\cosh(\eta_2 z)}{\cosh(\eta_2 H)}\right] \tag{2-16}$$

2.2 Transversely Isotropic Material

For a plate that is isotopic about the x_3 axis, the stress-strain law can be written as

$$\begin{Bmatrix}\sigma_{11}\\ \sigma_{33}\\ \sigma_{13}\end{Bmatrix} = \begin{bmatrix}C_{11} & C_{13} & 0\\ C_{13} & C_{33} & 0\\ 0 & 0 & (C_{11}-C_{13})\end{bmatrix}\begin{Bmatrix}u_{1,1}\\ u_{3,3}\\ \frac{1}{2}(u_{1,3}+u_{3,1})\end{Bmatrix}$$

Define bulkwave velocities to be

$$c_{1L} = \sqrt{\frac{C_{11}}{\rho}} \qquad c_{3L} = \sqrt{\frac{C_{33}}{\rho}} \qquad c_{3T} = \sqrt{\frac{C_{44}}{\rho}}$$

Define

$$\pm A_{1,2} = k\sqrt{\frac{-A \pm \sqrt{A^2 - 4B}}{2}}$$

Where

$$A = \frac{c^2}{C_{3L}^2} + \frac{c^2}{C_{3T}^2} - \frac{C_{11}C_{33} - C_{13}^2 - 2C_{13}C_{44}}{C_{33}C_{44}} \text{ and } B = \left(\frac{c^2}{C_{3T}^2} - 1\right)\left(\frac{c^2}{C_{3L}^2} - \frac{C_{11}}{C_{33}}\right)$$

2.2.1 Symmetric Mode

Dispersion Equation

$$\frac{\tanh(kA_1H)}{\tanh(kA_2H)} = \frac{A_1\left[A_2^2 - \frac{C_{11}}{C_{13}}\left(\frac{c^2}{C_{1L}^2} - 1\right)\right]\left[\frac{C_{13}}{C_{33}}\left(\frac{C_{13}}{C_{44}} + 1\right) + A_1^2 + \frac{C_{11}}{C_{44}}\left(\frac{c^2}{C_{1L}^2} - 1\right)\right]}{A_2\left[A_1^2 - \frac{C_{11}}{C_{13}}\left(\frac{c^2}{C_{1L}^2} - 1\right)\right]\left[\frac{C_{13}}{C_{33}}\left(\frac{C_{13}}{C_{44}} + 1\right) + A_2^2 + \frac{C_{11}}{C_{44}}\left(\frac{c^2}{C_{1L}^2} - 1\right)\right]} \quad (2\text{-}17)$$

2.2.2 Anti-Symmetric Mode

Dispersion Equation

$$\frac{\tanh(kA_2H)}{\tanh(kA_1H)} = \frac{A_1\left[A_2^2 - \frac{C_{11}}{C_{13}}\left(\frac{c^2}{C_{1L}^2} - 1\right)\right]\left[\frac{C_{13}}{C_{33}}\left(\frac{C_{13}}{C_{44}} + 1\right) + A_1^2 + \frac{C_{11}}{C_{44}}\left(\frac{c^2}{C_{1L}^2} - 1\right)\right]}{A_2\left[A_1^2 - \frac{C_{11}}{C_{13}}\left(\frac{c^2}{C_{1L}^2} - 1\right)\right]\left[\frac{C_{13}}{C_{33}}\left(\frac{C_{13}}{C_{44}} + 1\right) + A_2^2 + \frac{C_{11}}{C_{44}}\left(\frac{c^2}{C_{1L}^2} - 1\right)\right]} \quad (2\text{-}18)$$

2.3 Anisotropic Material Constants

$$C_{11} = \frac{E_{11}}{1 - \nu_{13}\nu_{31}}$$

$$C_{13} = \frac{E_{11}\nu_{31}}{1 - \nu_{13}\nu_{31}}$$

$$C_{33} = \frac{E_{33}}{1 - \nu_{13}\nu_{31}}$$

Chapter 3

3.1Shape functions for linear elements

Shape Functions of 2D 4-node element

1D 2-node element

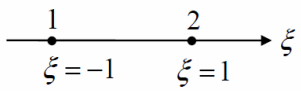

$$N_1(\xi)=\frac{1}{2}(1-\xi)$$

$$N_2(\xi)=\frac{1}{2}(1+\xi)$$

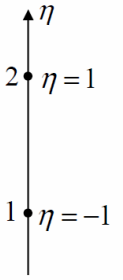

$$N_1(\eta)=\frac{1}{2}(1-\eta)$$

$$N_2(\eta)=\frac{1}{2}(1+\eta)$$

2D 4-node element

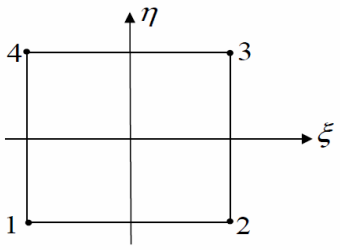

$$N_1(\xi,\eta)=N_1(\xi)N_1(\eta)=\frac{1}{4}(1-\xi)(1-\eta)$$

$$N_2(\xi,\eta)=N_2(\xi)N_1(\eta)=\frac{1}{4}(1+\xi)(1-\eta)$$

$$N_3(\xi,\eta)=N_2(\xi)N_2(\eta)=\frac{1}{4}(1+\xi)(1+\eta)$$

$$N_4(\xi,\eta)=N_1(\xi)N_2(\eta)=\frac{1}{4}(1-\xi)(1+\eta)$$

3.2 Analytical Solution to Surface Load Response in an Isotropic Plate

The solution is derived in [29], a summary is given here. The surface load displacement response of an anti-symmetric problem is

$$U_x(\omega,x,z)=-\sum_{k_a}\frac{i\eta_{2a}\bar{P}(k_a,\omega)}{2\mu R_a'(k_a)}[(2k_a^2-k_2^2)\sinh(\eta_{1a}H)\sinh(\eta_{2a}z)$$

$$-2k_a^2\sinh(\eta_{1a}z)\sinh(\eta_{2a}H)]e^{ik_ax}$$

(3-1)

$$U_z(\omega,x,z)=-\sum_{k_a}-\frac{k_a\bar{P}(k_a,\omega)}{2\mu R_a'(k_a)}[2\eta_{1a}\eta_{2a}\cosh(\eta_{1a}z)\sinh(\eta_{2a}H)-(2k_a^2$$

$$-k_2^2)\sinh(\eta_{1a}H)\cosh(\eta_{2a}z)]e^{ik_ax}$$

(3-2)

For the symmetric problem,

$$U_x(\omega,x,z) = -\sum_{k_s} \frac{i\eta_{2s}\bar{P}(k_s,\omega)}{2\mu R_s'(k_a)}[(2k_s^2 - k_2^2)\cosh(\eta_{1s}H)\cosh(\eta_{2s}z) - 2k_s^2\cosh(\eta_{1s}z)\cosh(\eta_{2s}H)]e^{ik_sx}$$

(3-3)

$$U_z(\omega,x,z) = -\sum_{k_s} -\frac{k_s\bar{P}(k_s,\omega)}{2\mu R_s'(k_s)}[2\eta_{1s}\eta_{2s}\sinh(\eta_{1s}z)\cosh(\eta_{2s}H) - (2k_s^2 - k_2^2)\cosh(\eta_{1s}H)\cosh(\eta_{2s}z)]e^{ik_sx}$$

(3-4)

Where *R'* are the derivative of the left-hand side of the dispersion equation w.r.t *k* and evaluate at the root of the dispersion equations.

Anti-symmetric mode

$$R'_a = 8k(2(k^2 - k_2^2)\sinh(\eta_1H)\cosh(\eta_2H) + \frac{((2(k^2) - k_2^2)^2)kH}{\eta_1}\cosh(\eta_1H)\cosh(\eta_2H) + \frac{((2k^2 - k_2^2)^2)kH}{\eta_2}\sinh(\eta_1H)\sinh(\eta_2H) - 8k\eta_1\eta_2\cosh(\eta_1H)\sinh(\eta_2H) - \frac{4k^3\eta_2}{\eta_1}\cosh(\eta_1H)\sinh(\eta_2H) - \frac{4k^3\eta_1}{\eta_2}\cosh(\eta_1H)\sinh(\eta_2H) - 4k^3\eta_2H\sinh(\eta_1H)\sinh(\eta_2H) - 4k^3\eta_1H\cosh(\eta_1H)\cosh(\eta_2H)$$

Symmetric mode

$$R'_s = 8k(2(k^2 - k_2^2)\cosh(\eta_1H)\sinh(\eta_2H) + \frac{\left((2(k^2) - k_2^2)^2\right)kH}{\eta_1}\sinh(\eta_1H)\sinh(\eta_2H) + \frac{\left((2k^2 - k_2^2)^2\right)kH}{\eta_2}\cosh(\eta_1H)\cosh(\eta_2H) - 8k\eta_1\eta_2\sinh(\eta_1H)\cosh(\eta_2H) -$$

$\frac{4k^3\eta_2}{\eta_1}\sinh(\eta_1 H)\cosh(\eta_2 H) - \frac{4k^3\eta_1}{\eta_2}\sinh(\eta_1 H)\cosh(\eta_2 H) - 4k^3\eta_2 H\cosh(\eta_1 H)\cosh(\eta_2 H) - 4k^3\eta_1 H\sinh(\eta_1 H)\sinh(\eta_2 H)$

Chapter 4

4.1 FML Sample ABD Matrices

ABD Matrices

[A] (N/m) Matrix

1.33538E+08	3.80092E+07	-6.51926E-09
3.80092E+07	1.33538E+08	-3.72529E-09
-6.51926E-09	-3.72529E-09	4.77618E+07

[B] (N) Matrix

0.00000E+00	0.00000E+00	0.00000E+00
0.00000E+00	0.00000E+00	0.00000E+00
0.00000E+00	0.00000E+00	0.00000E+00

[D] (N-m) Matrix

2.92693E+01	4.77335E+00	2.48712E+00
4.77335E+00	1.01984E+01	2.48712E+00
2.48712E+00	2.48712E+00	6.27200E+00

ABD Inverse Matrices

[A] Inverse (m/N) Matrix

8.14871E-09	-2.31939E-09	9.31353E-25
-2.31939E-09	8.14871E-09	3.18991E-25
9.31353E-25	3.18991E-25	2.09372E-08

[B] Inverse (1/N) Matrix

0.00000E+00	0.00000E+00	0.00000E+00
0.00000E+00	0.00000E+00	0.00000E+00
0.00000E+00	0.00000E+00	0.00000E+00

[D] Inverse (1/N-m) Matrix

3.74165E-02	-1.53819E-02	-8.73768E-03
-1.53819E-02	1.14876E-01	-3.94539E-02
-8.73768E-03	-3.94539E-02	1.78549E-01

4.2 Manufacturing of FML Panel

A 12”x12” Ti/CFRP plate is made for experiments, and the details are shown in Figure 4-1.

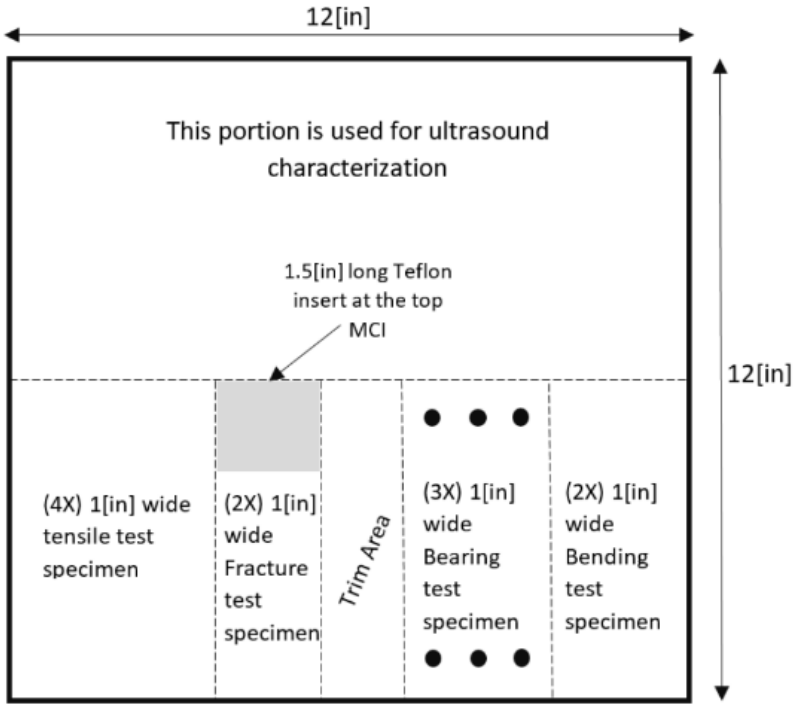

Figure 4-1 FML sample to be manufactured for different experimental program

The plate would be sectioned into tensile test, bending test, bearing test, and fracture test after some ultrasound inspection. In the following section, a brief description of the manufacturing process is described. The layup procedure is very similar to conventional CFRP. The layup is done on a glass plate mold, and it is done with care to avoid wrinkle in the lamina (Figure 4-2).

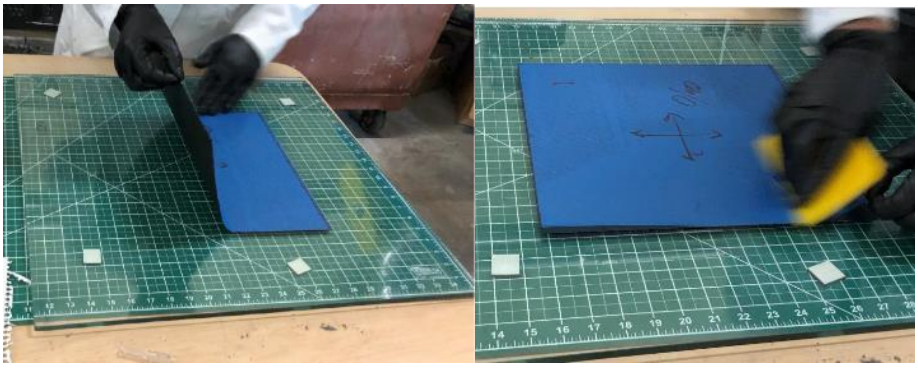

Figure 4-2 Layup of the composite ply shall be done to avoid ply wrinkle

The Ti plies are first treated with So-gel surface treatment agent. The So-gel is a non-hazardous and can yield good surface bonding with composite [96] and thus being chosen. One additional debulking step (apply vacuum pressure, Figure 4-3) is required for the Ti ply because the original Ti sheet stock has a slight curvature and before curing the adhesion between the Ti surface and the CFRP pre-preg is small.

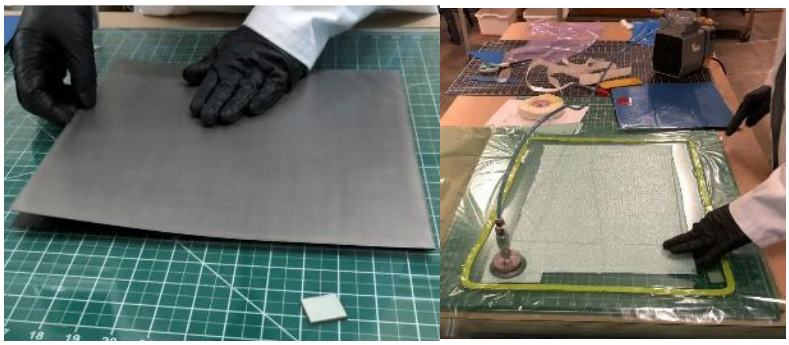

Figure 4-3 The Ti plies have slight curvature and does not adhere to composite plies well and a debulking step (apply vacuum pressure) is added

A release film of 1.5[in] by 2[in] is placed at the location shown in Figure 4-4 to create a disbond between the Ti and composite ply.

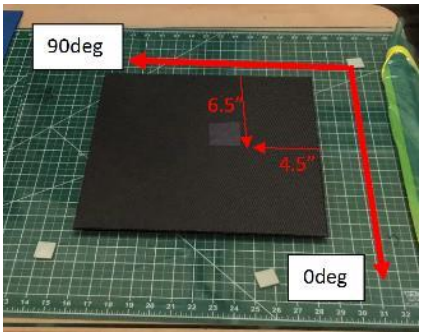

Figure 4-4 A release film is placed at a specific location to create a disbond between the Ti and CFRP ply

The FML panel is then placed into an autoclave to be cured with the curing profile as shown in Figure 4-5

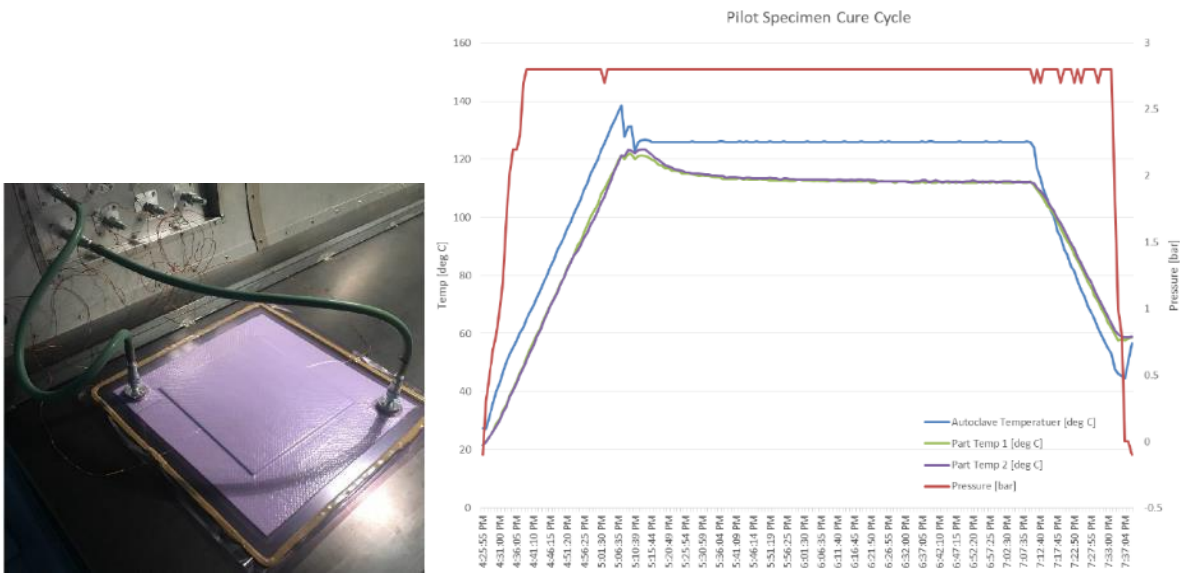

Figure 4-5 FML in autoclave, under vacuum pressure, subjected to the temperature and pressure as shown in curing profile

The FML panel quality is inspected by a water submersion C-scan. Figure 4-6 shows the part has good surface finishing. C-scan also shows no significant variation in the pristine area, and the disbond is clearly visible.

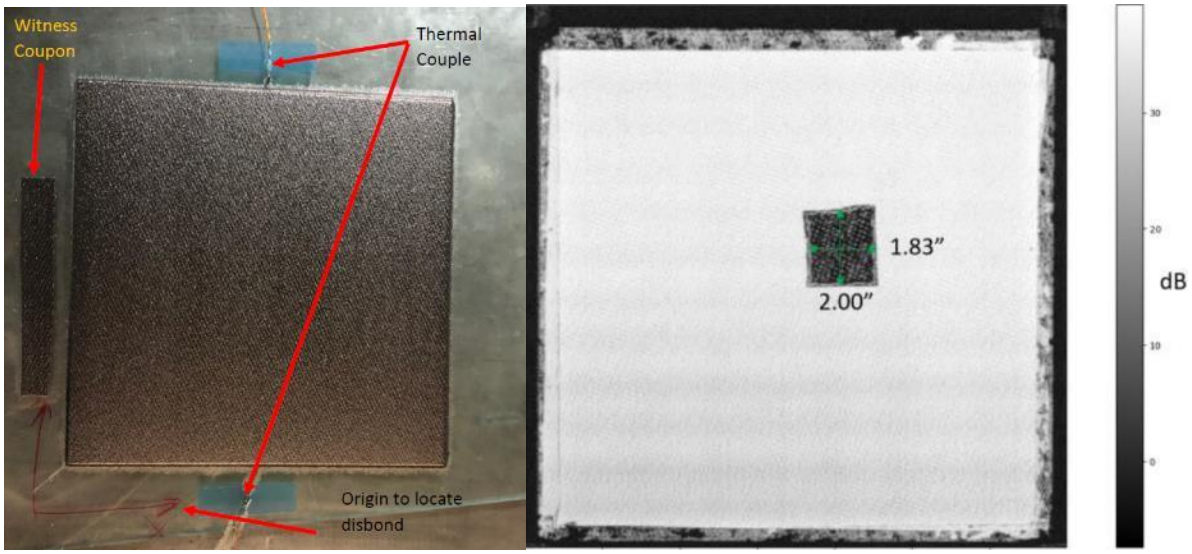

Figure 4-6 The post cure panel on the mold, and the C-scan of the panel

Table 4-1 shows the thickness measurement, done by micrometer at the four corners, the total weight of the specimen. The computed effective density is found to be 2.365 [g/cc].

Table 4-1 FML sample post cure measurements

Measurement	Measure 1	Measure 2	Measure 3
Weight [kg]	0.9285	0.9280	0.9280
Thickness at 0,0 [mm]	3.571	3.576	3.583
Thickness at 12”, 0 [mm]	3.591	3.614	3.614
Thickness at 12”, 12” [mm]	3.561	3.604	3.576
Thickness at 0”, 12” [mm]	3.581	3.583	3.578
1 Ply Thickness [mm]	0.396	0.398	0.391

BIBLIOGRAPHY

[1] E. Lindgren, D. Mollenhauer and M. Flores, "Damage Tolerance for Life Management of Composite Structures Part 2: Nondestructive Evaluation," AFRL, El Paso, 2015.

[2] ASNT, "Introduction to Nondestructive Testing," ASNT, 2017. [Online]. Available: https://www.asnt.org/MinorSiteSections/AboutASNT/Intro-to-NDT. [Accessed 15 11 2018].

[3] Air Force Space Command Space And Missile Systems Center, "Evaluation and Test Requirements for Liquid Rocket Engines," 26 July 2017. [Online]. Available: http://www.dtic.mil/dtic/tr/fulltext/u2/1037878.pdf. [Accessed 15 11 2018].

[4] V. Memmolo, L. Maio and N. D. Boffa, "Damage detection tomography based on guided waves in composite structures using a distributed sensor network," *Optical Engineering*, vol. 55, no. 1, pp. 1-11, 2015.

[5] H. Mei, M. F. Haider, R. James and V. Giurgiutiu, "Pure S0 and SH0 Detections of Various Damage Types in Aerospace Composites," *Composites Part B: Engineering,* vol. 189, 2020.

[6] A. De Luca, D. Perfetto, A. De Fenza, G. Petrone and F. Caputo, "Guided Wave SHM System for Damage Detection in Complex Composite Structure," *Theoretical and Applied Fracture Mechanics,* vol. 105, 2020.

[7] SpaceX, "Anomaly that occurred in preparation for the AMOS-6 mission," SpaceX, 2 January 2017. [Online]. Available: https://www.spacex.com/news/2016/09/01/anomaly-updates. [Accessed 15 November 2018].

[8] T. Kundu, Advanced Ultrasonic Methods for Material and Structure Inspection, Newport Beach: Instrumentation and Measurement Series, 2007.

[9] A. Vlot and L. B. Vogelesang, "Towards Application of Fibre Metal Laminates in Large Aircraft," *Aircraft Engineering and Aerospace Technology,* vol. 71, no. 6, pp. 558-570, 1999.

[10] C. Vermeeren, "An Historic Overveiw of the Development of Fibre Metal Laminates," *Applied Composite Materials,* vol. 10, pp. 189-205, 2003.

[11] R. C. Alderliesten and R. Benedictus, "Fiber/Metal Composite Technology for Future Primary Aircraft Structures," *Journal of Aircraft,* vol. 45, no. 4, pp. 1182-1189, 2008.

[12] T. Sinmazcelik, E. Avcu and M. Bora, "A Review: Fibre Metal Laminates, Background, Bonding Types and Applied Test Methods," *Materials and Design,* vol. 32, pp. 3671-3685, 2011.

[13] A. Fink, P. Camanho and J. Andres, "Hybrid CFRP/Titanium Bolted Joints: Performance Assessment and Application to a Spacecraft Payload Adaptor," *Composites Science and Technology,* vol. 70, pp. 305-317, 2010.

[14] H. Lamb, "On Waves in an Elastic Plate," *Proceeding of the Royal Society*, vol. 1, pp. 114-128, 1917.

[15] R. D. Mindlin, An Introduction to the Mathematical Theory of Vibration of Elastic Plates, Fort Momouth, New Jersey: US Army Signal Corps Engineering Laboratories, 1955.

[16] I. A. Viktorov, Rayleigh and Lamb Waves, New York: Plenum Press, 1967.

[17] J. L. Rose, Ultrasonic Guided Waves in Solid Media, New York: Cambridge University Press, 2014.

[18] W. T. Thomson, "Transmisson of Elastic Waves Through a Startified Solid Medium," *Jounral of Applied Physics,* vol. 22, pp. 89-93, 1950.

[19] N. A. Haskell, "The Dispersion of Surface Waves on Multilayered Media," *Bulletin of the Seismological Society of America,* vol. 43, pp. 17-34, 1953.

[20] L. Knopoff, "A Matrix Method for Elastic Wave Problems," *Bulletin of the Seismological Society of America,* vol. 54, no. 1, pp. 431-438, 1964.

[21] A. Mal, "Guided Waves in Layered Solids with Interface Zones," *International Journal of Engineering Science,* vol. 26, no. 8, pp. 873-881, 1988.

[22] A. Mal, "Wave Propagation in Layered Composite Laminates Under Peroidic Surface Loads," *Wave Motion,* vol. 10, pp. 257-266, 1988.

[23] A. Mal and C. C. Yin, "Guided Waves in Fiber-Reinforced Composite Plates," in *Seminar for 65th Birthday Celebration of Professor S.C. Dasgupta*, 1988.

[24] M. J. Lowe, "Matrix Techniques for Modeling Ultrasonic Waves in Multilayered Media," *IEEE Transactions on Ultrasonics, Ferroelectrics, and Frequency Control,* vol. 42, no. 4, p. 525, 1995.

[25] M. J. Lowe, Plate Waves for the NDT of Diffusion Bonded Titanium, London: Imerial College of London, 1992.

[26] H. S. Samajder, Lamb wave propagation in elastic plates under various loads, Los Angeles: Electronic Thesis and Dissertations UCLA, 2015.

[27] B. Mace and D. Duhamel, "Finite Element Prediction of Wave Motion in Structural Waveguides," *Acoustical Society of America,* vol. 117, no. 5, pp. 2835-2843, 2005.

[28] D. Duhamel, B. R. Mace and M. J. Brennan, "Finite Element Analysis of the Vibrations of Waveguides and Periodic Structures," *Journal of Sound and Vibrations,* vol. 294, pp. 205-220, 2006.

[29] M. Maess, J. Herrmann and L. Gaul, "Finite Element Analysis of Guided Waves in Fluid-Filled Corrugated Pipes," *Journal of Acoustic Society,* vol. 121, no. 3, pp. 1313-1323, 2007.

[30] C. Schaal, S. Bischoff and L. Gaul, "Analysis of Wave Propagation in Periodic 3D Waveguides," *Mechanical Systems and Signal Processing,* vol. 40, pp. 691-700, 2013.

[31] C. Dorz, Z. Zergoune and R. Boukadia, "Vibro-acoustic Optimisation of Sandwich Panels using the Wave/Finite Element Method," *Composite Structures,* vol. 156, pp. 108-114, 2016.

[32] C. Schaal, S. Tai and A. Mal, "On the Assumption of Transverse Isotropy of a Honeycomb Sandwich Panel for NDT Applications," in *Health Monitoring of Structural and Biological Systems 2017*, Protland, 2017.

[33] J. M. Renno and B. R. Mace, "Calculating the Forced Response of Tow-Dimensional Homogeneous Media Using the Wave and Finite Element Method," *Journal of Sound and Vibration,* vol. 330, pp. 5913-5927, 2011.

[34] A. Jan, Wave Propagation in Elastic Solids, North Holland: Elsevier, 1984.

[35] I. Nedospasov, V. Mozhaev and I. Kuznetsova, "Unusual Energy Properties of Leaky Backward Lamb Waves in a Submerged Plate," *Ultrasonics,* vol. 77, pp. 95-99, 17.

[36] R. M. Jones, Mechanics of Composite Materials, Blacksburg, Virginia: Taylor & Francis, 1999.

[37] L. J. Gibson and M. F. Ashby, Cellular Solids: Structure and Properties, Cambridge: Cambridge University Press, 1999.

[38] A. Mal and L. Knopoff, "A Differential Equation for Surface Waves in Layers with Varying Thickness," *Journal of Mathematical Analysis and Applications,* vol. 21, pp. 431-444, 1968.

[39] A. Mal and L. Knopoff, "Transmission of Rayleight Waves Past a Step Change in Elevation," *Bulletin of the Seimological Society of America,* vol. 55, no. 2, pp. 319-334, 1965.

[40] J. A. Hudson and L. Knopoff, "Transmission and Reflection of Surface Waves at a Corner," *Journal of Geographical Research,* vol. 69, no. 2, pp. 275-280, 1964.

[41] N. Vasudevan and A. Mal, "Response of an Elastic Plate to Localized Transient Sources," *Journal of Applied Mechanics,* vol. 52, pp. 356-362, 1985.

[42] A. Mal and S.-s. Lih, "Elastodynamic Response of a Unidirectional Composite Laminate to Concentrated Surface Loads: Part I," *Journal of Applied Mechanics,* vol. 59, pp. 878-886, 1992.

[43] S.-s. Lih and A. Mal, "Elastodynamic Response of a Unidirectional Composite Laminate to Concentrated Surface Loads: Part II," *Journal of Applied Mechanics,* vol. 59, pp. 887-892, 1992.

[44] C. Schaal and A. Mal, "Lamb Wave Propagation in a Plate with Step Discontinuities," *Wave Motion,* vol. 66, pp. 177-189, 2016.

[45] C. Schaal, S. Zhang and H. Samajder, "An Analytical Study of the Scattering of Ultrasonic Guided Waves at a Delamination-Like Discontinuity in a Plate," *Journal of Mechanical Engineering Science,* vol. 0, pp. 1-14, 2017.

[46] Y. Cho and J. Rose, "A Boundary Element Solution for a Mode Conversion Study on the Edge Reflection of Lamb Waves," *The Journal of the Acoustical Society of America,* vol. 99, no. 4, pp. 2097-2109, 1996.

[47] P. P. Delsanto, R. S. Schechter and H. H. Chaskelis, "Connection Machine Simulation of Ultrasonic Wave Propagation in Materials II: The Two-Dimensional Case," *Wave Motion,* vol. 20, pp. 295-314, 1994.

[48] Y. Shen and C. Cesnik, "Efficient Modeling of Nonlinear Scattering of Ultrasonic Guided Waves from Fatigue Cracks Using Local Interaction Simulation Approach," in *ASME International Mechanical Engineering Congress and Exposition*, Phoenix, 2016.

[49] Y. Shen and C. Cesnik, "Hybrid local FEM/Global LISA Modeling of Guided Wave Propagation and Interaction with Damage in Composite Structures," in *SPIE Smart Structures and Materials + Nondestructive Evaluation and Health Monitoring*, San Diego, 2015.

[50] Z. A. Ahmad, Numerical Simulations of Lamb Waves in Plates Using a Semi-Analytical Finite Element Method, Magdeburg: Otto-von-Guericke Universitaet Magdeburg, 2011.

[51] W. Ostachowicz, P. Judela, M. Krawczuk and A. Zak, Guided Waves in Structures for SHM: The Time-domain Spectral Element Method, West Sussex: Wiley, 2012.

[52] J. Doyle, Wave Propagation in Structures: Spectral Analysis using Fast Discrete Fourier Transforms, New York: Springer-Verlag, 1997.

[53] S. A. Rizzi and J. F. Doyle, "Spectral Analysis of Wave Motion in Plane Solids with Boundaries," *Journal of Vibration and Acoustics,* vol. 114, no. April, pp. 133-140, 1992.

[54] D. Samaratunga, R. Jha and S. Gopalakrishnan, "Wavelet Spectral Finite Element for Modeling Guided Wave Propagation and Damage Detection in Stiffened Composite Panels," *Structural Health Monitoring,* vol. 15, no. 3, pp. 317-334, 2016.

[55] D. B. Goetschel, S. B. Dong and R. Muki, "A Global Local Finite Element Analysis of Axisymmetric Scattering of Elastic Waves," *Journal of Applied Mechanics,* vol. 49, no. December, pp. 816-820, 1982.

[56] M. Koshiba, S. Karakida and M. Suzuki, "Finite-Element Analysis of Lamb Wave Scattering in an Elastic Plate Waveguide," *IEEE Transactions on Sonics and Ultrasonics,* vol. 31, no. 1, pp. 18-24, 1984.

[57] Y. N. Al-Nassar, S. K. Datta and A. H. Shah, "Scattering of Lamb Waves by a Normal Rectangular Strip Weldment," *Ultrasonics,* vol. 29, no. March, pp. 125-132, 1991.

[58] Z. Chang and A. Mal, "A Semi-Numerical Method for Elastic Wave Scattering Calculations," *Geophysics Journal International,* vol. 143, pp. 328-334, 2000.

[59] C. Schaal, R. M'Closkey and A. Mal, "A Semi-analytical Method for Caculating Resonator Energy Loss into Plate Substrates," *IEEE International Symposium on Inertial Sensors and Systems,* pp. 17-20, 2016.

[60] C. Schaal, R. M'Closkey and A. Mal, "Parametric Studies for Semi-Analytical Investigation of Plate Mounted Resonators," in *SPIE Health Monitoring of Structural and Biological Systems*, 2017.

[61] C. Schaal, H. Samajder, H. Baid and A. Mal, "Rayleigh to Lamb Wave Conversion at a Delamination-like Crack," *Journal of Sound and Vibration,* vol. 353, pp. 150-163, 2015.

[62] C. Schaal and A. Mal, "Lamb wave propagation in a plate with step discontinuities," *Wave Motion,* vol. 66, pp. 177-189, 2016.

[63] A. Mal and Z. Chang, "A semi-numerical method for elastic wave scattering calculations," *Geophysics International Journal,* vol. 143, pp. 28-334, 1999.

[64] SIMULIA, "Abaqus 6.14 Documentation," 2014. [Online]. Available: http://abaqus.software.polimi.it/v6.14/index.html. [Accessed 2018].

[65] A. Mal and C. Yin, "Analysis of Acoustic Pulses Reflected from Fiber-Reinforced Composite Laminates," *ASME Journal of Applied Mechanics,* vol. 91, 1991.

[66] A. Mal and Y. Bar-Cohen, "Wave Attenuation in Fiber-Reinforced Composites," *Mechanics and Mechanisms of Material Damping,* vol. 1169, pp. 245-261, 1992.

[67] T. Kundu and A. Mal, "Elastic Waves in a Multilayered Solid due to a Dislocation Source," *Wave Motion,* vol. 7, pp. 459-471, 1985.

[68] E. Botelho and R. Silva, "A Review on the Development and Properties of Continuous Fiber/Epoxy/Aluminum Hybrid Composites for Aircraft Structures," *Materials Research,* vol. 9, no. 3, pp. 247-256, 2006.

[69] P. Linde and J. Pleitner, "Modelling and Simulation of Fibre Metal Laminates," in *ABAQUS Users' Conference*, 2004.

[70] P. Cortes and W. J. Cantwell, "The Prediction of Tensile Failure in Titanium-Based Thermoplastic Fibre-Metal Laminates," *Composites Science and Technology,* vol. 66, pp. 2306-2316, 2006.

[71] P. Camanho, C. Davila and S. Pinho, "Prediction of in situ Strengths and Matrix Cracking in Composites Under Tranverse Tension and In-plane Shear," *Composites: Part A,* vol. 37, pp. 165-176, 2006.

[72] C. Davila and P. Camanho, "Failure Criteria for FRP Laminates," *Journal of Composite Materials,* vol. 39, pp. 323-345, 2005.

[73] M. J. Hinton and A. S. Kaddour, "A Comparison of the Predictive Capabilities of Current Failure Theories for Composite Laminates, Judged Against Experimental Evidence," *Composites Science and Technology,* vol. 62, pp. 1725-1797, 2002.

[74] Z. Hashin, "Failure Criteria for Unidirectional Fiber Composites," *Journal of Applied Mechanics,* vol. 47, pp. 329-334, 1980.

[75] A. Puck and H. Schuermann, "Failure Analysis of FRP Laminates by Means of Physically Based Phenomenological Models," *Composites Science and Technology,* vol. 58, pp. 1045-1067, 1998.

[76] J. Hundley, J.-M. Yang and T. Hahn, "Bearing Strength Analysis of Hybrid Titanium Composite Laminates," *AIAA Journal,* vol. 46, no. 8, pp. 2074-2085, 2008.

[77] P. Maimi, P. P. Camanho, J. A. Mayugo and C. C. Davila, "A Continuum Damage Model for Composite Laminates: Part I Constitutive Model," *Mechanics of Materials,* vol. 39, pp. 897-908, 2007.

[78] P. Maimi, P. P. Camanho, J. A. Mayugo and C. G. Davila, "A Continuum Damage Model for Composite Laminates: Part II Computational Implementation and Validation," *Mechanics of Materials,* vol. 39, pp. 909-919, 2007.

[79] I. Lapczyk and J. Hurtado, "Prgressive Damage Modeling in Fiber-Rinforced Materials," *Composites: Part A,* vol. 38, pp. 2333-2341, 2007.

[80] Y. X. Gan, "Effect of Interface Structure on Mehcanical Properties of Advanced Composite Materials," *International Jorurnal of Molecular Science,* vol. 10, pp. 5115-5134, 2009.

[81] Y. Fu, J. Zhong and Y. Chen, "Thermal Postbuckling Analysis of Fiber-Metal Laminated Plates Including Interfacial Damage," *Composites: Part B,* vol. 56, pp. 358-364, 2014.

[82] G. Lawcock, L. Ye, Y.-W. MMai and C.-T. Sun, "Teh Effect of Adhesive Bonding Between Aluminum and Composite Prepreg on the Mechanical Properties of Carbon-Fiber Reinforced Metal Laminates," *Composites Science and Technology,* vol. 57, pp. 34-45, 1997.

[83] J. G. Carrillo and W. J. Cantwell, "Mechanical Properties of a Novel Fiber-Metal Laminate Based on a Polypropylene Composite," *Mechanics of Materials,* vol. 41, pp. 828-838, 2009.

[84] Autodesk, "Composite material design simulation tool," Autodesk, 2020. [Online]. Available: https://www.autodesk.com/products/helius-composite/overview?plc=ACMPDS&term=1-YEAR&support=ADVANCED&quantity=1. [Accessed 6 July 2020].

[85] P. P. Camanho, A. Fink, A. Obst and S. Pimenta, "Hybrid Titanium - CFRP Laminates for High Performance Bolted Joints," *Composites: Part A,* vol. 40, pp. 1826-1837, 2009.

[86] B. A. A. A. J Blaber, "Ncorr: Open-Source 2D Digital Image Correlation Matlab Software," 2015.

[87] National Institute for Aviation Research, Composites Materials Handbook vol. 3 Polymer Matrix Composites: Materials Usage, Deisgn, and Analysis, Wichita: SAE International, 2012.

[88] F. Ricci, E. Monaco, L. Maio, N. Boffa and A. Mal, "Guided waves in a stiffened composite laminate with a delamination," *Structural Health Monitoring,* vol. 15, no. 3, pp. 351-358, 2016.

[89] C. Schaal, X. Cao and A. Mal, "The Influence of Stiffeners on the Propagation of Guided Ultrasonic Waves," in *Proceedings of the 10th International Workshop on Structural Health Monitoring* -- *IWSHM*, Palo Alto, CA, USA, 2015.

[90] Z. Chang, D. Guo and A. Mal, "Lamb Wave Propagation Across a Lap Joint," *Review of Progress in Quantitative Nondestructive Evaluation,* vol. 15, pp. 185-192, 1996.

[91] T. Koh, S. Feih and A. Mouritz, "Experimental determination of the structural properties and strengthening mechanisms of z-pinned composite T-joints," *Composite Structures*, vol. 93, no. 9, pp. 2222-2230, 2011.

[92] T. Q. Cobb, W. S. Johnson and S. E. Lowther, "Optimization of Surface Treatment and Adhesive Selection for Bond Durability in Ti-15-3 Laminates," *The Journal of Adhesion,* vol. 71, no. 2-3, pp. 115-141, 1999.

[93] V. Memmolo, L. Maio, N. Boffa, E. Monaco and F. Ricci, "Damage Detection Tomography based on Guided Waves in Composite Structure Using a Distributed Sensor Network," *Optical Engineering,* vol. 55, p. 011007, 2016.

[94] C. Zhang, Z. Zhang, H. Ji, J. Qui and C. Tao, "Mode Conversion Behavior of Guided Wave in Glass Fiber Reinforced Polymer with Fatigue Damage Accumulation," *Composites Sicence and Technology,* vol. 192, 2020.

[95] A. Vlot, Fibre Metal Laminates - An Introduction, Springer, 2001.

[96] S. Tai, F. Kotobuki, L. Wang and A. Mal, "Modeling Ultrasonic Elastic Waves in Fiber-Metal Laminate Structures in Presence of Sources and Defects," *Journal of Nondestructive Evaluation, Diagnostics and Prognostics of Engineering Systems,* pp. 1-42, 2020.

[97] S. Tai, L. Wang, L. Araque, A. Mal and C. Schaal, "Effects of Homogenization and Quasi-Isotropy Assumptions on Guided Wave-Based Nondestructive Testing Methods," in *International Workshop on Structural Health Monitoring 2019,* Stanford , 2019.

[98] A. Srivastava and F. Lanza di Scalea, "Quantitative Structural Health Monitoring by Ultrasonic Guided Waves," *Journal of Engineering Mechanics,* vol. 136, pp. 937-944, 2010.

[99] A. Spada, M. Capriotti, R. Cui and F. Lanza di Scalea, "Improved global-local model to predict guided-wave scattering patterns from discontinuities in complex parts," in *SPIE Spart Structures + Nondestructive Evaluation*, Denver, 2019.

[100] V. Memmolo, L. Maio and N. D. Boffa, "Damage detection tomography based on guided waves in composite structures using a distributed sensor network," *SPIE*, vol. 55, no. 1, 2015.

[101] M. Lowe, Plate Waves for the NDT of Diffusion Bonded Titanium, London: University of London, 1992.

[102] M. Lowe, "Matrix Techniques for Modeling Ultrasounic Waves in Multilayered Media," *IEEE Transactions on Ultrasonics, Ferroelectrics, and Frequency Control*, vol. 42, no. 4, pp. 525-542, 1995.

[103] G. R. Johnson and W. H. Cook, "Fracture Characteristics of Three Metals Subjected to Various Strains, Strain Rates, Temperatures and Pressures," *Engineering Fracture Mechanics*, vol. 21, no. 1, pp. 31-48, 1985.

[104] M. F. Haider, B. Poddar and V. Giurgiutiu, "Experimental Validation of an Analytical Method to Predict Lamb Wave Scattering from a Discontinuity," *Smart Materials and Structures*, vol. 28, 2018.

[105] M. F. Haider and V. Giurgiutiu, "An Improved Analytical Method to Overcome Convergece Issues in Composites Guided Wave Prediction," in *Proceedings of SPIE*, Denver, 2019.

[106] J. Galan and R. Abascal, "Numerical simulation of Lamb wave scattering in semi-infinite plates," *International Journal for Numerical Methods in Engineering*, vol. 53, pp. 1145-1173, 2002.

[107] P. Delsanto, R. Schechter, H. Chaskelis, R. Mignogna and R. Kline, "Connection machine simulation of ultrasonic wave propagation in materials. II: The two-dimensional case," *Wave Motion*, vol. 20, pp. 295-314, 1994.

[108] S. Datta and A. Shah, Elastic Waves in Composite Media and Structures, Boca Raton: Taylor & Francis Group, 2009.

[109] G. Cloud and E. Patterson, "Joining Technologies for Composites and Dissimilar Materials," in *Proceedings of the 2016 Annual Conference on Experimental and Applied Mechanics*, 2016.

[110] S. Banerjee, P. Banerji, F. Berning and K. Eberle, "Lamb Wave Propagation and Scattering in Layered Composite Plates," in *SPIE NDE for Health Monitoring and Diagnostics*, San Diege, 2003.

[111] R. Alderliesten, Fatigue and Fracture of Fibre Metal Laminates, Cham: Springer, 2017.

[112] Z. A. Ahmad, J. M. Vibar-Perez and U. Gabbert, "Semi-analytical finite element method for modeling of lamb wave propagation," *CEAS Aeronautical Journal*, vol. 4, no. 1, pp. 421-433, 2013.

[113] Rayleigh, "On the Free Vibration of an infinite plate of homogeneous isotropic elastic matter," *Proceeding of the London Mathematical Society*, vol. 20, pp. 225-234, 1889.